Università degli Studi di Ferrara

DOTTORATO DI RICERCA IN
FISICA

CICLO XXVII

COORDINATORE Prof. Vincenzo Guidi

Crystals with curved diffracting planes for hard X-ray optics

Settore Scientifico Disciplinare FIS/03

Dottorando
Dott. Bellucci Valerio

_____
(firma)

Tutore
Prof. Guidi Vincenzo

_____
(firma)

Anni 2012/2014

CONTENTS

List of figures

Abstract

Crystals with curved diffraction planes (CDP crystals) are an emerging technology in hard X-ray optics. Through them, it is possible to condition hard X-ray beams with high energy efficiency and flexibility. Optical instruments for visible light are not effective to manipulate high-energy radiation. In fact, the phenomena of reflection and refraction on which they are based become unimportant for electromagnetic waves with high energy. For this reason, optics of hard X-rays and gamma rays has been up to now based direct view instruments.

In contrast, diffraction phenomena can be important even at high energies. Therefore, it is possible to condition hard X-ray beams by Bragg diffraction. Bragg diffraction is called Laue diffraction when the electromagnetic wave goes through the crystal. Due to the length of penetration of high-energy photons, this configuration appears to be preferable than diffraction in reflection geometry (Bragg diffraction). Recently, optical systems have been developed based on perfect crystals or mosaic crystals. However, instruments based on these materials have constructive difficulties, poor reproducibility, and finally a limited efficiency.

Crystals with curved lattice planes have an efficiency in the manipulation of X-rays that approaches the unity. Through the curvature of their plans, they offer a continuum of possible angles of diffraction to incident radiation. Thus, the curvature of planes allows to influence photons in a wide range of energies. It is also possible to apply more than one curvature to a single crystal, deforming the symmetry, thus turning it into a focusing element.

The curved crystals have elective application in the construction of lenses for hard X-rays (Laue lenses), composed by a set of crystal with diffraction planes oriented towards a common point, so as to diffract the incident radiation towards the focus of the lens. This tool is especially useful in the field of astrophysics and medical physics. The observation of the sky over energy of 70 keV is still left to direct view instruments. These have a low angular resolution, a low signal to noise ratio, and a high weight, which is an important parameter because the observation of X-rays is only possible out of the atmosphere. The cosmic sources of X-rays produce a very low flux of photons, so the signal to noise ratio of the instrument becomes a key factor for the investigation of these sources. Today, only the spectra of the most intense sources are known at energies above 70 keV.

Another discipline that can benefit from the use of CDPs crystals is nuclear medicine. Indeed, it would be possible to increase the sensitivity and accuracy of instruments for nuclear medicine by using focusing optics based on curved crystals. The spatial resolution of the instrument would be increased to a sub-millimeter precision, with which it would be possible to accurately locate tumors and other phenomena of interest, and to provide more information on the same. Due to the high reflectivity of the CDPs crystals, even the number of photons that can be collected on the detector would be increased, with a consequent improvement in the sensitivity of the instrument, and a decrease in the dose of radio-drug to be injected into the patient.

The formalism developed so far under the dynamical theory of diffraction allows to describe effectively crystals with flat diffraction planes, or crystals with diffraction planes strongly deformed. Various applications require CDPs with low curvatures, in particular when crystals with high atomic number are used. In this case, the formalism of dynamical theory is not applicable in a simple way. To know the performance of the CDPs crystals in these areas of application, it is necessary the

development of a treatment dedicated to the purpose. The theoretical work has touched the development of the dynamic theory of diffraction in order to cover its weaknesses for CDPs with low curvature.

The work of technological development and construction of hardware for scientific research focused on the development and production of innovative crystals for the construction of hard X-ray lenses. The construction of Laue lenses has been simplified with the introduction of focusing crystals. The thesis work was partially carried out within the LAUE Project, funded by ASI, whose purpose was the construction of a large-area Laue lenses. The work done during the doctoral thesis has led to a rethinking of the project in order to use focusing crystals and thus to increase the resolution and sensitivity of the lens.

The work on crystals for Laue lenses did not end with the LAUE Project, but it continued with a series of technological innovations with the aim to increase the maximum resolution and sensitivity achievable by Laue lenses. These innovations include the introduction of crystals with multiple curvatures and focusing crystals, the study of novel methods with which to produce crystals with CDPs, the construction of stacks of multi-crystals, the use of curved asymmetric diffraction planes. The experimental tests were performed at the facilities of ESRF (European Synchrotron Radiation Facility, Grenoble, France), ILL (Institut Laue-Langevin, Grenoble, France) and LARIX (LARge Italian X-ray facility, Ferrara, Italy).

Simulations were also performed to estimate the possible interferences that a Laue lens could suffer in orbit because of the interaction with cosmic rays and the consequent production of parametric X-rays. This source of X-rays may interfere with measurements of celestial X-ray sources. The work has led to the exclusion of this possibility, since the emission of parametric X-rays would be less than the sensitivity of the lens itself.

Finally, the technologies developed to produce CDPs crystals were used for the construction of a crystalline undulator built as a prototype of X-ray source with high-energy and high flux. Lattice planes of a crystals where shaped in an undulated structure. Characterization of these lattice planes showed near-ideal results. High-energy charged particles channeled through these planes would produce coherent X-rays. The prototype will be part of an experiment at the SLAC accelerator (San Francisco, USA).

1 Introduction to diffractive optics

1.1 Background – instrumentation for X and Gamma ray optics

The lenses used to manipulate visible light are composed of transparent material with refractive index significantly different from 1. There are no materials with similar properties when the energy of electromagnetic waves reaches the X-ray or gamma ray band. In fact, in this energy band the refractive index of materials is very near to 1. The mirrors that are used to manipulate visible or ultraviolet light have a low efficiency too in reflecting X-rays. Indeed, photons of high energy poorly interact with matter. It is possible to build mirrors that reflect X-rays up to 70 keV, but the reflection occurs only if the angle of incidence with the surface of the mirror is very small, usually between 10 arcmin and 2 degrees. Currently, the most efficient tools to manipulate X-rays are collimators and monochromators, while solid state or gas detectors are used for the detection of photons.

In recent years there have been many efforts on the development of optics for hard X-rays based on Bragg diffraction, using crystals as active elements for manipulating X and gamma rays. Diffraction is a phenomenon very efficient for photons of energy from a few keV to 1 MeV. Diffraction allows to treat the beam without reducing too much the intensity of the same, and without the need overly complex systems. The high efficiency of diffraction phenomena also allows manipulating X-rays with incidence angle near to the normal to the surface of the optical apparatus. Thus, it is possible to substantially reduce the size of the instrument itself. This type of diffraction is called Laue diffraction, and occurs by interaction of the radiation with lattice planes crossing the crystal. Lenses of this type were initially developed for astronomy in the X-ray band, but they soon found applications in nuclear medicine too. Here are some tools used in X-ray optics up to the latest developments, and some applications of the same.

1.1.1 Collimators

Collimators are mechanical devices for stopping part of the photons that pass through the collimator itself. The simplest type of collimator is a plate of absorbent material with an opening with size equal to the desidered size of the exit beam. Usually collimators are made of materials with high atomic number so as to present a high rate of absorption to incident radiation (the most common materials are Lead or Tungsten). Additionally, materials that do not present edge absorption or fluorescence in the range of energies of the incident photons are preferred. Indeed, materials with an absorption edge would result in the production of radiation by the same collimator. When this choice is not possible, it is necessary the use of collimators made up of layers of different materials, which are chosen in such a way as to mitigate the fluorescence.

The collimators are used to manipulate beams of X-rays, or to increase the resolution of detectors. X-ray sources produce emission with spatial dimensions too high to be usable. Collimators are used to reduce the size and the divergence of the beam (as well as monochromators) so as to obtain a useful beam size and divergence. This configuration is widely used in experiments that use artificial X-ray sources. For example, if you use X-rays to analyze a sample, it is useful to have a beam as narrow as possible and free of divergence, to ensure high resolution and a precise analysis.

Often the collimators used for these purposes have adjustable openings made by mobile slits, in order to vary the size of the beam at the exit of the collimator.

Collimators are used in detectors to limit their angle of view, so to have directional information from the measured radiation, increasing the resolution and reducing the background noise caused by photons from other directions. For this application, the simplest collimators have the shape of a box or of a pipe open at the ends, at one end the sensing face of the detector is located. In Figure 1-1, if A is the area of the sensitive face of the detector, equal to the opening of the collimator, and h is the height of the collimator, the solid angle observable will be about A/h^2, centered around the axis of the collimator. The photons that originate from an angle outside of this field of view impinge on the walls of the collimator and they are absorbed. If the collimator does not present cylindrical symmetry around the center of the detector, the angle of view θ changes with the variation of the angle φ around the axis of the collimator.

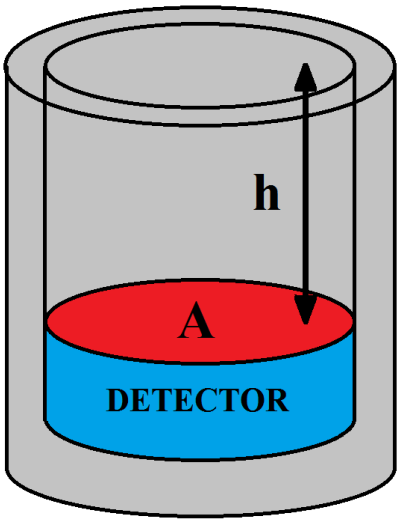

Figure 1-1

Simple example of a collimator (in gray), where A is the sensitive area of the detector, h is the distance between the detector and the opening of the collimator.

Collimators with this geometry are used in X-ray astronomy. In this case, the collimators must meet three requirements. The first requirement is to be as absorptive as possible, to block the photons out of the angle of view. The last requirements are to be light and not very bulky, to be easy to use in balloon or satellite experiments. In some cases, it is necessary to place on top of the detector a collimator of a complex shape (ex. Figure 1-2) that covers part of the detector. In this case it is even more important that the collimator is not bulky, to ensure a wide opening for the photons inside the angle of view. Usually the absorption of a material increases with its atomic number, and therefore of its weight. Therefore, it is necessary to optimize the thickness of the walls of the collimator in order to find a compromise between the requirements. For example, in the case of the detector PDS mounted on BeppoSAX (Orlandini, 2008/2009), it was used a collimator consists of pipes of Tantalum with hexagonal section, with length of 20 cm and thickness of 50 μm. The inside of the tubes was covered with a double layer of tin (100 pM) and Copper (50 um) in the first 4 cm from the base. The layer of tin had the purpose of mitigating the fluorescence emission from the K shell of tantalum (Kα = 57.07 keV, Kβ = 65.56 keV) while the copper layer attenuates the X-ray emission by fluorescence from tin (Kα = 25.1 keV, Kβ = 28.5 keV). This configuration is called grading shielding, and it allowed to keep 80% of the effective area of the detector.

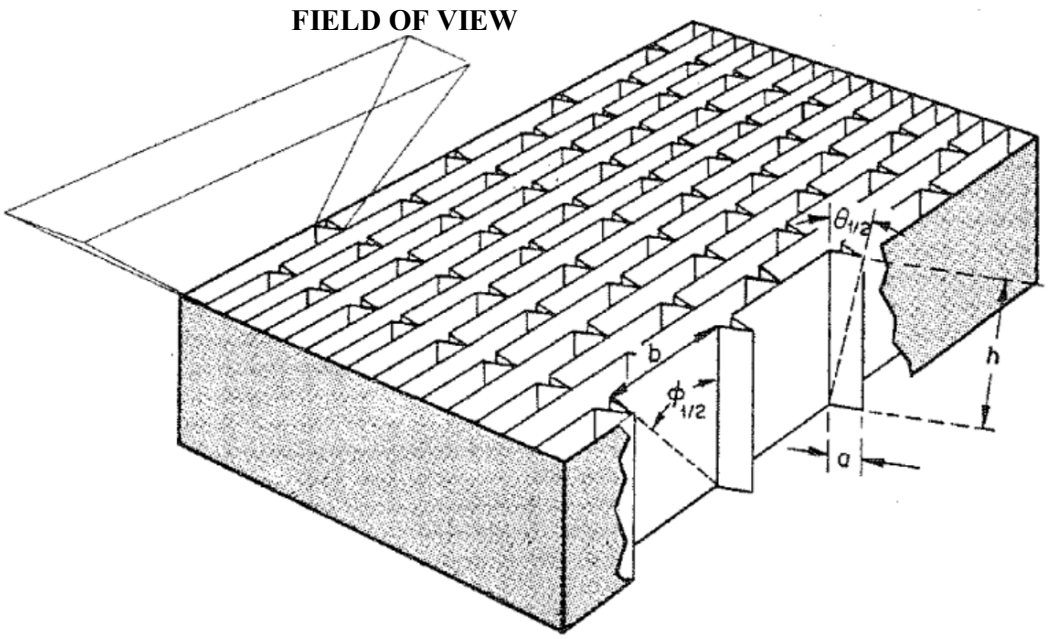

Figure 1-2

Collimator made of a series of rectangular tubes, height h and section a × b. This collimator was placed on the detector PDS mounted on BeppoSAX (Orlandini, 2008/2009). The X-rays that strike the walls of the collimator do not reach the detector. The field of view has a different extension in the two perpendicular directions, with φ = arctg(b/h), θ = arctg(a/h).

1.1.2 Monochromators

Most of artificial X-ray sources produces polychromatic radiation with high divergence, and high spatial extension. For example, an X-ray tube emits radiation in the typical continuous spectrum of Bremsstrahlung. The photons are emitted in all directions, but with preferential direction towards the exit of the tube, thus producing a beam with large divergence and large spatial extent. A synchrotron produces radiation with less divergence and spatial extent, but not enough to be used in most of the experiments. It is possible to partially reduce the divergence and the spatial extent of a beam by collimators, but collimators do not allow to reduce the range of energies contained in a beam. Indeed, it is necessary to introduce at least a monochromator in the system to obtain a highly monochromatic (high energy resolution) and low divergence (high angular resolution) photon flux. A monochromator is composed of one or more crystals. An X-ray beam enters the monochromator and it undergoes multiple Bragg diffraction (at least two diffraction) by the lattice planes of the crystals composing the monochromator. Only the photons entering the monochromator at a certain angle and at a certain energy, defined by Bragg's law $n\lambda = 2dsin\theta$ $n = nhc/E$, undergo diffraction by

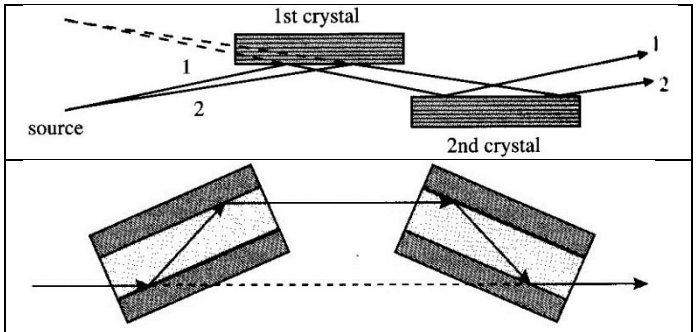

Figure 1-3

Examples of monochromators (Authier A. , 2001). (a) monochromator composed of two crystal, the output direction of the beam is fixed. (b) channel-cut monochromator with four reflections, with fixed output beam.

all the crystals composing the monochromator, thus they exit the monochromator without being absorbed. Usually the monochromators consists of perfect crystals, whose angle tolerance for diffraction (and therefore the tolerance in energy) is equal to the Darwin width δ_w. In good monochromators the divergence of the output beam is equal to or less than the Darwin width of the material used in the monochromator. The energy spectrum of the photons that constitute the beam is cut, and only a small energy band can pass. Many types of monochromators exist, each type best suits the analysis to perform (Figure 1-3).

1.1.3 Polarizers

Many experiments require X-rays with linear or circular polarization. As an example, measurements on magnetic materials for the detection of X-ray magnetic scattering, or for the detection of the signal of X- Ray Magnetic Circular Dichroism (XMCD) or of X-Ray Magnetic Linear Dichroism (XMLD) require linear or circular polarization. In the first case, the fact that the scattering cross section contains also a term of magnetic origin (Hannon, 1988) allows measurements of diffraction or reflectivity highlighting both the contributions of structural origin and those of a magnetic nature. Therefore, it is possible to derived structural information about the order, and on the magnetic field by working near the absorption thresholds (Wilkins, 2003). In the last two cases (XMCD and XMLD), measurements are made by recording the absorption spectra close to the absorption thresholds of the material to be studied. The XMCD signal is obtained by taking the difference between the absorption spectrum collected with radiation with circular right polarization and the radiation collected with circular left polarization. This procedure allows to obtain the value of the magnetic moment. Conversely, the XMLD signal is obtained by comparing the absorption spectra obtained with two linear polarizations orthogonal to each other. The difference between XMCD and XMLD lies in the fact that the first is used to study ferromagnetic materials, while the second is used to study the antiferromagnetic type materials (Kuiper, 1993) (Stöhr, 1999).

Synchrotron radiation is plane polarized in the plane of the orbit, while it becomes elliptically polarized far from this plane. Radiation from X-ray tubes is unpolarized, but it can be polarized using phase retarders or Bragg diffraction. Linear polarization is achieve by eliminating one of the two components of the polarization. Different types of polarizers have been used to achieve this result. The two polarization directions have different absorption coefficients near the Bragg angle. In this case, one of the two absorption coefficient is much larger than the other one, then the part of the X-ray beam polarized in that direction is completely absorbed (Staudenmann, 1985). Another type of linear polarizer take advantage of Bragg diffraction. Lattice planes for which the Bragg angle is close to $\pi/4$ cannot diffract the π-polarized component of the X-ray beam, so only the σ-polarized components is diffracted (Chandrasekaran, 1959). This method cannot be used for hard X-rays because the Bragg diffraction angle becomes too small. However, even at high energy the two polarization directions are diffracted with different efficiency. Then, linear polarization is attained by multiple diffractions in channel-cut crystals (Sato, 2000). Single-crystal phase retarders are used to attain circularly polarized X-rays. X-ray birefringence occurs in a perfect crystal that is oriented in the near of a Bragg reflection, giving rise to phase shifts between the σ and π polarization components of the beams propagating through the crystal. This results in diffracted beams whose polarization ellipticity and handedness can be adjusted according to the crystal thickness and angular deviation from the Bragg condition. In recent years the availability of good quality diamond crystal wafers has

made them popular for use as phase retarders, owing to diamond's small absorption coefficient (Berman, 2002).

1.1.4 Coded Masks

A coded mask is a mask with zones which are transparent or opaque to X-rays. It is placed at the opening of a detector. The projected image on the detector allows to get images with spatial resolution through a decoding algorithm (Skinner, 2004). The type of approach followed is similar to that used in dark rooms with visible light. These tools require two different processes: the encoding process of the external image that occurs through the mask, and the decoding process of the projected image on the detector, through which spatial information on the original image is obtained. The photons produced by the source are distributed on the whole area of the detector, the decoding code then reconstructs the precise shape of the image. The shadow produced by the mask is in fact called code. The noise produced on the detector by the environmental photons is isotropic, then the decoded image suffers the noise on the entire detector. In contrast, using optical focusing systems the image of a point source is concentrated in a small area on the detector, and it suffers only a small part of the noise. Therefore, for the same collecting area, a device that uses focusing optics has always a higher sensitivity than an instrument that uses a coded mask.

There are two possible types of codes: spatial or temporal codes (or a combination of the two). A spatial code is nothing more than a series of zones transparent or opaque to radiation (Figure 1-4). A position-sensitive detector (i.e. divided into pixels) is needed for decoding the image projected on the detector thus to get the original image. A time code is produced by a mask whose position relative to the plane of the detector changes over time. Therefore, the shadow casted on the detector changes periodically. The simplest example of temporal coding is the movable collimator. If the direction of a collimator is rotated through a zone in which there is a point source, the number of photons counted on the detector per second is a function of the time spent over that area. Indeed, the distribution of photons have a triangular shape. The position of the maximum of the function provides the position of the source along the scanning direction, while the height of the maximum of the function is proportional to the flux emitted by the source. With a second scan along a different direction, it is possible to locate the position of the source on the surface of a sphere. If the source is extended, or if there are multiple sources, multiple scans are required. The coded mask is an indirect method and usually inefficient to obtain images. However, coded masks were the first instruments that have yielded images of cosmic sources in the hard X-ray band (e.g. INTEGRAL).

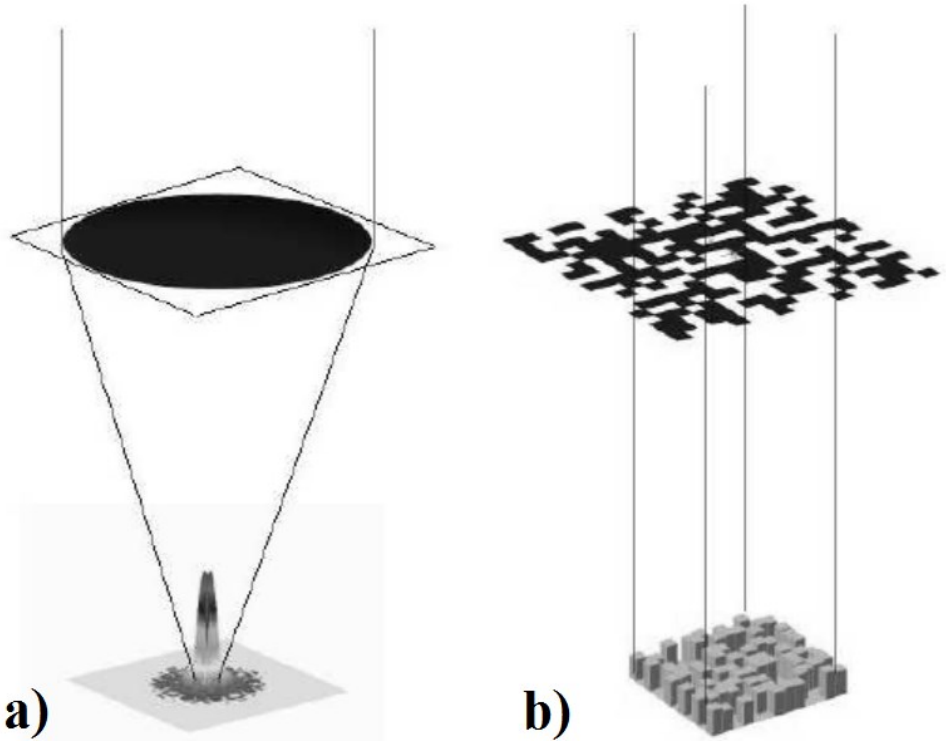

Figure 1-4

Comparison between the images produced on the detector by focusing optics (a) and by a coded mask (b). Image taken from (Skinner, 2004).

1.1.5 Grazing incidence mirrors

Grazing incidence mirrors were the first tools to make possible the focusing of X-rays. They were already employed in the satellite "Einstein" in 1978 to concentrate photons of energy up to 2 keV. These tools allow to focus radiation with an angular resolution of the arcsec, and to locate the source of photons with similar precision. Furthermore, the reduction of the detection area allows a significant increase in the signal to noise ratio, with a consequent increase in sensitivity compared to systems of mechanical collimators (1.1.1 Collimators, 1.1.4 Coded Masks). The reflection of the grazing X-rays occurs by the same mechanism through which visible light is reflected. However, the X photons have energy much greater than the binding energy of the electrons of the outer shell of the material that composes the mirror, thus the refractive index is slightly less than unity. By applying the Snell's law, reflection takes place only up to a certain critical angle of incidence θ_c (complement of the angle between the incident beam and the normal to the plane of the mirror) such that:

$$cos\theta_c = n$$

Where n is the refractive index of the material that can be written as $n = 1-\delta$ where δ defines how much the index of refraction of the medium deviates from the unit. If you consider θ_c small, with a series expansion $cos\theta_c \sim 1 - \theta_c^2/2$ it can be derived:

$$\theta_c \sim \sqrt{2\delta}$$

If the energy of the incident radiation does not coincide with an absorption edge of the material, it is possible to write δ as:

$$\delta = 2\pi r_0 \lambda^2 N_e$$

Where λ is the wavelength of the incident radiation, r_0 is the classical electron radius, N_e is the electron density of the material. Therefore, θ_c is proportional to the wavelength of the incident radiation, or inversely proportional to its energy. To diffract photons of higher energies, it is necessary to reduce the angle of incidence, with a consequent increase of the focal length of the instrument. In fact, the devices that use grazing incidence mirrors are not efficient for energies of incident radiation above 20 keV. The critical angle also depends on the electron density, which is approximately the atomic number of the material. Therefore, it is preferable to use materials with high atomic number. The response of a grazing incidence mirror also depends on the level of polishing of the surfaces, which must present imperfections less than the wavelength of the incident radiation, of the order of 10^{-10} m.

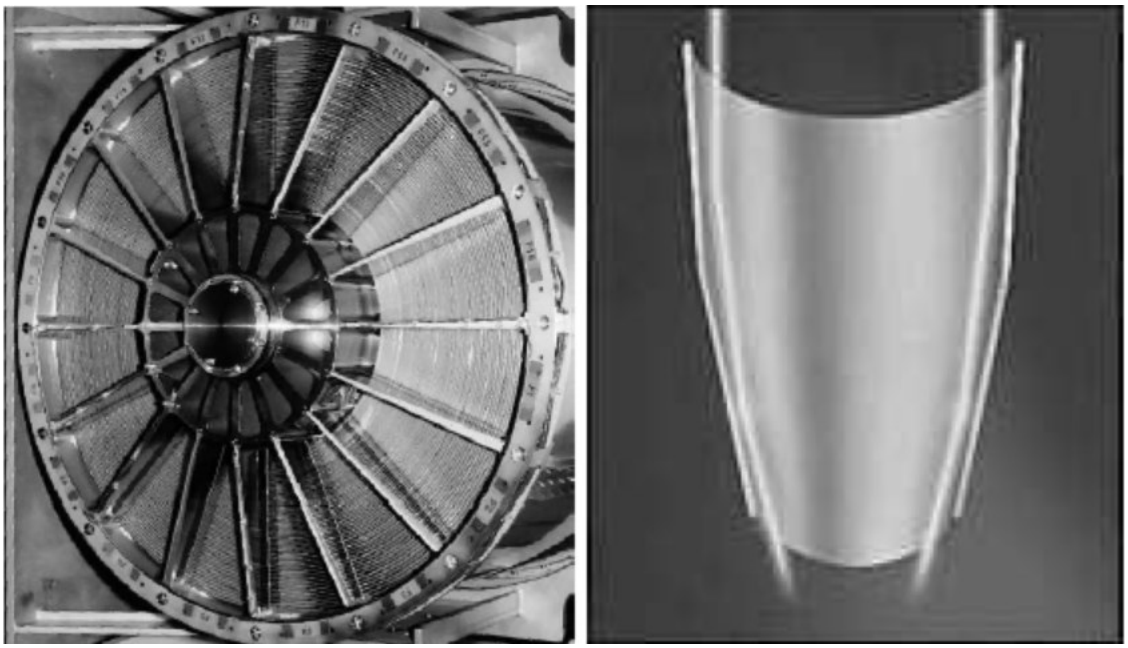

Figure 1-5

Grazing incidence mirror mounted on the satellite XMM-Newton (left), and working principle (right) based on coaxial mirrors. The first mirror has the shape of a paraboloid, the second has the shape of a hyperboloid. Image taken from (Orlandini, 2008/2009).

An X-ray beam is reflected almost completely if the angle of incidence is less than θ_c, but the reflected percentage drops quickly to zero if the angle of incidence exceeds θ_c. Usually θ_c is very small, this fact leads to very high focal lengths. To reduce the focal length and aberrations, optical systems consist of concentric mirrors have been developed (Figure 1-5). The configuration called Wolter I is the most used. It is composed of two coaxial mirrors, the first with the shape of a paraboloid, the second with the shape of a hyperboloid (Figure 1-6). Optics of this type have been used in the Chandra satellite (NASA) and XMM-Newton satellite (ESA). This optics is efficient for

energy of the incident radiation up to 10 keV. The use of new materials or new geometries is unlikely to extend further the energy range in which this technology is used.

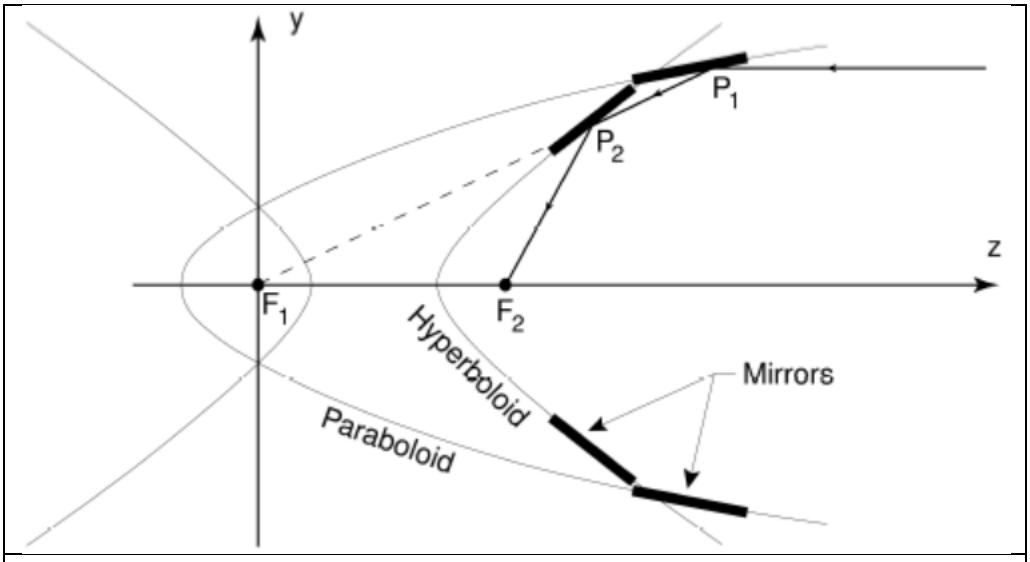

Figure 1-6

Wolter I configuration for an X-ray telescope based on grazing incidence mirrors. The focal length is reduced by coupling the reflection on a parabolic surface to a second reflection on a hyperbolic surface. The two surfaces have a common focus F1, while the photons incident on the optics are concentrated in the fire F2 of the hyperbole. Image taken from (Orlandini, 2008/2009).

1.1.6 Supermirrors

Multilayer mirrors have been developed to reflect and to focus X-rays at energies higher than those possible with the grazing incidence mirrors (1.1.5 Grazing incidence mirrors), and with angles of incidence of the beam greater than the critical angle for grazing incidence mirrors. The supermirrors are composed of many layers of two or more materials with variable thickness (Figure 1-7). Each pair of layers is composed of a material with high atomic number (and high reflectivity), and a material with low atomic number which acts as a spacer for the high reflectivity layers. Some pairs of materials used are silicon and tungsten, platinum and carbon, nickel and carbon. The multilayer mirrors behave as grazing incidence mirrors when the angle of incidence of photons on the surface of the mirror is less than the critical angle. When the angle of incidence becomes greater than the critical angle, the radiation tends to penetrate into the material, and it is partially reflected at each interface between the layers of the material.

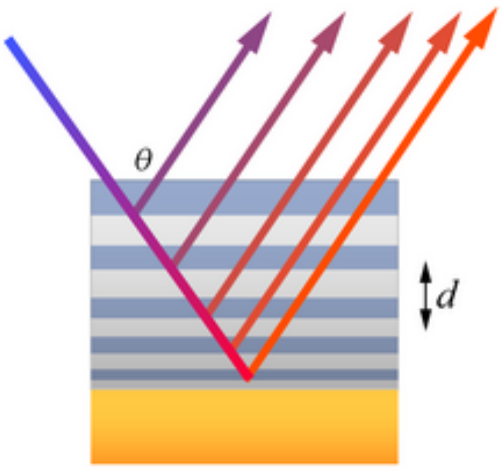

Figure 1-7

Multilayer structure of a supermirror. In each layer of material with high atomic number part of the beam is reflected.

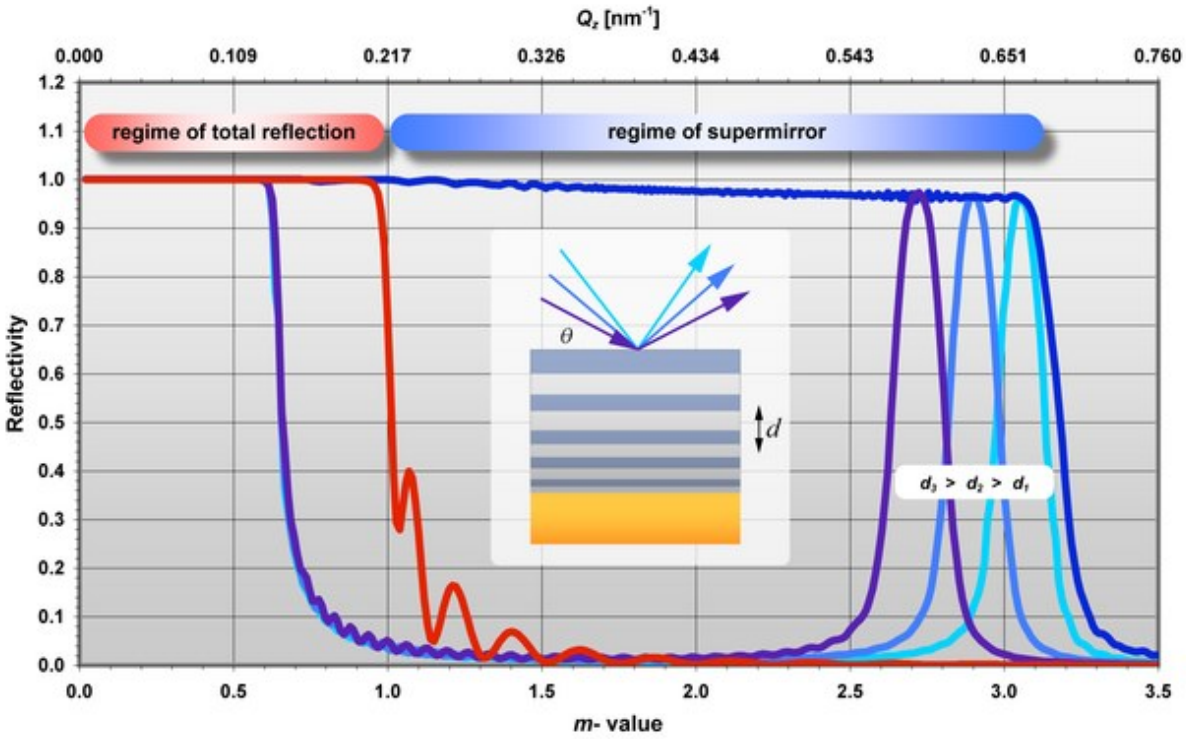

Figure 1-8

Performance of the reflectivity in a multilayer mirror for different operating modes. The value m is the angle of incidence of the beam expressed in units of the critical angle $m=\theta/\theta_c$. Before the critical angle, the mirror works as a grazing incidence mirror. After the critical angle, the mirror in the example continues to reflect radiation up to three times the critical angle.

The multilayer structure is a mono-dimensional artificial lattice, where the distance and the thickness of the various layers are carefully chosen. By this method, it is possible to obtain constructive Bragg diffraction between the scattered waves from each interface. The supermirror exploit this property to produce a wide range of angles where the Bragg diffraction occurs continuously (Figure 1-8), so as to extend the angle within which an X-ray beam can be reflected. With this method it is possible to efficiently reflect and focus photons up to 70 keV of energy, but it is not possible to go much further. Indeed, reflection still plays an important part in the functioning of multiplayer, a phenomenon that becomes less efficient with the increase of the energy of radiation. Recently, the construction of high-reflectivity multilayer mirrors working at energies up to several hundreds of keV was attained (Della Monica Ferreira, 2013). Nevertheless, these new supermirrors work at very low grazing incidence angles, below 0.1°, thus featuring a very low acceptance area for the incident photons.

1.1.7 Fresnel zone plates

A zone plate is a device used to focus light using diffraction instead of refraction or reflection. A zone plate Fresnel zone plates for X-rays can be absorbing or phase shifting. Absorbing zone plates consists of a set of radially symmetric rings, known as Fresnel zones, which alternate between opaque and transparent to radiation. The opaque zones are made of an X-ray absorbing material, as heavy metals, on a substrate transparent for X-rays. X-rays that hit the zone plate diffract around the opaque zones. The zones are spaced so that the diffracted radiation constructively interferes at the focus of the lens. Indeed, the optical path between the source and the focal point varies by $\lambda/2$ from one zone to the next (Baez, 1952). In phase shifting zone plates, all the zones are transparent to X-rays, but the phase shifts alternatively from 0 to π from one zone to the other (Lai, et al., 1992). The efficiency of phase plates is higher than the efficiency of absorbing plates, but in practice a zone plate always operate in a mixed regime, partially in absorption and partially in phase shifting. Zone plates are typically small, with size under the mm. The typical size of the focal spot is under the size of the μm, for this reason zone plates are ideal for X-ray microscopes (Schmahl, 1993). A particular type of zone plate is the Bragg-Fresnel lenses. They are phase zone plates manufactured from perfect crystals (usually silicon) to combine Fresnel diffraction with Bragg diffraction. Bragg-Fresnel lenses are particularly useful in last generation synchrotron sources because they preserve the coherence of the X-ray beam (Aristov, 1992).

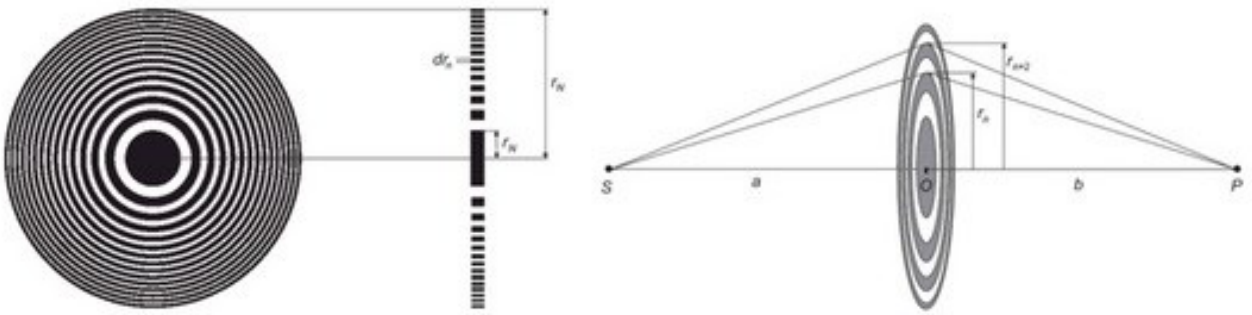

Figure 1-9

Sketch of a zone plate. Typical zone plates have diameters of 100 microns and smallest zone widths below 100 nm. The focal spot can be as small as 10 nm. Image taken from (PSI, 2015).

1.1.8 Compound refractive lenses

The refractive index of materials for X-rays is close to 1. Typically, the difference of refractive index from 1 is 10^{-6} for hard x-rays. Hence, a single refractive lens for X-rays has an extremely long focal length. In addition, X-rays attenuate as they pass through a material so that refractive lenses are impractical to focus X-rays. However, using many lenses in series it is possible to achieve a reasonably short focal length (Figure 1-10). The absorption of the lens is minimized by using light materials as aluminum, beryllium, or lithium. For X-rays, the refractive index is always smaller than 1, the opposite than for visible light. Therefore, the focusing lens must have a concave form. If the distance between the lenses is far smaller than the focus distance, the focusing power of the compound lens is just the sum of the focusing power of the single lenses:

$$\frac{1}{f} = \sum_{i=1}^{n} \frac{1}{f_i} = \frac{n}{f_i}$$

The last result is true if all the single lenses are made of the same material.

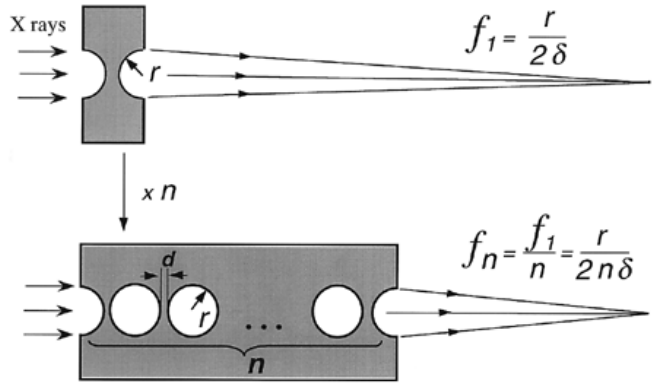

Figure 1-10

Sketch of the functioning of compound refractive lenses. The functioning of a single refractive X-ray lens in sketched in the top figure. r is the curvature radius of the lens, f_1 is the focal length, δ the difference of the refractive index of the material from 1. The refractive index for X-rays is negative, so a focusing lens have concave shape. Because the refractive index is very similar to 1, the focal length for a single lens is very large. For this reason, multiple lenses are stacked together to reduce the focal length of the compound lens, sketched in the bottom figure. f_n is the focal length of the compound lens, while n is the number of single lenses stacked together. If all the lenses are made of the same material, the focal length of the compound lens is the focal length of a single lens divided for the number of lenses stacked together. Image taken from (Sansosti, 2015).

The first compound lenses have been built by drilling holes in a parallelepiped of bulk material (Figure 1-11). Compound lenses can focus in one or two dimensions. A compound lens that focus in two dimensions is built by drilling holes in the lens in both the vertical and horizontal directions. To form a good compound refractive lens, the lens should be as thin as possible. The curvature radius of the single lenses should be small (~0.25 mm), and approximately ~100 holes are sufficient to achieve a reasonably small focus distance. The materials that yielded the best results for a cylindrical compound refractive lens have been beryllium and aluminum. A refractive compound lens is effective for focusing X-rays in the energy range from 5 to 40 keV (Lengeler, 1998).

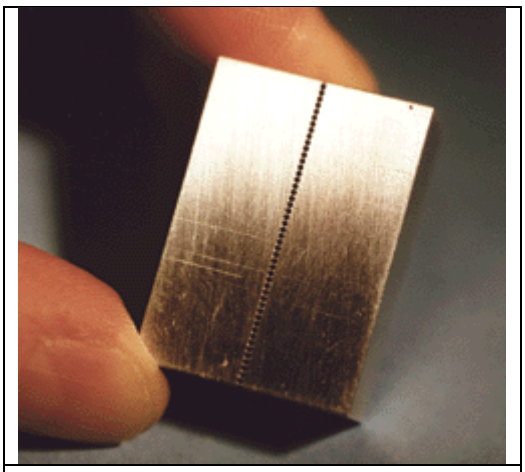

Figure 1-11

Image of Al compound lens taken from (Sansosti, 2015). Compound lenses are very robust and small (5-10 cm in length. Their geometric aperture is usually smaller than 1 mm.

In the last 15 years, refractive X-ray lenses have developed up to be present in almost all synchrotron radiation facilities worldwide. Modern compound lenses are biconcave with parabolic shape (Figure 1-12) in order to minimize aberrations. The geometric aperture varies from a few 100μm to a few mm. This matches well the dimensions of the x-ray beams of most synchrotron radiation sources. Particular designs of refractive lenses have been tested for energies from 2 keV to 150 keV. Beryllium is the material of choice up to about 40keV. Above that energy Aluminum and Nickel are more appropriate. Metallic lens materials are superior to plastics

since they do not suffer from radiation damage. Be lenses are able to withstand the intense beam of x-ray free-electron lasers. Refractive lenses are used as focusing and imaging components in all techniques that use synchrotron radiation, like spectroscopy, diffraction, reflection or coherent scattering.

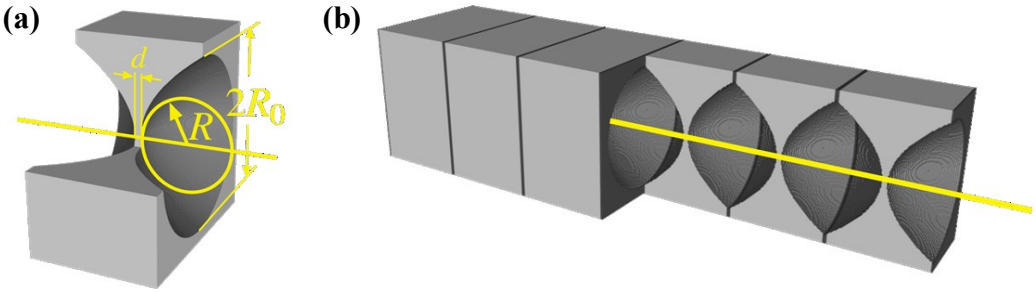

Figure 1-12

(a) Biconcave parabolic single refractive lens. The parabolic shape allows to minimize aberrations. The thickness d of the lens must be as small as possible to minimize absorption. (b) Compound refractive lens built by stacking single biconcave parabolic refractive lenses. Image taken from (RXoptics, 2015).

1.1.9 Policapillarity lenses

Polycapillary optics are arrays of small hollow glass tubes. X-rays are collected from thousands of channels, and they are guided down these curved tubes by multiple reflections. This results in relatively efficient collection, especially from large divergent sources such as conventional X-ray tubes. X-rays are confined inside a curved hollow tube as long as the tube is small enough, and it is bent gently enough, to keep the angles of incidence less than the critical angle for total reflection θ_c. The critical angle for borosilicate glass is approximately $\theta_c \approx (30 \text{ keV/E})$ mrad that is approximately 1.7° for 1 keV photons and 0.086° for 20 keV photons (MacDonald, 2010). The requirement that the incident angles remain less than the critical angle necessitates the use of small channel sizes, typically between 2 and 50 μm. Submicron channel sizes have been studied in the last years.

Polycapillary focusing optics collect a large solid angle of X-rays from the source. The typical diameter of the collecting area is 1 cm – 1 mm, and the focus spot can be as small as 10 μm. The X-ray flux density obtained is a few orders of magnitude higher than that obtained with a conventional pinhole collimator. Polycapillary optics are well suited for clinical, in situ, or laboratory-based applications such as X ray fluorescence and X ray diffraction, especially on small samples (Kumakhov, 2000). Polycapillary lenses are based on reflection, then they are achromatic, and thus they are appropriate for broadband applications. The main application of these optics is micro X-ray fluorescence (μXRF) analysis, which has been widely used for thin film and plating analysis, precious metal evaluation, alloy measurement, and monitoring of electric circuit board coatings. The optics can also be used on the detection side in applications such as confocal XRF analysis and superconducting energy-dispersive X-ray spectrometers.

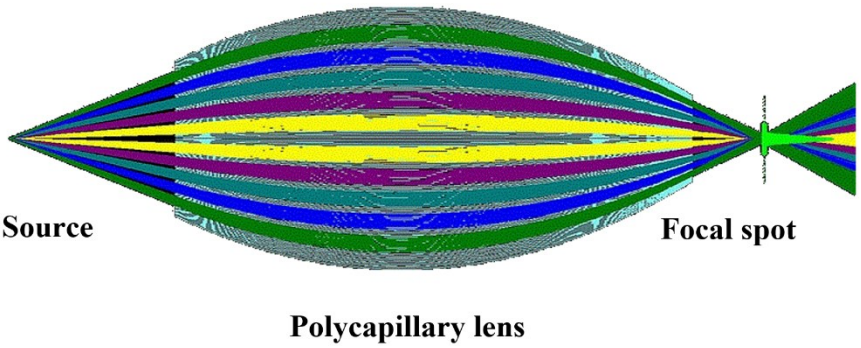

Figure 1-13

Sketch of a polycapillary lens. X-rays emitted from the source are channeled inside the capillaries of the lens by grazing incidence reflection. The lens concentrate the polychromatic and divergent beam emitted from the source in the lens focus. Image taken from (Unisantis, 2015).

1.1.10 Laue lenses

A Laue lens is a hard X-ray concentrator conceived as an ensemble of many crystals oriented in such a way that the radiation passing through them is diffracted to the lens focus. The aim is to concentrate as much radiation as possible over a selected energy band (Frontera F. &., 2010). Diffraction is an efficient process for photon energy from keV up to 1 MeV. Then, choosing the crystals carefully, one can design a hard X-ray diffractive lens with performances as near as possible to a refractive lens. The thickness of the lens can vary from fraction of a millimeter up to several centimeters for photon energy approaching 1 MeV.

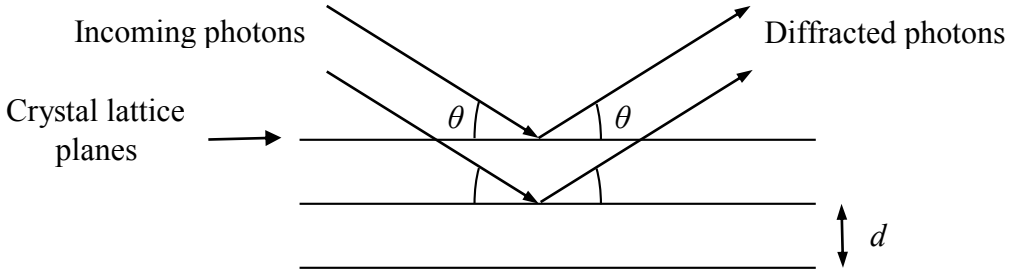

Figure 1-14 *– Diffraction in Bragg (reflection) geometry in perfect flat crystals*

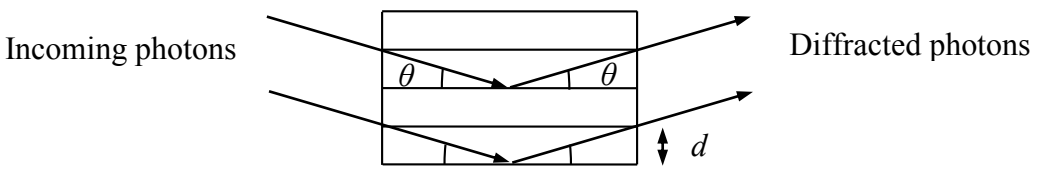

Figure 1-15 *– Diffraction in Laue (transmission) geometry in perfect flat crystals*

Laue lenses of modern design have the shape of a spherical calotte with curvature radius R and focal length $f \approx R/2$. Diffraction planes are perpendicular to the lens calotte. Then, a photon with direction parallel to the optical axis will be deviated by two times the Bragg angle and focused to the detector. The focal length of Laue lenses are rather large because of the small diffraction angle for high energy photons. The best geometry for placing the crystals in a Laue lens is the Archimedean spiral. With this geometry, the energy of photon focused by the lens changes smoothly from one crystal to the following. Anyway, the construction of lenses with this geometry is difficult because of technological problems. A lens composed of concentric rings is technologically more feasible. In this case, the energy of photon focused changes from ring to ring with a less-smooth transition.

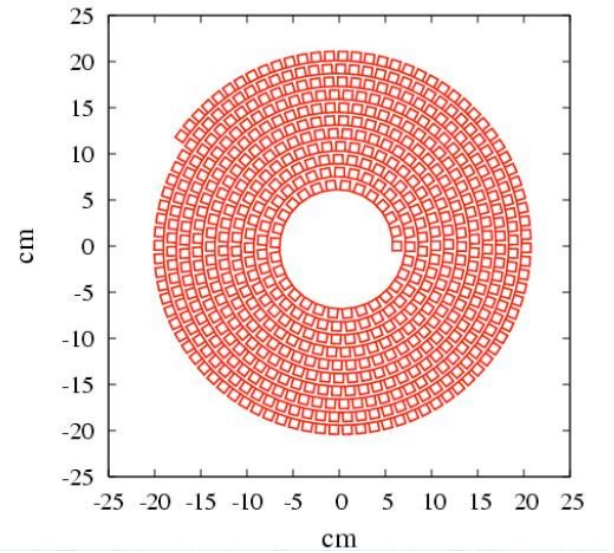

Figure 1-16

Crystals disposed on a Laue lens calotte following the Archimedean spiral.

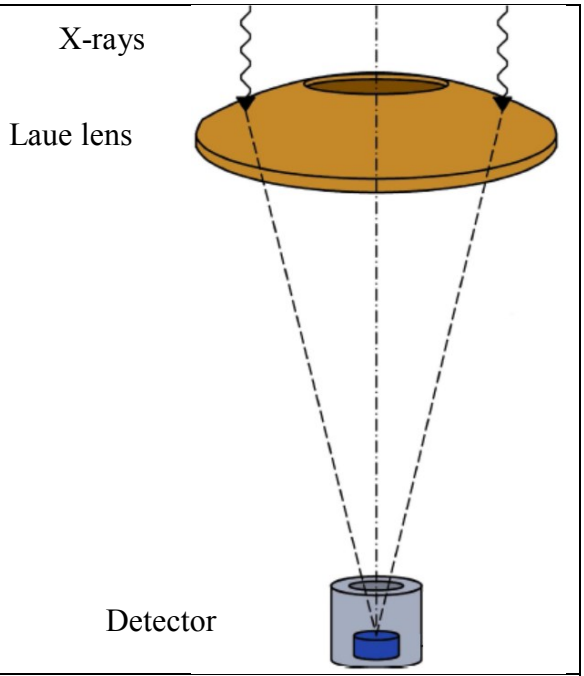

Figure 1-17

Sketch of a Laue lens. An X-ray beam parallel to the lens axis is focused onto the detector.

The energy range of X-rays a Laue lens can focus depends from the dimension of the lens, from its focal length, and from the diffraction planes. Then, a Laue lens can focus photons with energy between E_{min} and E_{max}

$$E_{min} = \frac{hc}{2dsin\theta_{max}} \sim \frac{hcf}{dr_{max}}$$

$$E_{max} = \frac{hc}{2dsin\theta_{min}} \sim \frac{hcf}{dr_{min}}$$

where h is the Planck's constant, c is the velocity of light, d is the interplanar distance of diffraction planes, θ_{min} and θ_{max} are the minimum and maximum Bragg's angles in the lens, f is the focal length, r_{min} and r_{max} are the minimum and maximum radius of the lens calotte. It is possible to notice that photons of low energy are diffracted by the external part of the lens, while high energy photons are diffracted by the inner part.

The reflectivity of the lens strongly depends upon the passband for photon diffraction of the crystals composing the lens. A crystal with large passband diffracts a large portion of the incoming photons, while a crystal with narrow passband does not. For perfect crystals, the passband is the Darwin width, which is very narrow for high-energy photons. As an example, the Darwin width for diffraction of 150 keV photons by Si (111) planes is about 0.35 arcsec. The small passband of perfect crystals strongly hampers the possibility to diffract a large portion of the incident photons. Moreover, the diffraction efficiency of a perfect crystal in Laue geometry is limited to a maximum of 50 % (1.2.2 Perfect flat crystals). The passband for photon diffraction can be enlarged using mosaic (1.2.3 Mosaic crystals) or curved crystals (1.2.4 Curved Diffracting Planes (CDPs) crystals). The small misalignment between the crystallites composing mosaic crystals enlarges the passband for photon diffraction. Copper or germanium mosaic crystals have been employed to build the Laue lenses developed up to now. However, the diffraction efficiency of mosaic crystals is limited to 50 % because each crystallite is a perfect crystal, with diffraction efficiency limited to 50 %. Moreover, real mosaic crystals usually show a non-ideal distribution dominated by random errors induced by the production process. CDPs crystals are perfect crystals with bent lattice planes. They are usually produced by bending perfect straight crystals. CDPs crystals offer a continuum of diffracting angles to the incoming X-ray beam, thus increasing the passband for diffraction. Diffraction efficiency of CDPs crystals can approach 100 % because the continuous change in the incidence angle produced by the curvature prevents re-diffraction of diffracted photons. Moreover, a crystal can have more than one curvature along different directions. With this technique, it is possible to adapt the shape of the crystal to the lens calotte, turning each crystal in a small Laue lens. Focusing crystals can reduce the dimension of the diffraction spot on the detector. Moreover, focusing crystals can have any dimension, without increasing the dimension of the diffraction spot, which means large crystals can produce the same resolution of smaller ones. Therefore, a small number of focusing crystal is needed for building a Laue lens. The reduction of the number of crystals simplifies the technological feasibility of Laue lenses.

1.2 Crystals for diffractive optics

1.2.1 Generalities of crystals

The crystals for X-ray optics are usually made from flat monocrystalline blocks. The crystalline perfection is critical to obtain good performances. The best mono-crystals that the technology is now capable of producing are silicon or germanium crystals, whose growth techniques have been refined for applications in electronics. For this reason silicon or germanium crystals are usually employed as crystals for X-ray optics.

An ideal crystal is composed of an infinite spatial repetition of identical structural units. In a crystal two points which differ by a translation vector linear combination of the length of the sides of the structural unit have the same fundamental physical properties. This structure is shown schematically by means of a regular distribution of mathematical points, the set of these points is called lattice. It is possible to define the lattice with three vectors, $\mathbf{a_1}$ $\mathbf{a_2}$ $\mathbf{a_3}$, such that the arrangement of the atoms in the crystal is the same when viewed at the point **r** or at each point **r '**, where

$$\mathbf{r'} = \mathbf{r} + u_1\mathbf{a_1} + u_2\mathbf{a_2} + u_3\mathbf{a_3}$$

where u_1, u_2 e u_3 are arbitrary integers. The vectors $\mathbf{a_i}$ are define as the lattice constants. The volume built on these vectors is called lattice cell. Each lattice point contains one or more atoms: the position of the atoms defined by each lattice point forms the basis. Lattice and base define the crystal, as the basis indicates the positions occupied by different atoms in the cell and their type, while the reticle provides the information on the periodicity of the crystal. The fundamental characteristic of the crystals is their invariance, for appropriate translations and rotations, of their physical properties, such as the optical, chemical, electrical and elastic properties.

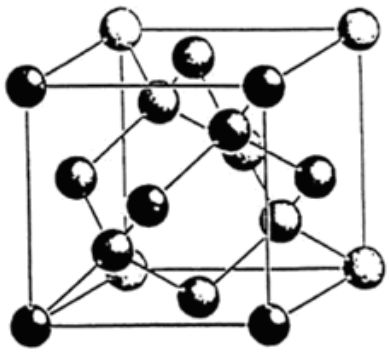

Figure 1-18

Silicon fundamental cell.

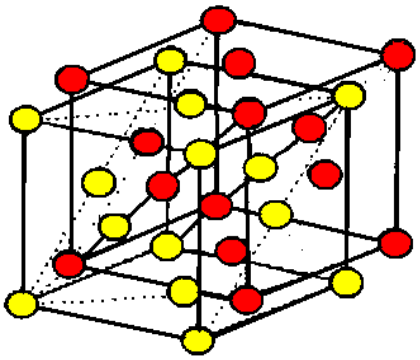

Figure 1-19

Fundamental cell of silicon view as two interpenetrating fcc.

The space group that identifies each type of crystal defines these degrees of freedom. Base and reticle are not uniquely defined, there are endless combinations equivalent to describe the same crystal. A cell is called primitive if it contains only one lattice point. For example, the lattice of silicon

is face-centered cubic (fcc: faced centered cubic). The base of silicon has two identical atoms in the coordinates (0,0,0) and (a/4, a/4, a/4), where a is the lattice constant (5.43 Å) and identifies the side of the conventional cubic cell (Figure 1-18). In silicon, it is not possible to choose a lattice so that the base contains only one atom. This crystalline structure can also be represented as two interpenetrating face-centered cubic lattices, where the base of the second is located at the point (a/4, a/4, a/4). This type of lattice is called a diamond lattice (Figure 1-19).

Directions and planes in the crystal lattice are defined by the Miller indices. A family of planes is determined by three integers *lmn*, said Miller indices, representing the vector perpendicular to the family of planes. The Miller indices in parentheses represent the plane, the Miller indices in square brackets represent the direction perpendicular to the plane. The crystallographic directions are fictitious lines that connect the atoms in the crystal, as atomic planes are fictitious planes connecting atoms. Depending on the density of atoms along the directions or planes, and depending on the types of bonds present, the physical properties of the directions and planes change:

- Optical properties
- Chemical properties
- Electrical properties
- Mechanical and elastic properties

The distance of the atoms from the first neighbors changes according to the plan considered. As the same the properties of the crystal vary.

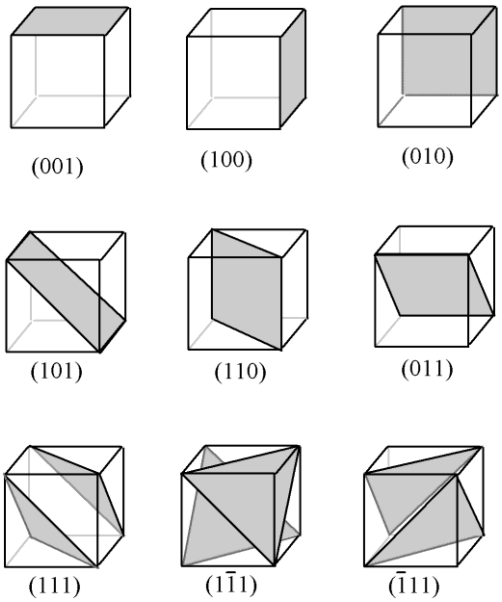

Figure 1-20

Planes with various Miller indices in a cubic lattice.

It is preferable to use crystals as possible similar to the ideal model, i.e. a uniform overlap of atomic planes, free of lattice defects. It is useful to treat the parameters that describe how a crystalline wafer deviates from the ideal model. The main ones are:

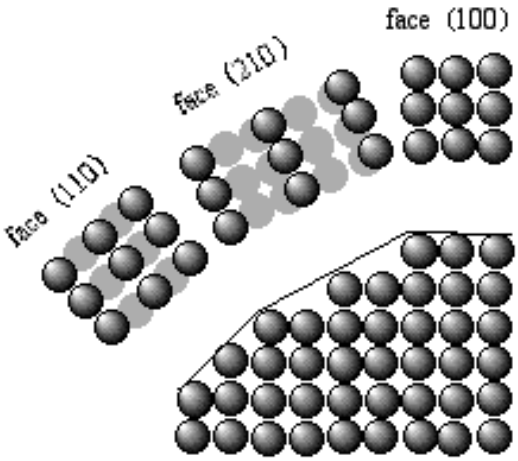

Figure 1-21

Section of different crystallographic planes.

• Miscut angle of axes: is the angle between the nominal crystallographic direction of the wafer and its actual crystallographic direction. It is caused by the error in the cutting process of the original ingot.

• TTV (Total Thickness Variation): measures the maximum variation in thickness of the wafer. It is the error on the wafer thickness.

• Bowl: measures the morphological radius of curvature of the wafer. It is usually produced during the process of lapping.

• Planarity: measures the morphological deformation of the wafer which is not included in the curvature measured by the bow.

• Roughness: represents how much the wafer surface is irregular and jagged on a small scale.

1.2.2 Perfect flat crystals

Crystalline materials are usually produced as ingots where the lattice planes are perfect and flat. Pieces of these crystals are used as X-ray optical elements acting by Bragg diffraction. The reflectivity of diffractive optical systems strongly depends upon the passband for photon diffraction of the crystals composing the systems. A crystal with large passband diffracts a large portion of the incoming photons, while a crystal with narrow passband does not. For perfect crystals, the passband is very narrow for high-energy photons. As an example, the Darwin width for diffraction of 150 keV photons by Si (111) planes is about 0.35 arcsec. The small passband of perfect crystals strongly hampers the possibility to diffract a large portion of the incident photons. Moreover, the diffraction efficiency of a perfect crystal when the beam traverses the crystal (Laue geometry) is limited to a maximum of 50 %. Indeed, a photon has the same probability to undergo an odd or even number of reflections traversing the crystal, then the same probability to exit the crystal in the diffraction or transmission direction. The process is sketched below in Figure 1-22

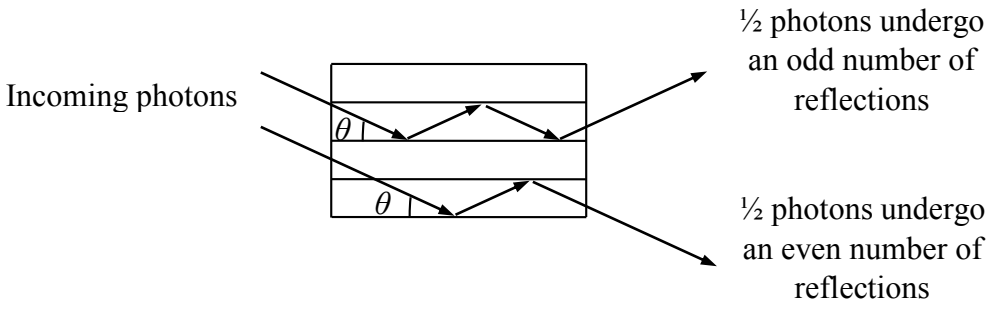

Figure 1-22 *– Diffraction in Laue geometry in a perfect crystal*

The passband for photon diffraction can be enlarged using mosaic or curved crystals, which are described in in the following sections (1.2.3 Mosaic crystals, 1.2.4 Curved Diffracting Planes (CDPs) crystals).

1.2.3 Mosaic crystals

Mosaic crystals are crystals composed of an ensemble of small crystals (crystallites) nearly parallel to each other. Crystallites are slightly misaligned around a principal direction. The dispersion of misalignments is ideally represented by a Gaussian function

$$W(\Delta) = \frac{1}{\sqrt{2\pi}\eta} e^{\left(-\frac{\Delta^2}{2\eta^2}\right)}$$

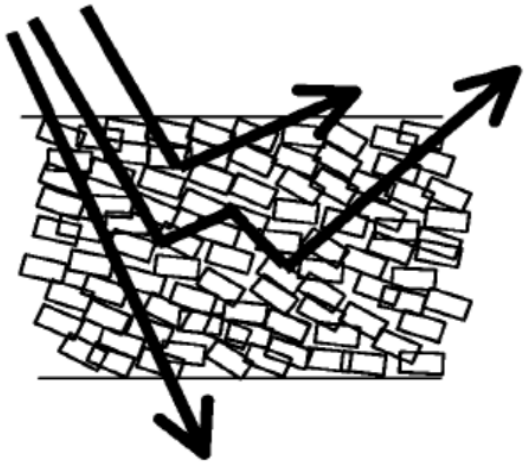

Figure 1-23

A mosaic crystal is composed of an ensemble of microscopic perfect crystals slightly misaligned. An incoming X-ray beam will encounter a multitude of possible diffraction angles.

where Δ is the mean misalignment of crystallites around the principal direction, η is the standard deviation of the distribution. The full width half maximum (FWHM) of the Gaussian distribution defines the dispersion of crystallites, this quantity is called mosaicity $\beta = 2{,}35\ \eta$. Crystallites are far smaller than the dimension of the crystal, thus producing a continuous distribution. Each crystallite diffracts photons at a different Bragg angle, then the energy band the entire crystal can diffract is enlarged (Figure 1-23). The mosaicity typically ranges from tens of arcsec to tens of arcmin. The diffraction efficiency of mosaic crystals can be derived as

$$\frac{I_{mosaic}}{I_0} = \frac{1}{2}(1 - e^{-2\sigma T_0})e^{-\frac{\mu T_0}{cos\theta}}$$

where I_0 is the intensity of the incoming beam, I_{mosaic} the intensity of the diffracted beam, μ is the absorption coefficient of the material composing the crystal at the energy E, T_0 is the crystal thickness and σ is a parameter dependent from the dimension of crystallites, from the Gaussian distribution of orientation of crystallites and from the energy of the incoming photons. The diffraction efficiency of mosaic crystals is limited to 50 % because each crystallite is a perfect crystal, with diffraction efficiency limited to 50 %. Then, the fraction of the beam absorbed has to be removed. Some mosaic copper crystals produced at ILL (Grenoble, France) have been tested at the LARIX laboratories at the University of Ferrara. The experimental reflectivity of the mosaic crystals approached 20%.

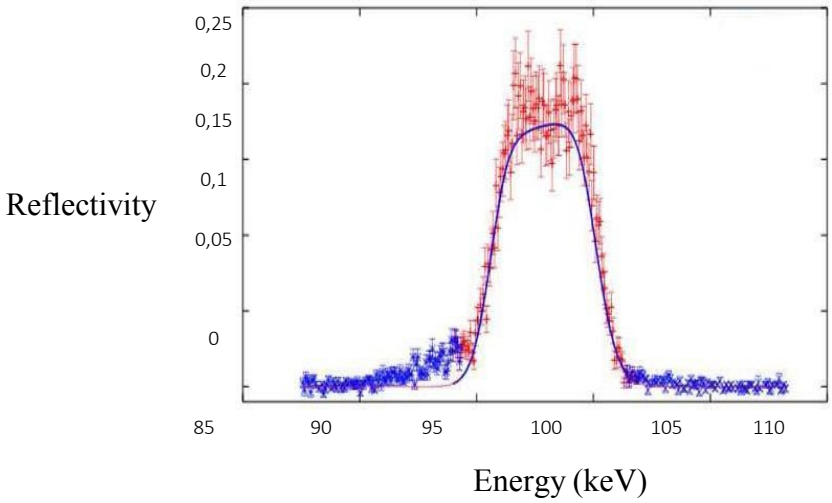

Figure 1-24

Experimental output for a mosaic copper crystal by diffraction through (220) planes.

The energy passband of mosaic crystals depends upon the distribution of the orientation of crystallites. Although this distribution should be ideally Gaussian, real mosaic crystals usually show

a non-ideal distribution dominated by random errors induced by the production process. Indeed, this distribution is poorly reproducible for real crystals. Furthermore, the maximum reflectivity is attained for crystallites of infinitesimal dimension, a condition clearly non-achievable in real crystals. Indeed, the dimension of crystallites usually is between tens and hundreds of microns.

1.2.4 Curved Diffracting Planes (CDPs) crystals

Curved diffracting planes crystals (CDPs crystals) are perfect crystals with bent lattice planes. CDP crystals are usually produced by bending perfect straight crystals (even if there have been some attempts to produce $Si_{1-x}Ge_x$ crystals with bulk CDP (Abrosimov, 2005). Therefore, they are less influenced by the manufacturing process than mosaic crystals. CDPs crystals offer a continuum of diffracting angles to the incoming X-ray beam, thus increasing the passband for diffraction. The increase in passband is proportional to the curvature and to the traversed thickness. Moreover, diffraction efficiency of curved crystals is not limited to 50 % maximum. Indeed, the continuous change of the incidence angle induced by the curvature prevents re-diffraction inside the crystal (Figure 1-25). Thus, diffracted photons cannot be diffracted again, and they all exit the crystal in the diffraction direction. Therefore, the diffraction efficiency of a CDPs crystal can approach 100 % (Barriére N. G.-X., 2010).

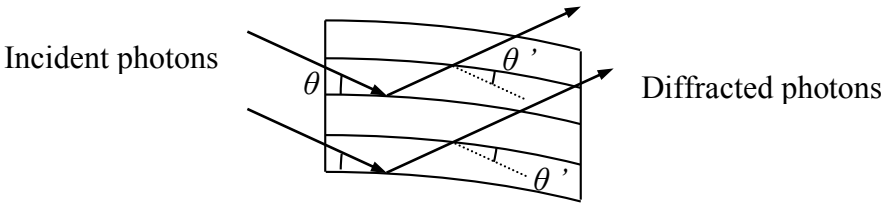

Figure 1-25

Diffraction in Laue (transmission) geometry in CDP crystals

1.2.5 State of the art for CDPs crystals production

Various methods have been developed over time to fabricate CDPs crystals. The easiest method, and historically the first to be applied, has been to induce a deformation to a perfect crystal through mechanical means. For example, mechanically bent silicon crystals are used in the latest generation of synchrotrons as high efficiency monochromators. This method for bending the crystals requires the presence of a holder to keep the crystal bent. This means that a part of the crystal is covered by the holder, which may be disadvantageous when it is necessary to maximize the area of incidence of the beam on the crystal. Because of the size of the holder, it is also difficult to use the crystals in geometries more complex than those of a simple monochromator, as in the case of Laue lenses. The same weight of the holder can be problematic for astrophysical devices that need to be used in orbit.

Another method to produce CDPs crystals is the application of a thermal gradient. This technique allows to obtain a uniformly spherical profile of excellent quality. However, this method becomes difficult to apply when it is necessary to obtain a deformation profile different than a sphere, especially for large samples. Maintaining the temperature gradient requires a considerable expenditure of energy that is not always available, for example in equipment that must work in space.

A method to grow crystalline blocks with lattice planes inherently curved is to use an alloy of Silicon - Germanium in which there is a concentration gradient of the two materials along the growth axis (Abrosimov, 2005). The increase in concentration of germanium deforms the silicon lattice, producing a spherical deformation of the crystallographic planes perpendicular to the axis of growth. Since the concentration of germanium remains small in the whole crystal, the curvature is approximately proportional to the concentration of germanium $\nabla C_{Ge} \sim \varepsilon / R$, where ∇C_{Ge} is the concentration gradient of germanium, ε is a constant, and R is the radius of curvature of the lattice planes. If we consider a spherical curvature, the concentration gradient of germanium can be put in relation to the range of possible diffraction angles α provided by the curvature of the crystal $\nabla C_{Ge} \sim \varepsilon \alpha / t$ where t is the thickness of the sample. To produce crystals with a uniform bending a great stability of the concentration gradient along the growth axis of the ingot is required. However, the presence of two materials with different lattice parameters within the same crystal leads to the formation of a high number of lattice imperfections, which results in a poor reproducibility of samples produced, and in most cases lowers the diffraction efficiency to the levels of crystal mosaic (Figure 1-26). Moreover, the manufacturing process is not simple to implement for the production of crystals in large quantities.

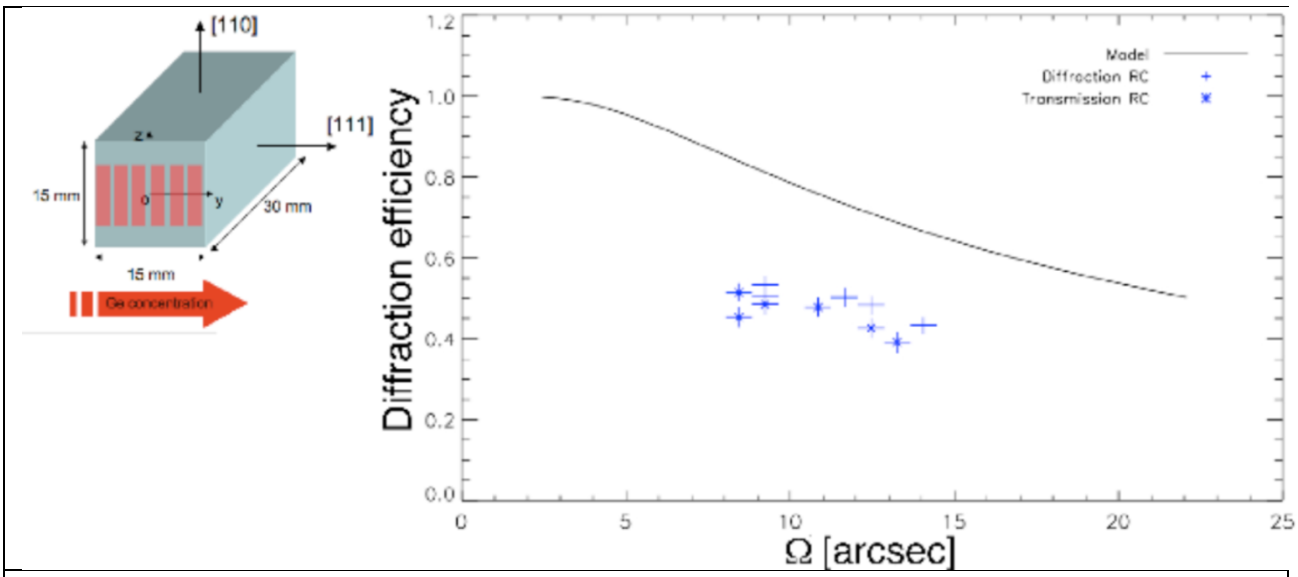

Figure 1-26

Left: design of a SiGe sample with size (15mm × 15mm × 30mm) analyzed at ILL (Grenoble, France) using a beam size of 7.6mm × 1.7mm and with a divergence of 2 arcsec, with photon energy 517 keV. The sample was analyzed in 6 points (red rectangles), through the thickness of 30 mm, the diffraction occurs on the planes (111). Right: the diffraction efficiency measured in the six points is analyzed as a function of the opening angle measured in the same points (using the FWHM of the rocking curves). In all cases, the diffraction efficiency was about 50%, and the angular aperture varies considerably between one point and another. The images and data are taken from (Barriére N. v., 2007).

Recently, it was proved that grooving the surface of a silicon crystal leads to a plastic deformation of the entire crystal (3.3 The indentation method and our crystals), which causes a permanent bend of the same (Figure 1-27). This method is particularly interesting because it is not necessary to apply external forces to maintain the curvature. If the indentations are periodic, it is possible to obtain extremely uniform cylindrical or spherical curvatures, depending on the geometry with which the grooves are manufactured. Crystals of this type have shown a nearly-ideal diffraction efficiency, and a comparable angular aperture (Figure 1-28).

A last method still under study to produce curved crystals is to deposit a tensile film on the surface of a crystal to deform the entire structure. It is possible to apply this method by the deposition of a crystalline layer of material, or by the deposition of an amorphous layer. In the first case (heteroepitaxial growth), the deposited material grows into a crystalline structure with lattice parameter different from the crystalline structure of the substrate. At the interface between the two materials the different lattice parameters deform to match each other. This process results in a surface tension able to deform the entire crystal. In this case, one tries to minimize the number of dislocations at the interface that cause a relaxation in the material, thus maximizing the surface tension. For this reason, it is preferable to use materials with similar crystal structure and lattice parameters. In the second case (deposition of an amorphous) the surface tension is produced by the different index of thermal expansion of the two materials. The amorphous layer is deposited at high temperatures, under these conditions there is no surface tension. When the system is brought to room temperature, the thermal expansion undergone by the substrate and the film is different, thus generating a surface tension capable of imparting a deformation to the material. The study of these methods to obtain curved crystals with applications in the hard X-ray diffraction is still in its early stages, and little information is available regarding the diffraction efficiency reached and the uniformity of the curvature.

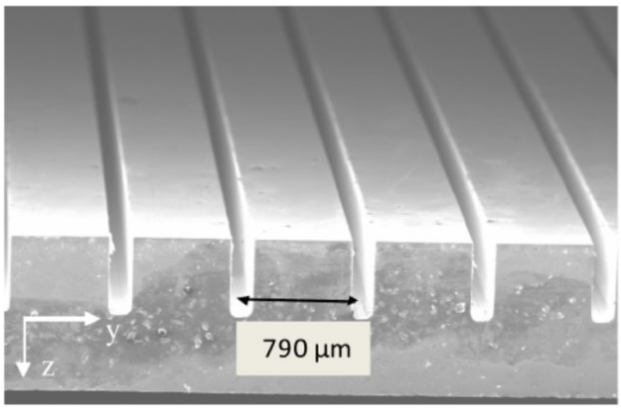

Figure 1-27

SEM image of the surface of a grooved silicon crystal.

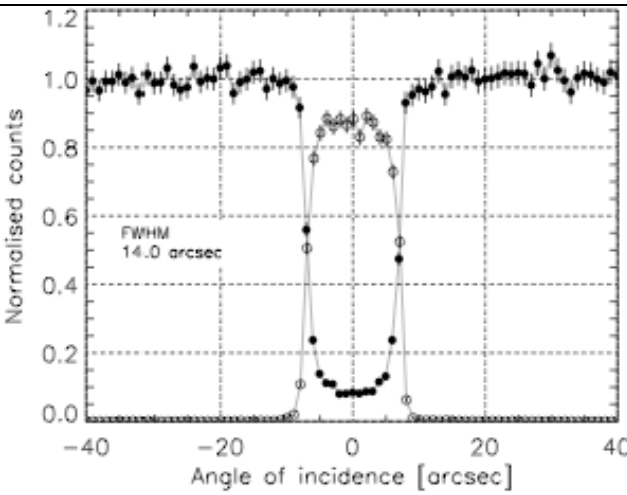

Figure 1-28

Rocking curves in Laue diffraction of a silicon crystal bent by indentation, beam energy E = 150 keV, opening angle α = 14 arcsec, traversed thickness of 1 cm.

1.3 Theory of diffraction

Two theories of diffraction can be distinguished: the Kinetic theory and the Dynamical theory.

The first studies the propagation of X-rays by geometric optics, the second by wave fields.

1.3.1 Kinetic theory of diffraction

1.3.1.1 X-ray diffraction basics

X-rays were discovered in 1895 by German physicist Wilhelm Röntgen. The peculiar phenomenon of this radiation was its high power of penetration in matter, and it was immediately used for the analysis of various types of materials. Amorphous solids, liquids and gases irradiated by X-rays produced continuous images. In contrast, crystalline solid with a macroscopic structure (the first crystals known) produced figures with spots. Indeed, the incident radiation was in part reflected for certain combinations of the wavelength and of the incident direction.

The first explanation of this phenomenon was provided by W. L. Bragg, hypothesized that the crystalline solids consisted of parallel planes of ions, away from one another of a distance *d*. Bragg suggested that X-rays were reflected as in a mirror from crystalline planes, and a peak occurred when X-rays reflected from successive planes interfered constructively with each other. Because the rays reflected from successive planes are in phase with each other, the path difference between the two must be an integer number of wavelengths. In this way, we obtain the known Bragg's law:

$$n\lambda = 2dsin\theta$$

Where n is the order of diffraction, λ the wavelength of the incident radiation, d is the interplanar distance, θ the angle of incidence of the beam on the atomic planes.

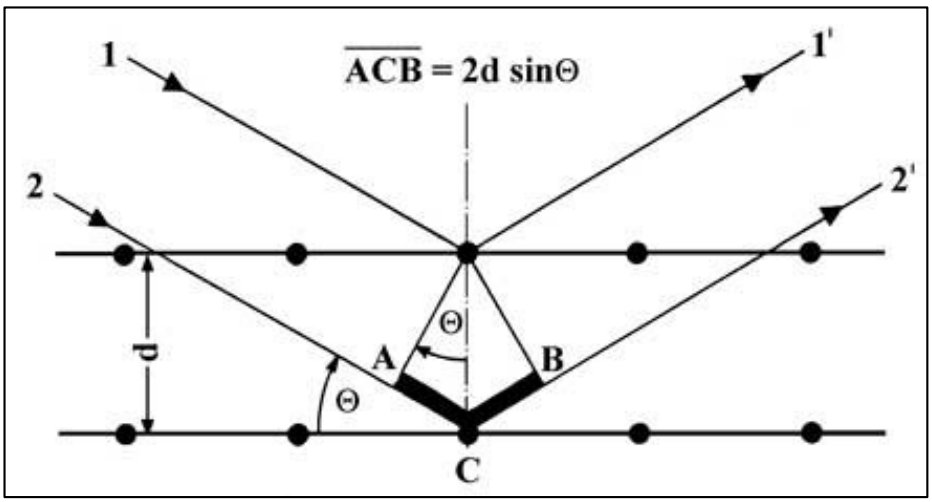

Figure 1-29

Sketch of Bragg diffraction. The black circles represent atoms connected by the atomic planes of the crystal. If the path difference between the two beams is an integer number of the wavelength, the waves sum together constructively.

In the periodic structure of a crystal an infinite number of atomic planes can be identified. Therefore, if the X-ray beam is not monochromatic, but it is composed of a wide range of energies (white-light beam), there are many possible reflections, and the image is composed of many spots. This is a direct image of the reciprocal lattice of the crystal. The reciprocal lattice is defined as the set of wave vectors $\boldsymbol{K}$ which identify plane waves with the periodicity of the crystalline lattice (Ashcroft, 1976). If we denote by $\boldsymbol{R}$ a generic vector belonging to the crystalline lattice, a wave vector $\boldsymbol{K}$ belongs to the reciprocal lattice if:

$$e^{i\boldsymbol{K}\cdot(\boldsymbol{r}+\boldsymbol{R})} = e^{i\boldsymbol{K}\cdot\boldsymbol{r}}$$

Simplifying, in mathematical form, it is possible to define the reciprocal lattice as the set of vectors that satisfy the condition:

$$e^{i\boldsymbol{K}\cdot\boldsymbol{R}} = 1 \qquad \textit{Equation 1}$$

The crystalline lattice composed of all the vectors $\boldsymbol{R}$ is said direct lattice. The reciprocal lattice is in turn a Bravais lattice, which can be expressed by means of basis vectors. If $\boldsymbol{a_1}$, $\boldsymbol{a_2}$, $\boldsymbol{a_3}$, are the basis vectors of the direct lattice, the reciprocal lattice is generated by the basis vectors $\boldsymbol{b_1}$, $\boldsymbol{b_2}$, $\boldsymbol{b_3}$, defined as:

$$\boldsymbol{b_1} = 2\pi \frac{\boldsymbol{a_2} \times \boldsymbol{a_3}}{\boldsymbol{a_1} \cdot (\boldsymbol{a_2} \times \boldsymbol{a_3})}$$
$$\boldsymbol{b_2} = 2\pi \frac{\boldsymbol{a_3} \times \boldsymbol{a_1}}{\boldsymbol{a_1} \cdot (\boldsymbol{a_2} \times \boldsymbol{a_3})}$$
$$\boldsymbol{b_3} = 2\pi \frac{\boldsymbol{a_1} \times \boldsymbol{a_2}}{\boldsymbol{a_1} \cdot (\boldsymbol{a_2} \times \boldsymbol{a_3})}$$

In general, a vector of the reciprocal lattice is defined by 3 not parallel vectors of the direct lattice as:

$$\boldsymbol{b_i} = 2\pi \frac{\boldsymbol{a_j} \times \boldsymbol{a_k}}{\boldsymbol{a_i} \cdot (\boldsymbol{a_j} \times \boldsymbol{a_k})} \qquad \textit{Equation 2}$$

For as these vectors have been defined, the following property is true $b_i \cdot a_j = 2\pi\delta_{ij}$. Define v_1, v_2, v_3 as integer numbers, a generic vector belonging to the reciprocal lattice can be expressed as:

$$\boldsymbol{K} = v_1\boldsymbol{b_1} + v_2\boldsymbol{b_2} + v_3\boldsymbol{b_3}$$

There is a close relationship between the vectors of the reciprocal lattice and the planes of the direct lattice, which is important to understand the role of the reciprocal lattice to describe the phenomenon of diffraction. A plane in the direct lattice is defined by two nonparallel vectors of the direct lattice $\boldsymbol{a_j}$, $\boldsymbol{a_k}$. For each pair of nonparallel vectors of the direct lattice, there exists a vector of the reciprocal lattice $\boldsymbol{b_i}$, identified via the relation in Equation 2, perpendicular to these two. A plane is defined by a vector perpendicular to it, thus the plane identified by $\boldsymbol{a_j}$, $\boldsymbol{a_k}$, is defined using the vector of the reciprocal lattice $\boldsymbol{b_i}$. The direction of this vector is orthogonal to the plane, and its modulus is $|\boldsymbol{b_i}| = 2\pi/d$, where d is the interplanar distance in the family of planes identified by the vectors $\boldsymbol{a_j}$, $\boldsymbol{a_k}$. This vector can in turn be expanded as a linear combination of the basis vectors of the reciprocal lattice. The integers v_i, v_j, v_k, with which it is expanded are the Miller indices of the plane, usually referred to as *(h, k, l)*. Recalling that a generic vector of the direct lattice can be written as $\boldsymbol{R} = n_1\boldsymbol{a_1} + n_2\boldsymbol{a_2} + n_3\boldsymbol{a_3}$, the condition (Equation 1) because a vector belongs to the reciprocal lattice is satisfied if:

$$\boldsymbol{K} \cdot \boldsymbol{R} = 2\pi(v_1 n_1 + v_2 n_2 + v_3 n_3)$$

The Bragg's approach to explain the diffraction hypothesized the existence of atomic planes that reflect the incident radiation. However, the atomic planes are a mathematical construct. Therefore, even if this approach is simple and effective, it cannot be considered fully satisfactory. An alternative formulation of the conditions of diffraction was provided by Max von Laue. Laue did not specify a priori condition regarding the existence of atomic planes, nor that reflection should be specular. On the contrary, he consider the crystal composed of tiny scatterers (atoms or ions) placed in lattice sites. Consider the scattering process fully elastic. When a radiation beam impinges the crystal, the scatterers radiate the incident radiation in all directions in the form of spherical waves. Spherical waves have an evanescent trend with the distance of the type *1/r*. At large distance from the crystal, peaks are observed only in the directions where the scattered waves from all the atoms interfere constructively. For simplicity we consider only two scatterers (Figure 1-30), separated by a vector $\boldsymbol{d}$. Parallel X-ray beams impinge with direction $\hat{\boldsymbol{n}}$ and wave vector $\boldsymbol{k} = \frac{2\pi}{\lambda}\hat{\boldsymbol{n}}$. At great distance from the system $r >> d$, a diffracted beam is observed only in the directions where the difference between the paths followed by the rays scattered by the two atoms is equal to an integer multiple of the wavelength λ. Therefore, the directions where diffraction occurs are defined by:

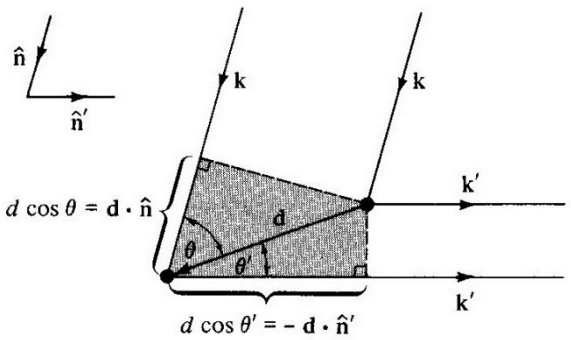

Figure 1-30

Bragg condition for two scatterers. Image taken from (Ashcroft, 1976).

$$d\cos\theta + d\cos\theta' = \boldsymbol{d} \cdot (\hat{\boldsymbol{n}} - \hat{\boldsymbol{n}}') = v\lambda$$

Where v is an integer. Multiplying the expression for $2\pi/\lambda$ is obtained:

$$\boldsymbol{d} \cdot \left(\hat{\boldsymbol{k}} - \hat{\boldsymbol{k}}'\right) = 2\pi v$$

The condition is true even for an endless chain of scatterers (one-dimensional problem). If now the problem is extended to a three-dimensional network composed of a periodic and ideally infinite set of scatterers, the condition must be satisfied simultaneously for the three base vectors $\mathbf{a_1}$, $\mathbf{a_2}$, $\mathbf{a_3}$, with which it is possible to define the lattice:

$$\begin{aligned}
\boldsymbol{a_1} \cdot \left(\hat{\boldsymbol{k}} - \hat{\boldsymbol{k}}'\right) &= 2\pi v_1 \\
\boldsymbol{a_2} \cdot \left(\hat{\boldsymbol{k}} - \hat{\boldsymbol{k}}'\right) &= 2\pi v_2 \\
\boldsymbol{a_3} \cdot \left(\hat{\boldsymbol{k}} - \hat{\boldsymbol{k}}'\right) &= 2\pi v_3
\end{aligned}$$

Where v_1, v_2, v_3, are integer numbers. The condition must be met for any vector of the direct lattice that is a linear combination of $\mathbf{a_1}$, $\mathbf{a_2}$, $\mathbf{a_3}$. The condition can be re-written as:

$$\boldsymbol{R} \cdot \left(\hat{\boldsymbol{k}} - \hat{\boldsymbol{k}}'\right) = 2\pi(v_1 n_1 + v_2 n_2 + v_3 n_3) = 2\pi v$$

Since v is an integer number, the vector $\left(\hat{\boldsymbol{k}} - \hat{\boldsymbol{k}}'\right)$ satisfies the condition that a wave vector can be considered a vector of the reciprocal lattice:

$$e^{i(\hat{\boldsymbol{k}} - \hat{\boldsymbol{k}}') \cdot \boldsymbol{R}} = 1$$

Then Bragg diffraction occurs when the variation of the wave vector during the diffraction process is equal to a vector of the reciprocal lattice

$$\left(\widehat{\boldsymbol{k}}' - \widehat{\boldsymbol{k}}\right) = \Delta\boldsymbol{k} = \boldsymbol{K}$$

This vector defines a plane of the direct lattice perpendicular to the same vector. This plane is the diffraction plane in accordance with the Bragg's formulation. The shorter wave vector that meets this condition has modulus $2\pi/d$, where d is the interplanar distance of the diffraction planes. The condition $\Delta\boldsymbol{k} = \boldsymbol{K}$ is also satisfied for every integer multiple of the same vector. Then, the possible values of K are $K = 2\pi n / d$ where n is an integer. From Figure 1-31, the module of this vector can be expressed as $K = 2k\ sin\theta$. Then, recalling the definition of wave vector $k = 2\pi / \lambda$, it is possible to derive the Bragg's law

$$2ksin\theta = \frac{2\pi n}{d} \rightarrow 2dsin\theta = n\lambda$$

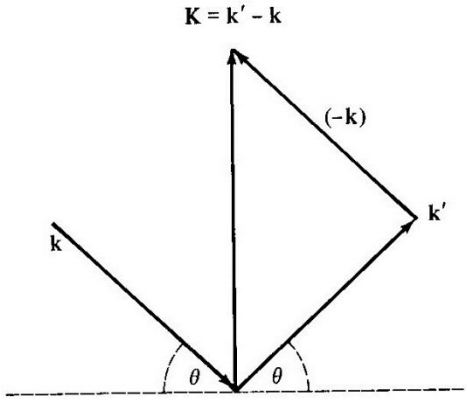

Figure 1-31

Bragg condition in vector form on an atomic plane. Image taken from (Ashcroft, 1976).

A beam incident on a crystal may undergo diffraction by more than one lattice plane, or it may not undergo any diffraction if it does not meet the Bragg's condition. A simple method to describe the possible diffractions in a complex lattice is the Ewald's sphere. A beam undergoes diffraction when the difference between the wave vector of the incident and diffracted beam is equal to a vector of the reciprocal lattice. $\boldsymbol{k}$, $\boldsymbol{k'}$, $\boldsymbol{K}$, are vectors of reciprocal space. In this space it is possible to build a sphere (Ewald sphere) with radius equal to the vectors $\boldsymbol{k}$, $\boldsymbol{k'}$. The vectors $\boldsymbol{k}$, $\boldsymbol{k'}$ are connected by the vector $\boldsymbol{K}$ (Figure 1-32). The reciprocal lattice is described as a set of periodic points in the reciprocal space. When the Ewald's sphere intersects simultaneously at least two points of the reciprocal lattice, the diffraction condition is satisfied. In the case when the incident beam is polychromatic, there are many values of k for which the Bragg condition is satisfied, which are defined by the interval of energies that composes the incident beam. In this case, the Ewald's sphere becomes a spherical surface with a certain thickness. The thickness is defined by the possible values of k. The Bragg condition is met for all the vectors of the reciprocal lattice that are located inside of the spherical surface. Therefore, multiple beams are diffracted, and the image produced is a direct image of the reciprocal lattice (Figure 1-33).

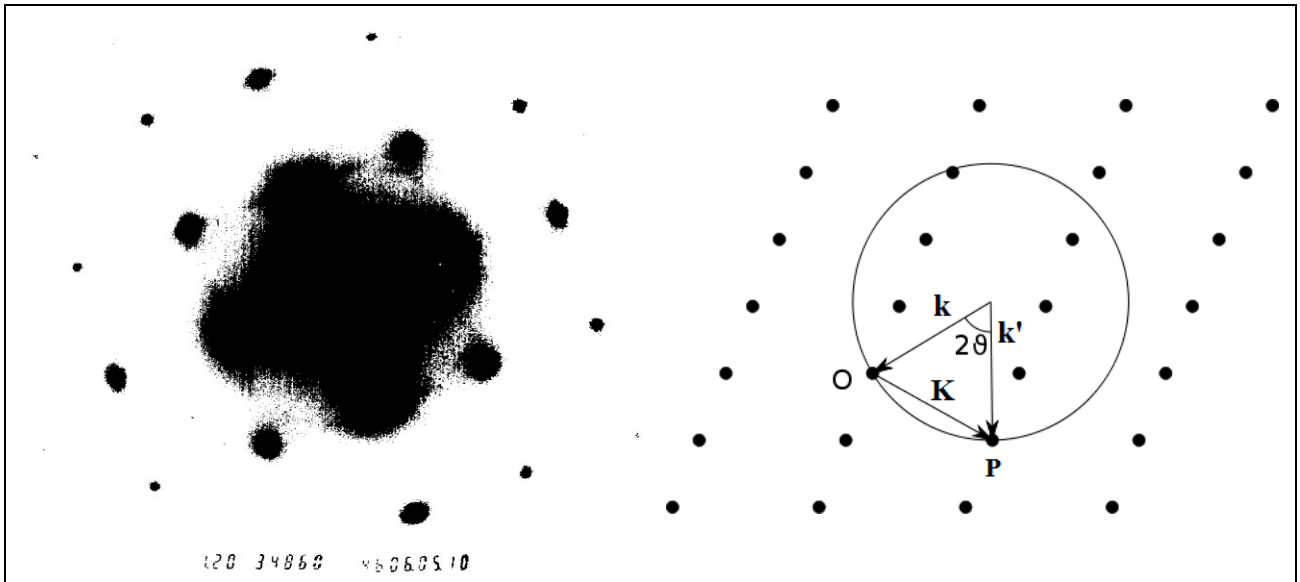

Figure 1-32

Diffraction image produced by a polychromatic beam diffracted by a silicon plane with orientation (220). At the center of the image a stain produced by the direct beam is visible. The other points correspond to integer multiples and symmetries of the reflection (220).

Figure 1-33

Section of the Ewald's sphere on a plane in the reciprocal space. Diffraction occurs when the sphere intersects simultaneously at least two points of the reciprocal lattice.

1.3.1.2 Form factors

The intensity of the diffracted beam, nor the distribution of intensity, appear in in Bragg's law or in the alternative development of Laue. Indeed, it is necessary to analyze how the process of scattering occurs to obtain quantitative information. We start by analyzing how a single electron scatters the incident electromagnetic wave (Zachariasen, 1945). For simplicity, the electromagnetic wave can be regarded as flat and monochromatic. Therefore, its electric field is:

$$\boldsymbol{E} = \boldsymbol{E_0} e^{i(\omega t - \boldsymbol{k}\cdot\boldsymbol{x})}$$

When the electromagnetic wave interacts with a material, it produces a periodic force $\boldsymbol{F} = -e\boldsymbol{E_0}e^{i\omega t}$ on the electrons of the material. The electron moves slightly from its original orbit, then the restoring force can be considered negligible. In this case, the electron can be considered free, that its equation of motion is:

$$\boldsymbol{F} = m\frac{d^2\boldsymbol{x}}{dt^2} == -e\boldsymbol{E_0}e^{i\omega t}$$

Where $\boldsymbol{x}$ is the displacement of the electron. If you choose as origin the average position of the electron, the solution of the equation of motion is:

$$\boldsymbol{x} = \frac{e}{m\omega^2}\boldsymbol{E_0}e^{i\omega t}$$

The periodic displacement of the electron generates an oscillating dipole moment in the form:

$$\boldsymbol{p} = -e\boldsymbol{x} = \frac{e^2}{m\omega^2}\boldsymbol{E_0}e^{i\omega t}$$

An oscillating electric dipole generates an electromagnetic wave in the space, with the magnetic field and electric field in the form:

$$\boldsymbol{H'_e} = \boldsymbol{u} \times \boldsymbol{E_0}\frac{e^2}{mc^2}\frac{1}{R}e^{i(\omega t - \boldsymbol{k'}\cdot\boldsymbol{R})}$$
$$\boldsymbol{E'_e} = (\boldsymbol{u} \times \boldsymbol{E_0}) \times \boldsymbol{u}\frac{e^2}{mc^2}\frac{1}{R}e^{i(\omega t - \boldsymbol{k'}\cdot\boldsymbol{R})}$$

Where **R** = R**u** is the position vector between the center of the dipole and the observation point, $\boldsymbol{k'}$ is the wave vector of the scattered radiation. The electromagnetic wave emitted is a spherical wave, with decreasing trend with distance like *1/R*.

An atom of the crystal has Z electrons, which in first approximation interact independently with the incident radiation. If you take the atomic nucleus as the origin of a reference system, at a given instant the positions of the electrons can be described by Z independent vectors $\mathbf{r_i}$. If the electrons are considered independent of each other, and considering the retraction force of each electron toward its original position negligible, the solution of the equation of motion of each electron is:

$$\boldsymbol{x_i} = \frac{e}{m\omega^2}\boldsymbol{E_0}e^{i(\omega t - \boldsymbol{k}\cdot\boldsymbol{r_i})}$$

Each electron behaves as an oscillating dipole, which radiates electromagnetic waves with electric field:

$$\boldsymbol{E'_{e_i}} = (\boldsymbol{u_i} \times \boldsymbol{E_0}) \times \boldsymbol{u_i}\frac{e^2}{mc^2}\frac{1}{R}e^{i(\omega t - \boldsymbol{k'_i}\cdot\boldsymbol{R_i})}e^{-i\boldsymbol{k_i}\cdot\boldsymbol{r_i}}$$

Where $\boldsymbol{R_i} = R\boldsymbol{u_i}$ is the position vector between the center of the i-th dipole and the observation point. This vector can be written as $\mathbf{R_i} = \mathbf{R} - \mathbf{r_i}$. The electromagnetic waves radiated from the entire atom are the sum of the electromagnetic waves radiated from each electron:

$$\boldsymbol{E_{at}}' = \sum_{\boldsymbol{i}}^{\boldsymbol{Z}} \boldsymbol{E'_{e_i}}$$
$$= \sum_{\boldsymbol{i}}^{\boldsymbol{Z}} (\boldsymbol{u_i} \times \boldsymbol{E_0}) \times \boldsymbol{u_i}\frac{e^2}{mc^2}\frac{1}{R}e^{i(\omega t - \boldsymbol{k'_i}\cdot\boldsymbol{R} + \boldsymbol{k'_i}\cdot\boldsymbol{r_i})}e^{-i\boldsymbol{k_i}\cdot\boldsymbol{r_i}}$$

At large distances holds $\boldsymbol{R_i} \sim \boldsymbol{R}$, $\boldsymbol{k'_i} \sim \boldsymbol{k'}$, and defining $\boldsymbol{s} = \boldsymbol{k'} - \boldsymbol{k}$ as the vector difference between the wave vector of the scattered radiation and the wave vector of the incident radiation , we can write:

$$\boldsymbol{E_{at}}' = \boldsymbol{E'_e}\sum_{i}^{Z} e^{i\boldsymbol{s}\cdot\boldsymbol{r_i}} \qquad \textit{Equation 3}$$

This expression represents the amplitude of the electric field of the electromagnetic wave scattered in the position $\boldsymbol{R}$. The quantity $\boldsymbol{s}\cdot\boldsymbol{r_i}$ represents the phase difference between the wave scattered by an electron in the position $\boldsymbol{r_i}$ and the wave scattered by an electron in the origin.

The position of the electrons inside the atom change constantly. It is therefore necessary to calculate a mean value of the summation in Equation 3 to obtain the intensity of the radiation scattered. The electrons that make up the electron cloud can be considered as a charge distribution, so their position is described by a probability density function ρ. In this case, it is possible to write the summation as an integral over the volume of the atom, called the atomic form factor:

$$f(\boldsymbol{s}) = \sum_{i}^{Z} e^{i\boldsymbol{s}\cdot\boldsymbol{r}_i} = \int \rho(\boldsymbol{s}) e^{i\boldsymbol{s}\cdot\boldsymbol{r}} dV \qquad \textit{Equation 4}$$

The above expression is the ratio of the amplitude of the radiation scattered from a particular atom and a single electron in the same condition. The distribution of the electrons within an atom is usually calculated numerically. For diffraction condition $\boldsymbol{s} = \boldsymbol{K} \rightarrow s = \frac{2\pi}{d} = \frac{4\pi sin\theta}{\lambda}$. The atomic form factor is tabulated as a function of $\boldsymbol{s}$ for most of the compounds. Note that $\boldsymbol{s}$ depends on the energy of the incident radiation. The amplitude of the radiation scattered by each atom in diffraction condition is:

$$\boldsymbol{E_{at}}' = \boldsymbol{E'}_e f(\boldsymbol{s}) = \boldsymbol{E'}_e f(\boldsymbol{K})$$

In a crystal, the atoms occupy the lattice sites, thus the scattered waves from each atom interfere with each other. The crystal is a periodic structure whose minimum unit is represented by the primitive cell. The amplitude of the radiation scattered by a primitive cell is proportional to the factor:

$$F_{\boldsymbol{K}} = \sum_{j=1}^{n} f_j(\boldsymbol{K}) e^{i\boldsymbol{K}\cdot\boldsymbol{d_j}} \qquad \textit{Equation 5}$$

Where n is the number of atoms composing the primitive cell, the vector $\boldsymbol{d_j}$ indicates their position within the cell. $F_{\boldsymbol{K}}$ is called geometrical structure factor. In case the crystal is composed of atoms of the same type $f_j(\boldsymbol{K})$ is a constant. The interference of the waves inside the cell can lead to the suppression of diffraction peaks, or to their modulation. The amplitude of the radiation scattered by each primitive cell is:

$$\boldsymbol{E_c}' = \boldsymbol{E'}_e F_{\boldsymbol{K}}$$

The intensity of the radiation contained in the diffraction peaks is proportional to $|\boldsymbol{E_c}'|^2$, then it is proportional to the square modulus of the geometric structure factor $F_{\boldsymbol{K}}$.

1.3.1.3 Diffraction by a Small Crystal

The kinetic theory of diffraction describes the diffraction phenomena by a purely geometrical approach. It analyzes the difference between the straight paths of the rays that undergo interference between them (Zachariasen, 1945). It is reasonable to assume that the amplitude of the scattered wave at a great distance from the crystal is given by the sum of the scattered waves from each primitive cell, taking into account the phase difference between the scattered waves from each cell. Define $\boldsymbol{A_L} = L_1\boldsymbol{a_1} + L_2\boldsymbol{a_2} + L_3\boldsymbol{a_3}$ as the position vector that identifies the cell L, and define F_s as the structure factor of the cell. The amplitude of the wave scattered by the entire crystal is:

$$\boldsymbol{E_{tot}} = \boldsymbol{E'}_e F_s \sum_{L} e^{i\boldsymbol{s}\cdot\boldsymbol{A_L}}$$

For simplicity we consider a crystal with the shape of a parallelepiped with sides of length $N_1 a_1$, $N_2 a_2$, $N_3 a_3$. The number of unit cells contained in the parallelepiped is $N_1 N_2 N_3 = N$. Then the summation can be developed as the product of three summations:

$$\sum_L e^{i\boldsymbol{s}\cdot\boldsymbol{A_L}} = \sum_{L_1}^{N_1-1} e^{iL_1\boldsymbol{s}\cdot\boldsymbol{a_1}} \sum_{L_2}^{N_2-1} e^{iL_2\boldsymbol{s}\cdot\boldsymbol{a_2}} \sum_{L_3}^{N_3-1} e^{iL_3\boldsymbol{s}\cdot\boldsymbol{a_3}}$$

Each summation has the form of a geometric series, and therefore it can be developed as:

$$\sum_L e^{i\boldsymbol{s}\cdot\boldsymbol{A_L}} = \prod_i^3 \frac{e^{iN_i\boldsymbol{s}\cdot\boldsymbol{a_i}} - 1}{e^{i\boldsymbol{s}\cdot\boldsymbol{a_i}} - 1}$$

For simplicity, we set the dielectric constant of vacuum and the velocity of light both equal to 1. Then, the intensity of radiation scattered along a particular direction defined by the vector $\boldsymbol{s}$ can be written as the square modulus of $\boldsymbol{E_{tot}}$:

$$I_{tot} = I_e |F_s|^2 \prod_i^3 \frac{sin^2 \frac{1}{2} N_i \boldsymbol{s}\cdot\boldsymbol{a_i}}{sin^2 \frac{1}{2} \boldsymbol{s}\cdot\boldsymbol{a_i}}$$

Where I_e is the intensity of the radiation scattered by a single electron. The function has a maximum when the following three conditions apply:

$$\boldsymbol{a_1}\cdot\boldsymbol{s} = \boldsymbol{a_1}\cdot\left(\widehat{\boldsymbol{k}'} - \widehat{\boldsymbol{k}}\right) = 2\pi v_1$$
$$\boldsymbol{a_2}\cdot\boldsymbol{s} = \boldsymbol{a_2}\cdot\left(\widehat{\boldsymbol{k}'} - \widehat{\boldsymbol{k}}\right) = 2\pi v_2$$
$$\boldsymbol{a_3}\cdot\boldsymbol{s} = \boldsymbol{a_3}\cdot\left(\widehat{\boldsymbol{k}'} - \widehat{\boldsymbol{k}}\right) = 2\pi v_3$$

This condition matches the Laue's conditions for diffraction to get. Then, there is a maximum when $\boldsymbol{s} = \boldsymbol{K}$ is a vector of the reciprocal lattice. For this condition the intensity of the diffracted radiation is:

$$I_{tot} = I_e |F_{\boldsymbol{K}}|^2 N^2$$

Where *N* is the number of cells in the crystal.

The function obtained presents a clear paradox, as it grows indefinitely as the number of cells that compose the crystal. Therefore, the intensity of diffracted radiation could become larger than the intensity of the incident radiation, fact that does not respect the principle of conservation of energy. Furthermore, the size of the peak of the distribution is reduced indefinitely as the number of cells increases, thus converging to a Dirac delta function. For a large number of cells, the position of the first minimum is proportional to $\boldsymbol{s}\cdot\boldsymbol{a_i} \sim \pi/N$, then the width of the base of the

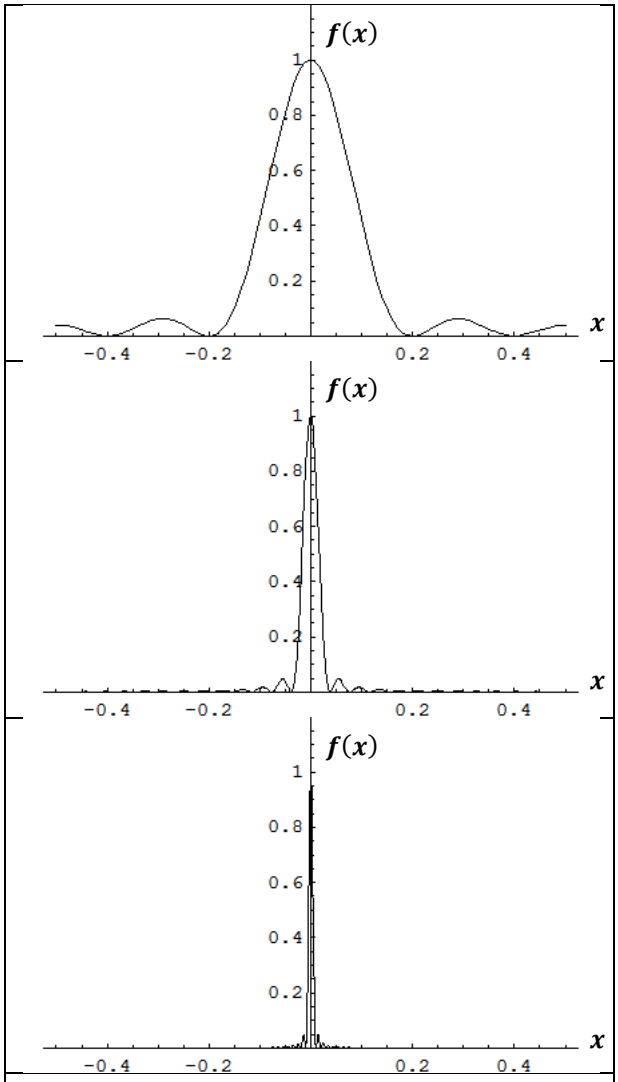

Figure 1-34

Performance of a function of the type $f(x) = (sinNx/sinx)^2$ *as a function of x, for values of N = 5, 25, 100. The maximum is normalized to 1.*

distribution is $\sim 2\pi/N$ in each direction. Furthermore, the intensity and the shape of the diffraction peaks depend on the geometric shape of the crystal. This trend is correct only for analyzing a thin crystal, so that only an infinitesimal part of the radiation that composes the beam interacts with the atoms. Indeed, in this case the effect of multiple scattering is negligible. The next sections show how to extend the solution to macroscopic crystals.

1.3.1.4 Temperature of a crystal

The temperature influences the diffraction properties of a crystal. Here follows the derivation of the classical Debye-Waller factor (Kittel, 1986). As the temperature of the crystal increases, the intensity of the diffraction peaks decreases, but their angular aperture (Darwin width) does not vary. Even at room temperature, the position of atoms is far enough away from the equilibrium position, to change the periodic structure of a crystal and interfere with the processes of diffraction.

Intuitively, it is expected that the Darwin width increases for lattices whose atoms undergo high thermal agitation. In contrast, even at high temperatures, the diffraction peaks are always well defined. The solution to this problem was found by Debye analyzing how the displacement from the equilibrium position affects the structure factor of the material, and then the intensity of scattered radiation. Define $\boldsymbol{r_j}$ the equilibrium position of the atom in the primitive cell j, $\boldsymbol{u}(t)$ is its displacement from the equilibrium position at time *t*, $\boldsymbol{r}(t) = \boldsymbol{r_j} + \boldsymbol{u}(t)$ its position in the primitive cell at time *t*. The structure factor of a crystal is the sum of terms of the form:

$$\langle f_j e^{-i\boldsymbol{G}\cdot\boldsymbol{r}(t)} \rangle = f_j e^{-i\boldsymbol{G}\cdot\boldsymbol{r}_j} \langle e^{-i\boldsymbol{G}\cdot\boldsymbol{u}(t)} \rangle$$

Where f_j is the form factor of the atom *j*, $\boldsymbol{G}$ is a vector of the reciprocal lattice, the operator $\langle \quad \rangle$ represents the thermal average. Until the solid remains in the crystalline state, the thermal shift $\boldsymbol{u}(t)$ is small compared to the relative distance between the atoms, and it is possible to expand the last exponential in series:

$$\langle e^{-i\boldsymbol{G}\cdot\boldsymbol{u}(t)} \rangle = 1 - i\langle \boldsymbol{G}\cdot\boldsymbol{u}(t) \rangle - \frac{1}{2}\langle (\boldsymbol{G}\cdot\boldsymbol{u}(t))^2 \rangle + \cdots$$

The thermal means in the series take the form:

$$\langle \boldsymbol{G}\cdot\boldsymbol{u}(t) \rangle = G\langle u \rangle \langle cos\theta \rangle = G\langle u \rangle \frac{1}{2\pi} \int_0^{2\pi} \cos\theta \; d\theta = 0$$

$$\langle (\boldsymbol{G}\cdot\boldsymbol{u}(t))^2 \rangle = G^2\langle u^2 \rangle \langle cos^2\theta \rangle = G^2\langle u^2 \rangle \frac{1}{2\pi} \int_0^{2\pi} \cos^2\theta \; d\theta = \frac{1}{3} G^2\langle u^2 \rangle$$

Then is obtained:

$$\langle e^{-i\boldsymbol{G}\cdot\boldsymbol{u}(t)} \rangle \sim 1 - \frac{1}{6} G^2\langle u^2 \rangle$$

This expansion is the same that is obtained for the function:

$$e^{-i\frac{1}{6}G^2\langle u^2\rangle} \sim 1 - \frac{1}{6}G^2\langle u^2\rangle$$

Where $\langle u^2\rangle$ is the mean square displacement from the equilibrium position. So you can replace:

$$\langle e^{-\boldsymbol{G}\cdot\boldsymbol{u}(t)}\rangle \sim e^{-\frac{1}{6}G^2\langle u^2\rangle}$$

The intensity of diffracted radiation is proportional to the square of the structure factor, and it can be written as:

$$I = I_0 e^{-\frac{1}{3}G^2\langle u^2\rangle}$$

Where I_0 is the intensity diffracted by a perfect lattice. The exponential is called Debye-Waller factor. If one considers each atom similar to a three-dimensional harmonic oscillator, the thermal average of its potential energy can be written as:

$$\langle U\rangle = \frac{1}{2}C\langle u^2\rangle = \frac{1}{2}M\omega^2\langle u^2\rangle = \frac{3}{2}k_B T$$

Where C is called force constant, M is the mass of the atom, ω is the frequency of the oscillator, and we know that $\omega^2 = C/M$. The diffracted intensity is:

$$I = I_0 e^{-\frac{k_B T G^2}{M\omega^2}}$$

The vector of the reciprocal lattice $\boldsymbol{G}$ represents the atomic plane on which the diffraction occurs, while the quantity ω is tabulated. $\boldsymbol{G}$ is the numerator of the exponent, then the correction due to the thermal motion grows with the increase of the order of the diffraction peak. The decrease in diffracted intensity due to the Debye-Waller factor is of the order of a few percentage points, at room temperature and for reflections with small Miller's indices. The quantity I represents the intensity diffracted at the Bragg angle. The photons lost compared to I_0 undergo inelastic scattering and becomes part of the isotropic diffuse background, or they excite oscillations of the lattice.

Seeing every atom that makes up the crystal as a three-dimensional harmonic oscillator is useful for a qualitative evaluation of the effect of temperature on the diffraction efficiency, but it is not enough when an accurate quantitative estimation is required. In this case the theoretical development of an efficient model that produces a correct Debye-Waller factor is difficult to achieve, even when the force constant is known, because of the non-harmonic components in the oscillation of the atom around its average position. In this case, it is possible to use semi-analytical models that take into account the non-harmonic components of the oscillation. These components consider how the density of states of phonons change in the crystal. The accuracy of the results obtained with this method depend on the accuracy of the experimental measurements on the density of states of phonons. For most common crystals the phonon density of states is measured with an accuracy of 2−3%, this is also the precision for the calculated Debye-Waller factor. The Debye-Waller factor is usually referred to as e^{-2W}, where the exponent is in the form $2W = (qu)^2$, where $q = k_{out} - k_{in}$ represents the variation of the wave vector between the incident wave and the diffracted wave, u represents the mean square displacement of the atom from its equilibrium position. Since the conditions of diffraction $q = |\boldsymbol{G}| = 2\pi/d = (4\pi/\lambda)sin\theta$ and $B = 8\pi^2 u^2$, the exponent can be expressed as

$$2W = 2B[(sin\theta)/\lambda]^2$$

Using the quasi−harmonic approximation to describe the atomic oscillations, the exponent can also be expressed as

$$2W = \omega_r \int_0^\infty \coth(\hbar\omega/2kT)[g(\omega)/\omega]d\omega$$

Where $\hbar\omega_r = (\hbar q)^2/2M$ is an energy term, ω is the frequency of oscillation of phonons, $g(\omega)$ is the density of phonons normalized to 1:

$$\int_0^\infty g(\omega)d\omega = 1$$

Actually, $g(\omega)$ does not depend only on ω, but also on the crystallographic plane of diffraction in a non-isotropic material, then the anisotropy also affects the Debye-Waller factor. However, this quantity is isotropic in crystals with the diamond lattice, and it is nearly isotropic for the other crystalline lattices. For the series expansion is useful to introduce the reduced variables $x = \omega/\omega_m$, $y = T/T_m$ where ω_m is the maximum frequency of the phonons, and $kT_m = \hbar\omega_m$. Then you can write:

$$2W = (\omega_r/\omega_m) \cdot J(y)$$

where:

$$J(y) = \int_0^1 \coth(x/2y)[f(x)/x]dx$$

Where $f(x) = \omega_m g(\omega)$ is the reduced density of phonon states:

$$\int_0^1 f(x)dx = 1$$

For which the quantity *B* can be written as

$$B = (4\pi^2\hbar/m\omega_m) \cdot J(y)$$

If you expand the quantity $J(y)$ developing the hyperbolic cotangent in series, you obtain:

$$J(y) = 2f_{-2}y + \frac{1}{6y} - \frac{f_2}{360y^3} + \cdots$$

Where $f_n = \int_0^1 x^n f(x)dx$, the f_n are obtained experimentally, except for $f_0 = 1$. You can split the performance of the functions described in two regimes: for low and high temperatures. In the case of low temperatures $y \to 0$, then $x \to 0$, in this case the normalized density of phonon states goes as $f(x) \to \alpha x^2$ where α is a constant to be determined experimentally. The function $J(y)$ takes the form:

$$J(y) \to f_{-1} + \left(\frac{\pi^2}{3}\right)\alpha y^2 \qquad per\ y \to 0$$

While for high temperatures it is necessary to maintain the shape of $J(y)$ truncated at the third term. The trends for low and high temperatures meet in a point, which can be taken as a point of discontinuity between the two functions. Experimentally it is obtained that for the majority of the crystals the function for low temperatures well fits the measurements when $y \lesssim 0.2$, while the function for high temperatures can be used when $y \gtrsim 0.2$.

$$J(y) = \begin{cases} f_{-1} + \left(\frac{\pi^2}{3}\right)\alpha y^2 & y \lesssim 0.2 \\ 2f_{-2}y + \frac{1}{6y} - \frac{f_2}{360y^3} & y \gtrsim 0.2 \end{cases} \qquad (3.5\_20)$$

From $J(y)$ it is possible to derive the Debye-Waller factor. The constants $\alpha, f_{-2}, f_{-1}, f_2$ are tabulated and they are well known for the majority of the crystals commonly in use.

1.3.1.5 Polarizability of matter

Consider a material with a continuous distribution of charges. Under the influence of the propagating electromagnetic wave, the local electric charges oscillate as described in (1.3.1.2 Form factors) and the material becomes polarized. If ***D*** is the electric field in a medium, the polarizability is related to the electric field by $\boldsymbol{D(r)} = \varepsilon\boldsymbol{E(r)} = \varepsilon_0\boldsymbol{E(r)} + \boldsymbol{P(r)} = \varepsilon_0[1 + \chi(\boldsymbol{r})]\boldsymbol{E(r)}$, where ε is the dielectric constant of the material, while χ is the dielectric susceptibility (polarizability). For X-rays far from the absorption edge the polarizability can be written as $\chi = \chi_n + \chi_a + i\chi_i$, where χ_a and χ_i are called anomalous dispersion corrections (Authier A. , 2001). The polarizability is a complex number, so it can be divided in its real and imaginary part $\chi = \chi_r + i\chi_i$. The term χ_n can be expressed as

$$\chi_n(r) = -\rho(r)R\lambda^2/\pi \qquad \textbf{\textit{Equation 6}}$$

The form of χ_n shows that the polarizability of matter for X-rays is very small, negative, and proportional to the electronic density. In anisotropic materials as crystals the electronic density changes with the orientation, so the polarizability varies with the lattice plane considered. In a crystalline medium, $\rho(\boldsymbol{r})$ is a periodic function of the space coordinates and so it is the polarizability. Therefore, applying the Fourier transform to Equation 6, the polarizability of the lattice plane with reciprocal space vector ***h*** is:

$$\chi_h = -\frac{R\lambda^2}{\pi V}\int \rho(\boldsymbol{r})e^{-i\boldsymbol{h}\cdot\boldsymbol{r}}d\tau = -\frac{R\lambda^2}{\pi V}F_h$$

Where $d\tau$ is the volume element. The integral is extended to the volume of the unit cell. Therefore, the polarizability is a function of the structure factor of the lattice plane F_h (Equation 5). The polarizability of the lattice plane is a complex number that can be divided in its real part $\chi_{rh} = -R\lambda^2F_{rh}/\pi V$ and imaginary part $\chi_{ih} = -R\lambda^2F_{ih}/\pi V$. Therefore, the structure factor of the lattice plane can be re-written as

$$F_h = F_{rh} + iF_{ih} = \sum_j \left(f_j + f_j' + if_j''\right)e^{-M_j - i\boldsymbol{h}\cdot\boldsymbol{r_j}}$$

Where f_j is the form factor of the atom j (Equation 4), f_j' and f_j'' are the anomalous dispersion corrections and e^{-M_j} is the Debye-Waller factor. The summation is over all atoms of the unit cell. The real part of the polarizability is typically from 10^{-5} to 10^{-7} depending on the energy of photons, on the material and on the lattice plane considered. The anomalous dispersion corrections f_j' and f_j'' are tabulated for most materials. The index of refraction is given by the relation $n = \sqrt{\varepsilon/\varepsilon_0}$, and since $\chi << 1$, $n \sim 1 + \chi_0/2 = 1 - R\lambda^2 F_0/(2\pi V)$. Therefore, the index of refraction is slightly smaller than 1 for X-rays.

1.3.1.6 Absorption

The main effects that contribute to the absorption are:

- The photoelectric absorption (μ^{PE})
- Inelastic scattering due to the Compton effect (μ^{C})
- Inelastic scattering due to thermal diffuse scattering (μ^{T})

The total linear absorption coefficient is the sum of the three $\mu = \mu^{PE} + \mu^{C} + \mu^{T}$. The photoelectric coefficient is the largest component. The absorption coefficients are tabulated for most materials in a wide range of energies. The fraction of a beam remaining after passing through a thickness t of material is

$$\eta_{abs} = e^{-\mu t}$$

1.3.2 Dynamical theory of diffraction

1.3.2.1 Fundamentals

The dynamic theory of diffraction considers the radiation that interacts with a crystal as a series of waves. The theory analyzes the interaction of these waves with the periodic potential of the crystal, taking into account the effects of multiple scattering (Authier A. , 2001). Dynamical theory considers the small effects of refraction in diffraction processes. We can reconsider the formation of Ewald's sphere with refraction effects. Consider a wave propagating in vacuum with wave number k. When the wave enters a medium with index of refraction n, the wave number of the wave becomes nk. Consider that this wave satisfies the diffraction condition, so there is a refracted wave $\boldsymbol{K_o}$ and a diffracted wave $\boldsymbol{K_h}$ connected by the vector of the reciprocal lattice $\boldsymbol{h}$. $\boldsymbol{K_o}$ and $\boldsymbol{K_h}$ can be seen as the radii of two spheres in the reciprocal space (Figure 1-35). The point representing the condition for diffraction (reflection domain) in reciprocal space is on the intersection of the two spheres with $nk = (1 + \chi_0/2)k$ as radius. These spheres are inside the larger spheres with radius k, as the index of refraction n is always smaller than 1 for X-rays.

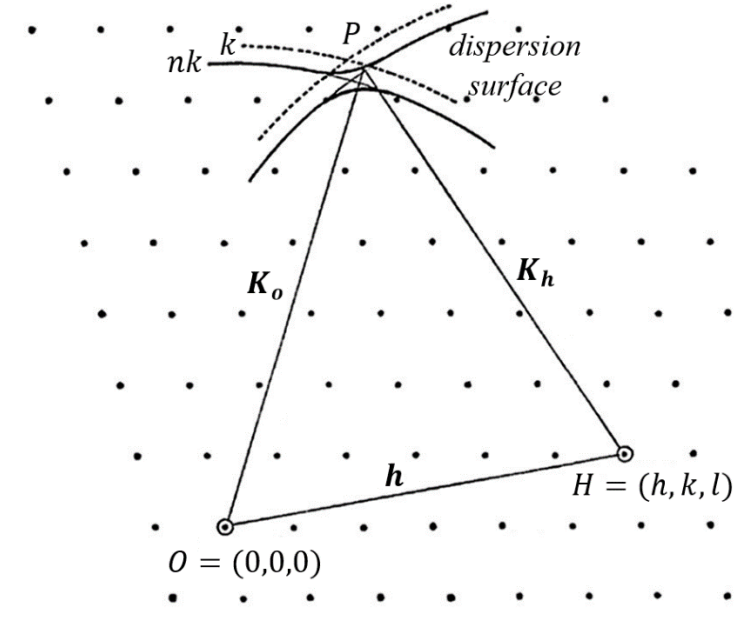

Figure 1-35

2D projection of the formation of the dispersion surface. $O = (0,0,0)$ and $H = (h,k,l)$ are points of the reciprocal lattice, $\boldsymbol{h}$ is a vector of the reciprocal lattice, while $\boldsymbol{K_h}$ and $\boldsymbol{K_o}$ are the wave vectors of the diffracted and refracted waves, P is the point where these two vectors touch. These vectors are the radii of two spheres that intersect where diffraction occurs (reflection domain). For every point in the reflection domain there is a diffracted and a refracted wave, so the point P cannot be on either of the two spheres, but it lies on a connecting surface between the two spheres, called dispersion surface. Image taken from (IUCr, 2015).

When the crystal is rocked through the reflection domain, it is not physically possible that the reflected beam occurs for only one angular position of the crystal. Indeed, in this case the intensity of the reflected wave would be zero and diffraction phenomena would not be detectable. Moreover, for every position of the crystal within the reflection domain there is a reflected wave $\boldsymbol{K_h}$ and a refracted wave $\boldsymbol{K_o}$ and these two vectors touches in a point P. The point where these two wave-vectors touch cannot belong to any of the two spheres, indeed, there is no reason for this point to lie on one sphere rather than on the other one. Therefore, this point lies on a connecting surface between the two spheres. This surface is called dispersion surface. The angular width of the diffraction (reflected domain) is represented in reciprocal space by the size of this connecting surface between the two spheres. This width characterizes the strength of the interaction between X-rays and crystal. We have seen that the structure factor estimates the intensity of interaction between radiation and crystals. Therefore, the larger the structure factor, the stronger the interaction and the larger the reflection domain. This structure is similar to band structure of solids for the propagation of electrons. Indeed, both the band theory of solids and the dynamical diffraction theory study the properties of a wave in a periodic medium. In the case of electrons this leads to the well-known band gap structure.

It is necessary to distinguish two different geometries in which the diffraction process takes place (Figure 1-36): Bragg geometry (reflection geometry) or Laue (transmission geometry). For each lattice plane, the incident wave generates a reflected wave and a transmitted wave. The waves thus generated in turn produce a reflected wave and a transmitted wave when crossing a plane lattice. C. G. Darwin showed that the balance between the transmitted and the reflected wave in correspondence to each atomic plane could be described by recursive equations. By solving these equations, it is possible to derive the expression of the reflected wave and the transmitted wave through a crystal. Darwin developed his theory for the Bragg geometry (reflection geometry), but the solution can be easily extended to the Laue geometry (transmission geometry), as shown in (Prins, 1930). If the thickness of the crystal can be considered infinite, and the crystal presents no absorption, the rocking curve of the crystal have a typical flat shape, similar to a rectangle, centered at the Bragg angle if one neglects refraction phenomena. The height of the rocking curves is equal to the ratio between the intensity of diffracted radiation and the intensity of transmitted radiation. This ratio is called diffraction efficiency of the crystal, which in this case is equals to 1. The ratio of the intensity of the diffracted beam over the intensity of the incident beam is defined reflectivity of a crystal.

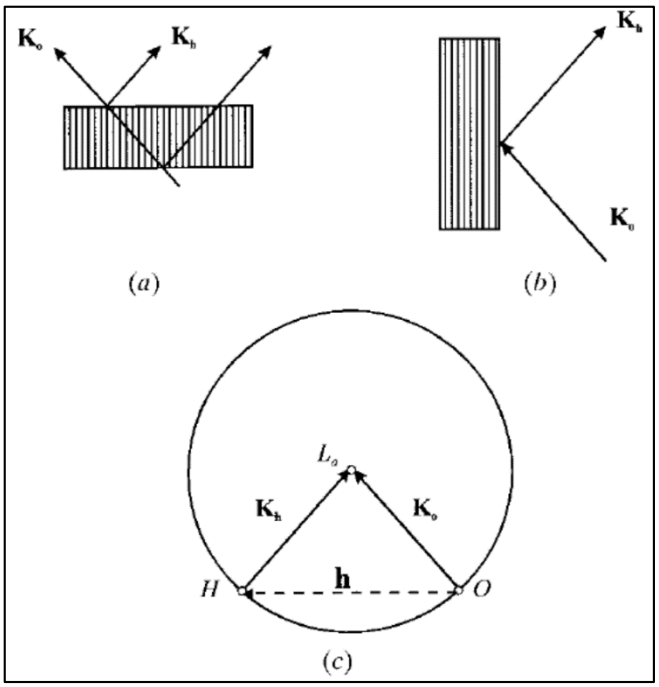

Figure 1-36

(a) Laue transmission geometry. Both the diffracted and the transmitted beams traverse the entire thickness of the crystal. (b) Bragg reflection geometry. The diffracted beam do not traverse the entire thickness of the crystal. (c) Condition of diffraction in reciprocal space, where ***h*** *is a vector of the reciprocal lattice,* $\boldsymbol{K_o}$ *is the incident wave vector,* $\boldsymbol{K_h}$ *is the diffracted wave vector.*

Moreover, the dynamical theory considers the orientation of lattice plane respect to the morphological shape of the crystal. A lattice plane not parallel to any morphological surface of the crystal is named asymmetric plane. The diffraction properties of this plane are influenced by its misalignment with the morphological surfaces of the crystal. Define β the asymmetry angle, which is equal to 0 for symmetric Laue planes, while it is equal to – Pi/2 for symmetric Bragg planes. Define $\gamma_o = \cos(\beta + \theta_B)$ and $\gamma_h = \cos(\beta - \theta_B)$ the cosines of the angles between the normal to the crystal surface and the incident and reflected directions respectively. The parameter estimating the effect of asymmetry is named asymmetry ratio, and it is defined as

$$\gamma = \frac{\gamma_h}{\gamma_o} = \frac{\cos(\beta - \theta_B)}{\cos(\beta + \theta_B)}$$

The effect of asymmetry is particularly prominent at low energy, because γ depends on the difference between the asymmetry angle and the Bragg angle. For high energy photons $\theta_B \to 0$ so $\gamma \to 1$ for any β. γ, γ_o and γ_h are always positive in Laue geometry, while γ and γ_h are always negative in Bragg geometry.

Define φ as the polarization angle of an incident polarized beam. The polarization factor *C* is:

$$C = \sqrt{cos^2\varphi + sin^2\varphi\, cos^2(2\theta_B)}$$

For unpolarized radiation, the polarization factor C is the mean of the previous equation:

$$C = \sqrt{[1 + cos^2(2\theta_B)]/2}$$

In Bragg geometry, it can be shown (Authier A. , 2001) that most of the radiation is diffracted in a thickness called extinction length. Even if a crystal is infinitely thick, only the crystal volume within the extinction length contributes considerably to the diffraction in Bragg geometry. Upon Laue diffraction, intensity is shuffled from the transmitted beam into the diffracted beam until extinction. The diffracted beam itself fulfills the Bragg condition and shuffles intensity back into the primary direction. This round-trip period is called the Pendellösung period. The extinction length is related to the Pendellösung period. Indeed, they can be written by the same expression

$$\Lambda_0 = \frac{\pi V\sqrt{\gamma_o|\gamma_h|}}{R\lambda C\sqrt{F_h F_{\bar{h}}}}$$

where V is the volume of the unit cell of the crystal, C is the polarization factor, F_h is the structure factor of the plane in which the diffraction occurs (with vector of the reciprocal lattice $\boldsymbol{h}$), while $F_{\bar{h}}$ is the structure factor of the opposite plane (with vector of the reciprocal lattice $\boldsymbol{h}$), r_e is the classical electron radius, λ is the wavelength of the incident radiation, θ_B is the Bragg angle of diffraction, γ_o and γ_h are defined above. Λ_0 is the extinction length when γ is negative (Bragg geometry) while Λ_0 is the Pendellösung period when γ is positive (Laue geometry). Then we should define

$$\delta_{os} = \frac{d}{\Lambda_0}\frac{|\gamma_h|}{\sin 2\theta_B}$$

where d is the interplanar distance of the diffracting plane. The real part of $2\delta_{os}$ is the spatial extension of the reflection domain (full width half-maximum of the rocking curve) and it is called Darwin width δ_w. For Laue symmetric diffraction ($\gamma = 1$) the Darwin width reduces to

$$\delta_w = 2\frac{d}{\Lambda_0}$$

The condition for reflection in a real crystal slight deviates from the Bragg's angle because of refraction. Then we should define the deviation from Bragg's angle due to refraction as

$$\Delta\theta_{os} = -\frac{\chi_o(1-\gamma)}{2sin2\theta_B}$$

$\Delta\theta_{os}$ is zero for symmetric Laue diffraction, while it is never zero in Bragg geometry. However, $\Delta\theta_{os}$ is far smaller than the Bragg's angle. Then we should define η as the deviation of the beam from Bragg's condition is units of the Darwin width:

$$\eta = \frac{\Delta\theta - \Delta\theta_{os}}{\delta_{os}}$$

where $\Delta\theta$ is the deviation of the angle of the beam from Bragg's condition. The parameters Λ_0, δ_{os}, $\Delta\theta_{os}$, η are reduced parameters called deviation parameters and they are used to express the equations of the dynamical theory.

The reflectivity of a thick and perfect crystal in Bragg geometry is

$$I_h^{Bragg} = \left|\eta - S(\eta_r)\sqrt{\eta^2 - 1}\right|^2$$

Where $S(\eta_r)$ is the sign of the real part of η. The integrated intensity (intensity integrated over the entire rocking curve) is $I_{hi}^{Bragg} = 8\delta_{os}/3$. When there is no absorption, the rocking curve assumes the well-known flat top shape (Figure 1-37). When there is absorption (the polarizability has an imaginary part), the rocking curve becomes asymmetric (Figure 1-38). The asymmetry is mainly due to what is called anomalous absorption. Indeed, absorption is stronger if the standing wave propagating in the crystal (the electromagnetic wave in diffracting condition) has its anti-nodes on the lattice planes, i.e. where the absorbing atoms are, while absorption is weaker if the anti-nodes are between the planes. The standing wave shifts from one condition to the other on each side of the plateau of the rocking curve. For this reason the rocking curve in an absorptive crystal has an asymmetric shape. Finally, the reflectivity of a thin and perfect non-absorptive crystal in Bragg geometry can be expressed as:

$$I_h^{Bragg} = \frac{1 - cos^2(\pi t/\Lambda)}{\eta^2 - cos^2(\pi t/\Lambda)}$$

When the crystal is thin enough, the interference between the waves diffracted by the scatterers is visible in the rocking curve (Figure 1-37) in the form of an oscillation in the function. In Bragg geometry, when the thickness of the crystal is small, there is a diffracted beam and a transmitted beam. The diffracted beam exits from the surface through which the incident beam entered in the crystal, while the transmitted beam exits the crystal through the opposite face.

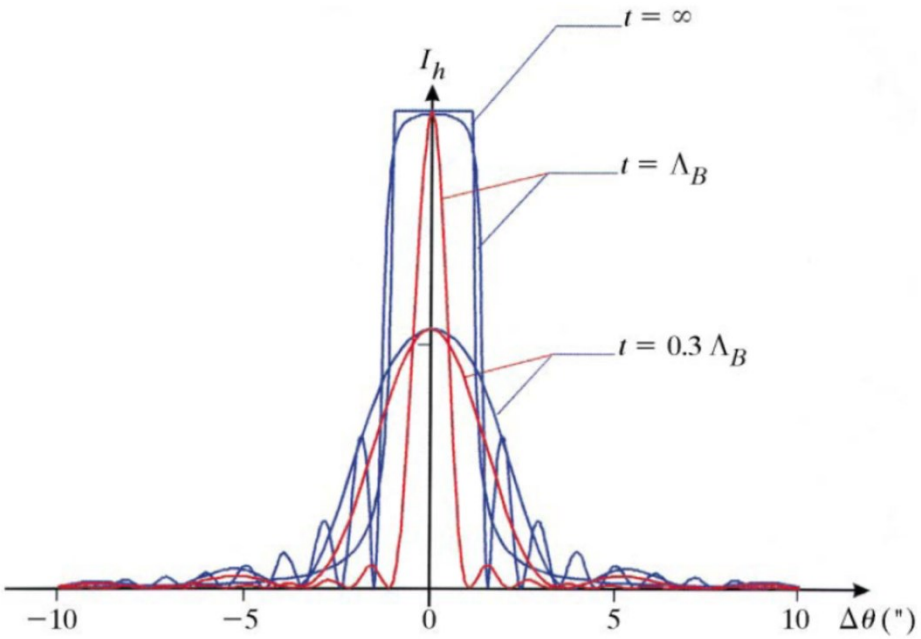

Figure 1-37

Comparison between the rocking curves calculated using the kinetic theory (red) and the dynamical theory (blue) in Bragg geometry, for a silicon crystal (220) without considering absorption. The energy of incident X-rays is the typical Mo Kα. Curves are calculated for different thicknesses of the crystal t = 0.3 Λ, t = Λ, t = ∞. $\boldsymbol{I_h}$ *represents the intensity of the diffracted beam, whose wave vector has undergone a change equal to* $\boldsymbol{h}$ *vector of the reciprocal lattice. Δθ (") represents the deviation from the Bragg angle in arcsec. When thickness decreases, the kinematic rocking curve approaches the dynamic rocking curves. For t = ∞, the kinematic rocking curve becomes a Dirac delta function, while the dynamic rocking curve assumes a square shape. Image taken from (Authier A. , 2001).*

In the Laue geometry, both the diffracted beam that the transmitted beam exit the crystal through the opposite face with respect to which the incident beam entered in the crystal. The radiation inside the crystal produces a diffracted and a transmitted wave every time that it crosses a crystalline plane. The waves thus produced in turn interact with the crystalline planes. Due to the geometry of the system, there is not a favored output direction from the crystal. Therefore, the intensity of the wave in the crystal oscillates between the diffraction direction and the transmission direction. The oscillations in intensity between the transmitted and diffracted beam are said Pendellösung oscillations.

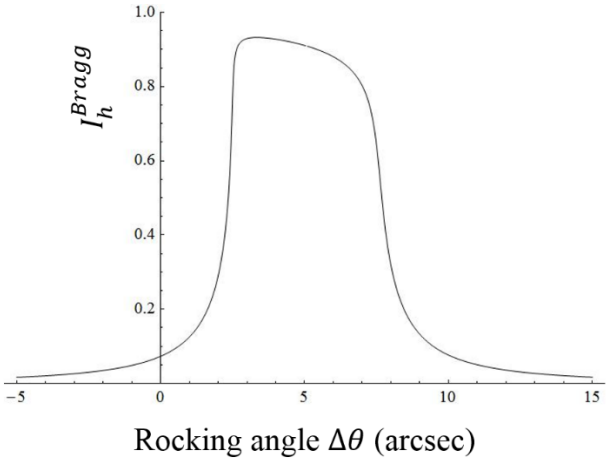

Figure 1-38

Rocking curve in Bragg geometry of a thick Si (111) crystal, asymmetry angle 4°.

The reflectivity of a thick and perfect crystal in Bragg geometry is

$$I_h^{Laue} = e^{-\frac{\mu_j t}{\gamma_o}} \left|\frac{F_h}{F_{\bar{h}}}\right| \frac{\gamma^{-1}}{4(1+\eta_r^2)}$$

Where t is the thickness of the crystal, μ_j is the absorption coefficient with anomalous absorption, η_r is the real part of the reduced parameter η. Finally, the reflectivity of thin and perfect non-absorptive crystal in Laue geometry can be expressed as:

$$\eta_{Laue} \propto \frac{sin^2(\pi t/\Lambda)}{\gamma(1+\eta^2)}$$

For the same case, the relationship between the transmitted beam and the incident beam (transmission efficiency) can be expressed as:

$$\tau_{Laue} \propto \frac{\eta^2 + cos^2(\pi t/\Lambda)}{1+\eta^2}$$

Naturally $\eta_{Laue} + \tau_{Laue} = 1$ for conservation of energy. The diffracted and transmitted intensities are oscillating functions of the thickness of the crystal. The diffracted beam and the transmitted beam periodically exchange energy, thus the fluctuations in intensity of the two are complementary. When one is at the maximum, the other is to the lowest point and vice versa (Figure 1-39). The integrated intensity for diffraction in Laue geometry is:

$$\frac{I_{int}^{din}}{I_0} = \frac{r_e \lambda^2 C_p |F_{hkl}|}{2V_c sin\theta_B} \int_0^{2\pi t/\Lambda} J_0(z)dz \qquad (2.4\_6)$$

This behavior as a function of the thickness of the crystal is shown in Figure 1-40. When the thickness of the crystal is small, the integrated intensity grows linearly, which is the trend expected from the kinetic theory. For thicker crystals, the function oscillates, and the oscillations tend to converge to a stationary value. This trend is also recognizable in the oscillations in the intensity in Figure 1-39. In Figure 1-39 the oscillating pattern of reflectivity and of transmission efficiency converge towards a

stationary value. In Laue geometry, the direction of diffraction is symmetrical to the direction of transmission and neither of them is privileged. Therefore, on average half of the incident radiation goes in the diffracted beam, and half goes in the transmitted beam. This condition is attained for t → ∞ and it is visible in Figure 1-41. Therefore, a thick non-absorptive crystal in Laue geometry has a maximum reflectivity of 0.5.

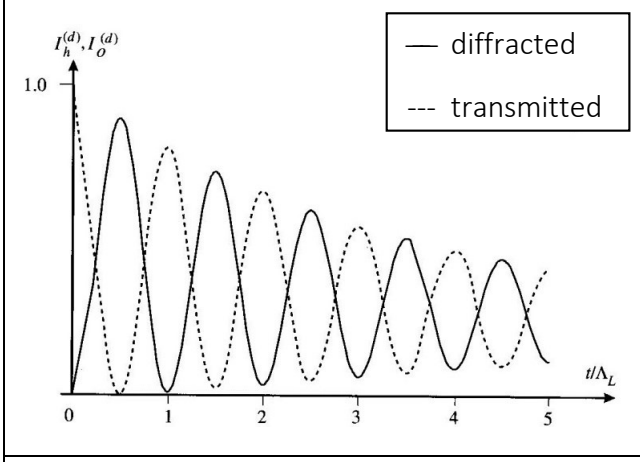

Figure 1-39

Pendelosung oscillations as a function of the thickness of the crystal, for an absorptive Si (220) crystal under a Cu K α X-ray beam. $\boldsymbol{I_h}$ *represents the intensity of the diffracted beam, the wave vector which has undergone a change equal to the vector* $\boldsymbol{h}$ *of the reciprocal lattice.* $\boldsymbol{I_0}$ *is the intensity of the transmitted beam, whose wave vector is unchanged. Image taken from (Authier A. , 2001).*

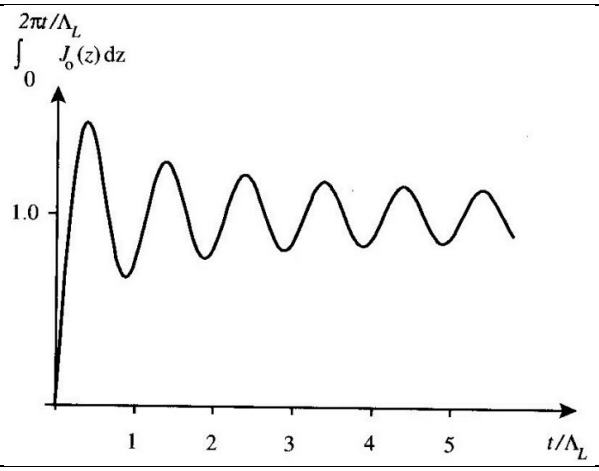

Figure 1-40

Integral of the Bessel function of zero order as a function of the thickness. This integral is proportional to the integrated intensity in Laue geometry. Image taken from (Authier A. , 2001).

When the thickness of the crystal decreases, the intensity of the diffracted radiation calculated by the dynamical theory tends to the value of the intensity calculated by the kinetic theory. The integrated intensity (intensity integrated over the entire rocking curve) calculated using the kinetic theory and the dynamical theory are related by:

$$I_{int}^{din} = I_{int}^{kin} \frac{\tanh(\pi t/\Lambda)}{\pi t/\Lambda}$$

Where t is the thickness of the crystal. The two intensities are related by a correction factor, which tends to one when t/Λ tends to zero (Figure 1-37). For example, for $t/\Lambda = 0.1, 0.05, 0.01$ the correction factor assumes the values 0.968, 0.992, 0.999. By increasing the energy of the incident radiation, the extinction length increases and the factor t/Λ is reduced, thus improving the kinetic approximation. This expression is valid for diffraction both in Bragg or Laue geometry, since it is valid when $t << \Lambda$ and in this case the intensities diffracted in the two cases is very similar.

The rocking curves obtained by non-absorptive crystals in Laue and Bragg geometry are compared in Figure 1-41 and Figure 1-42. The peak of reflectivity in Bragg geometry increases with the thickness. The peak of reflectivity in the Laue geometry fluctuates with the thickness. It reaches the maximum $\eta_{Laue} \sim 1$ for $t = \Lambda/2$, it reaches the minimum $\eta_{Laue} \sim 0$ for $t = \Lambda$, and it tend to the average value of $\eta_{Laue} \sim 0.5$ for $t \to \infty$. What we have seen so far is true for flat crystals. For crystals whose lattice structure is deformed, the processes described must be corrected (1.3.2.2 Uniformly curved diffraction planes).

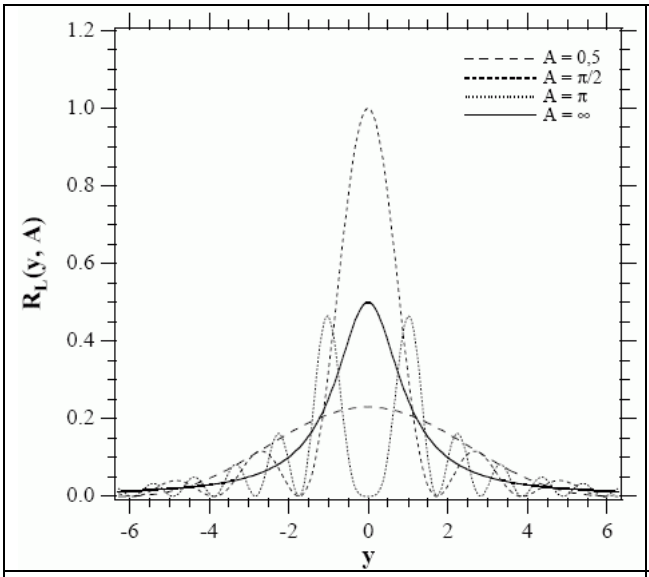

Figure 1-41

Reflectivity rocking curves of a non-absorptive crystal in Laue geometry for various values of the thickness of the crystal, where $y = \frac{2\Delta\theta}{\delta_w}$, $A = \pi t/\Lambda$.

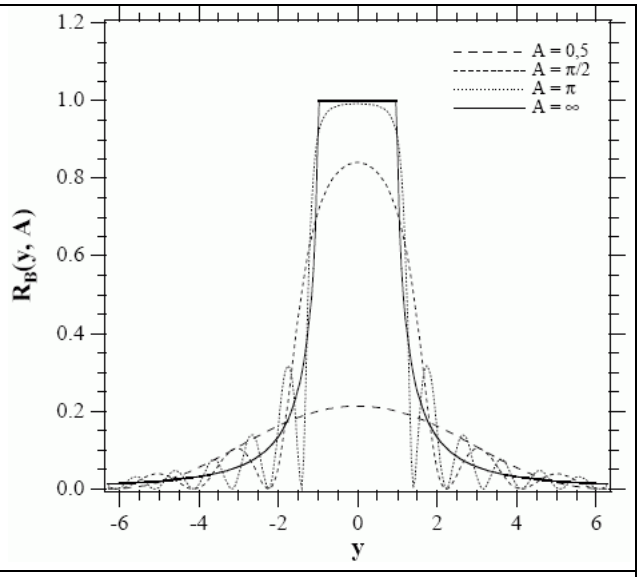

Figure 1-42

Reflectivity rocking curves of a non-absorptive crystal in Bragg geometry for various values of the thickness of the crystal, where $y = \frac{2\Delta\theta}{\delta_w}$, $A = \pi t/\Lambda$.

1.3.2.2 Uniformly curved diffraction planes (CDPs)

The equations of dynamical diffraction theory have to be revised for deformed crystals. A case of particular interest for our applications is uniformly curved crystals. Because of the uniform curvature, the dynamical diffraction equations are the same in all the crystal, so the same equations reduce to a simple form. To understand how the equations of dynamical diffraction theory change, it is necessary to focus on how the extinction length (or Pendellösung length) changes. Indeed, a flat crystal can diffract just in a narrow energy bandwidth, but all the crystal thickness is available to diffract X-rays in this bandwidth. At the opposite, a curved crystal can diffract in a large bandwidth, but just a portion of the thickness is available to diffract a certain energy. If this portion becomes smaller than the extinction length Λ, diffraction phenomena have to be rethink. First, re-diffraction of photons is prevented because of the continuous change of the incidence angle. Indeed, consider $\delta_0 = \Lambda/\mathrm{R}$ the angle of rotation of diffraction planes over an extinction length. If $\delta_0 > \delta_w$, diffracted photons cannot be diffracted again, because they would be misaligned respect to the Bragg angle of more than the Darwin width of the diffraction plane. We can express δ_0 in unities of the Darwin width as $\delta_0 = k\delta_w$, where $k = \Lambda/R\delta_w$. Then, we have to consider that the extinction length varies with the curvature. If on a length Λ a curved crystal should offer to the radiation at a range of diffraction angles equal to $(k+1)\delta_w$, it means that a length equal to $\Lambda/(k+1)$ is available to diffract each component of the beam. Each component with a certain beam energy is entirely diffracted X (total extinction) if the portion of the thickness of the crystal suitable diffract that energy is equal to or more than the length of extinction Λ. Therefore, the length necessary to diffract the entire beam is:

$$\Lambda_C = \Lambda \cdot (k+1) = \Lambda \cdot \left(\frac{\Lambda}{R\delta_w} + 1\right)$$

Following (Authier A. B., 1970) (Malgrange, 2002), the variation of the incidence angle on the diffracting plane is

$$\partial\theta = \frac{1}{ksin2\theta}\frac{\partial}{\partial s_h}(\boldsymbol{h}.\boldsymbol{u})$$

Where (s_0, s_h) is a coordinate system parallel to the incident and reflected beams respectively, $\boldsymbol{h}$ is the reciprocal lattice vector of the diffracting plane, $\boldsymbol{u}$ is the displacement vector and $k = 1/\lambda$. The condition for small distortion can be written as

$$\frac{1}{ksin2\theta}\frac{\partial^2}{\partial s_0 \partial s_h}(\boldsymbol{h}.\boldsymbol{u}) \ll \frac{\delta_w}{\Lambda}$$

For the applications in this thesis, we are particularly interested in the symmetrical Laue geometry that we analyze in the following. Define the parameter β as:

$$\beta = \frac{1}{cos^2\theta}\frac{\partial^2}{\partial s_0 \partial s_h}(\boldsymbol{h}.\boldsymbol{u})$$

Then the conditions for which the perturbation to diffraction due to curvature are too small to be significant becomes

$$\beta \ll \frac{1}{\Lambda} \; or \; \beta\Lambda \ll 1$$

On the contrary, when $\beta\Lambda \gg 1$ the correction to diffraction process due to curvature is dominant, and diffraction efficiency (rate between diffracted and transmitted intensity) is:

$$\eta = 1 - e^{-\frac{\pi^2}{\beta\Lambda}}$$

For uniformly curved planes $\beta = \Lambda/dR$ where d is the interplanar spacing of the diffracting plane. Then diffraction efficiency can be written as

$$\eta = 1 - e^{-\frac{\pi^2 dR}{\Lambda^2}}$$

It is possible to notice that

$$\eta = 1 - e^{-\frac{\pi^2\delta_w}{2\delta_0}} = 1 - e^{-\frac{\pi^2 1}{2\,k}}$$

The reflectivity of the curved crystal can be written as

$$I = e^{-\mu t}\left(1 - e^{-\frac{\pi^2 dR}{\Lambda^2}}\right)$$

Where $e^{-\mu t}$ is due to absorption. μ is the absorption coefficient of the material, t is the thickness traversed.

2 Extension of the Dynamical Theory

In this section, a model is proposed to calculate the diffraction efficiency of CDPs with arbitrary radius of curvature. The model generalizes the results based on dynamical theory of diffraction, which are valid only for crystals with a radius of curvature lower than the critical curvature R_C (1.3.2.2 Uniformly curved diffraction planes). The model is proposed for any kind of crystal, and its efficiency tends to one half in the limit of a thick flat crystal. Based on the model, it was possible to reconsider the results of recently observed diffraction efficiency for curved crystals. Finally, the model casts an upper limit for diffraction efficiency of low-curvature curved crystals, this latter being useful in applications as the construction of a Laue lens.

Diffraction efficiency strongly depends on the curvature radius R of CDPs. In the case $R << R_C$, the formula below (1.3.2.2 Uniformly curved diffraction planes) provides a good approximation for diffraction efficiency:

$$\eta_{diff} = 1 - e^{-\frac{R\pi^2 d}{\Lambda^2}} \qquad \textit{Equation 7}$$

Of course, Equation 7 does not work for crystals with low curvature. Indeed, it would approach to the unity as the curvature radius tends to infinity, instead of approaching to 0.5, i.e. the diffraction efficiency of a flat crystal. To date, there exists no analytical theory that quantitatively calculates the diffraction efficiency for crystals with low curvature. In this case, a complete resolution of the Takagi-Taupin equations would be needed, which is not simple and often not possible (Authier A. , 2001). Indeed, the applications of CDP crystals sometimes require a curvature radius in the range where Equation 7 is not valid. For this reason, we worked the model described in this section.

2.1 Theoretical and modelling

Photons undergo multiple diffractions traversing a flat crystal in Laue symmetric geometry. In this process, virtually all the photons have been diffracted at least once after traversing a thickness defined as the Pendellösung length $\Lambda_L = \frac{\pi V \cos\theta_B}{r_e \lambda C |F_h|}$. V is the volume of the unit crystalline cell, θ_B the Bragg angle, r_e the classical electron radius, λ the wavelength of the incident photons and C their polarization factor, F_h the structure factor of the diffracting planes. The same concept holds for Bragg symmetric diffraction, in this case the significant thickness is named extinction length Λ_B. The quantity $2\delta_W$ is called the Darwin width, it quantifies the width of the intensity profile while rocking a flat perfect crystal around the Bragg position (RC). For diffraction in Laue symmetrical geometry, δ_W is given by $\delta_W = \frac{d}{\Lambda_L}$, where d is the interplanar spacing between the diffraction planes.

The physical quantity $R_C = \frac{2\Lambda_L}{\delta_W \pi}$ is called the critical radius of curvature of the CDPs. As will be explained below, diffraction efficiency is influenced by two phenomena: the variation of the fraction of the incident beam that undergoes extinction (prevalent for $R \ll R_C$), and re-diffraction inside the traversed crystal thickness (prevalent for $R \gg R_C$). Equation 7 holds when the radius of curvature of CDPs is smaller than the critical radius $R \ll R_C$.

Indeed, in a CDPs crystal where $R \ll R_C$, it is not possible to obtain complete extinction of the incident beam as for a flat crystal. In fact, for a flat crystal, the entire thickness t_0 is available for diffracting the photons at a particular energy. In the case of a highly curved crystal, only a fraction of the crystal thickness can diffract the photons at a particular energy, due to the large change of incidence angle between photons and lattice planes. Photons passing through a lattice are diffracted if their angle of incidence differs less than δ_W from the Bragg angle θ_B. In other words, the Darwin width is the tolerance on the tilt for diffraction. Photons undergoing diffraction with a flat lattice are completely diffracted at least once after traversing a thickness Λ_L, i.e. Λ_L is the thickness needed to entirely diffract a photon beam. If a crystal is curved, the lattice planes rotate changing the incidence angle between bean and planes. If the rotation angle over the length Λ_L becomes larger than δ_W, the beam exits the Bragg condition before the entire beam is diffracted. In other words, the length needed for full extinction in a flat crystal is not Λ_L, but it is larger. Equation 7 express this physical phenomenon, thus the equation is valid only when the rotation of lattice planes over a length Λ_L is larger than the Darwin width.

The phenomenon that dominates for small curvatures $R \gg R_C$ is re-diffraction. If the rotation between two locations in a CDP lattice is smaller than δ_W, a photon diffracted in the first location can be re-diffracted in the second location. Consider the diffraction efficiency for a flat and very thin crystal in Laue geometry. In this case, diffraction efficiency is an oscillating function of the crystal thickness. It approaches the unity as the thickness is equal to $\Lambda/2$ and the angle between the beam and the diffraction planes is exactly the Bragg angle. If the incoming beam is slightly misaligned from the Bragg condition, diffraction efficiency falls off. Following (Zachariasen, 1945), the dependence of diffraction efficiency on misalignment can be approximated by a Gaussian distribution, whose maximum attains the unity at zero misalignment, and its FWHM equals to the Darwin width, i.e., the standard deviation of the Gaussian is $\sigma = 2\delta_w/2.35$. Thus, we define the misalignment function as $Exp(-(\Delta\theta)^2/2\sigma^2)$, where $\Delta\theta$ is the tilt from the Bragg angle.

X-ray propagation in a crystal is considered without absorption and perfectly at the Bragg angle for the first interaction. The basic approach is to divide the crystal into finite elements, which is similar to the initial assumption of the lamellar model (White, 1950). Although, multiple diffraction is considered in this thesis work, with the consequent re-diffraction effects produced by the misalignment of neighboring elements. From this point forward, we set $\Lambda_L = \Lambda$ to make the notation leaner. One can regard a CDP crystal as a series of very thin flat crystals (lamellae) slightly misaligned one another. The thickness of these crystals is set equal to half of the Pendellösung length (Figure 2-1), because within this length, 96 % of the photons in the X-ray beam undergo a single interaction with the crystal (Authier A. , 2001). Thus, the total crystal thickness t_0 is divided into N lamellae of thickness $\Lambda/2$, i.e., $t_0 = N\Lambda/2$. The relative misalignment between two subsequent lamellae is $\delta_0 = \Lambda/2R$ and depends on the curvature, which is considered to be perfectly cylindrical. The beam is assumed monochromatic and arbitrarily narrow. Here we introduce a simplification that we will correct afterwards: the beam is considered to diffract with the lattice every $\Lambda/2$. In this case, the totality of the photons in the beam can be considered to interact with the lamella, but the interaction is free of re-diffraction processes. In some intuitive and simplified sense, it would be possible to define a lamella as a crystal thickness within which the totality of the photons interact only once with the crystal. Naturally, the thickness of a lamella is dependent on photon energy and the nature of the crystal, because Λ is a function of energy, too. Then, propagation of an x-ray beam in a curved crystal can be studied once the relative misalignments between the lamellae is known.

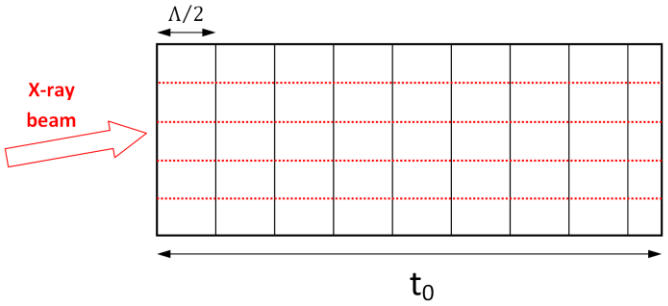

Figure 2-1

Schematic representation of the diffraction process in Laue (transmission) crystal. Dotted lines represent the diffraction planes. The X-ray beam interact with the crystal by traversing the entire crystal thickness t_0. The crystal can be divided into elements with thickness $\boldsymbol{\Lambda/2}$.

The process of diffraction and re-diffraction can be separated in two independent phenomena. The first phenomena is the variation of diffraction efficiency as a function of the misalignment from the Bragg angle $Exp(-(\Delta\theta)^2/2\sigma^2)$. The second phenomena is the variation of the fraction of the incident beam undergoing diffraction as a function of the radius of curvature of the CDPs, namely expressed by Equation 7. Thereby, the expression for the diffraction efficiency profile of a single lamella is the product of the two individual distributions, namely it is the misalignment function $Exp(-(\Delta\theta)^2/2\sigma^2)$ multiplied by Equation 7.

$$f(\Delta\theta, R) = e^{-\frac{(\Delta\theta)^2}{2\sigma^2}}\left(1 - e^{-\frac{\pi^2 dR}{\Lambda^2}}\right) \tag{2}$$

Multiple diffraction splits the initial beam into several branches (Figure 2-2). The branches continue propagating and diffracting with the lattice every $\Lambda/2$, so that after n diffractions with the lattice, the initial beam is divided into 2^n branches. During this process, the misalignment between the branches propagating in the crystal and the diffraction planes varies because of the crystal curvature. As said, the relative misalignment between two subsequent lamellae is $\delta_0 = \Lambda/2R$. Then, the angle between a branch propagating in the transmission direction and the crystallographic planes varies of $+\delta_0$ from one lamella to the subsequent lamella. Conversely, the angle between a branch propagating in the diffraction direction and the crystallographic planes varies of $-\delta_0$ from one lamella to the subsequent

one. The process of formation and misalignment of the branches continues all over the crystal thickness.

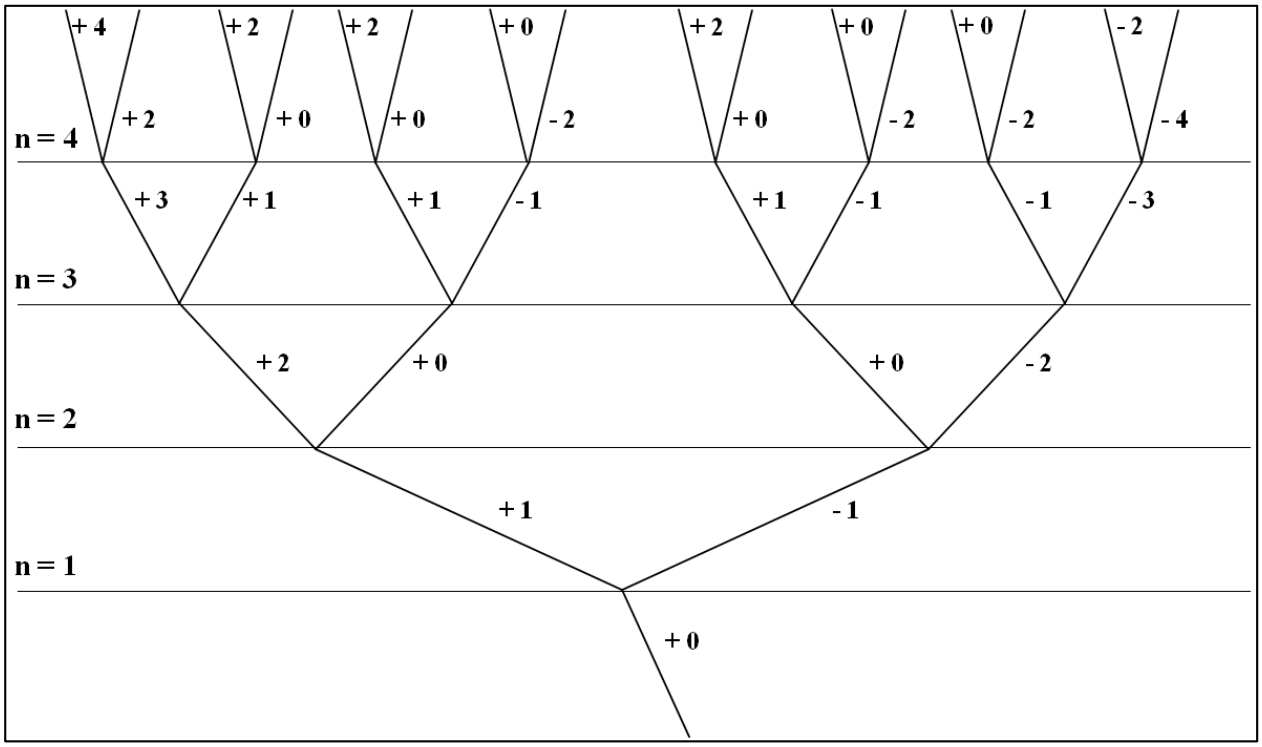

Figure 2-2

Sub-division of the initial beam into branches inside the crystal for subsequent steps n (Borrmann triangle). The number besides each branch represents the misalignment in unity of δ_0 with respect to the Bragg angle at next interaction point of the beam with CDPs. The angles between the lines of different layers are physically the same, but in the figure they look different to avoid line overlap.

A matrix holds the information about the misalignment between branches and diffraction planes (Equation 8). The rows of such matrix represent the 2^n branches and the n columns represent the diffractions undergone by the beam. The entries of the matrix are expressed in units of δ_0. As an example, for $n = 3$, this matrix holds:

$$path_{i,j}^{(3)} = \begin{pmatrix} -1 & -1 & -1 \\ -1 & -1 & +1 \\ -1 & +1 & -1 \\ -1 & +1 & +1 \\ +1 & -1 & -1 \\ +1 & -1 & +1 \\ +1 & +1 & -1 \\ +1 & +1 & +1 \end{pmatrix} \qquad i = 1, \dots, 2^n \qquad j = 1, \dots, n$$

Equation 8

At the *n-th* order, the fraction of the initial intensity streaming into the *i-th* branch is:

$$\eta_{i,n} = \left| \frac{1 - path_{i,1}^{(n)}}{2} - e^{-\frac{\pi^2 dR}{\Lambda^2}} \right|$$

$$\prod_{j=1}^{n-1}\left|\left|\frac{path_{i,j}^{(n)}+path_{i,j+1}^{(n)}}{2}\right|-\left(e^{-\frac{\left(\delta_0\sum_{k=1}^{j}path_{i,k}^{(n)}\right)^2}{2\sigma^2}}\cdot\left(1-e^{-\frac{\pi^2 dR}{\Lambda^2}}\right)\right)\right|$$

Diffraction efficiency of the entire crystal after *n* interactions is equal to the sum of the intensities held by the branches oriented in the diffraction direction.

$$\eta_n=\sum_{i=1}^{2^n}\eta_{i,n}\cdot\frac{1-path_{i,n}^{(n)}[i,n]}{2}$$

For completeness, the transmission efficiency of the same is $\tau_n=1-\eta_n$ or

$$\tau_n=\sum_{i=1}^{2^n}\eta_{i,n}\cdot\frac{1-path_{i,n}^{(n)}[i,n]}{2}$$

According to the model, in the case of a flat crystal, the intensity of the initial beam is a single branch, which is either the diffracted beam if *n* is an odd number or the transmitted beam if *n* is even. Hence, diffraction efficiency for a flat crystal results either 1 or 0, respectively.

The elaboration of the model has called forward the discretization at "deterministic" locations of the interaction between X-rays and lattice, but for real situations, the interaction occurs continuously. For a thick crystal, the effect of continuous interaction, ruled by the laws of probability, changes the effective thickness within which the beam is completely diffracted. This stochastic effect is equivalent to a crystal with deterministic diffraction locations but with thickness uncertainty $\Lambda/2$. Thus, for a given thickness t_0, the real diffraction efficiency of the outgoing diffracted beam is the average of the diffraction efficiency η_n for a crystal of thickness $t_0-\Lambda/2$ and the diffraction efficiency η_{n+1} of a crystal of thickness t_0. For a flat crystal, these two extreme values are 0 and 1, then diffraction efficiency holds 0.5. The same holds for a curved crystal. Hence, the real diffraction efficiency of the entire crystal at the *n-th* order is the average between the intensity held by the branches in the diffraction direction at the order *n* and at the order (*n*+1).

$$\eta_{ntot}=\frac{\eta_n+\eta_{n+1}}{2} \tag{6}$$

Since it has to be considered the contribution to diffraction efficiency up to the order $n+1$, the corresponding number of lamellae is $N=n+1=2t_0/\Lambda$.

Figure 2-3 shows the calculation through the model of diffraction efficiency η_{ntot} for a Ge crystal as a function of the curvature radius for some values of *n*. Diffraction efficiency tends to 0.5 as $R\to\infty$, i.e., for a flat crystal. Indeed, diffraction efficiency perfectly overlaps with the expectation of the dynamical theory (Equation 7) in the range $R\ll R_C$. As the crystal becomes thicker (increase of *n*), the change in the efficiency curve due to the variation of thickness (variation of *n*) becomes even less important. Indeed, the diffraction efficiency tends to stabilize for large thickness. The critical radius is the condition at which δ_0 is equal to the Darwin width. Since δ_0 depends on the curvature, as the curvature radius exceeds the critical radius $R\gg R_C$, the effect of misalignment between near points of the lattice dominates over the effect of variation of the Pendellösung length. The phenomena of re-diffraction is inhibited, therefore the diffraction efficiency increases if compared to the case of a flat crystal. Meanwhile, the diffraction efficiency is not decreases from the

variation of Pendellösung length, since this variation is negligible for $R \gg R_C$. As the curvature radius becomes smaller than the critical radius $R \ll R_C$, the effect of variation of the Pendellösung length dominates, thus reducing diffraction efficiency. Moreover, for $R \ll R_C$ the tilt between lamellae δ_0 is so larger than the Darwin width, that re-diffraction is fully prevented and just the first diffraction process is important.

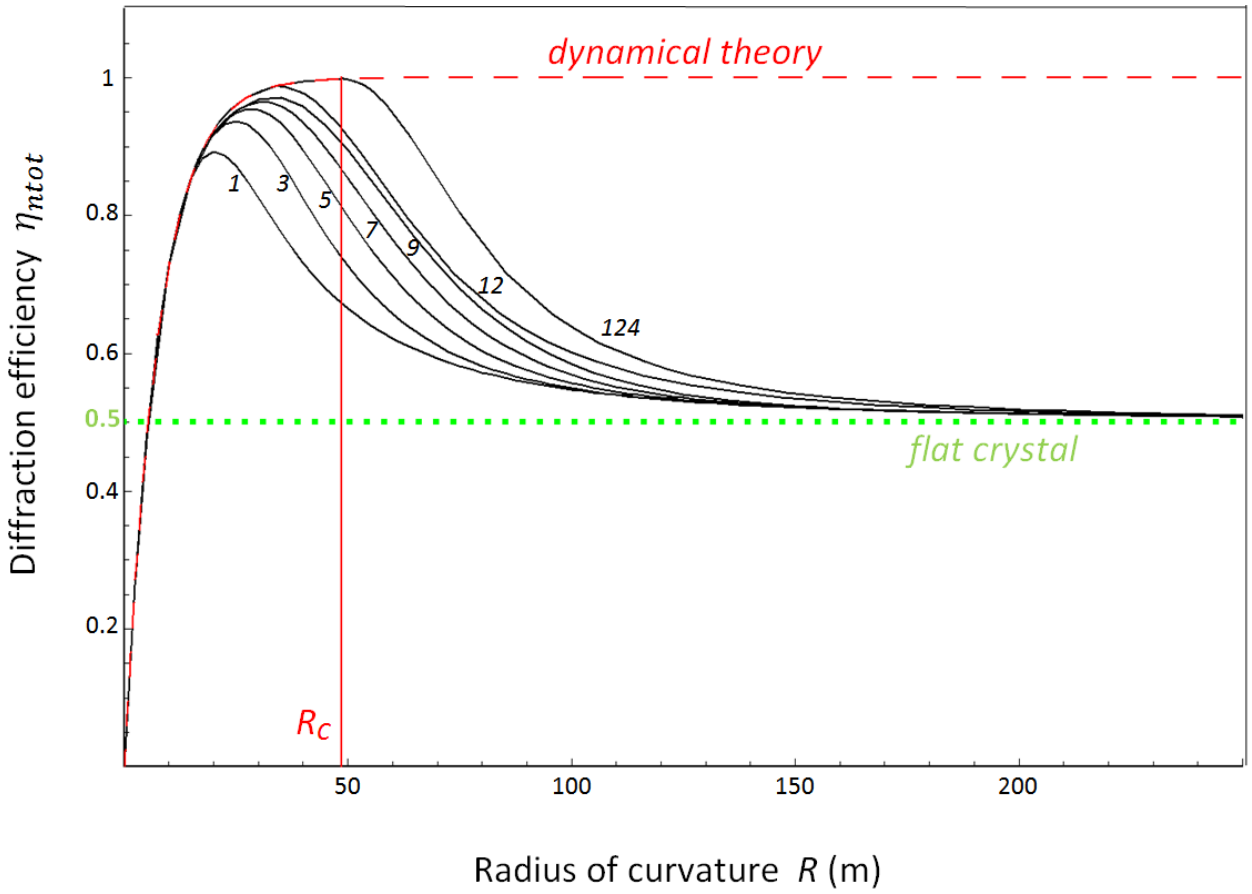

Figure 2-3

Diffraction efficiency vs. curvature radius in a Ge crystal. Photons with energy E = 150 keV are diffracted by (111) CDPs. The dashed curve represents the prediction of dynamical diffraction theory through Equation 7. The vertical line indicates the critical radius, R_C = 48.6 m for (111) Ge. The dotted horizontal line is the theoretical limit to diffraction efficiency for a flat crystal (η = 0.5). The set of curves are the diffraction efficiency η_{ntot} at n = 1,3,5,7,9,12,124, corresponding to a number of lamellae N = n + 1 = 2,4,6,8,10,13,125. Being $\boldsymbol{\Lambda/2}$ = 78.8 μm, the corresponding crystal thicknesses are t_0 = (0.158, 315, 0.473, 0.630, 0.788, 1.024, 9.85) mm. The latter thickness is the thickness of a Ge crystal that was experimentally tested in Figure 2-5 b. An increase in the number of lamellae tends to be even less effective.

The analysis has been repeated for Si, which has also been used to fabricate curved crystals for X-ray diffraction. Si presents similar crystalline structure but lower atomic number and electronic density than Si. These characteristics lead to a larger Pendellösung length Λ, thus a larger critical radius R_C. As an example, for diffraction of photons with energy E = 150 keV by (111) Ge CDPs, the critical radius is R_C = 48.5 m, while for (111) Si CDPs the critical radius is R_C = 267 m. For a given n, diffraction efficiency can be expressed in terms of normalized curvature radius R/R_C as in Figure 2-4. Here, diffraction efficiency as a function of R/R_C is the same for both materials as a representation that the critical radius conveys the whole information regarding X-ray diffraction in a bent crystal.

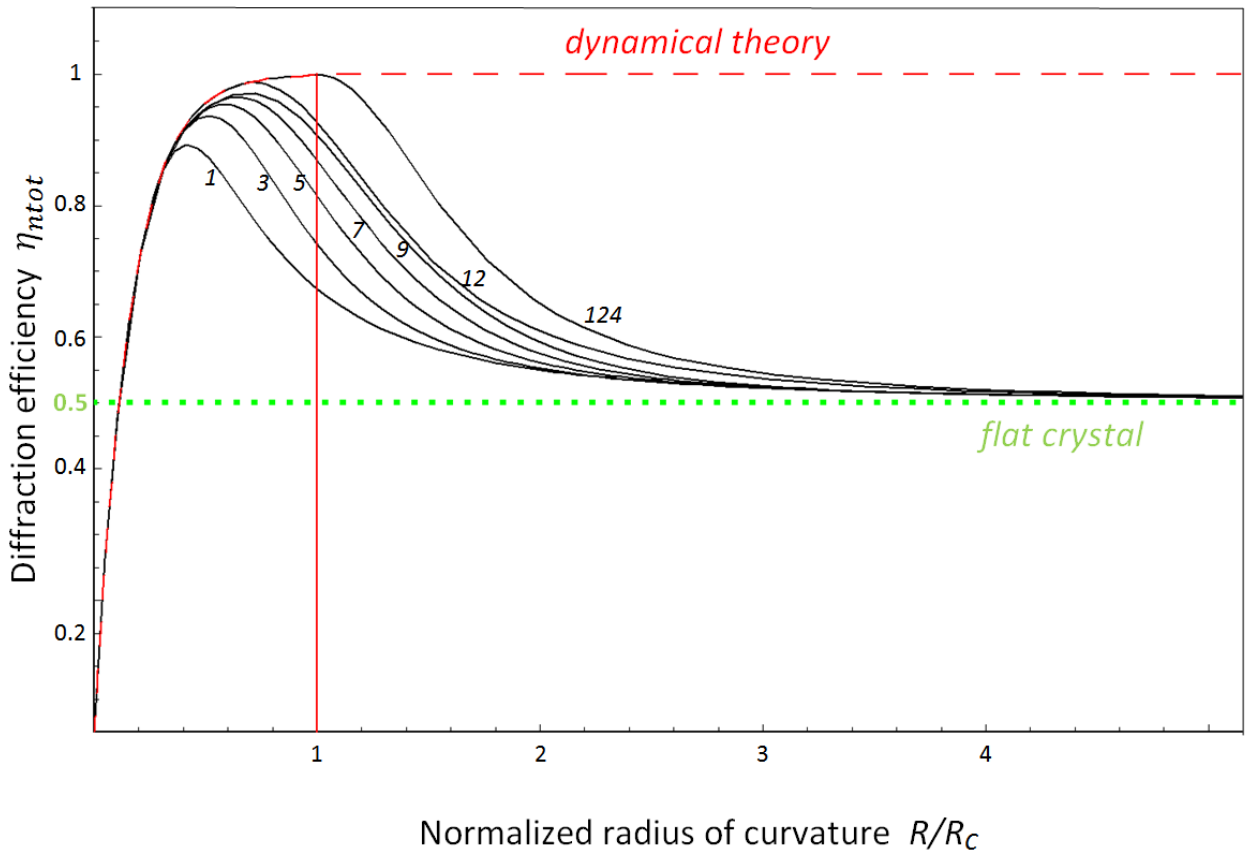

Figure 2-4

Same meaning of physical quantities as in Figure 2-3 as a function of normalized radius. In addition to Figure 2-3 the simulation was repeated within the interval of photon energy 150 – 5000 keV with steps of 150 keV in the cases of both Si and Ge. For each number of lamellae all the curves overlap to each other irrespective of the energy and of the material.

2.2 Experimental and conclusions

The results of this model allowed to interpret experimental data from an old measurement campaign run at ESRF. A series of Si and Ge grooved CDPs crystals were analyzed by X-ray diffraction. A typical RC diffraction plot for a Si crystal is shown in Figure 2-5. For the samples with moderate curvature the experiment highlighted a discrepancy between measured efficiency and the theoretical expectations relying on dynamical theory of diffraction (Table 2-1). Indeed, under some conditions of application, the curvature radius of crystals exceeded the critical radius. Measured diffraction efficiency for Si is consistent with the prediction of the model. In fact, predicted efficiency is (93.1 ± 4.2) % while it was experimentally recorded a diffraction efficiency of (94.0 ± 3.0) %. For Ge, diffraction efficiency was somewhat lower than the theoretical prediction, inasmuch as predicted efficiency is (67.6 ± 4.4) % while experimental diffraction efficiency was (58.1 ± 1.9) %. However, for the samples of that run, grooving of Ge samples for bending was found to be too aggressive, resulting in lower diffraction efficiency b. In fact, as determined by the slope of this curve in Fig. 6b, the crystal highlighted a mosaicity β = (3.5 ± 0.4) arcsec.

	E (keV)	*R/R_C*	*η_{exp} (%)*	*η_{dyn} (%)*	*η_{th} (%)*
Si	150	1.28 ± 0.09	94.0 ± 3.0	100	93.1 ± 4.2
Ge	150	1.89 ± 0.15	58.1 ± 1.9	100	67.6 ± 4.4

Table 2-1

A Si crystal plate with dimensions (25.5×25.5×1.0) mm³ was analyzed through one of its longest sides, the error on geometrical dimensions is ± 25 μm. Photons with energy E = 150 keV were diffracted by (111) CDPs. In these conditions, the critical radius was R_C = 275 m, while the curvature radius of the diffraction planes was R = (341 ± 25) m. Analysis was repeated with a Ge crystal of dimension (9.8×9.8×1.0) mm³ analyzed through one of its longest side with same photon energy and diffraction planes. In these conditions the critical radius was R_C = 48.5 m while the curvature radius of the diffraction planes was R = (92 ± 7) m. The errors on theoretical diffraction efficiency η_{th} are calculated by propagating the error bounds of experimentally measured curvature radius and thickness, as half the difference between the extreme values of efficiency.

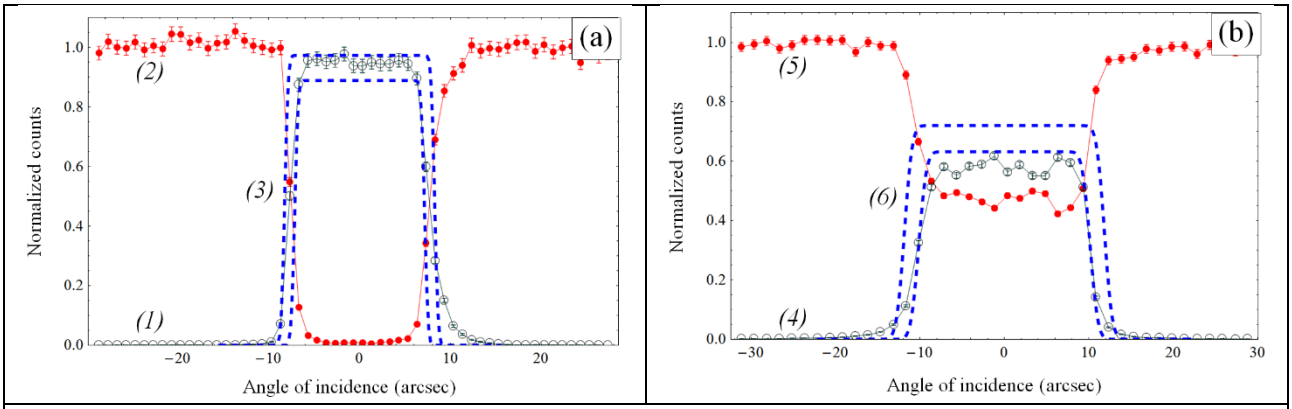

Figure 2-5

(a) Rocking curve of a (111) Si curved crystal with size (25.5×25.5×1.0) mm³ analyzed through one of its longest side by 150 keV photons. At this energy, the crystal thickness traversed by x-rays is t_0 = 25.5 mm, corresponding to N = 139 lamellae. (1) Empty circles: intensity of diffracted beam divided by the intensity of the transmitted beam, i.e. diffraction efficiency. (2) Full circles: intensity of transmitted beam over the intensity of transmitted beam when no diffraction occurs, i.e. transmission efficiency. Experimental diffraction efficiency is (94.0 ± 3.0) %, while the FWHM of the distribution is (15.4 ± 1.1) arcsec. (3) Dashed lines: prediction of the model for the theoretical diffraction efficiency (93.1 ± 4.2) %. The simulation accounts for the uncertainties of experimental parameters.

(b) Rocking curve of a (111) Ge curved crystal with size (9.8×9.8×1.0) mm³ analyzed through one of its longest side by 150 keV. At this energy, the traversed crystal thickness t_0 = 9.8 mm, corresponding to N = 125 lamellae. (4), (5), (6) Same meanings as for curves (1), (2), (3) respectively. Experimental diffraction efficiency is (58.1 ± 1.9) % while the FWHM of the distribution is (22.0 ± 1.7) arcsec. Theoretical diffraction efficiency is (67.6 ± 4.4) %, a value slightly larger than experimental diffraction efficiency due to partial mosaicity in the crystalline structure.

Then, a dedicated experiment was set at ESRF (beamline ID15) for testing the model. The model was tested by recording the peak diffraction efficiency of (111) oriented CDPs while changing their curvature radius, in order to reproduce the graphic in Figure 2-4. The tested sample was a flat perfect Si crystal with size 5 × 5 × 45 mm³. The two faces with size 5 × 45 mm² were oriented as (111) and (110) respectively, while the 5 × 5 mm² face was oriented as (211). A curvature was induced in the (111) planes by a proper designed holder. The holder is set at the resting position (ideally unbent

holder) then the ends of the crystal were fixed at the clamping points of the holder. The clamping mechanism produced a small curvature is the crystal, which is not controllable nor eliminable. Then, the holder was bent by turning a screw, thus bending the (111) surface with a cylindrical primary bending along the direction 45 mm long. An anticlastic curvature occurred on the orthogonal direction 5 mm long. The anticlastic curvature was used for testing the model. Indeed, the anticlastic CDPs were far from the clamping points, so far from a source of inhomogeneity in the curvature. The X-ray beam entered the crystal at the center of the (110) oriented face. The beam passed through 5 mm of material and it diffracted through the (111) anticlastic CDPs. The curvature was increased by bending the holder, and RCs were recorded. The analysis stopped when the holder could not be bent any more. Because of the complex geometry of the holder and the strong stiffness of the crystal, it is not possible to know a priori the curvature radius of the CDPs. Anyway, the curvature of CDPs can be measured from the enlargement of the RC profiles. The model has to be tested in the region $R \gtrsim R_C$, where the width of the measured RCs is comparable with the Darwin width of the diffracting planes. For this reason, the beam was monochromatized by reflection from (511) oriented Si planes, which have Darwin width far smaller than the Darwin width of the (111) Si planes of the sample. Then, a very precise rotary stage with resolution 0.12 arcsec was employed to perform the RCs. The radii of curvature attainable by bending the holder were limited, thus it was impossible to explore the entire range for $R/R_C > 1$ with a single X-ray energy. Anyway, it was possible to explore the entire range for $R/R_C > 1$ by changing the beam energy, so changing the critical radius of CDPs. In particular, the experiment was repeated for two photon energies 50 keV and 100 keV. The critical radius of curvature for these two energies for diffraction by Si (111) planes is respectively 30.6 m and 122.1 m. Because of the heavy overload on the requested instrument, it was possible to schedule just 3 shifts (1.5 days) for this experiment, comprehensive of the assembly of the experimental setup. Thus, a limited number of data were recorded.

The recorded RCs usually presented a discrepancy between diffracted and transmitted RC profile for the same holder position (Example Figure 2-6). This problem may be due to the small curvature of CDPs involved in this experiment. Indeed, if the curvature is very small, any error have an important contribution to the RC. For example, crystalline imperfections that enlarge the RC of a fraction of the Darwin width are not usually detected in experiments. On the contrary, for the output of this experiment they have a relevant contribute, which is not easily detectable. As the same, small torsions due to the holder manufacture tolerances may lead to enlargement of the RCs or fluctuations in the diffraction and transmission efficiencies. A combination of these effects is also possible. Then, the maximum and minimum value of a measure was considered as the tolerance range for this measure. For a certain the experimental point, the widths of the diffracted and transmitted RCs was taken as the tolerance for the RC width.

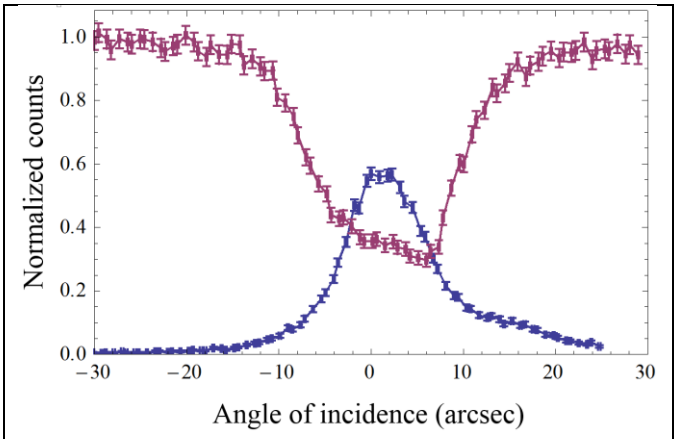

Figure 2-6

Diffracted (blue) and transmitted (red) RC for diffraction of photons with energy 50 keV by Si (111) CDPs planes at a certain holder position. Experimental errors have a main impact on the measures, and the two RCs are not perfectly specular. The maximum and minimum value of the measured physical properties (FWHM and peak intensity) are considered as the tolerance of the physical property. The RCs in this figure correspond to the third data point from the right in Figure 2-7.

As the same, the diffraction efficiency of the diffracted RC and the transmission efficiency of the transmitted RC was taken as the tolerance for the diffraction efficiency of the experimental point. The resulting experimental points are shown in Figure 2-7. Even though the large error bars, the experimental points fit quite well the model. Surely, a more detailed series of data is necessary for validating the model. The data shown here will be the core for the proposal of an experiment at ESRF beamline ID15 for the next year (2015).

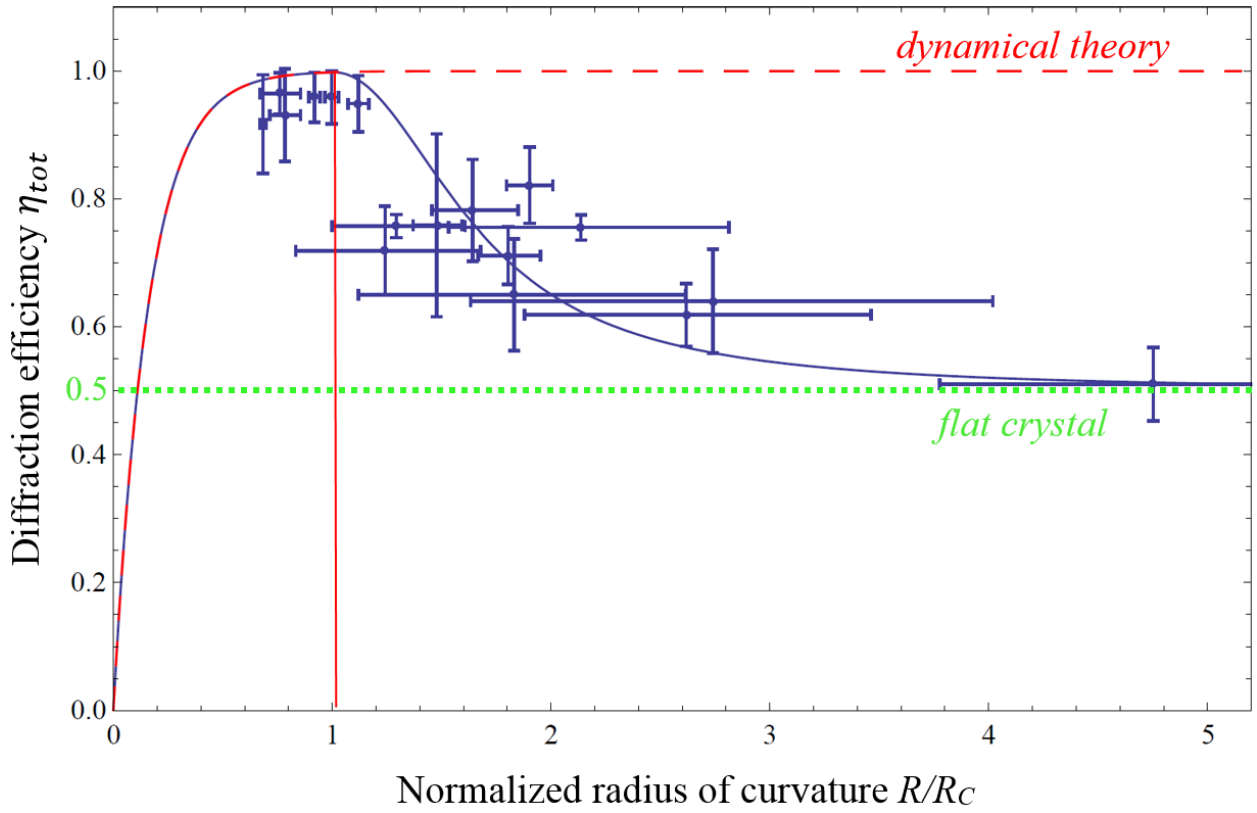

Figure 2-7

Diffraction efficiency for Si (111) CDPs as a function of the normalized radius of curvature for the theoretical expectation from the model (blue curve) as compared with the experimental data (blue crosses). It is possible to distinguish two groups of data points, corresponding to photon energy 50 and 100 keV. Data recorded with photon energy 100 keV are concentrated at the top of the theoretical curve. Data recorded with photon energy 50 keV are spread along the tail of the theoretical curve. The latter group of data presents the widest error bars. Indeed, the effect of crystalline imperfections dominate at low energy.

In conclusion, a model of Laue diffraction in curved crystal has been developed, whose results agree very well with those of dynamical theory for $R << R_C$. The model also produces the same results for a flat crystal when the curvature radius is infinitely large ($R \rightarrow +\infty$) and provides a quantitative description of diffraction efficiency when neither these cases are applicable. The model casts an upper limit of efficiency for CDP crystals, even in the region $R > R_C$. This knowledge is an important information when designing new schemes for a Laue lens in next generation satellite-borne experiments in astrophysics.

3 The Laue Project

The Laue Project is a R&D project funded by ASI (Italian Space Agency), with the purpose to build and test a petal of a focusing lens for hard X-/soft γ-rays. The energy of photons to focus is in the range 90 – 300 keV. The project is intended to increase the technology readiness level (TRL) of Laue lenses. The success of the project may lead the community of astrophysicists to invest in Laue lenses for the building of a ready-for-launch hard X-ray lens.

A Laue lens can be composed of more than 10,000 crystal tiles. The construction of the lens was divided in parts, following a modular approach. Hundreds of the basic elements (crystals) are assembled into petals. Inside a petal, each crystal tile is independently aligned. Then, the petals are accommodated in an optical bench, and they are aligned to the lens focus.

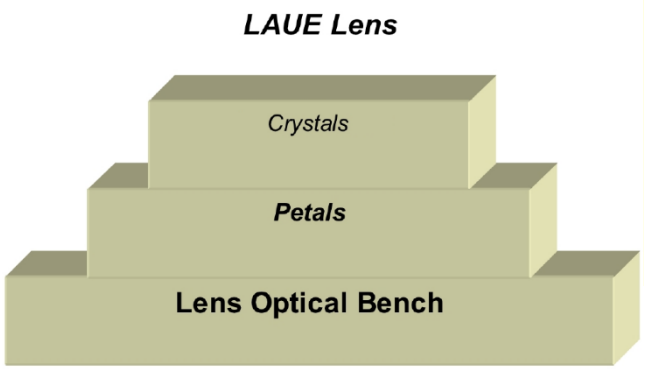

Thales Alenia Space performed feasibility studies on the optical bench for modularity, structural and thermal stability. The purpose of the Laue project is not the construction of a full lens, but the construction and test of a petal. Nevertheless, some tests on the optical bench of the petals are required. The energy passband of the petal has been optimized on two factors: the flux of cosmological X-ray sources and the maximum dimension for a lens to be used in a space mission. Indeed, the flux of X-ray sources typically decreases with the energy of the emitted photons. A method to overcome the problem of the low flux at high energies is to increase the collecting area of the lens. However, the lens cannot be indefinitely large, because it has to fit in the hold of a rocket. Therefore, the best compromise was a maximum dimension of the petal of 60 cm, and a limited energy passband ($\lesssim$ 300 keV). The employed crystal tiles were Ge (111) QM crystals and GaAs (220) mosaic crystals. Ge tiles were built at the Sensors and Semiconductors Laboratories (SSL) at the University of Ferrara, and they are part of this thesis work. GaAs tiles were built at the Institute of Materials for Electronics and Magnetism – National Research Council (IMEM-CNR) in Parma.

Figure 3-1

(a) Description of the lens specifics. (b) Sketch of a full Laue lens. A lens petal is highlighted in blue. (c) Disposition of the Ge and GaAs crystalline tiles on the petal. The petal contains 155 Ge tiles and 119 GaAs tiles. The Ge sectors spans the energy range 90 – 267 keV, while the GaAs tiles span the 148-304 keV range.

(a) Petal specifics

Passband	*90–304 keV*
Focal Length	*20 m*
N° rings	*18*
N° crystals	*274*
Crystal size	*3 × 1 × 0.2 cm²*
Crystals material	*Ge - GaAs*

(b) Full Laue lens	*(c) Petal materials*
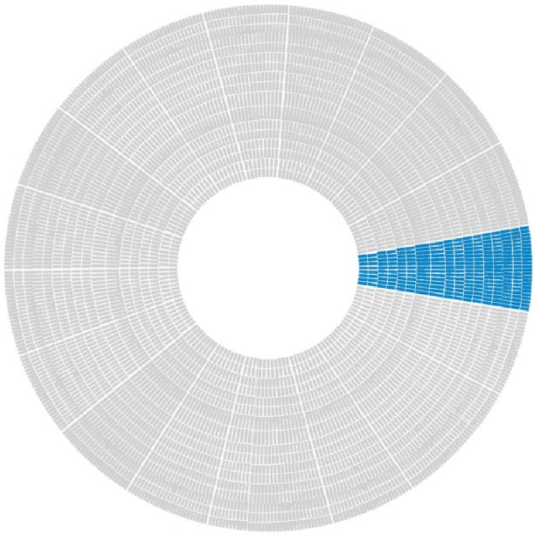	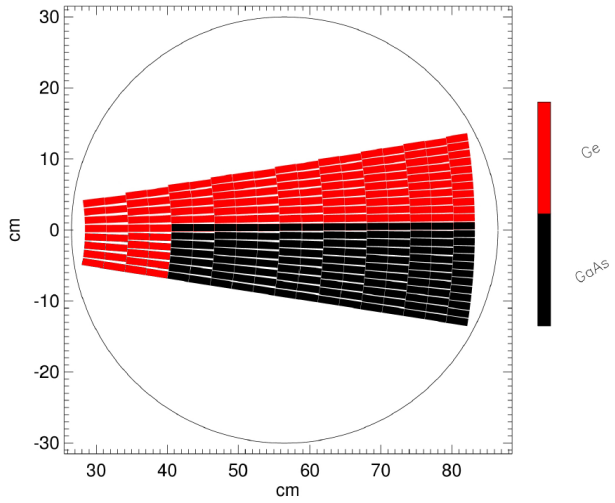

The petal frame is a carbon fiber plate realized from the superposition of 10 layers of carbon fiber. The total thickness of the plate is 2.3 mm. The frame is drilled in correspondence of the central positions of the crystals. Crystal tiles are directly placed on the carbon fiber support using a robot, furnished by DTM Technologies (Figure 3-3). Under an X-ray beam, a tile is aligned to the lens focus. The tolerance for the alignment is 10 arcsec. Then, through the corresponding hole, a resin is injected for fixing the tile to the frame. The lens petal frame holds the crystal tiles in position.

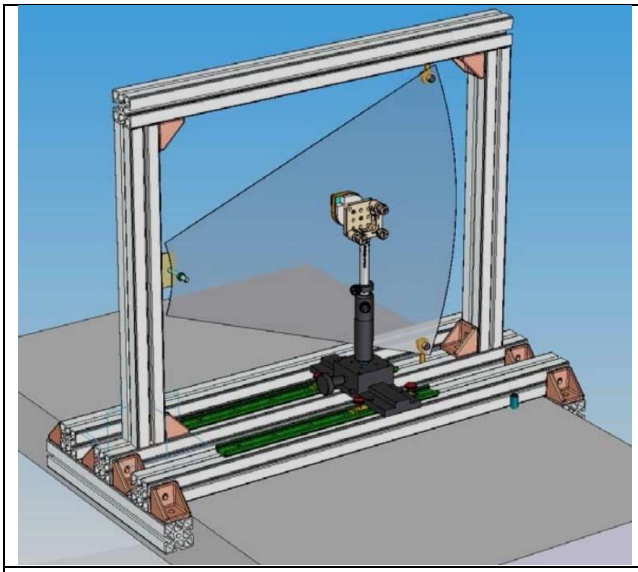

Figure 3-2

Sketch of the petal frame (opaque) and of the system used to place crystals on the frame. The frame is hold in position by a 3-point support. A robot places each crystal in position and aligns it.

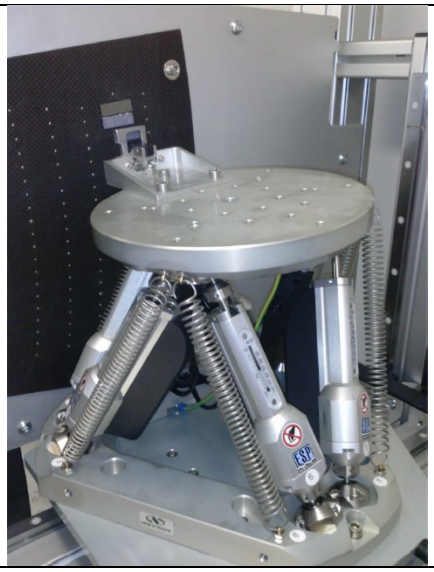

Figure 3-3

Picture of the carbon fiber frame, of the crystals and of the hexapod system used to align and place each crystal in the proper position.

3.1 Background – Applications of X-ray lenses

A gamma-ray focusing instrument would have a huge advantages in terms of increasing the signal-to-noise ratio. Focusing would lead to a sensitivity leap respect to today direct-view instruments. Today X-rays detection is based on direct-view instrument (e.g. gamma cameras), which means the X-ray beam impinges on the detector without any conditioning. For a detector of a given thickness, the background counts N are proportional to its geometric area $N \propto A_g$. Instead, the intensity of the signal S is proportional to the collecting area $S \propto A_r$. The information about the source is obtained by subtracting the number of counts due to noise from the total counts. Then, the standard deviation of the counts of the source is $\sigma_S = \sqrt{\sigma_{tot}^2 + \sigma_N^2}$, where σ_{tot} and σ_N are respectively the standard deviations of the total number of counts, and the standard deviation of the counts due to the noise. If the number of counts follows the Poisson statistic, the standard deviations are written as $\sigma_S = \sqrt{S}$, $\sigma_N = \sqrt{N}$, $\sigma_{tot} = \sqrt{S+N}$. The number of counts due to the background N and the total number of counts (S + N) are directly measured. Then, the standard deviation of the counts of the source is written as $\sigma_S = \sqrt{(S+N)+N} \sim \sqrt{2N}$ considering that in the detection of hard X-rays from celestial sources usually S << N. The instrument sensitivity is defined as the ratio between the signal from the source and its uncertainty. For a given instrument the sensitivity is:

$$\frac{S}{\sigma_S} \propto \frac{S}{\sqrt{N}} \propto \frac{A_r}{\sqrt{A_g}}$$

For direct-view instruments, the collecting area coincides with the area of the detector ($A_g = A_r$), and the ratio between the signal and its error goes as $\sqrt{A_r}$. Then, to increase by an order of magnitude the sensitivity of a direct-view instrument, a detector 100 times larger is needed. As we will see, this is a strong limitation, especially for application in celestial observation. Indeed, detectors for X-ray astronomy must operate outside the atmosphere. Therefore, excessive dimensions and weight would make the mission economically and technologically unfeasible.

In the case of focusing optics, the area of the detector and the collecting area are independent of each other, then the sensitivity of the instrument will be linearly proportional to the area of collection A_r, and inversely proportional to the area of the detector A_g. Then, a lens with large collecting area would concentrate the incident photons on a small detector, increasing orders of magnitude the sensitivity of the instrument, and considerably reducing the weight. For simplicity, if we consider the collecting area and the detector both circular with a radius r_r, r_g, the sensitivity of the instrument would be:

$$\frac{S}{\sigma_S} \propto \frac{r_r^2}{r_g}$$

So it is easy to understand how a focusing system for hard X-rays can increase the sensitivity of instruments working in this band of energy.

An other important quantity for X-ray detection instruments is the angular resolution. Angular resolution is defined as the minimum angle between two objects that an optical system can distinguish. In optics, the two points are resolved if the central maximum of the diffraction pattern of one falls on the first minimum of the diffraction pattern of the other or more distant. The resolution of an instrument is limited by the size of the collecting area. In fact, for an instrument with a circular collecting area, the separation angle for which two points are resolved is at minimum $\varphi_0 \sim 1.22\lambda/D$, where λ is the wavelength of the radiation collected, and D is the diameter of the area of collection. The angular resolving power is the inverse of this angle $1/\varphi_0 \sim D/(1.22\lambda)$. The larger the collecting area of the instrument, the better the resolution becomes. The linear resolution of an instrument is defined as the minimum distance between two objects that the optical system is able to distinguish. Known the angular resolution of an instrument, it is easy to derive the linear resolution. Let f be the distance between the collecting surface and the detector, the minimum distance between two separable points is $\varepsilon = f \cdot tan\varphi_0 \sim f \cdot \tan(\frac{1.22\lambda}{D}) \sim \frac{1.22\lambda f}{D}$ in the limit of small φ_0 angles. Due to the aberrations of an optical system, often the image of a point source on the detector is not the typical diffraction pattern described by the Airy disk, but it takes different shapes. For this reason, two point sources are said experimentally separable if the distance between the centers of their images on the detector is at least equal to the FWHMs of the images (considering the two identical images). If the distance between the two images is less than the FWHM, the spatial distributions of the counts of the two point sources sum together producing a single continuous peak (Fig 1.1_18). For an optical system to produce a good image, it is important that the images produced by point sources on the detector are as narrow as possible.

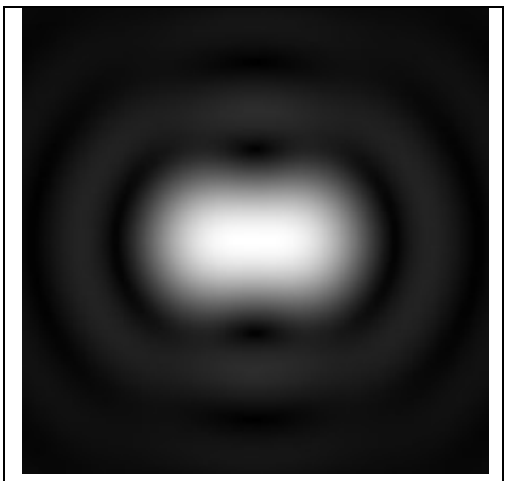

Figure 3-4

Image of two point sources whose distance is equal to the FWHM of the intensity distributions. This image is located at the limit of the resolution of the instrument.

The detection of hard X-rays plays an increasingly important role in modern astronomy. The instruments currently operating in this part of the electromagnetic spectrum, however, do not use focusing optics, i.e., the measured signal is collected directly on the sensitive part of the detector itself. Multilayer optics achieve high-efficiency focusing up to 80 keV X-rays, though beyond this limit the efficiency of such optics critically falls off (Madsen, 2009). The construction of high-reflectivity multilayer mirrors working at energies up to several hundreds of keV was attained very recently (Della Monica Ferreira, 2013). Nevertheless, these new multimirrors work at very low grazing incidence angles, below 0.1°, thus featuring a very low acceptance area for the incident photons. Moreover, the assembly of a focusing instrument relying on this technology appears to be rather complex. Up to now, the energy range above 80 keV is left to instruments detecting photons with no focusing, resulting in low signal-to-noise ratio (Harrison F. A., 2013). Today, the spectra above 80 keV are well determined only for the most intense sources. For many other objects, above 80 keV the spectra are little known (Figure 3-5).

The scientific community is searching for a focusing device to overcome the present limitations (Lindquist, 1967). In astrophysics, a Laue lens would allow high sensitivity and high-angular resolution observation of cosmic phenomena producing X-ray emissions (Frontera F. &., 2010). Observing the sky in the sub-MeV range is very rich in physics, with a lot of different processes

involving conditions that are not reproducible in the laboratory. For instance, extreme magnetic fields near magnetized neutron stars or extreme gravitational fields near black holes. Detailed mapping of X-ray sources along with characterization of their high-energy emission spectrum is mandatory to determine their intimate nature. Fine angular scale and high-sensitivity observations have long been awaited to cast new light on the origin of the positrons that we observe in the galactic center through the 511 keV line due to electron-positron annihilation. This line has been observed for more than 30 years from the galactic center, yet it is still unclear whether known sources can account for it (Knödlseder J., 2005). New observations are needed but both improved sensitivity and improved angular resolution are required. A Laue lens could probe small sky regions to check for patterns in the emission distribution, and probe some candidate sources. Laue lenses would also improve the study of supernova dynamics. Supernovae IA are used as a cosmological standard candle to determine extra-galactic distances. Their study has led to the astonishing result that the expansion of the Universe is accelerating, suggesting the existence of a dark energy (Riess, 1998) (Perlmutter, 1999). However, we don't understand why the luminosity of supernovae IA can be normalized (Phillips, 1993). This is related to our lack of understanding of the physics of the explosion. The spectroscopy and light curve of the line at 847 keV emitted by the decay chain of 56Ni, which is massively synthesized in supernovae IA, would discriminate between the currently competing models.

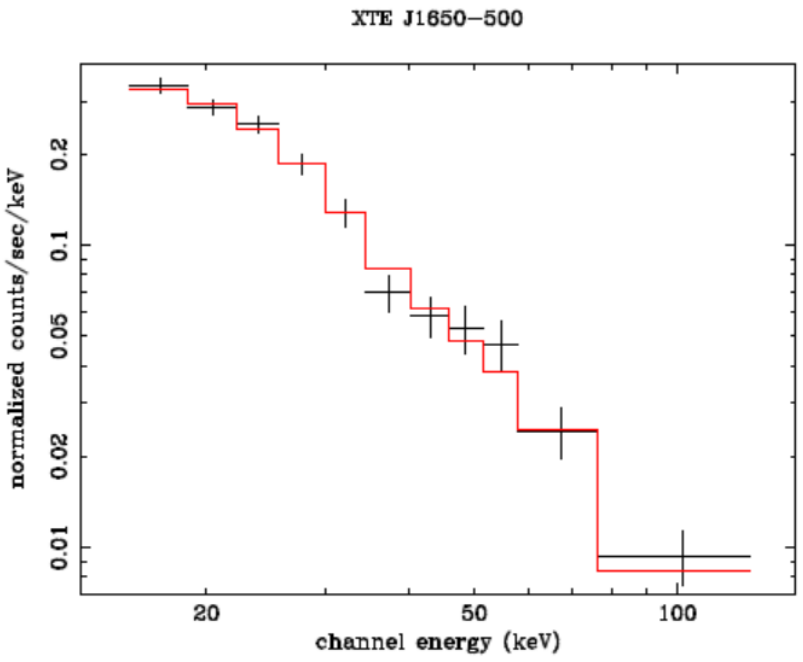

Figure 3-5

Spectrum of the transient source XTE J1650-500 (discovered by Rossi XTE September 5, 2001), black hole candidate observed by the PDS on BeppoSAX in October 2001 during its 2001/2002 outburst. Despite the high exposure time, of the order of 10^5s, the photon counts at energies above 70 keV are barely detectable.

The possibility of focusing X-ray by diffraction through crystalline materials has been demonstrated for the first time in June 2004, when the Crab nebula was observed in the hard X-ray band during the balloon experiment CLAIRE. The instrumentation consists of a gondola on which is mounted a Laue lens composed of 556 mosaic crystals. Crystals are made of germanium-silicon alloy, and they have a mosaicity between 1 and 2 arcmin. Crystals are mounted on eight concentric rings in a titanium frame with diameter 45 cm (Figure 3-6). The total exposed area is 511 cm^2, the focal length of the lens is 277 cm. The energy passband of the lens peaks at 170 keV, with a bandwidth of 3 keV (von Ballmoos et al., 2004). On the 14th June of 2004, CLAIRE was launched from the Gap-Tallard base in the French Alps, and it has been recovered after a flight of about six hours, near Bergerac in south-western France. During the flight, CLAIRE has collected 33 photons with energy of about 170 keV from the Crab nebula. The performance of the instrument was severely limited by the low reflectivity of the crystals used. However, the mission shown that the method is feasible. The use of crystals with extremely higher performance, such as the CDP crystals proposed in this thesis, will lead to a significant increase of the performance of the focusing instruments in the hard X-rays.

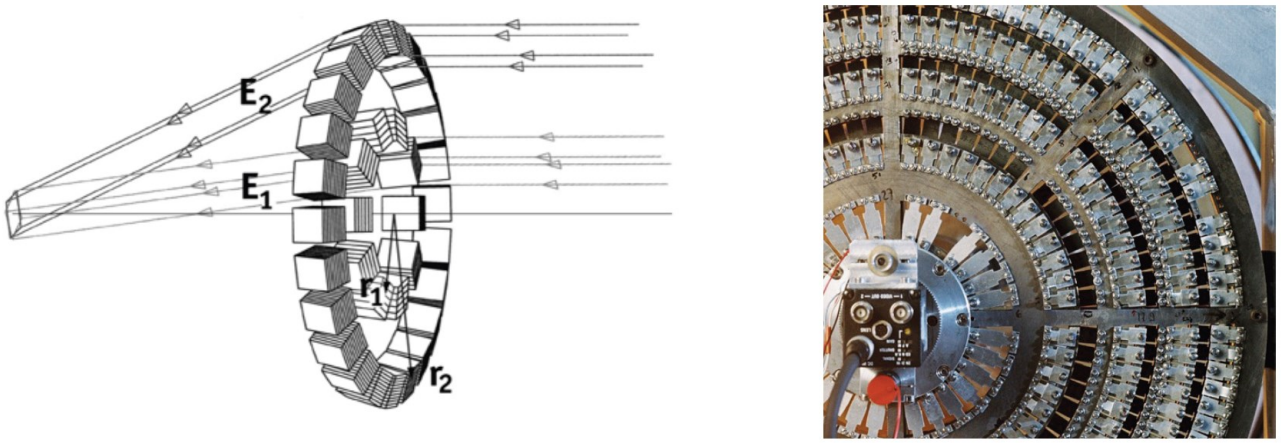

Figure 3-6

The basic scheme of the Laue lens (a) use during the CLAIRE experiment and photos of the lens mounted on the frame of the gondola (b). The images are taken from (von Ballmoos et al., 2004).

Another discipline that can benefit from the use of Laue lenses is nuclear medicine. Patient diagnostic and treatment would be enhanced by the advent of gamma-ray optics. The nuclear imaging systems involve the selective absorption of radio drugs, organic compounds containing a radioactive isotope, to detect tumors and other physiological processes. The radio drugs usually emit photons of energies in the range 100 keV - 200 keV, for example, the Tc-99m emits photons with energy of 140.6 keV. The current methods for detecting this emission are based on direct view instruments (such as groups of gamma camera or SPECT tomography), and use complex deconvolution algorithms to produce the final image. Currently, the majority of imaging tools has a spatial resolution between 7 mm and 15 mm. PET, the latest diagnosis system based on nuclear medicine, may reach a maximum resolution of 4-5 mm. The radionuclides used in PET have a short half-life. Then, the PET machines need to be located near a radionuclide production facility to minimize the decay. Because of the fast decay of the radio-nuclei used, it is also necessary to give the patient an important dose of radio-drug to be able to conduct the analysis. A focusing optics based on curved crystals would increase the number of counts collected on the detector. Then, the sensitivity of the instrument would increase, allowing a reduction in the dose of radio-drug injected into the patient. The spatial resolution of the instrument would also improve up to the sub-millimeter resolution. Such resolution would allow to locate early tumors, or it would allow to image tumors and other phenomena of interest with great precision, providing more information on the same. Another potential field of application concerns treatment, where a high dose needs to be delivered in a small volume of tissues. Conventional methods for radiotherapies involve the use of short-lived highly active isotopes, which are expensive on the long run and dangerous for the medical workers who manipulate them. A Laue lens coupled to an X-ray generator could be an interesting alternative producing a focused beam over a continuum of energies.

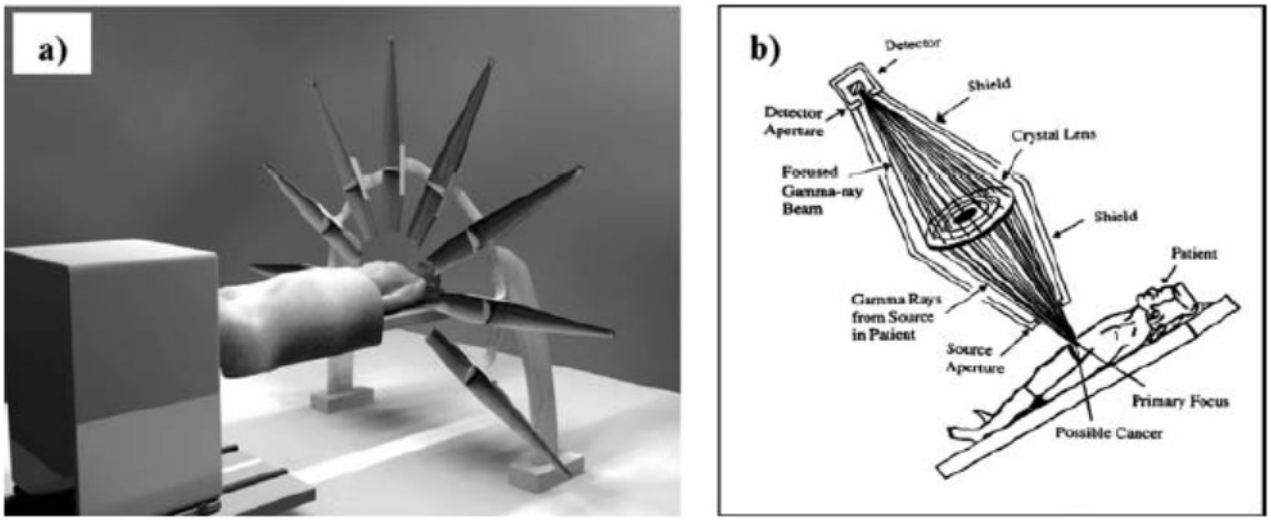

Figure 3-7

(a) Representation of a medical imaging system consisting of a series of Laue lenses (b) Schematic diagram of the operation of a single Laue lens. The images are taken from (Roa, 2005).

3.2 Theoretical performances of CDPs crystals

3.2.1 Primary CDPs

The most immediate method to obtain CDP crystals for the construction of a Laue lens is to impart a curvature to the entire sample. The CDP thus obtained are employed to diffract the X-ray incident beam. This configuration is called the primary mode as the lattice planes undergoing the primary curvature are used as diffractive elements. In the following theoretical estimations it is considered that the other crystallographic planes do not have any curvature. Although their eventual curvature would make very few changes to the response of the CDP in this configuration. In this section we analyzed the response of the crystal in this mode. The performance of CDP crystals are evaluated regardless of the way the curvature was attained. Silicon and germanium mono-crystals are the best single crystals produced with the present technology. Their growth techniques have been refined because of the applications these materials find in electronics. Si and Ge crystals have the same lattice structure (diamond lattice), and they are taken as examples of materials employable in the development of CDP crystals for optical applications. In Si and Ge the (111) lattice planes have the highest electron density. For this reason (111) planes are used to achieve the maximum diffraction efficiency. These crystal planes are the standard diffraction planes in the calculations.

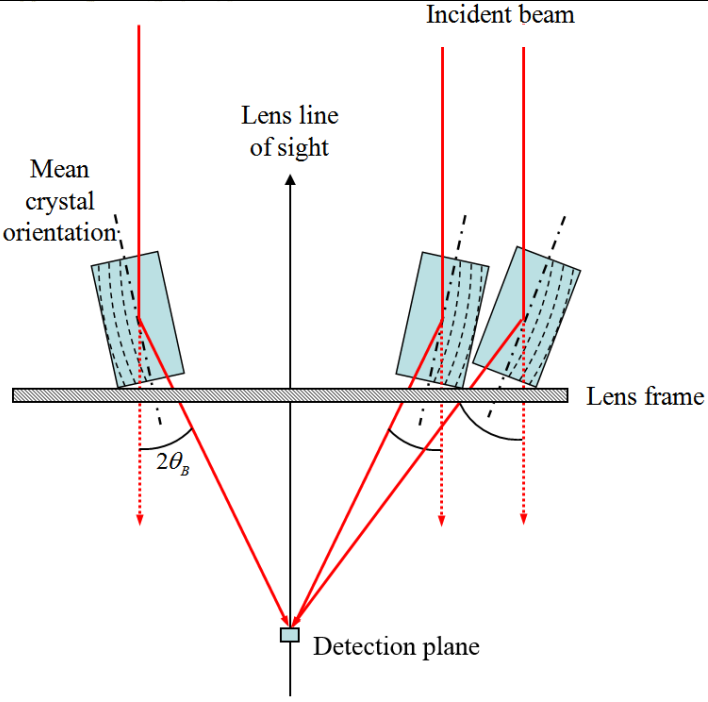

Figure 3-8

Sketch of the functioning of primary CDPs crystals in a Laue lens.

3.2.1.1 Local efficiency

The crystals that exploit the primary mode exhibit to incident radiation an isotropic entrance surface. The photons that enter at any point on the entrance surface are diffracted if they are located within the same energy passband. The energy passband is defined by the curvature of the crystal. For this reason, it is possible to analyze the diffraction phenomena that occur along a single line and consider them representative for the phenomena that occur in the entire crystal. For X-ray optics, the reflectivity η is the parameter to maximize. Reflectivity expresses the ratio between the diffracted beam emerging from the crystal and the incident beam. When the curvature is uniform and sufficiently large (Uniformly curved diffraction planes), the reflectivity of the CDP can be written as

$$\eta = \frac{I_D}{I_0} = \left(1 - e^{-\frac{t\pi^2 d}{\Lambda^2 \alpha}}\right) e^{-\frac{\mu t}{cos\theta}}$$

Where I_0 is the intensity of the incident beam, I_D is the intensity of the diffracted beam, t is the thickness of the crystal, d is the interplanar distance of diffraction planes, α is the angle CDPs span, Λ is the extinction length, μ is the absorption coefficient of the material composing the crystal, θ is the Bragg angle. The first part of the equation $\left(1 - Exp(-t\pi^2 d/\Lambda^2\alpha)\right)$ rules the diffraction phenomena, and it is named diffraction efficiency. The second part $Exp(-\mu t/cos\theta)$ depicts the absorption phenomena.

CDP crystals diffract X-rays in a wide range of energy thanks to the continuous change of the angle of incidence on the crystal planes along the thickness of the crystal itself. From the Bragg law, it is possible to derive an expression of the energy bandwidth ΔE as a function of the angular spreading $\Delta\theta$ of CDP, and the energy of impinging photons E:

$$\Delta E \sim \frac{hc}{2d}\frac{1}{\theta^2}\Delta\theta = \frac{2d}{hc}E^2\Delta\theta$$

With the aim to maximize the diffraction performance of the crystal, reflectivity has to be maximized. As a rule of thumb, diffraction efficiency increases with the traversed thickness, while the absorption causes a decrease of the intensity of the exit beam which increases with the thickness. Thus, reflectivity has to be maximized looking at these two contributions.

As an example, consider a Si (111) CDP with angular opening of 30 arcsec diffracting photons with energy of 150 keV. For fixed energy, we can study the reflectivity as a function of the thickness. The curve obtained shows a maximum (). In this case the optimum thickness is 11 mm, and the best reflectivity is η = 0.578. It is also possible to study the inverse problem: given a crystal of a certain thickness and angular aperture, how the reflectivity varies as a function of the energy of diffracted photons. As before, the angular opening of CDP is 30 arcsec and the thickness is 11 mm. Its reflectivity as a function of the energy is visible in ().The maximum reflectivity is attained for 111 keV.

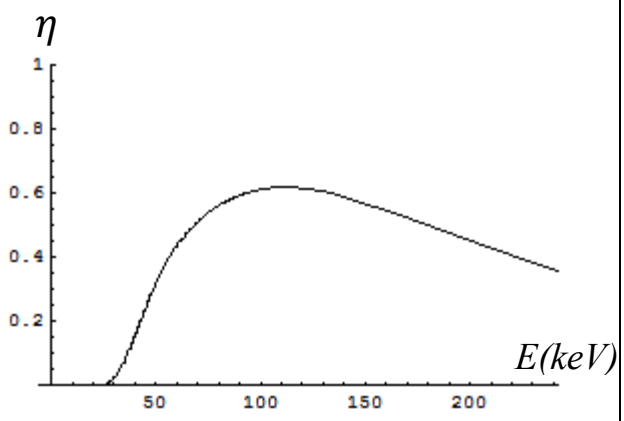

Figure 3-9

Trend of the reflectivity as a function of the energy of a photon beam incident on a Si (111) crystal in primary mode, thickness t = 11 mm, opening angle α = 30 arcsec.

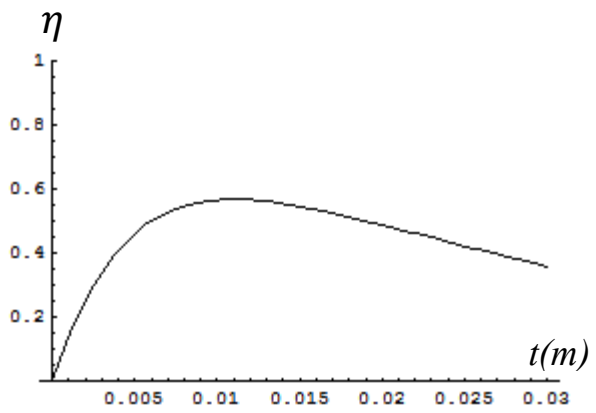

Figure 3-10

Trend of the reflectivity as a function of the crystal thickness, for a Si (111) crystal in primary mode, opening angle α = 30 arcsec, energy of the incident beam E = 150 keV.

The experimental analysis conducted on crystalline samples is usually of two types. You can analyze the crystal with a monochromatic beam at constant energy. In this case, the reflectivity is recorded while changing the angle of incidence of the beam on the crystal. The profile of reflectivity as a function of the angle of incidence is called rocking curve (RC). You can analyze a crystal while maintaining fixed the angle of incidence on it but varying the energy of the beam itself. The profile of reflectivity as a function the energy thus obtained is named energy response (ER). The last measurement can be run also by impacting a polychromatic beam with wide, uniform spectrum on the crystal, while the angle of incidence remains fixed. The profiles obtained from RC and ER can be calculated theoretically. The theoretical RC of the sample of example is visible in Figure 3-11, while its theoretical ER is visible in Figure 3-12. You may notice a bandwidth of 1.65 keV, while the bandwidth for a perfect crystal would be 17.55 eV (Darwin width δ_w = 0.32 arcsec).

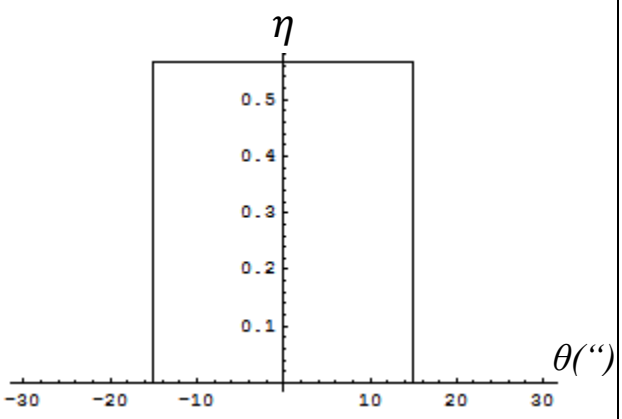

Figure 3-11

Theoretical RC of a Si (111) crystal in primary mode, thickness t = 11 mm, opening angle α = 30 arcsec, the incident beam energy is E = 150 keV. The RC is centered at the Bragg angle for the energy of the incident beam. The angle rocking θ is expressed in arcsec θ (").

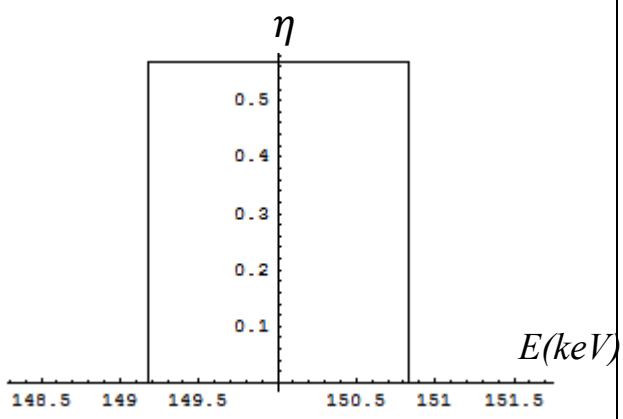

Figure 3-12

Theoretical ER of a Si (111) crystal in primary mode, thickness t = 11 mm, opening angle α = 30 arcsec, angle of incidence fixed at Bragg angle for the energy of the incident beam E = 150 keV. The distribution covers a width of E = 1.65 keV.

Figure 3-13 shows the reflectivity as a function of the crystal thickness and energy of incident photons together. Think of choosing a certain energy, and for every energy optimizing the thickness of the crystal in order to achieve maximum reflectivity. This condition is represented by the red curve in Figure 3-13. Then, once defined the material to be used and the angular aperture of the crystal, it is possible to optimize the thickness and the photon energy to achieve maximum reflectivity.

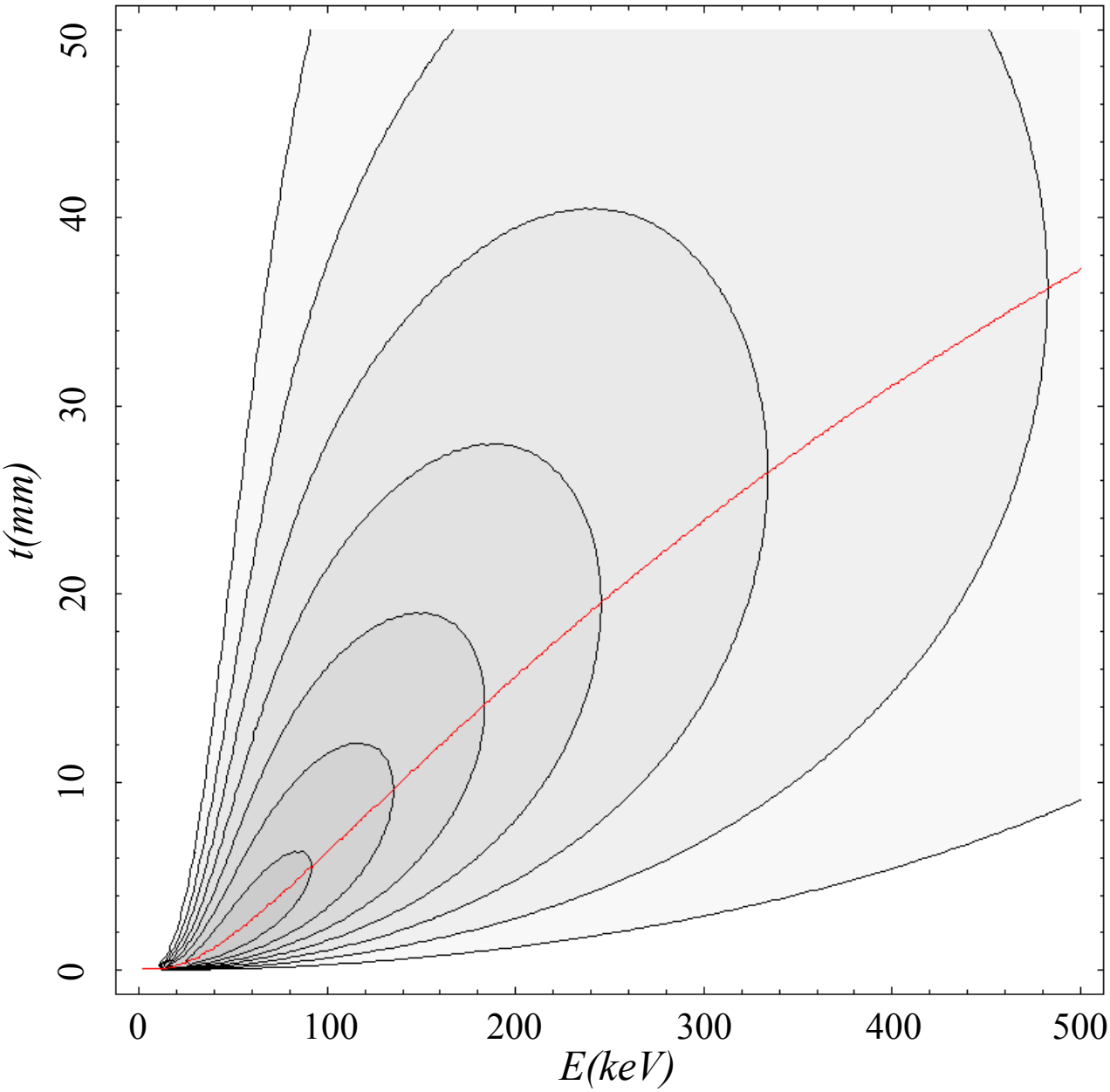

Figure 3-13

Reflectivity of a crystal Si (111) with opening angle α = 30 arcsec, as a function of thickness of the crystal t and energy of impinging photons E. Black contour lines have the same reflectivity in steps of 0.1. The red curve represents the line of maximum reflectivity as a function of the beam energy.

If we study the reflectivity as a function of the angular aperture of the crystal, a reduction in reflectivity with increasing angular opening is obtained. The reason why we choose to use curved crystals to build a lens Laue, instead of mosaic crystals, is the increased reflectivity that the first feature as compared to the latter. It is questionable whether this characteristic is maintained regardless of the magnitude of the aperture angle of the CDPs. In Figure 3-14 the maximum reflectivity of Si (111) CDPs is plotted as a function of the angular aperture of the crystal. The graph was obtained by maximizing the reflectivity function in a wide range of energy (100keV-1000keV) and thickness (0.1mm-50mm), while keeping the opening angle as a variable. The graph shows that CDP crystals

maintain a high reflectivity over the entire range of angular apertures useful for the production of a Laue lens (1arcsec-90arcsec), and this reflectivity is above 50% up to 60 arc-seconds.

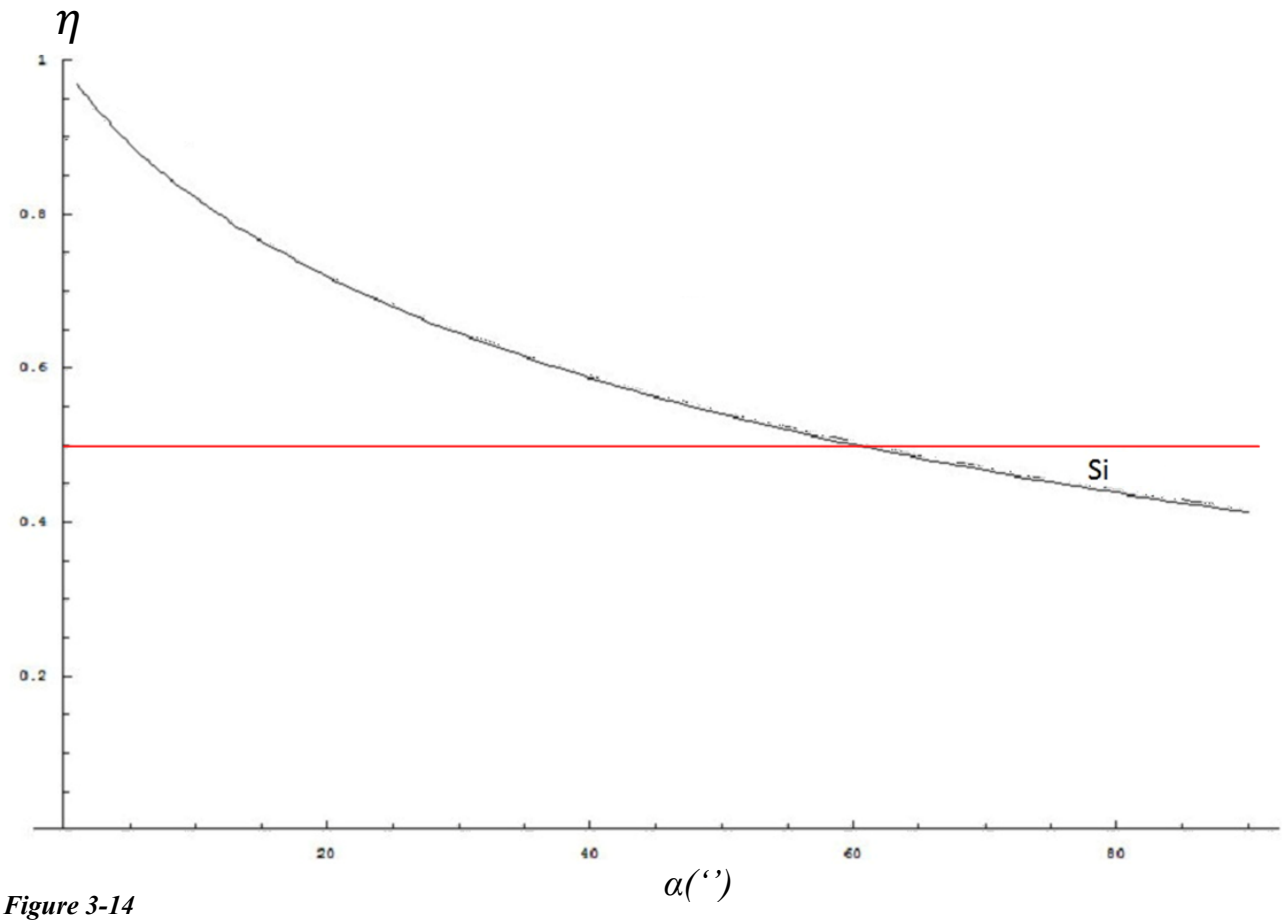

Figure 3-14

Curve of the maximum reflectivity for (111) Si CDPs as a function of the curvature angle in arcsec. The reflectivity was maximized for energy of incident X-rays in the interval E = (100keV, 1000keV) and thickness of the crystal in the interval t = (0.1mm, 50mm).

If we had used a germanium crystal with the same aperture angle, we would have had the same results but shifted to higher energies. Germanium has an atomic number greater than silicon, then an enhanced diffraction capability and a greater absorption. Then, it adapts better to diffract radiation of higher energies. If two crystals of silicon and germanium have the same angular aperture, they will reach the same maximum reflectivity, although for different energies (or different thickness). As an example, for Ge (111) CDPs with aperture angle $\alpha = 30$ arcsec under an X-ray beam with energy $E = 150$ keV, the optimal thickness would have been 2.3 mm, actually too small to be bent in primary mode.

3.2.1.2 Integrated reflectivity & integrated spreading

In this section we define and study the properties of two key parameters of crystals for Laue lenses: the integrated reflectivity and the integrated spreading. A key feature of crystals for Laue lenses is the quantity of photons they can diffract. This quantity is proportional to the reflectivity and to the energy passband. We define the integrated reflectivity η_I as

$$\eta_I(E_B) = \int_0^{\infty} \eta(E_B, E')\, dE' \qquad (3.3\_2)$$

Where E_B is the photon energy at the Bragg angle. For a primary CDP crystal, this quantity is nearly equal to the reflectivity times the energy bandwidth. Despite the quantitative importance of the integrated reflectivity, this quantity is not always easy to calculate because it depends from the working energy. Integrated reflectivity is not a representative quantity in the building process of CDPs crystals for the same reason. Therefore, we define the integrated spreading η_θ as

$$\eta_\theta(E_B) = \int_0^{\pi} \eta(E_B, \theta)\, d\theta \qquad (3.3\_6)$$

For a primary CDP crystal, this quantity is equal to the reflectivity times the angular spreading. η_I and η_θ can be related by the Bragg law $2d \cdot sin\theta_B = \lambda = hc/E_B \rightarrow E_B \simeq hc/2d\theta_B \rightarrow dE = \frac{hc}{2d}\frac{1}{\theta_B^2} \cdot d\theta = \frac{2d}{hc} E_B^2 \cdot d\theta$ considering the local reflectivity nearly constant

$$\eta_I(E_B) \sim \frac{2d}{hc} \cdot E_B^2 \cdot \int_0^{\pi} \eta(E_B, \theta)\ d\theta = \frac{2d}{hc} \cdot E_B^2 \cdot \eta_\theta(E_B) \qquad (3.3\_8)$$

Maximizing the integrated spreading leads to the maximization of the integrated reflectivity. Therefore, it is useful to study how the first varies. Figure 3-15 shows the curve of the maximum of η_θ as a function of the angular spreading. CDPs are Si (111), the reflectivity was maximized in the energy range (2-500 keV), and for thickness range (0.1-50 mm). There is a growing dependence between the opening angle α and the integrated spreading. However, this growth is dampened by the decrease of reflectivity caused by the increase of the opening angle.

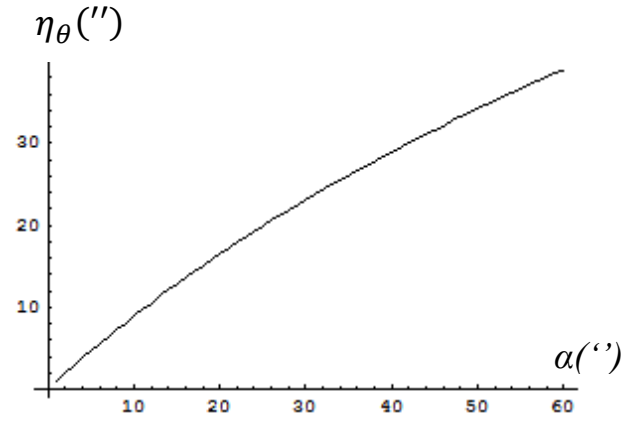

Figure 3-15

Maximum integrated spreading (in arcsec) of Si (111) CDPs as a function of the opening angle α of the crystal. The integrated spreading was maximized in the energy range (2-500 keV), thickness range (0.1-50 mm).

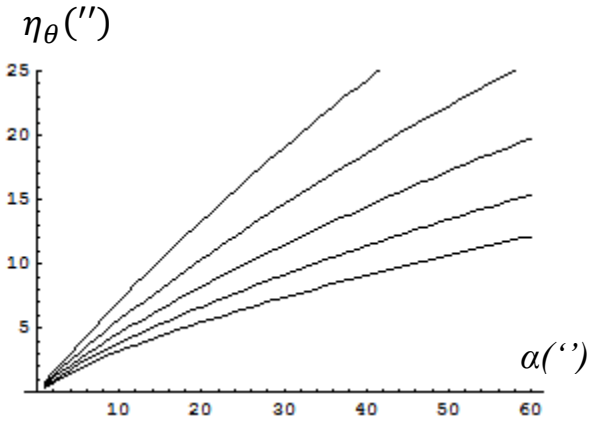

Figure 3-16

Maximum integrated spreading (in arcsec) of Si (111) CDPs as a function of the opening angle α of the crystal. The integrated spreading was maximized in the energy range (2-500 keV). The curves are calculated for different thicknesses t = 10-20-30-40-50 mm from the bottom upwards.

We conclude this analysis by evaluating how the angular area varies with the thickness of the crystalline block. Figure 3-16 shows the curves of maximum integrated reflectivity as a function of the opening angle, for various thicknesses. The integrated spreading increases as the thickness of the sample, in fact, the increased thickness tends to offset the loss of diffraction efficiency caused from increasing angular opening. One might conclude that the best crystals are represented by thick samples with large spreading. However, both the angular aperture that the thickness of the sample cause an increase in the divergence of the diffracted beam, as we will see in the following chapters. This leads to an increase in the size of the focal spot on the detector, with a consequent loss of spatial resolution.

3.2.1.3 Corrections for real conditions

As seen so far has been developed in the hypothesis of having an X-ray beam incident on a perfect ideal crystal. In fact, you can not get either beams or crystals without defects. For simulate the response of a real crystal, the following phenomena have to be considered:

1) Temperature of the crystal	4) Chromaticity of the beam
2) Spreading due to the Darwin width	5) Divergence of the beam
3) Mosaicity of the crystal	6) Variation of the interplanar distance

The correction due to the temperature tends to decrease the reflectivity of the crystal. The other five contributions do not affect the amount of radiation diffracted, but they scatter the photons, thus smoothing the edges of the rocking curves. In Fig.3.5_1 you can compare the differences between the rocking curve of an ideal crystal and the rocking curves obtained for real conditions.

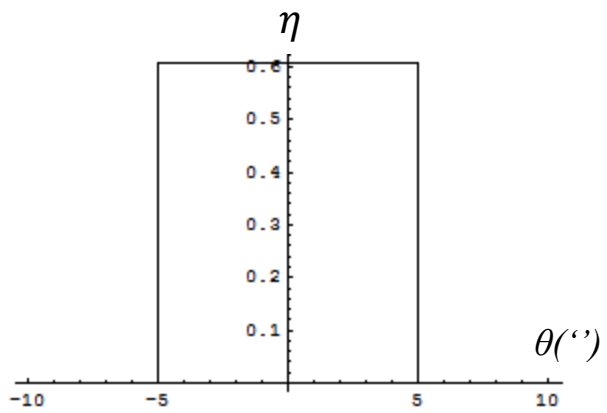

Figure 3-17

Calculated rocking curves for an ideal Si (111) crystal thickness t = 11 mm, opening angle α = 11 arcsec, where impinges an ideal beam of energy E = 100 keV. The angle θ is expressed in arcsec θ (").

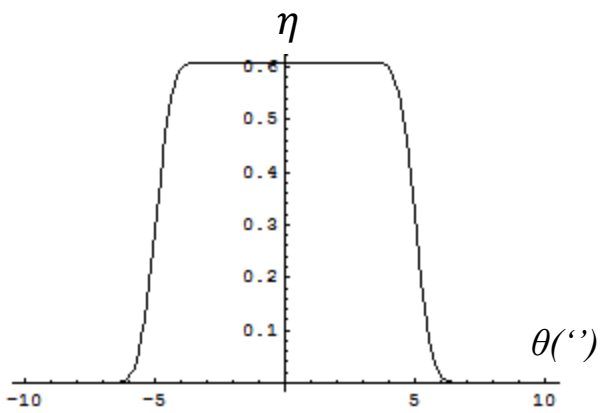

Figure 3-18

Calculated rocking curves for a real Si (111) crystal, thickness t = 11 mm, opening angle α = 11 arcsec, mosaicity β = 1 arcsec, temperature 20 ° C (the Debye-Waller factor is 0.974). A real beam impinges on it with energy E = 100 keV, chromaticity ΔE = 0.01 keV, divergence Δθ = 0.07 arcsec. In these conditions, the Darwin width is δ_w = 0.527 arcsec.

3.2.2 Quasi-mosaic CDPs

Quasi-mosaicity (QM) is an effect present in some anisotropic materials, induced by the deformation of the material itself. If you bend a sheet of isotropic material, this will assume an opposite curvature orthogonal to the first, named anticlastic curvature. The planes perpendicular to the sheet remain straight. In an anisotropic solid as a crystal the crystallographic planes perpendicular to the surface can undergo bending because of the particular structure of the material. This anisotropy-induced curvature is called quasi-mosaic curvature. In fact, historically, when the crystal was analyzed by X-rays, it showed a range of possible angles of diffraction, a behavior similar to that found in mosaic crystals.

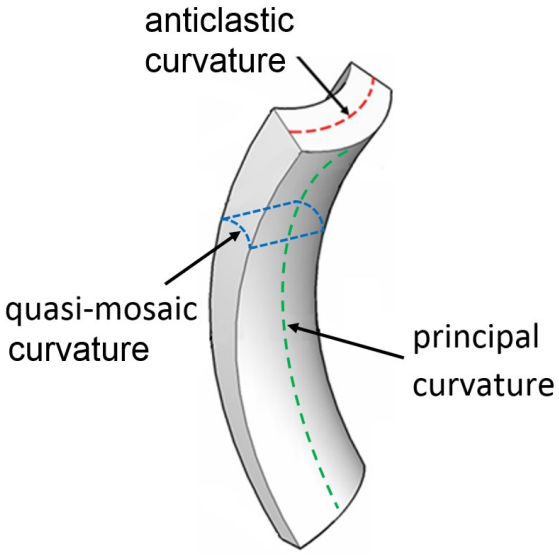

Figure 3-19

Sketch of a crystal showing the quasi-mosaic curvature. If a plate material undergoes a primary deformation of radius R, the plate also undergoes an anticlastic deformation in a perpendicular direction of radius R_{anti}. In some anisotropic materials, for some particular directions, the material undergoes a quasi-mosaic deformation R_{QM} in a direction perpendicular to the first two deformations.

The quasi-mosaic effect can turn a crystal in a small Laue lens. The planes affected by the quasi-mosaic curvature are used for diffraction, thus enhancing the integrating reflectivity of the crystal. The primary curvature is used to fit the profile of the crystal to the curvature of the entire lens, thus turning the crystal in a focusing element. The quasi-mosaic planes are aligned in the radial direction of the lens, so that the crystal diffract x-rays in the focus of the lens itself Figure (3-21). The diffraction spot of the crystal is a line with thickness dependent from aberration phenomena, but not from the dimension of the crystal. Thus, crystals expose a large face to the incident beam without increasing the dimension of the diffraction spot. Therefore, the number of focusing crystals needed for building a Laue lens is far smaller than the number of non-focusing crystals.

The use of quasi-mosaic crystals allows a strong reduction in the size of the focal spot, resulting in a gain in resolution of the instrument. QM crystals allow to reach an extremely high resolution if compare to mosaic crystals, or primary curved crystals (Primary CDP Primary CDP). In particular, a Laue lens built with QM crystals allows to increase the resolution of the instrument of more than an order of magnitude, as will be explained below, with respect to a Laue lens constructed with mosaic crystals or primary curved crystals. Achieving high resolution is a prerequisite for all possible applications of a Laue lens.

3.2.2.1 Modelling the quasi-mosaic curvature

Historically, quasi-mosaicity was discovered by Sumbaev (1957) in a seminal work. Quasi-mosaicity is fully understood in the framework of the theory of linear elasticity. A rectangular crystal plate subject to mechanical moments applied along the *x*- and *y*-axis directions undergoes primary deformation as depicted in Figure 3-20. If the surface stress is constant over the crystal surface, the ratio between primary and QM curvatures is independent from the size of the rectangular crystal plate.

The curvatures of internal planes can be calculated through the displacement field as a function of *u(r)*, *v(r)* and *w(r)*, which are the deformations along the *x*, y and *z* axes, respectively. All the stresses and tensions applied to the crystal can be reduced to a couple of momenta M_x and M_y applied to the plate borders. The normal (σ) and tangential (τ) components of the stress tensor are related to the mechanical moments M_x and M_y as

$$\sigma_x = \frac{M_x}{I_x} z,\ \sigma_y = \frac{M_y}{I_y} z,\ \sigma_z = 0$$

$$\tau_{yz} = 0,\ \tau_{xz} = 0,\ \tau_{xy} = 0$$

Where $I_x = \frac{l_x h^3}{12}$, $I_y = \frac{l_y h^3}{12}$ are the moments of inertia of the plate with sides l_x, l_y, thickness h, for the stress σ_x, σ_y. By definition, the mechanical moments are:

$$M_x = F_x l_x = \sigma_x A l_x = \sigma_x l_x l_y l_x = \sigma_x l_x^2 l_y$$

$$M_y = F_y l_y = \sigma_y A l_y = \sigma_y l_x l_y l_y = \sigma_y l_x l_y^2$$

Where *A* is the area of the largest face. As calculated in (7 Appendix I - Theory of elasticity at the first order), the displacement field *u(r)*, *v(r)*, *w(r)* along *x*, *y*, *z* direction are

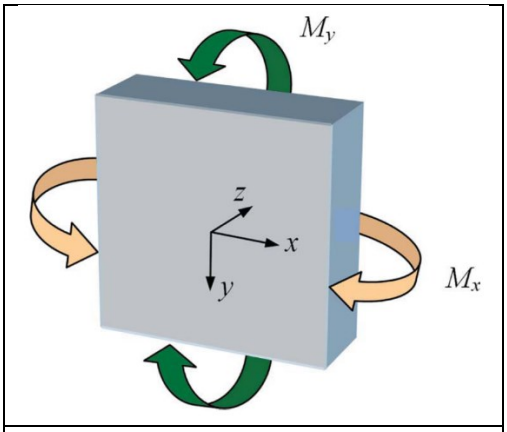

Figure 3-20

Sketch of a crystal plate with the coordinate system used for the modelling. Bent arrows symbolize applied moments M_x and M_y.

$$u = \frac{1}{2}\left[\frac{M_x}{I_x}(S_{51}z^2 + S_{61}yz + 2S_{11}xz) + \frac{M_y}{I_y}(S_{52}z^2 + S_{62}yz + 2S_{12}xz)\right] \quad \text{(C.38)}$$

$$v = \frac{1}{2}\left[\frac{M_x}{I_x}(S_{41}z^2 + 2S_{21}yz + S_{61}xz) + \frac{M_y}{I_y}(S_{42}z^2 + 2S_{22}yz + S_{62}xz)\right] \quad \text{(C.39)}$$

$$w = \frac{1}{2}\left[\frac{M_x}{I_x}(S_{31}z^2 - S_{11}x^2 - S_{12}y^2 - S_{16}xy) + \frac{M_y}{I_y}(S_{32}z^2 - S_{12}x^2 - S_{22}y^2 - S_{26}xy)\right] \quad \text{(C.40)}$$

S_{ij} being the elastic-tensor coefficients. If the surface stress is uniform $\sigma_x = \sigma_y = \sigma$, the curvature of the largest face along *x*, *y* (principal curvature) is:

$$\frac{1}{R_{Px}} = \frac{d^2w}{dx^2} = -\left(\frac{M_x}{I_x}S_{11} + \frac{M_y}{I_y}S_{12}\right) = -\sigma\frac{l_x l_y}{\frac{h^3}{12}}(S_{11} + S_{12})$$

$$\frac{1}{R_{Py}} = \frac{d^2w}{dy^2} = -\left(\frac{M_x}{I_x}S_{12} + \frac{M_y}{I_y}S_{22}\right) = -\sigma\frac{l_x l_y}{\frac{h^3}{12}}(S_{12} + S_{22})$$

Choosing y as the focusing direction, the quasi-mosaic curvature along it is:

$$\frac{1}{R_{QM}} = \frac{d^2v}{dz^2} = \frac{M_x}{I_x}S_{41} + \frac{M_y}{I_y}S_{42} = \sigma\frac{l_x l_y}{\frac{h^3}{12}}(S_{41} + S_{42})$$

The ratio between primary and QM curvature is

$$\frac{R_{QM}}{R_P} = -\frac{S_{41} + S_{42}}{S_{11} + S_{12}} \quad (1)$$

It follows that the QM curvature for focusing occurs only if S_{41}, S_{42} are not zero. As an example, a primary spherical bending of a (112) Si or Ge plate results in a QM curvature of the (111) diffracting planes orthogonal to the (112) surface.

3.2.2.2 Total efficiency

In a QM crystal the angle of incidence between the diffraction planes and the X-ray beam changes with both the depth in the crystal, both with the location on the main crystal surface (the entrance face of the beam into the crystal). The first effect is due to the QM curvature of the crystalline planes. The second effect is due to the primary curvature, which curves the entire crystal block with respect to the direction of the incident beam. This curvature causes the entrance face of the crystal to be not isotropic, as was obtained for primary bent crystals. Then, the rocking curve of the crystal as a whole will be different than the rocking curves of a point. For an impinging mono-dimensional line beam, QM diffraction planes produce a box-like RC with reflectivity η and width equal to the angular spreading of QM planes. Primary curvature contributes with a box-like distribution function wide as the angular spreading induced by primary curvature. This distribution is normalized to 1 for the conservation of energy. The RC of the QM crystal under a uniform X-ray beam becomes the convolution of the distribution functions of QM curvature and primary curvature, i.e. a trapezoidal RC. Name α the angular spreading due to QM curvature, and β the angular spreading due to primary curvature, the peak reflectivity for the QM crystal is $\eta(E) \cdot \alpha/\beta$. Nevertheless, the integrated spreading of the entire crystal is not diminished, as the integrated reflectivity.

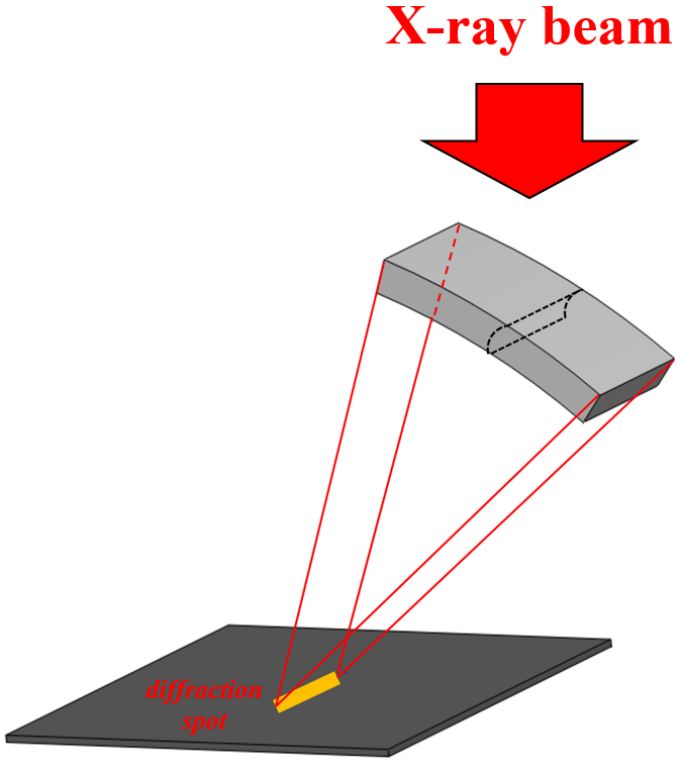

Figure 3-21

The primary curvature affects the shape of the main face, concentrating the diffracted rays in a line-shape diffraction spot. The quasi-mosaic curvature bents the diffraction planes, so increasing the diffraction efficiency and the bandwidth.

It is useful to introduce the concept of effective area, a parameter important in the realization of a Laue lens as the integrated reflectivity. Effective area is defined as:

$$A_{ef}(E) = \int_{\Sigma} \eta(E,\theta)\, dA$$

It is the integral of the distribution function of the reflectivity for a certain energy on the area of the entire lens. This quantity measures what is the area of the lens able to diffract a certain energy E, and with which reflectivity. As an example, the effective area of a primay CDPs crystal is $A_{ef}(E) = \int_{ymin}^{ymax} \int_{\mathrm{xmin}}^{xmax} \eta(E,\theta)\, dx\, dy = L_x L_y \eta(E)$, where L_x, L_y represent the dimensions of the crystal face exposed to the beam. The effective area of a QM CDPs crystal is $A_{ef}(E) = L \int_{\mathrm{rmin}}^{rmax} \eta(E,\theta)\, dr = LR \int_{\theta\mathrm{min}}^{\theta max} \eta(E,\theta)\, d\theta = LR \cdot \eta(E) \int_{\theta(E)-\frac{\alpha}{2}}^{\theta(E)+\frac{\alpha}{2}} d\theta = LR \cdot \eta(E) \cdot \alpha$

Where *L* is the size of the crystal face exposed to the beam, *R* is the primary radius of curvature, *θ (E)* is the Bragg angle at the energy E.

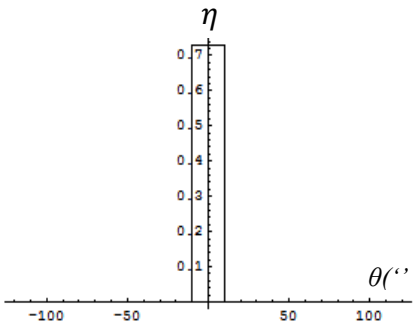

Figure 3-22

Expected RC for a Si (111) QM crystal under a mono-dimensional X-ray beam. The QM angular spreading is α = 20 arcsec, the thickness is t = 5 mm. The integrated spreading is 14.6.

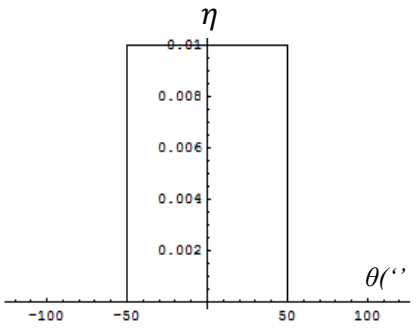

Figure 3-23

Distribution function produced by the primary curvature, normalized to 1. The angular spreading is β = 100 arcsec.

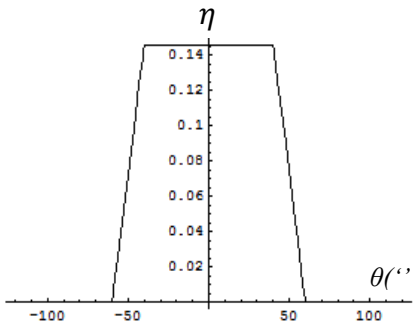

Figure 3-24

Expected RC for a Si (111) QM crystal. The QM angular spreading is α = 20 arcsec, the primary angular spreading is β = 100 arcsec, the thickness is t = 5 mm. The integrated spreading is 14.6.

3.2.2.3 Focusing properties

This section depicts the peculiar phenomenon of focusing that characterizes QM crystals, and how to use it in Laue lenses. The crystalline blocks that make up a Laue lens are positioned on the surface of the lens calotte with radial symmetry with respect to the axis of the lens itself. The blocks composing the same circle of the lens have the same distance from the axis of the lens, but the angle of rotation varies. The focal spot of the various blocks appear on the detector rotated relative to one other. The diffraction spots overlaps in a circular region in the center of the detector, where most of the diffracted photons concentrate. Then, the physical size of the blocks in the direction where no diffraction occurs is of little importance. Thus, the lens produces a very small focal spot, which does not depend on the size of the crystals composing the lens.

The performance of a Laue lens can be entirely valuated by the distribution function of photons diffracted on the detector. This distribution coincides with the distribution of irradiance on the plane of the detector normalized for the irradiance of the source. The distribution of the number of counts on the focal plane changes significantly when the lens is built using QM curved crystals, primary bent crystals, or mosaic crystals. For simplicity, the analysis is conducted on a single ring of the lens, the process can be repeated trivially on all links that constitute a Laue lens. In order to better compare the three cases, the construction parameters of the lens are optimized for the use of mosaic

crystals. A Laue lens usually has the shape of a spherical cap, with radius R = 40 m. We use the approximations for small angles, then the focal length of the lens is f = 20 m. We choose a realistic ring opening angle of β = 60 arcsec, and a transverse dimensions of the crystalline blocks of 15 mm. For homogeneity, Si (111) diffraction planes are used all through the analysis. The lens ring is optimized for focusing photons with energy 150 keV.

For each QM crystal, the distribution function of photons on the detector P_n is similar to a 3D step function (Figure 3-25).

$$P_n(x,y) \simeq \frac{\eta_I}{l_x \cdot l_y} \begin{cases} 1 & -\frac{l_x}{2} < x < +\frac{l_x}{2} \\ 1 & -\frac{l_y}{2} < y < +\frac{l_y}{2} \\ 0 & elsewhere \end{cases}$$

Where η_I is the integrated spreading, $l_x = L_x$= 15 mm is the dimension of the crystal in the direction where no focusing occurs, l_y is the spreading of the beam due to aberration effects. This last contribution is usually a very complex function (not a step function), but in our case the width of this function is very narrow. Then, for simplicity, it is approximated to a step function with width $l_y \sim$ 0.8 mm. The focal spots produced by the other crystalline blocks are rotated by an angle equal to $\theta_r = (n-1)\frac{360^\circ}{N}$ around the center of the detector. The distribution function of the normalized irradiance of the whole ring P_a is the mean of the N probability distributions of the crystals composing the ring (Figure 3-26).

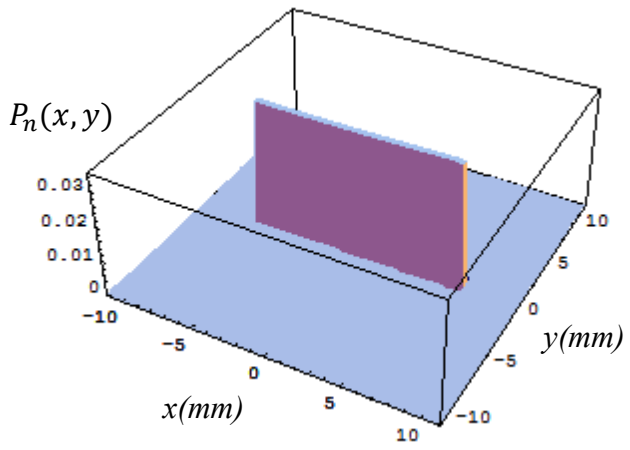

Figure 3-25

Distribution of normalized irradiance from a single QM crystal in the xy plane of the detector. The size of the crystal is L_x = 15 mm, L_y = 11.7 mm because it has to cover the ring opening angle of β = 60 arcsec, optimized at thickness = 5 mm. The curvature radius of CDPs is R_{qm} = 103.6 m, producing an angular spreading of α = 10 arcsec. The integrated reflectivity is η_I = 0.417 keV.

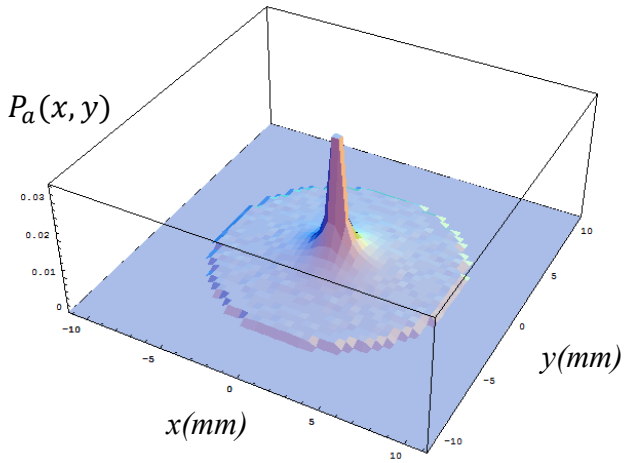

Figure 3-26

Distribution of normalized irradiance from a ring of a Laue lens composed of QM crystals, in the xy plane of the detector. The ring is composed by N = 217 crystals.

$$P_a(x,y) = \frac{1}{N}\sum_{n=1}^{N} P_n(x,y)$$

Where $1/N$ keeps the entire function normalized to η_I. The result is a quasi-continuous distribution. The averaged distribution function along a radial direction from the center of the detector behaves approximately as hyperbolic $P_a(r) = \int_0^{2\pi} P_a(r,\theta)\, r d\theta / \int_0^{2\pi} r\, d\theta = \int_0^{2\pi} P_n(r,\theta)\, d\theta / 2\pi r \sim \eta_I/(l_x \cdot l_y \cdot 2\pi r)$.

The analysis is repeated for a ring of Laue lens composed of primary CDPs crystals. For consistency with previous calculations, we choose crystals with same size. Although bending mono-crystals of this size is difficult, it is possible to construct crystalline blocks of this kind through the stacking of curved crystals, or by using crystalline blocks with internal planes intrinsically curved (eg. $Si_{1-x}Ge_x$ crystals). Along the direction where diffraction occurs, the shape of the focal spot is given by the convolution of enlargement given by the geometrical dimensions of the crystal, and the enlargement given by aberrations. The first distribution is a step function of width L_y. The second distribution can be approximated to a step function of width s = 5.4 mm. Then, P_n is a trapezoidal distribution (Figure 3-27).

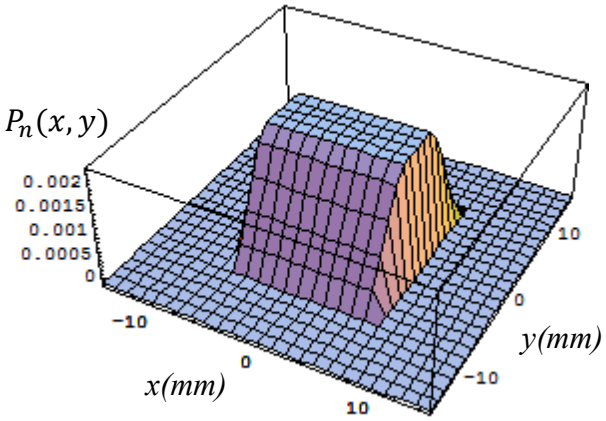

Figure 3-27

Distribution of normalized irradiance from a single primary bent crystal in the xy plane of the detector. The size of the crystal is L_x = 15 mm, L_y = 11.7 mm, optimized at thickness = 15.3 mm. The primary curvature radius of CDPs is R = 40 m, producing an angular spreading of $\alpha = \beta$ = 60 arcsec. The integrated reflectivity is η_I = 1.38 keV.

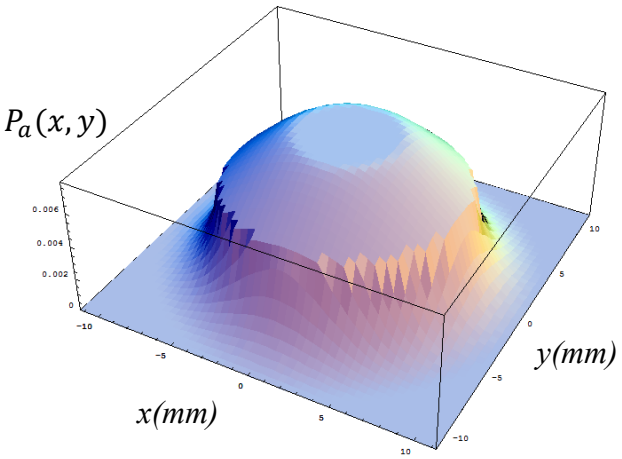

Figure 3-28

Distribution of normalized irradiance from a ring of a Laue lens composed of primary bent crystals, in the xy plane of the detector. The ring is composed by N = 217 crystals.

$$P_n(x,y) \simeq \frac{\eta_I}{l_x \cdot L_y} \begin{cases} 1 & -\frac{l_x}{2} < x < +\frac{l_x}{2} \\ 1 & -\frac{L_y - s}{2} < y < +\frac{L_y - s}{2} \\ +\frac{1}{s}x + \frac{L_y + s}{2s} & -\frac{L_y + s}{2} < y < -\frac{L_y - s}{2} \\ -\frac{1}{s}x + \frac{L_y + s}{2s} & +\frac{L_y - s}{2} < y < +\frac{L_y + s}{2} \\ 0 & altrove \end{cases}$$

It is easy to see that the focal spot size is much larger than in the case of QM crystals. The profile for the lens ring is obtain by summing up the contribution of all the crystals composing it (Figure 3-28). As expected, the distribution is less sharp than for a ring composed of QM crystals.

The analysis is repeated for a ring of Laue lens composed of mosaic crystals with same size. Ideally imperfect mosaic crystals are considered, with crystallites size going to zero. The size of the focal spot produced along the direction where no focusing occur is equal to the geometric dimension of the crystal $l_x = L_x = 15$ mm. Along the focusing direction, the focal spot is the convolution between the geometric dimension of the crystal L_y and enlargement caused by the misalignment between the crystallites. A Gaussian distribution can model this misalignment. The mosaicity is $\beta = 60$ arcsec, then the standard deviation of the Gaussian is $\sigma = \beta/2.35 = 25$ arcsec. So, the distribution function of normalized irradiance P_n produced by each mosaic crystal is:

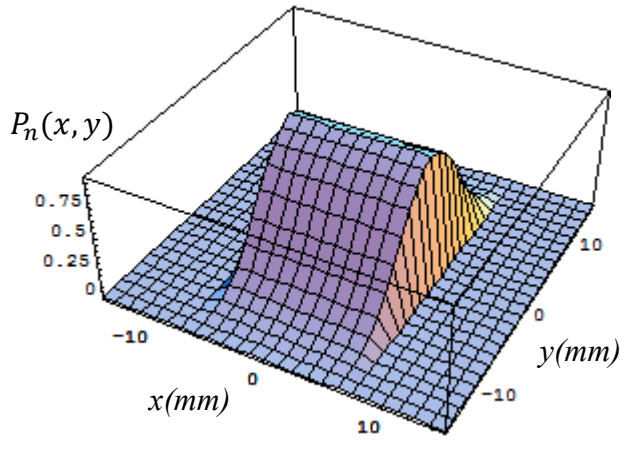

Figure 3-29

Distribution of normalized irradiance from a single mosaic crystal in the xy plane of the detector. The size of the crystal is L_x = 15 mm, L_y = 11.7 mm, optimized at thickness = 12.6 mm. The mosaicity is $\alpha = \beta$ = 60 arcsec. The integrated reflectivity is η_I = 1.107 keV.

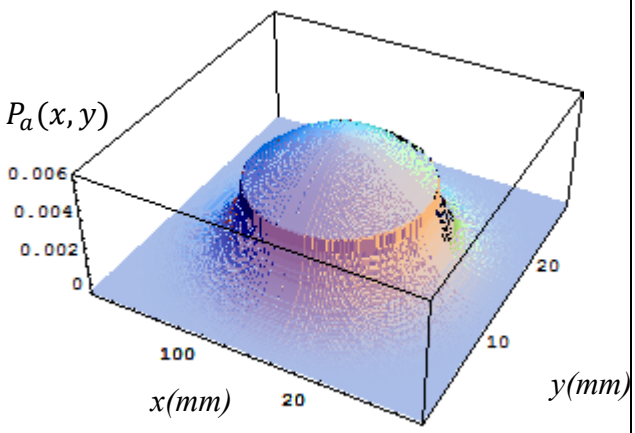

Figure 3-30

Distribution of normalized irradiance from a ring of a Laue lens composed of mosaic crystals, in the xy plane of the detector. The ring is composed by N = 217 crystals.

$$P_n(x,y) = \frac{\eta_I}{l_x \cdot L_y} \begin{cases} 1 & -\frac{l_x}{2} < x < +\frac{l_x}{2} \\ \frac{1}{\sqrt{2\pi}\sigma} \int_{-\infty}^{y} e^{-\frac{\left(y+\frac{L_y}{2}\right)^2}{2\sigma^2}} & -\infty < y < 0 \\ \frac{1}{\sqrt{2\pi}\sigma} \int_{-\infty}^{y} \left(1 - e^{-\frac{\left(y-\frac{L_y}{2}\right)^2}{2\sigma^2}}\right) & 0 \le y < +\infty \\ 0 & altrove \end{cases}$$

Figure 3-31 compares the profiles of irradiance distribution for a Laue lens built with mosaic crystals, primary curved crystals or QM crystals. The irradiance distribution is very narrow in the case of QM crystals. It is important to point out that the distribution for the crystals mosaic was obtained with crystallites size tending to zero, the limit condition for which the maximum reflectivity is obtained. In real mosaic crystals, the size of the crystallites is always finite, and with the production techniques of today, the reflectivity measured in real good mosaic crystals is lower than the reflectivity calculated theoretically. On the contrary, there are techniques that allow the production of curved crystals with nearly ideal response (Bellucci V. C., 2011b). Furthermore, the analysis was carried out optimizing the lens for the use of mosaic crystals.

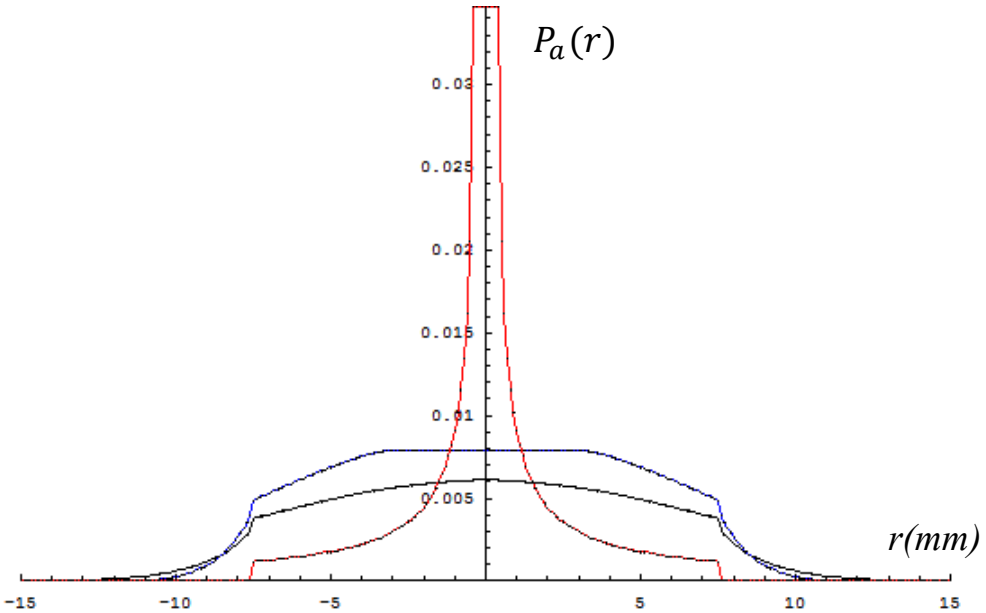

Figure 3-31

Average distribution of irradiance on the plane of the detector for a ring of Laue lens composed of mosaic crystals (black), primary curved crystals (blue), or QM crystals (red).

The resolution of an optical instrument corresponds to the FWHM of the distribution of irradiance produced from a point source on the plane of the detector. The FWHM of the distribution are respectively $FWHM_{QM} \approx 1.1$ mm, $FWHM_{P} \approx 15.2$ mm and $FWHM_{M} \approx 15.2$ mm. So the resolution of a Laue lens that employs QM crystals is always better than the resolution of the equivalent lens

that uses crystals in the other two modes. An X-ray source is much more detectable, as emerges from the background noise. For this reason it is important that the focal spot produced by a point source has an high peak. In this case $P_a^{QM}(0)/P_a^M(0) = 5.8$.

3.3 The indentation method and our crystals

The crystalline tiles we furnished for the Laue project were Ge (111) QM CDPs crystals. The primary curvature was adapted to the lens calotte of radius 40 m. The grooving method is an elective manufacturing system for a quick production of a large number of self-standing bent samples, that is a mandatory issue for a concrete realization of a Laue lens.

3.3.1 The indentation method

Grooving the surface of a solid material proved to be a method to induce permanent deformation into the bulk. The indentation method would bend a crystal with no need for external mechanical bending devices. Then, it would be ideal to produce CDPs crystals for observation of cosmic X-ray radiation through satellite experiments, where unnecessary weight is not permitted on board (Barriére N. G.-X., 2010).

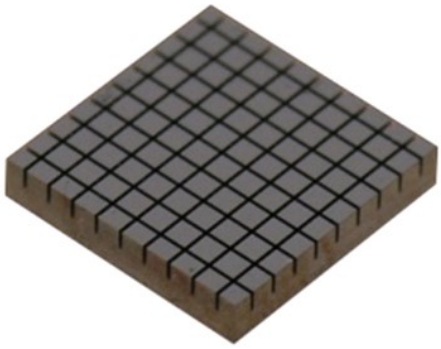

Figure 3-32

Square Si sample bent by grooving. Periodic grooves along its sides avoid unwanted asymmetries in the system, thus inducing an uniform stress field.

The effect of indentations can be rationalized in terms of a tensile film produced at the bottom of the grooves. A previous study showed that the region just in the neighborhood of an indentation is rich in dislocations and partly amorphous (Baricordi, 2005). Indeed, grooving a crystal degrades the quality of the material near the indentation, turning the mono-crystal in an amorphous or defected material. These material phases have a density smaller than the crystalline phase. It follows that, when a crystalline material is turned in an amorphous one, it expands, thus producing a tensile layer. The tensile layer is produced at the bottom of the grooves and over their walls. However, the stress the tensile layer produces on a wall compensates with the stress produced on the next wall, thus resulting in no curvature. The stress produced at the bottom of a groove does not compensate, but it sums up with the stress produced by near grooves. So, this stress creates a bending moment and a curvature in the object. The tensile layer produced by the grooves is buried in the material, and it cannot delaminate as a deposited tensile layer. Moreover, the grooving process removes some material, thus reducing the resistance of the object to be bent.

The defected region depends on the blade grit, width, advance speed and many other variables depending on the grooving manufacture process. However, the extent of the highly defected region is generally limited to some microns [8]. The stress produced by the defected region depends on many variables, some of them not well controllable, so a theoretical prevision of the entity of this stress is unfeasible. The stress can be gathered by observing the curvature induce to samples. Knowing the stress, an estimation of the curvature induced in similar samples is possible by an analytical or numerical (finite elements) approach. Indeed, as for any field of internal forces, crystal deformation occurs as it were caused by external moments. The crystal was thereby treated as an anisotropic body undergoing deformation through first-order elastic theory (Timoshenko, 1970).

Figure 3-32 show a square Si mono-crystal bent by grooving along two perpendicular directions, resulting in an uniform stress field. At SSL, indentations with variable depth are done by a high precision dicing saw (DISCO® DAD3220), equipped with a rotating blade of various size,

geometry and diamond grit size. The grit size and the blade advance speed needed special attention. The choice was the result of a tradeoff between the need to indent the sample rather harshly, to obtain a defected region with high stress, and prevention of excessive damage to the underlying crystalline bulk. Therefore, we usually employed a blade with 2 μm size diamond grains and the advance speed was set at most at 1 mm/s.

The deformation of the crystal was calculated for the cases in Figure 3-33 and displayed as a contour plot for comparison with experimental patterns. The actual deformation of the samples was measured by subtracting the surface profiles obtained before and after the indentation process. The profile of the surface with the grooves altered by their presence, making the analysis more difficult. Therefore, the analysis was carried out on the back face. In Figure 3-33, three representatives orientations were used, which reacted differently to indentation according to their elastic properties. All the samples deformed as an ellipse according to the theory of linear elasticity. It is interesting to note that the (111) plane was deformed as a spherical cap because of the isotropy of Young constant and Poisson module on this plane. Agreement between theoretical expectations and experimental observations is very good in all cases and that is representation of the correctness of the assumptions in the model. Since analysis was done on the back face, it also means that deformation penetrates through the whole sample.

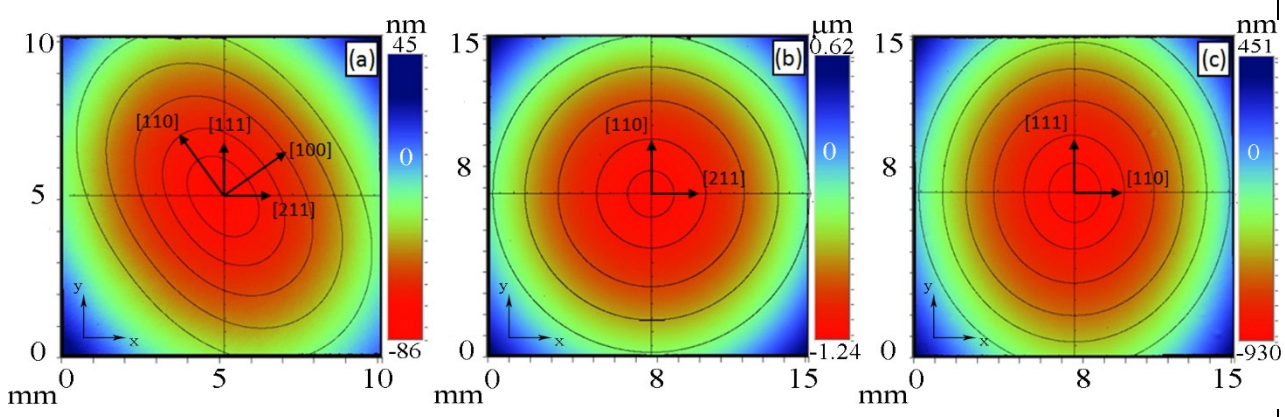

Figure 3-33

Interference profilometry was used to measure the deformational pattern of the backside of three differently oriented Si samples grooved on the front face. The direction normal to the plates and the plate thickness is (a) (110), t = 900 μm; (b) (111), t = 500 μm; (c) (211), t = 500 μm. The depth of the grooves is half of the thicknesses of the samples. Other crystalline orientations of interest are drawn. Silicon response is anisotropic with a direction-dependent deformation. The contour plots in the figures are the deformations expected according to the theory of linear elasticity.

According to the model, removal of the defected region in the neighborhood of the indentations would cause the entire sample to relax. Thus, we applied wet chemical treatment to a sample to etch this region. Interatomic bonds are weaker in a highly defected solid than for a crystal thereby they are easier to be attacked. Anisotropic etching was preferred to isotropic methods because the former allows better control of the process. In particular, 20% weight concentration of KOH at 40 °C does not attack (111) planes while it erodes the other principal planes with a rate of 7-10 μm/h. The samples under analysis were (111) oriented and therefore anisotropic etching would guarantee their thickness to remain constant.

Anisotropic etching by a KOH solution was imparted to three samples with different parameters. Etching attacked first the amorphous layer in proximity of the indentations at a rate of about 1 µm/min, then it slowed down as soon as the crystalline bulk was reached, consistently with the above rates for a crystal. This evidence agrees with the observations in (Baricordi, 2005) of an amorphous layer as 1-2 µm thick due to a cut or an indentation. Beneath the amorphous region a lower-density defected region with localized cracks lies. Figure 3-34 illustrates the curvature radius of the three samples after repeated chemical etching. The samples relaxed during the attacks until a stationary state of curvature was reached, corresponding to complete consumption of the amorphous region. It is evident from the figure that the amorphous phase contributed to about 20% of the curvature. The remaining fraction is ascribed to a dislocation field beneath the amorphous layer. This dislocation field consists of long-range cracks in the crystalline material.

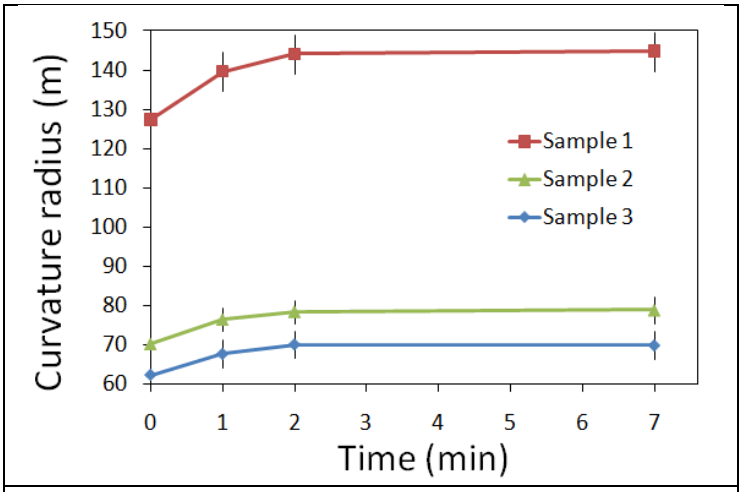

Figure 3-34

Relaxation of indented samples with different parameters after KOH etching with variable duration. Amorphous silicon is easier to attack by KOH than in the crystalline phase. Once the first microns of the amorphous layer in the neighborhood of the grooves are consumed, fast etching is halted. Gradual removal of highly defected region diminish the radius of curvature of the samples. Relaxation is not complete because of the action of the dislocations and cracks that are created by the blade deep into the crystal.

Manifold applications have been proposed for crystals bent by the grooving process out of the astrophysics sector. In the field of particle channeling in crystals, manipulation of high-energy particles via interaction in a bent crystal benefited by the indentation method. As was demonstrated, an indented diamond [2] or silicon [3] crystal bent by grooves to the wanted curvature and used as a deflector for high-energy particles. It was also demonstrated that grooving a Si sample can be employed to fabricate a prototype of a miniature undulator (Bellucci S. e., 2003). Channeled particles in such a periodical crystal emit x-ray coherent radiation, emulating the amplification mechanism occurring in a free electron laser.

3.3.2 Early experimentation with primary CDPs crystals

Silicon and germanium crystals with primary CDPs bent through the indentation method were tested through x-ray diffraction at beamline ID15A of ESRF (Grenoble, France). A highly monochromatic and quasi-parallel beam was set to an energy ranging from 150 to 600 keV thanks to a two-reflection Laue Si (111) unbent monochromator. The characterization was carried out by recording rocking curves (RCs), *i.e.*, by rotating the crystal exposed to the beam, while either diffracted or transmitted intensity was recorded as a function of the incidence angle. The angular distribution of diffracting planes (angular spread) is quantified by the FWHM of the RCs. The RCs also highlight the diffraction efficiency of the sample under investigation, i.e. the rate of diffracted photons. Experimentally,

diffraction efficiency is derived as the ratio of the diffracted beam intensity over the transmitted one, this latter being recorded when the crystal is not subject to diffraction conditions (Barrière, 2009).

Some of the analyzed samples are reported in Table 3-1. Samples were analyzed by diffraction of their (111) planes, the probe beam entering the sample at different depths from the grooved surface (coordinate *z*). Two different configurations were used, *i.e.*, the beam was set quasi-parallel (hereinafter referred to as parallel) or perpendicular to the grooves (Figure 3-35).

Code	Size (mm^3)	Number of indentations	Grooves direction	Grooves spacing (μm)	Grooves depth (μm)	Curvature radius (m)	
						x	y
S72	25.5×36.6×1	25	[211]	1000	400	93.7	460
S81	54.2×30.6×1	30	[110]	1000	400	380	140
2_G32	18.6×9.8×2	11	[110]	800	1000	95	320

Table 3-1

Fabrication parameters of the samples under analysis.

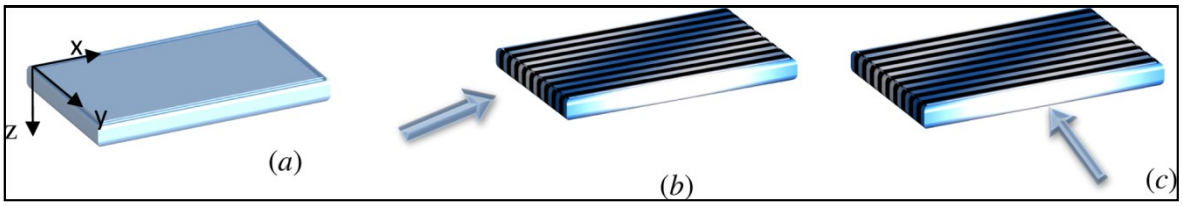

Figure 3-35

Sketch of the primary bent crystals during the X-ray analysis. Grooves were indented on the surface of a Si or Ge plate along one direction, either x or y (a). The pencil x-ray beam enters the sample parallel (b) or perpendicular (c) to the grooves.

The Si crystal labelled S81 was measured at 300 keV with the beam penetrating the sample through its 30.6×1 mm^2 surface, at fixed depth from the grooved side (coordinate *z*) and at different coordinates *y*. The beam was set parallel to the grooves. The bending angle of the sample measured by optical profilometry averaged 29.5 arcsec along [110] direction. Figure 3-36 shows both diffracted and transmitted RCs normalized to the transmitted beam intensity, so that diffraction efficiency is readily displayed. RCs exhibited flat-topped rectangular and uniform shapes with a FWHM of 26 arcsec, close to the optically determined crystal bending. This sample features a significantly high efficiency, about 82% constantly over the whole sample, showing that a curved crystal can amply break the 50%-efficiency limit. No dependence on coordinate *y* was recorded, meaning that curvature is homogeneous throughout the sample.

The Si sample S72 was measured perpendicular to the grooves. Efficiency showed a different behavior from the previous case. The sample was measured at 150 keV with the beam entering the Si crystal through its 25.5×1 mm^2 at different depths from the upper grooved side. Bending angle of the sample was measured by optical profilometry to be 55 arcsec along [211] direction. The RCs in Figure 3-36 still highlight flat-topped and uniform shapes though efficiency varies over the crystal depth. Indeed, diffraction efficiency is nearly 50% close to the grooved region, and it raises up to 79% deeper into the crystal. This feature can be ascribed to the fabrication process of indentations. In fact, the blade exerts a strong stress on the side walls of the groove, resulting in a large generation of defects perpendicular to the feed direction of the blade. Hence, the efficiency decrease throughout the whole

depth of the grooves. Outside the grooved area, high efficiency is restored, meaning that crystal structure is not significantly affected by defects. Sample S72 was also characterized *vs.* energy, the beam entering the crystal far from the grooved region and perpendicular to the grooves (Figure 3-37). The sample features significant diffraction efficiency up to 600 keV, ranging from 80% down to 20%. However, the decrease in efficiency with energy is completely in agreement with dynamical theory of diffraction.

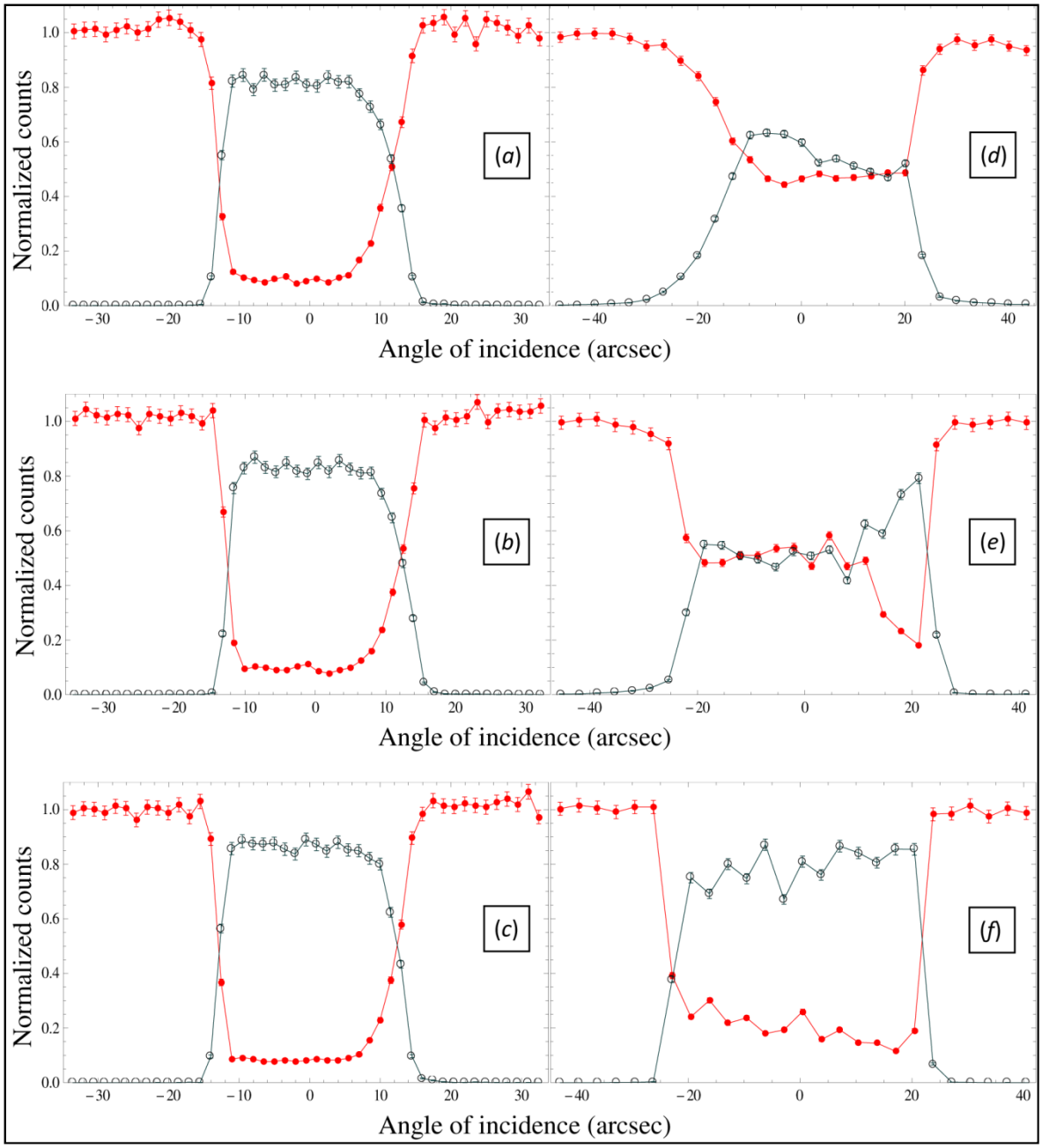

Figure 3-36

The left-hand side shows RCs of crystal S81 with the beam parallel to the grooves at a fixed distance from the grooved face and at (a) y = 5.0 mm, (b) y = 5.9 mm, (c) y = 6.8 mm. The right-hand side shows RCs of crystal S72 with the beam perpendicular to the grooves at different depths from the grooved surface, i.e., at (d) z = 0.05 mm, (e) z = 0.55 mm, (f) z = 0.75 mm. RCs with nearly rectangular shape were achieved in all cases, with an energy passband of the order of the crystal bending (about 26 arcsec for the sample S81 and 55 arcsec for S72). Efficiency is significantly high in all cases and up to 82% for sample S81.

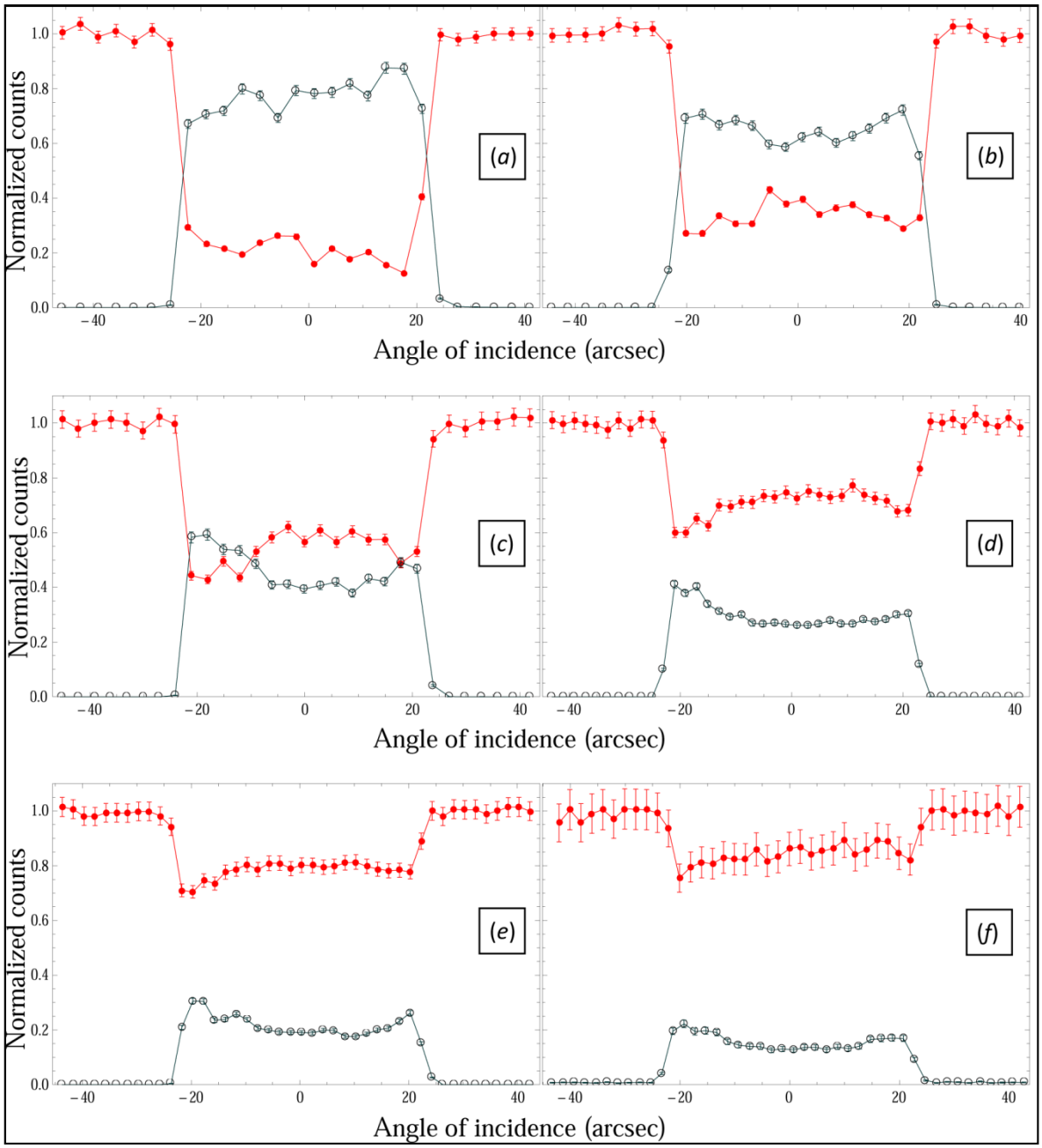

Figure 3-37

RCs of the crystal S72 with the beam perpendicular to the grooves, measured at z = 0.75 mm and x = 0.15 mm. Beam energy was set at (a) 150 keV, (b) 200 keV, (c) 300 keV, (d) 400 keV, (e) 500 keV and (f) 600 keV. Efficiency falls off with photon energy according to dynamical theory of diffraction. The nearly rectangular shape of the distribution is preserved.

Ge crystal 2_G32 was measured at 300 keV with the beam penetrating the sample through its 9.8×2 mm^2 surface at different depths from the grooved side and parallel to the grooves. Morphological bending angle of the sample was 42.4 arcsec along [110] direction. Figure 3-38 (a) shows diffraction efficiency as a function of coordinates *y* and *z*. Efficiency averages to 58% and it is quite uniform throughout the crystal. Though this is still a good performance, it's less than the 93% theoretically expected. The lower efficiency may be due to the non-perfect crystalline quality of the base material, or to the lower resistance of Ge to the grooving process. Figure 3-38 (b) shows that the angular spread is homogeneous throughout the crystal.

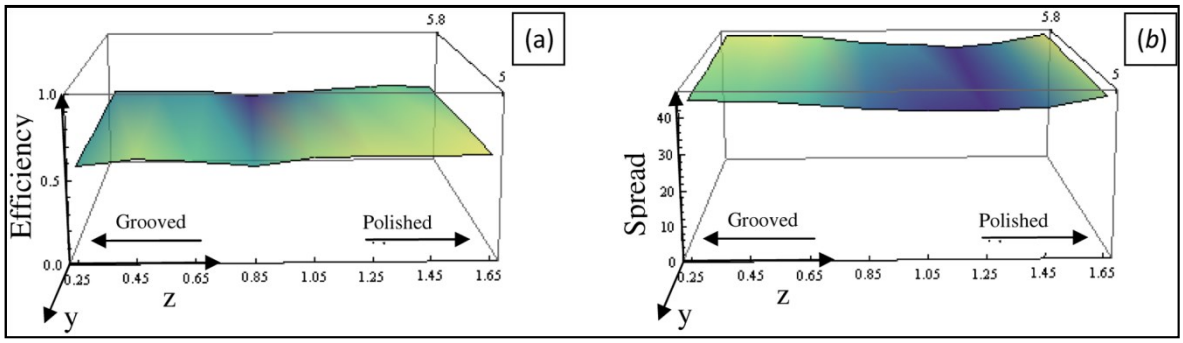

Figure 3-38

(a) Diffraction efficiency of the crystal 2_G32 vs. coordinate z (mm) at several positions within the crystal (coordinate y) with the beam perpendicular to the grooves. Efficiency is about 60% over the whole crystal depth. No dependence on coordinate y (mm) was recorded. (b) Angular spread vs. same dependence is shown. The spreading is about 42 arcsec all over the sample. No dependence on coordinate y (mm) was recorded.

Experimental data have been analyzed and compared to theoretical expectations. In Figure 3-39 (a) the experimental diffraction efficiency of sample S81 *vs*. coordinate *y*, is compared to the theoretical efficiency for a primary CDPs crystal and for a mosaic crystal. Theoretical efficiencies were calculated from the experimental FWHM of the RCs, thus an experimental uncertainty is included. The response is slightly lower than the theoretical efficiency for a bent crystal, meaning that indentations can produce good CDPs. In any case, the 50%-limit is overcome. In Figure 3-39 (b), the experimental diffraction efficiency of sample S72 was studied as a function of photon energy. It follows that the efficiency is always very close to its theoretical limit, falling off with photon energy according to dynamical theory of diffraction (Malgrange, 2002).

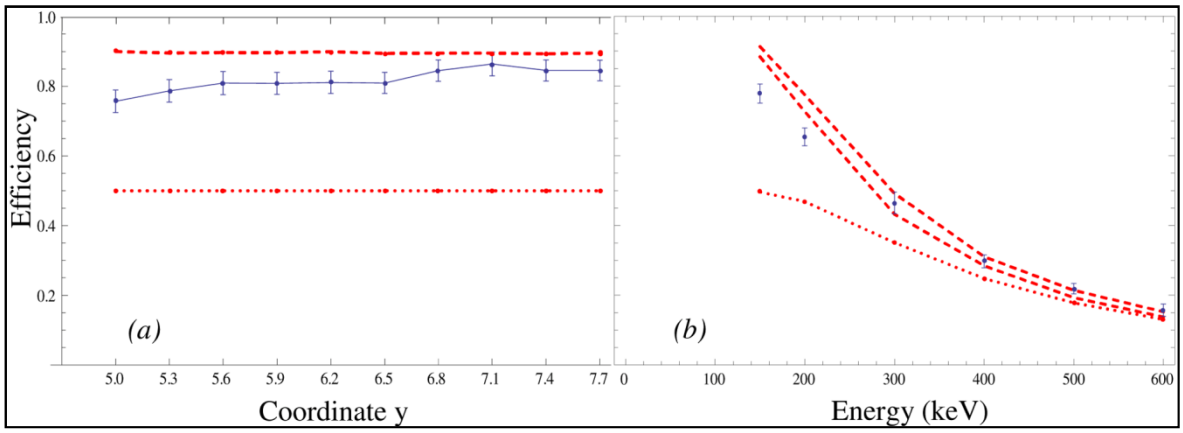

Figure 3-39

(a) Experimental efficiency (blue circles) vs. coordinate y (mm) for crystal S81 with the 300 keV pencil beam parallel to the grooves. Red dashed and dotted line represent theoretical efficiencies in case of a curved and of a mosaic crystal, respectively. An experimental uncertainty is included in both cases. Experimental efficiency slightly varies within the crystal, being always rather close to the theoretical limit yielded by a bent crystal. (b) Experimental and theoretical diffraction efficiencies vs. energy, for sample S72. RCs were carried out at z = 0.75 mm from the grooved face with the beam perpendicular to the grooves. Theoretical efficiency (red dashed line) was calculated taking into account the FWHM of the RCs, thus an experimental uncertainty is included. Measured diffraction efficiency is represented by blue circles with their error bars. Red dotted line represent theoretical efficiency for a mosaic crystal with angular spread equal to the FWHM of the RCs.

3.3.3 Early experimentation with quasi-mosaic CDPs crystals

Silicon and germanium crystals with QM CDPs bent through the indentation method were also produces at Sensor and Semiconductor Laboratory (Ferrara, Italy). As an example, we analyze the Si sample coded as G3. Crystallographic orientations and sample size are indicated in Figure 3-40. Commercially available pure Si wafer was diced to form a plate using a high-precision dicing saw (DISCO^{TM} DAD3220), equipped with rotating diamond blades of 150 μm wide and 5 μm diamond grain size. A permanent curvature was induced by grooving the largest surfaces of the crystal. Since a regular grid of grooves was done on the sample surface, a net curvature has been achieved. Then, the curvature was measured using an optical profilometer (VEECO^{TM} NT1100) with 1 μm lateral and 1 nm vertical resolution. It comes out that the sample is spherically bent. The primary radius of curvature is R = 38 m, resulting in a quasi-mosaic radius of curvature R_{QM} = 99 m. Indeed, the secondary-to-primary ratio is R_{QM}/R = 2.614 for the orientation we used.

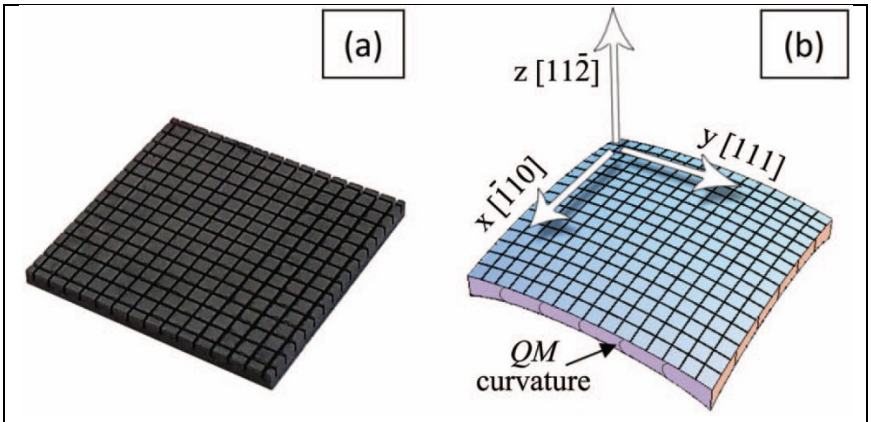

Figure 3-40

(a) Photo of the sample G3. It is possible to see the grid of grooves. (b) Schematic representation of the sample. Crystallographic orientation and QM curvature are highlighted. Tile size is 15 × 15 × 1 mm^3.

Sample G3 was tested through γ -ray diffraction at Institut Laue-Langevin (ILL) (Grenoble, France) at DIGRA facility, under a γ-ray beam of energy 181.931 keV and monochromaticity $\Delta E/E \approx 10^{-6}$. The γ-ray flux was produced by neutron capture in a gadolinium target inserted close to the nuclear reactor of ILL. Beam divergence after the Si (220) monochromator was 1 arcsec, as measured by recording a rocking curve (RC) of the monochromator itself. Collimated-beam size dimension was 1 mm on the diffraction plane (yz) and 3 mm on the plane (xz), z being the direction of the beam. A standard electrode coaxial Ge detector with 25% relative efficiency was used.

Characterization of the sample was carried out by performing RCs. Diffraction and transmission RCs were recorded one after the other, resulting in two complementary curves as a function of the beam incidence angle. Thus, the photon beam hit the $(11\bar{2})$ surface of the sample and was diffracted by bent (111) planes. Diffraction efficiency was recorded on the center of the sample and the experimental RC is reported in Figure 3-41. The gray zone represents the theoretical expectation. Theoretical RC was calculated from the curvature radius measured by the profilometer, thus an experimental uncertainty is included. The measured angular distribution consisted of the convolution between the portion of primary curvature, as seen by the beam, and the secondary curvature. The primary curvature seen by the beam was calculated from the width of the collimated beam (1 mm) and the primary radius of curvature. The divergence of the beam was also included, by convolving the obtained distribution with a gaussian of σ = 1 arcsec. Finally, a morphological factor was included to consider the part of the sample that cannot diffract, i.e., the portion of material

removed during the grooving process. Figure 3-41 shows a good agreement between experiment and theoretical expectation.

The key effect of quasi mosaicity, owing to the curvature of diffracting planes, is a raised diffraction efficiency. However, the measured RC does not rise above 0.5. It is not evident how diffraction efficiency increases since the contribute of the primary curvature to the convolution smoothens the increase in diffraction efficiency due to QM curvature over a large angular span. Indeed, the primary curvature contributes to the convolved RC with an angular aperture of 5.4 arcsec, while QM aperture is 2.1 arcsec. For comparison, we simulated the same crystal with the same primary curvature and orientation if there were no quasi mosaicity, i.e., if the diffracting crystalline planes were flat. In this case, the contribution in the convolution from the secondary curvature would be a Darwin-broadened distribution instead of a wider uniform distribution due to quasi mosaicity. Diffraction efficiency resulted in the dashed line in Figure 3-41, which is by far lower than for the case of curved diffracting QM planes.

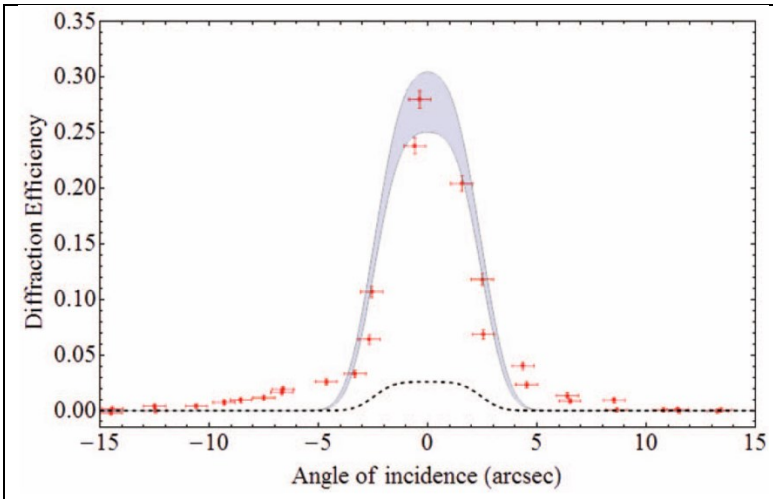

Figure 3-41

Experimental and theoretical RCs. Red circles plot the intensity of measured diffracted beam with their uncertainty bar. The gray area represents the expected result as calculated by taking into account the experimental uncertainties. Dashed black line represents diffraction efficiency if QM curvature was absent.

3.4 Crystals for the Laue project

The realization of a Laue lens for astronomical purposes involves the mass production of a series of crystalline tiles as optical components. For the Laue project, we realized 150 quasi-mosaic Ge samples, bent by grooving one of their largest surface.

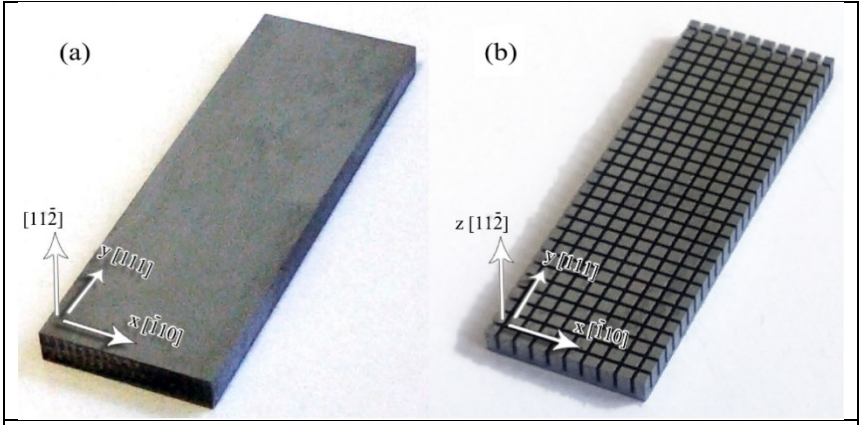

Figure 3-42

Photo of the Ge sample before (a) and after (b) the manufacture. Crystallographic orientation are highlighted. Tile size is 30 × 10 × 2 mm^3, grooves width is 250 μm, grooves distance is 1 mm. The primary radius of curvature is R = 40 m, the QM radius of curvature is R_{QM} = 95.6 m (angular passband 4.3 arcsec) because R_{QM}/R = 2.39 for Ge.

3.4.1 Production

The grooving method is a viable technique to manufacture QM CDPs crystals in a simple and very reproducible way, thus compatible with mass production. A regular grid of grooves was produced on the sample surface, thus achieving a net and homogeneous curvature, very close to a spherical surface. Indeed, grooves were produced regularly spaced and all having the same depth. In fact, a spherical curvature is required to obtain the QM effect for (111) planes (Guidi V. B. V., 2011b), i.e. the planes with the highest reflectivity. The curvature of the samples was measured using an optical profilometer. In order to account for the initial morphological non-planarity of

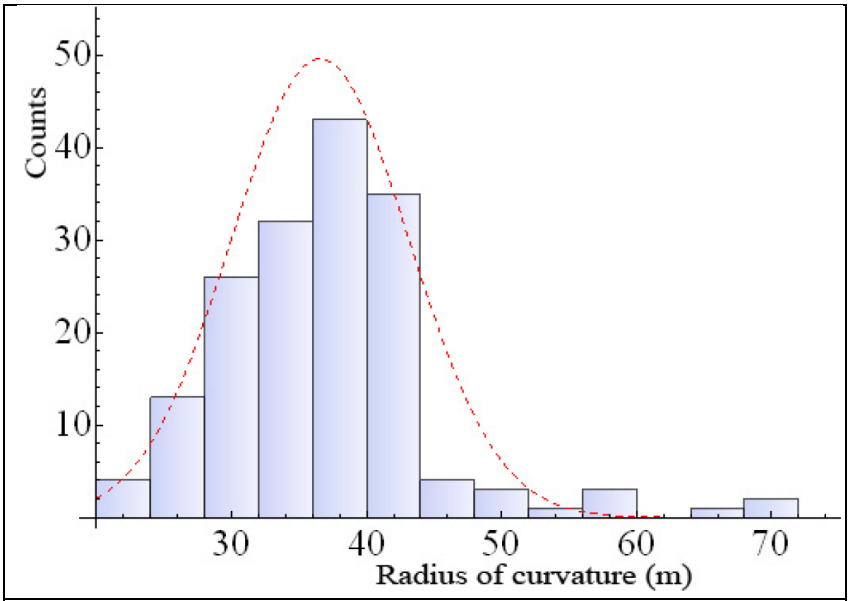

Figure 3-43

Distribution of primary radius of curvature, measured along the [111] direction. Although the distribution of primary radius of curvature is not symmetric, it was fitted with a Gaussian distribution (red dashed line). The Gaussian has mean 36.6 m and standard deviation 6.6 m.

the samples (wafers are generally not perfectly flat), subtraction of the profile before and after the grooving process was done.

During the production, some features are difficult to control. For example, there is an uncertainty on the crystals thickness, which can vary from sample to sample. The consequence is a partial reproducibility on the final curvature. Indeed, for each sample the curvature is homogeneous, but the resulting radius of curvature may vary from sample to sample. The series of 150 samples have been produced with a radius of curvature slightly lower with respect to the desired value of 40 meters, because of the sample over-bent can be adjusted one by one at the value of 40 meter thanks to the chemical etch. The distribution of the measured curvature radius for all the samples was recorded along the [111] direction, and it is reported in Figure 3-43.

The chemical etch is based on a H_2O_2 solution at low concentration, and it is capable of oxidizing Ge with speed depending on the crystalline phase of the material (Huygens, 2007). In fact, it is possible to selectively remove the most defected part of a sample, namely the material amorphized by the blade, thus lowering the state of tension and the curvature of the sample. As an example, a sample with curvature radius 36.8 m was relaxed to a curvature radius of 40.3 m by etching for 60 seconds.

3.4.2 Tests at ESRF/ILL facilities

Some crystalline tiles produced for the Laue project were tested by X-ray diffraction at the the European Synchrotron Radiation Facility (ESRF) and in the laboratories of the Institut Laue–Langevin (ILL), both in Grenoble, France. The analysis performed on a specific sample will be described in the following. The primary curvature radius of this sample is $R_P = (38.9 \pm 1.9)$ m, while the QM curvature radius is $R_{QM} = (92.9 \pm 4.6)$ m. Since the sample was 2 mm thick, the FWHM of the angular spread was expected to be 4.4 arcsec.

3.4.2.1 ID15

The diffraction efficiency of the sample was tested through X-ray diffraction at beamline ID15A of the ESRF. A highly monochromatic beam was set at 150 or 300 keV. The characterization of the samples was carried out by performing rocking curve (RC) measurements, as shown in Figure 3-44. The beam size was 50 × 50 mm wide, impinging on a region of the sample free of grooves. The FWHM of the RCs is a direct measurement of the angular distribution of the (111) diffracting planes. The expected FWHM of 4.4 arcsec was verified at both beam energies. The expected value of diffraction efficiency was 100% at 150 keV and 95% at 300 keV, but it resulted about 50% for both cases. We observed an effect similar to that reported in (Barriére N. G.-X., 2010) (Bellucci V. C., 2011b), namely the diffraction efficiency was pinned at 50% if diffraction occurred in a layer of material rich in defects and cracks. The authors interpreted this effect as a sort of partial mosaicization of the sample due to the grooving process. Indeed, if the material is cracked, its planes do not bend uniformly but they rotate relative to one another, producing a polygon-like curve. In this structure, some re-diffraction of diffracted photons may occur. From a microstructural point of view, the material close to the grooves is subjected to contact with numerous particles of the blade at the same moment, which cause different contact pressures and produce different depths of cut due to their different shape and size. Thus, metallization, plastic deformation and brittle fracture may occur

simultaneously (Gogotsi, 1999). The scarce knowledge of the distribution of dislocations, defects and cracks in the structure due to the grooving process makes unfeasible any attempt to predict analytically the diffraction efficiency. However, recorded values of diffraction efficiency are quite satisfactory, the performance being higher than for any other device relying on mosaic crystals.

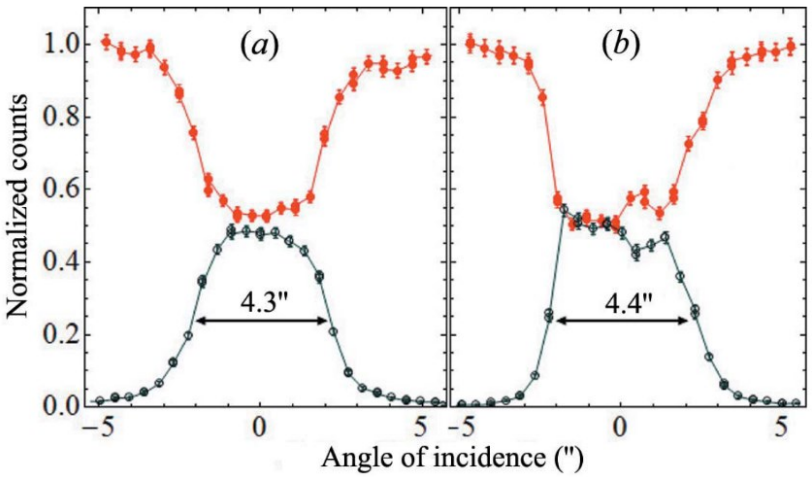

Figure 3-44

RCs of the crystal. The filled red circles plot the intensity of the transmitted beam, while the open black circles plot the intensity of the diffracted beam. (a) Beam energy at 150 keV. (b) Beam energy at 300 keV.

3.4.2.2 White-light diffractometer

In order to highlight the focusing effect driven by the sample curvature, the crystal was analyzed through a diverging and polychromatic X-ray source at the ILL (Guinier, 1949) (Hamelin B., 1998). The diffractometer used a high-voltage and fine-focus X-ray tube designed for industrial radiography, the X-ray energy range being between 80 and 420 keV. The beam impinged onto the sample with an angle depending on the position at the entry face of the crystal. Thus, X-rays with different energies were diffracted towards the image point, which depended on the curvature of the crystal. Sketches of the experimental configuration are shown in Figure 3-45. Diffraction by (111) planes was firstly analyzed with the beam impinging on the crystal surface as in Figure 3-45 (a). Then, the crystal was rotated by 180° around the x axis, as in Figure 3-45 (b). The source-to-sample distance was kept fixed at L_S = (4.45 ± 0.04) m, while the sample-to-detector distance L_D varied. The beam was limited by a collimator with sixe (9.5 × 9.5 ± 0.1) mm, positioned at (1.42 ± 0.1) m from the sample. Thus, the beam divergence was limited to 0.1°, and the portion of the crystal hit by the beam was l = (14.5 ± 0.6) mm. The source diameter was a = (1 ± 0.1) mm. Considering the geometrical configuration, the energy range of the diffracted beam turned out to be 160–227 keV. The crystal behaved as a cylindrical lens because the focusing effect occurred only in the scattering plane. Diffraction of a polychromatic and divergent beam produces a line on the detector (Stockmeier, 2008). The FWHM of the intensity profile, taken on a cross section perpendicular to the line, depends on several parameters. In the case of a perfect crystal with the sample-to-detector distance L_D equal to source-to-sample distance L_S, the width depends only on the X-ray source size and on the crystal thickness traversed by the beam. Conversely, a curved crystal can concentrate the diffracted X-rays at either smaller or larger distance. Indeed, under the small-angle approximation, it is possible to obtain

$$\frac{1}{L_i} = \frac{1}{L_S} + \frac{2}{R_P}$$

where L_i is the image distance for a crystal bent with primary radius of curvature R_P, diffracting photons at the Bragg angle. We set the convention $R_P < 0$ when the incoming beam enters the crystal through the concave surface, and $R_P > 0$ in the opposite case. The focusing capability of the sample

was proved by recording the width of the diffraction spot for different sample-to-detector distance L_D. The FWHM of the diffraction spot on the detector is expected to be

$$FWHM = \sqrt{a^2 + \left(\left| 2t\theta_B \left(1 + \frac{L_D}{L_S} \right) + 2L_D \frac{\mathrm{t}}{R_{QM}} \right| + l \left| 1 - \frac{L_D}{L_i} \right| \right)^2} \qquad \textit{Equation 9}$$

where t the sample thickness, θ_B the Bragg angle. R_{QM} is the curvature radius of the QM diffracting planes, the signs convention for R_P holds for R_{QM} too. The term $2t\theta_B$ represents the contribution of the sample thickness. The term $2L_D\, t/R_{QM}$ represents the contribution of quasi-mosaicity, which can modify the FWHM of the spot but not the distance L_i. If $L_D = L_S$ it is possible to obtain the formula described by (Neri, 2013) (Guidi V. B., 2013).

In order to verify the effect of the crystal curvature, the detector was positioned at five different points, indicated with P1, P2, P3, P4 and P5 in Figure 3-45, while L_S was kept fixed. L_D was increased by steps of 1.00 m, starting from 2.45 m for P1 to 6.45 m for P5. In Figure 3-45 (c) the widths of the measured diffraction profiles are plotted as a function of L_D, in agreement with their theoretical expectations. The thickness contribution to the FWHM in equation (2) was very small and could not be resolved by the experiment, given the experimental errors. Finally, Figure 3-45 (d) shows the measured diffraction profiles with L_D = 3.45 m (P2).

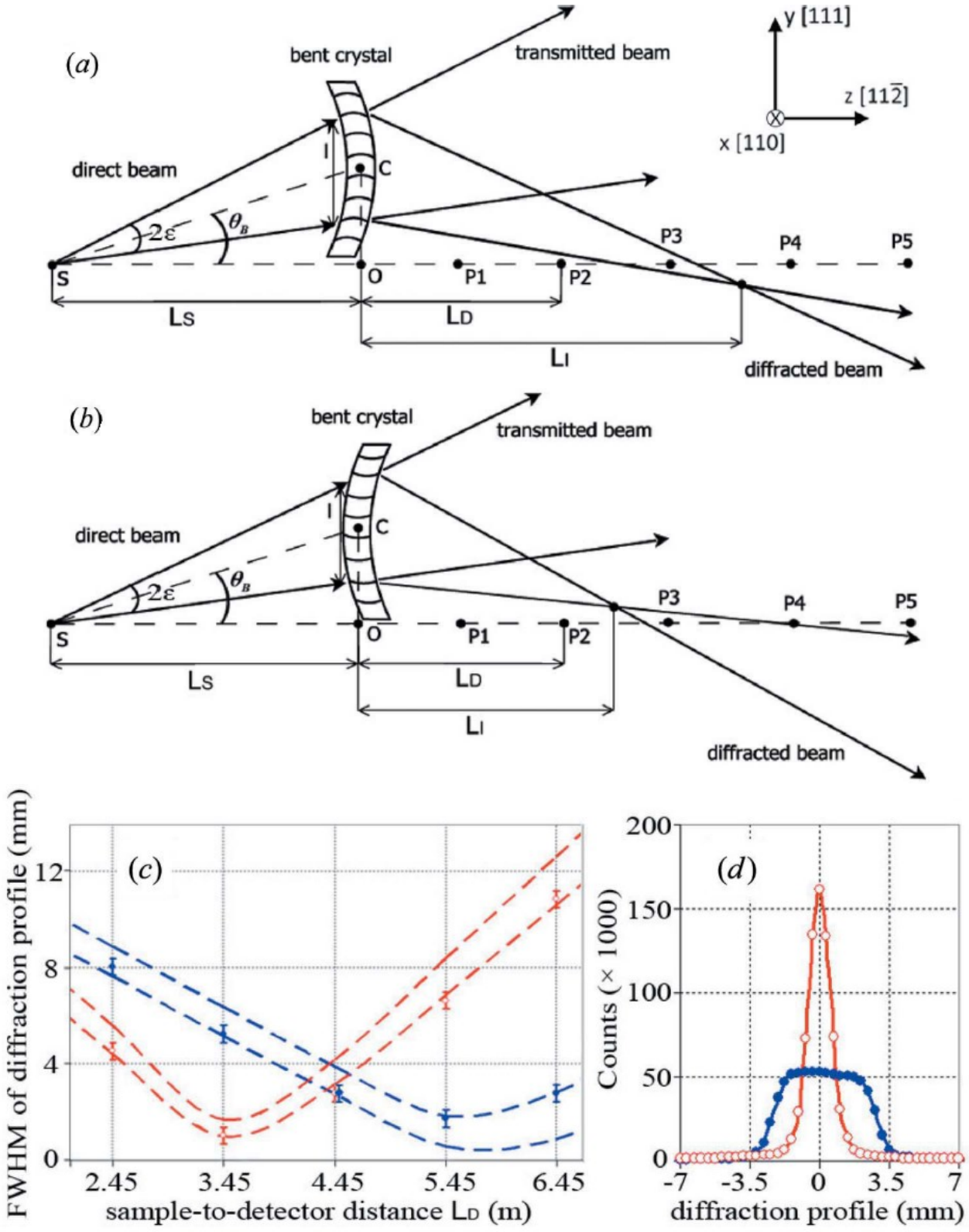

Figure 3-45

Schematic representation of the experiment, consisting in a divergent polychromatic X-ray beam hitting a bent crystal with a QM curvature in symmetric Laue geometry. Depending on the sign of R_P, the image distance increases (a) or decreases (b). (c) FWHM of the diffraction profile plotted as a function of sample-to-detector distance L_D. Blue filled circles plot the measured width related to (a) and red open circles plot the measured width related to (b). Dashed lines enclose the range of the theoretical width calculated by considering the uncertainty over parameters. (d) Diffraction profile with the detector in position P_2 (L_D = 3.45 m). Blue filled circles refer to (a) and red open circles refer to (b).

3.4.3 Tests at LARIX facility

The Ge crystals produced for the Laue project were measured at the LARIX facility of the University of Ferrara (Loffredo, 2005). A Siemens Polymat 50 model X-ray tube with maximum voltage 150 keV produces a polychromatic and wide-divergence X-ray beam. The X-ray tube has a tungsten anode, so the X-ray emission peaks at the fluorescence $K\alpha_1$ line at 59.2 keV. The beam travels across two collimators with adjustable slits. The beam can be as wide as the sample, or it can be limited to a narrow width for limiting the beam divergence. The minimum width aperture for the first and second collimator is 0.3 mm and 0.2 mm respectively. The resulting divergence value was estimated to be 11 ± 2 arcsec by recoding the RC of a perfect Silicon (111) crystal with Darwin width of 0.9 arcsec at 59.2 keV. A motorized crystal holder can be translated along 2 directions perpendicular to the beam and rotated around three orthogonal axes. The accuracies are 1 μm for the translations and 2 arcsec for the rotations. The X-ray beam traverses the sample and it diffracts in Laue geometry. The incident and diffracted beams are recorded with a detector. The LARIX facility employs two different detector: an HPGe spectrometer for local characterization of the samples, or an X-ray imager for recording the whole diffraction image of the samples. The curvature of the samples is tested by two different procedures, which use the HPGe spectrometer or the X-ray imager respectively.

The first method uses a repetitive local characterization of the sample by the HPGe spectrometer. The collimators are used for limiting the beam width to 0.2 mm. The resulting beam divergence of 11 arcsec is too large for testing the QM CDPs of the samples, which have an aperture angle of 4 arcsec. However, the peak of a RC identifies the Bragg angle, so the position of the lattice planes. If the crystal is horizontally shifted perpendicularly to the direction of the incident X-ray beam, the recorded RCs peak at different values of the rotation angle of sample. A linear relation exists between the incident point of the beam on the sample and the rotation angle. The slope of this line is the curvature of the sample (Figure 3-46). All the Ge (111) crystal tiles show a bending radius extremely uniform throughout the crystal, even if in some cases we found a discrepancy between the curvature measured by a profilometer at the LSS laboratory and the curvature measured at the LARIX facility.

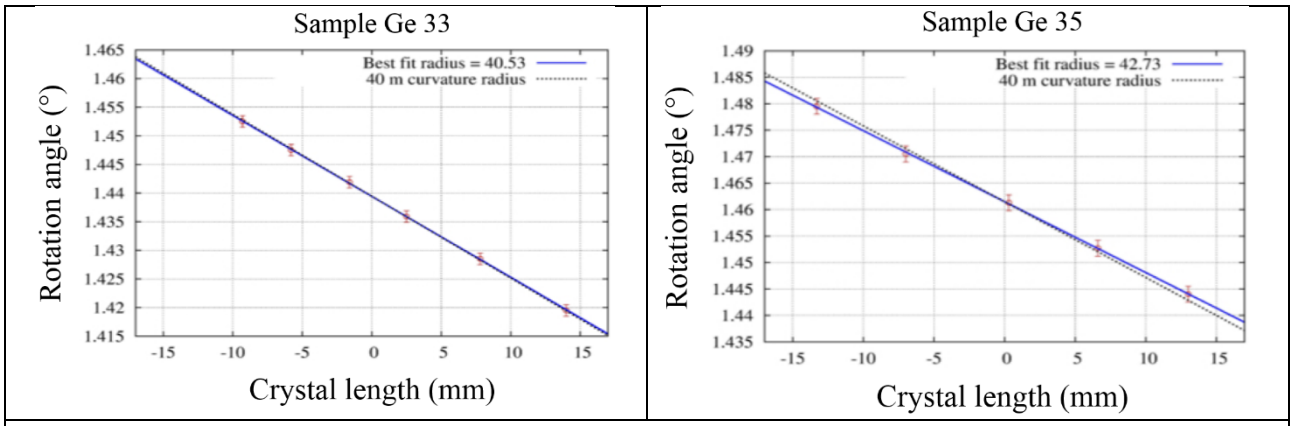

Figure 3-46

Experimental measurement of the curvature of two Ge QM CDPs (111) samples by multiple local characterizations. The radii of curvature attained by fitting the experimental points are compared with the expected radius of curvature of 40 m. The x and y axes show respectively the distance from the center of the crystal (zero), and the rotation angle of the sample required to diffract the 59.2 keV photons.

The second method uses the focusing properties of the crystals to measure their curvature. The collimators are fully opened, so the entire surface of the sample is irradiated. Consider the case of a perfect crystal source-to-sample distance L_S. The diffracted image attains the minimum width when the sample-to-detector distance L_D is equal to L_S. Conversely, a curved crystal can concentrate the diffracted X-rays either at a smaller or at a larger distance, as seen in (3.4.2.2 White-light diffractometer). Indeed, the position of the image becomes

$$\frac{1}{L_i} = \frac{1}{L_S} + \frac{2}{R_P} \qquad \textit{Equation 10}$$

where L_i is the image distance for a crystal bent with primary radius of curvature R_P, diffracting photons at the Bragg angle θ_B. We set the convention $R_P < 0$ when the incoming beam enters the crystal through the concave surface, and $R_P > 0$ in the opposite case. The curvature of the sample was measure by recording the width of the diffraction spot for different sample-to-detector distance L_D, i.e. while moving the X-ray imager along the direction of the beam. The position where the diffraction image attains the minimum FWHM is the image distance L_i (Figure 3-47). The source-to-sample distance L_S is fixed and it is L_S = 25.54 m for the experimental setup. Then, Equation 10 is used for calculating the radius of curvature of the samples. The radii of curvature calculated with the two methods are consistent.

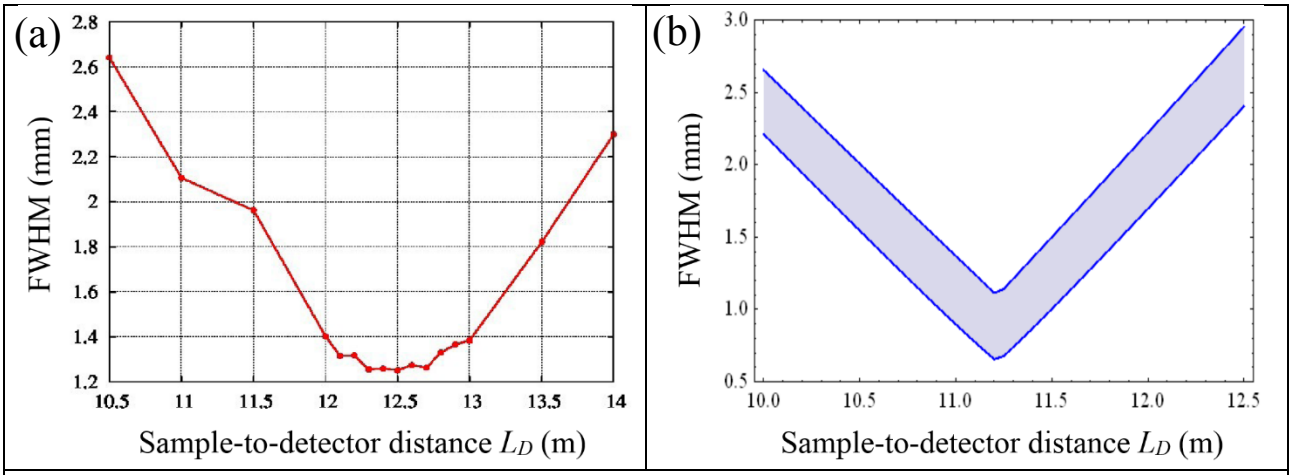

Figure 3-47

(a) Measurement of the FWHM of the diffraction image while moving the detector along the beam direction. The position with minimum FWHM is the image distance L_i. The radius of curvature of the sample is 48.5 m. (b) Expected FWHM of the diffraction image while moving the detector along the beam direction for a sample with radius of curvature 40 m. The blue band takes into account the tolerance of the experimental setup and the tolerance on the sample manufacturing. The tolerance on the radius of curvature of the samples is 5 %.

The width of the image at the position L_i (best focusing position) is a figure of merit for the quality of the crystal. Indeed, Equation 9 calculates the expected FWHM for the diffraction spot on the detector. The FWHM of the samples are compatible with the expectations (Figure 3-47 b). However, the samples shown deformations when they were clamped in the sample holder (Figure 3-48, 3-49) and when they were glued to the frame of the Laue lens (Figure 3-50, 3-51). The mechanical deformations of the samples were very small. However, the focusing properties of the samples are very sensitive to any deformation. Thus, the distortion of the diffraction image was important. Testing the deformation induced by the holding device is straightforward. It was possible to reduce this

deformation by decreasing the strength of the spring that holds the sample in position. However, it was not possible to eliminate this deformation, nor to decrease this deformation under an acceptable limit. A re-design of the holder may eliminate this deformation, but it would not eliminate the deformation due to gluing. The deformation induced by the gluing process was measure by gluing some samples on sheets of carbon fiber. This carbon fiber had the same characteristics of the carbon fiber used for the frame of the lens. Special care was put in using the same quantity of glue needed for the mounting of the samples on the lens frame. Indeed, the holes for the introduction of the glue were manufactured on lens frame during its production. Then, the position of the drop of glue on the samples cannot be changed. As an example, the samples named Ge 66 and Ge 131 were glued on a sheet of carbon fiber (Figure 3-50). The deformation of Ge 66 resulted non-uniform, and its diffraction image shown strong distortion (Figure 3-51 a – b). The deformation of Ge 131 resulted more controlled. Indeed, the diffraction image was not distorted. However, the radius of curvature of the sample changed from 48 m to 59.5 m, as it was measured by the change of the image distance L_i after the gluing process. However, a change in the curvature radius of 24 % after gluing is not acceptable for building a Laue lens. Then, it was necessary to work around the problem of the fragility of the crystals by minimizing any stress on the crystals themselves. It was possible to attain this result by using a slab of perfect Si for bearing the stresses due to holder and gluing. A tile of silicon with thickness 2 mm is glued on the side of the sample without indentations (Figure 3-52 a). The two crystals are glued in a single point near the edge of the crystals, in order to minimize the effects of the deformation induced by the glue. The absorption of radiation for 2 mm of silicon is modest, a few percent at 100 keV. The Si tiles have size slightly larger than the Ge samples, so the holder grabs the Si tile and not the Ge sample. Then, the Si tile is glued to the frame of the lens with a standard quantity of glue. Si has a very high strength, so a tile of Si with thickness 2 mm is very resistant. Therefore, the Si slabs hold the stress that the Ge samples could not bear without deformation. The two crystals are connected by just one point (a drop of glue with diameter about 2 mm), so eventual deformations of the Si slab are not transmitted to the Ge sample. Diffraction images of a stacked sample demonstrate that the sample do not deform during the stacking process (Figure 3-52 b).

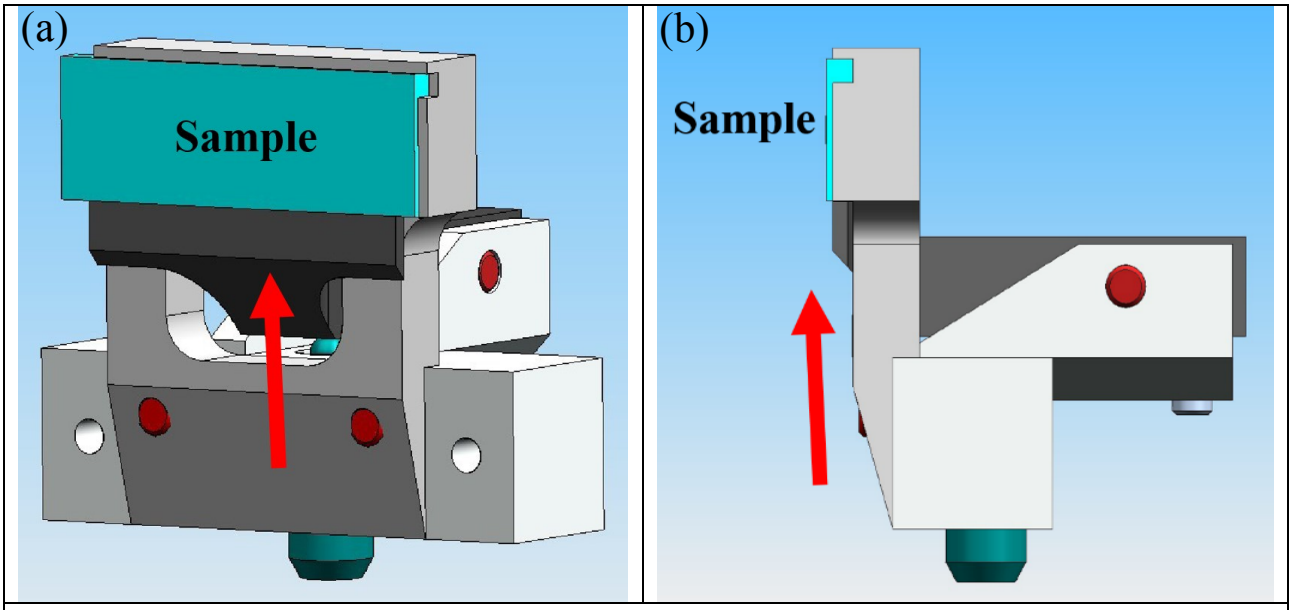

Figure 3-48

Sketch of the sample holder of the robot (Figure 3-3) designed for mounting the crystalline tiles on the frame of the Laue lens. (a) is a front view of the holder, while (b) is a side view of the same. The black part visible in (a) moves following the red arrow to support the sample.

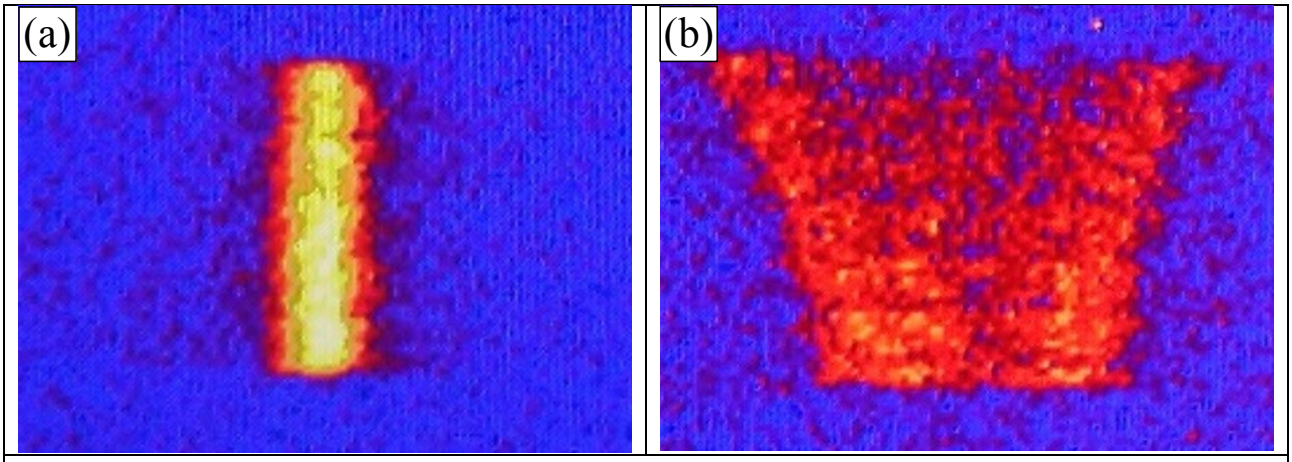

Figure 3-49

Diffraction image of a sample at the best focusing position (a) free from any holding device (b) after being mounted on the holder of the robot as in (Figure 3-48). The holding device deforms the sample and so the diffraction image.

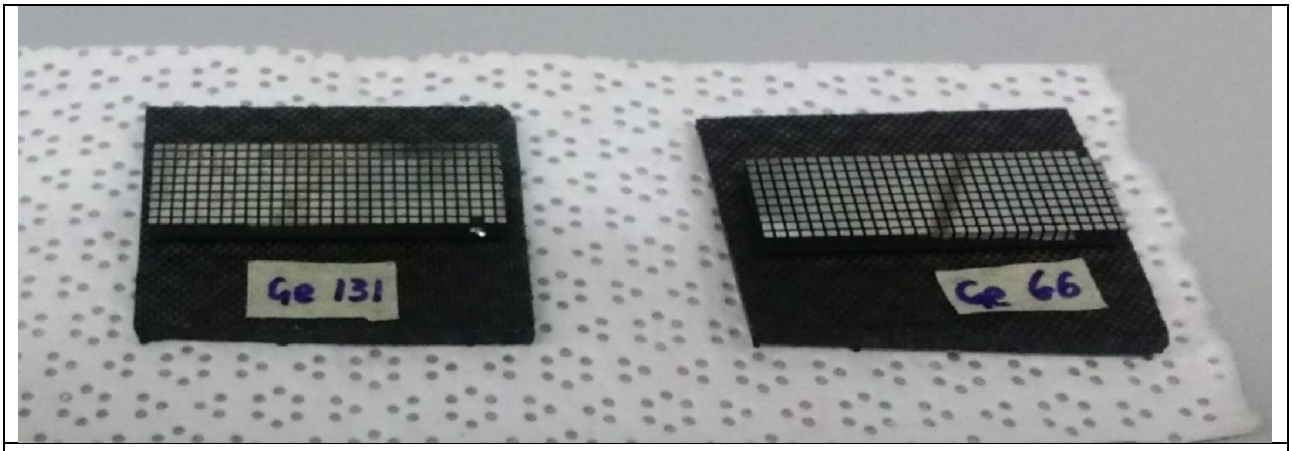

Figure 3-50

Ge (111) CDPs crystals produced by grooving were glued to sheets of carbon fiber of the same thickness and type used in the petal. This test was performed to measure the deformation of the samples after gluing. Samples with radius of curvature far different than 40 m were used for this test to save good samples. The radius of curvature of the samples named Ge 131 (left) and Ge 66 (right) is 48 m.

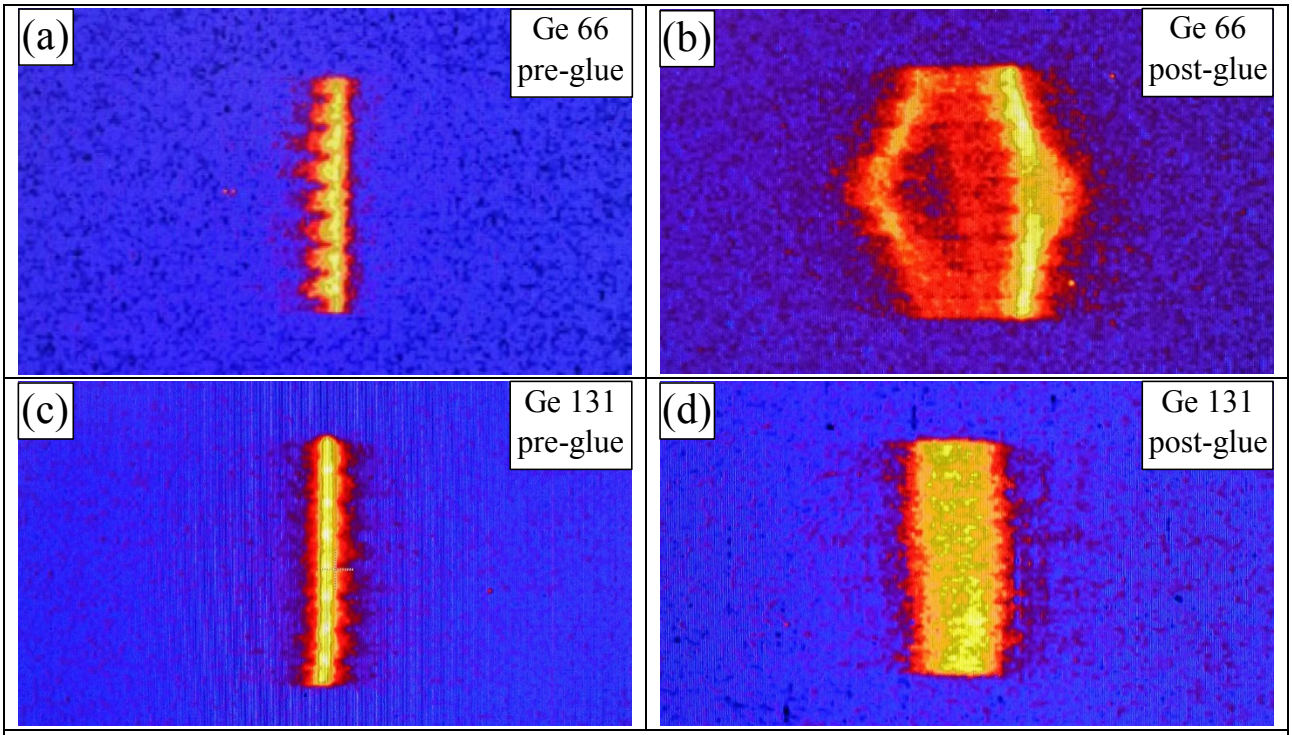

Figure 3-51

Diffraction images for the tested samples before (a)(c) and after (b)(d) the samples were glued on a sheet of carbon fiber. The diffraction images are recorded at the best image distance before the gluing L_i = 12.4 m. The FWHM before the gluing is 1.38 mm for Ge 66 and 1.25 mm for Ge 131. After gluing, the diffraction image of Ge 66 strongly distorts. The diffraction image of Ge 131 enlarges up to a FWHM of 3.85 mm but it does not distort. Indeed, it attains a FWHM of 1.35 mm for L_i = 13.7 m, corresponding to a radius of curvature of 59.5 m.

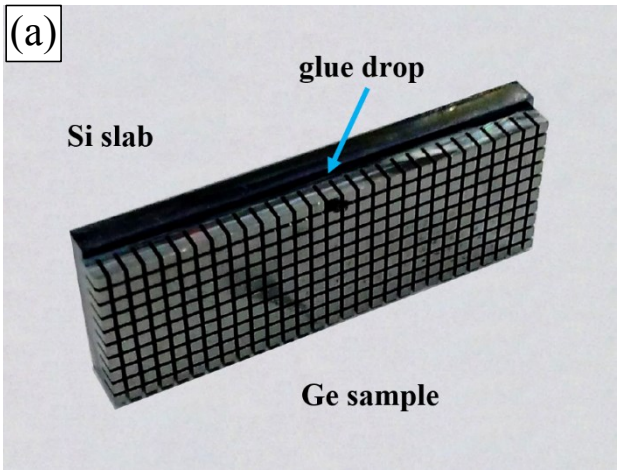

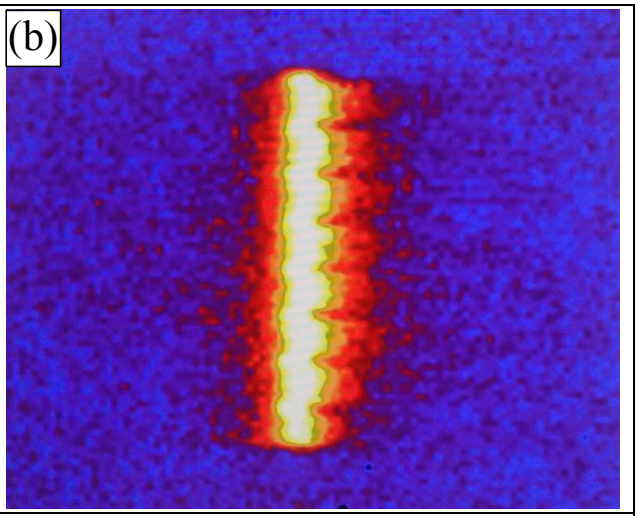

Figure 3-52

(a) Picture of a Ge (111) CDPs grooved crystal stacked on a perfect Si tile. The two crystals are connected by a drop of glue with diameter about 2 mm near the edge of the samples. The Si slab is slightly larger than the Ge sample, it has size 30 × 10.5 × 2 mm^3, so the holder do not touches the sample but the Si slab. (b) Diffraction image of the Ge sample after the stacking process. The FWHM before and after the process were respectively 1.62 mm and 1.61 mm, so the process did not deform the sample.

3.5 Very thick grooved crystals

Application of CDPs crystals for Laue lenses would require crystals as thick as possible. This holds true for both primary and QM CDPs crystals. Indeed, primary CDPs crystals need to be thick to expose a large area to the incident beam. Then, a smaller number of tiles is required to assemble the lens. QM CDPs should be thick as well in order to maximize the passband for photon diffraction. Indeed, an increase in the thickness of QM CDPs crystals leads to a rise of the flux of photons diffracted to the detector. Therefore, the sensitivity of the instrument employing the Laue lens would be enhanced.

Grooving the surface of a crystal proved to be a method to induce a permanent and reproducible curvature in Si and Ge wafers up to the thickness of 2 mm. The grooving method is difficult to apply for thicker crystals. Indeed, bending crystals thicker than 2 mm would require to remove a substantial fraction of the material during the grooving process. Moreover, the material left under the grooves would be a small fraction of the thickness, thus creating a very fragile crystal. Nevertheless, a successful application of the grooving technique to very thick crystals would be a technological advantage in building Laue lenses. The purpose of this section is to test the limit of the grooving method for bending thick crystals.

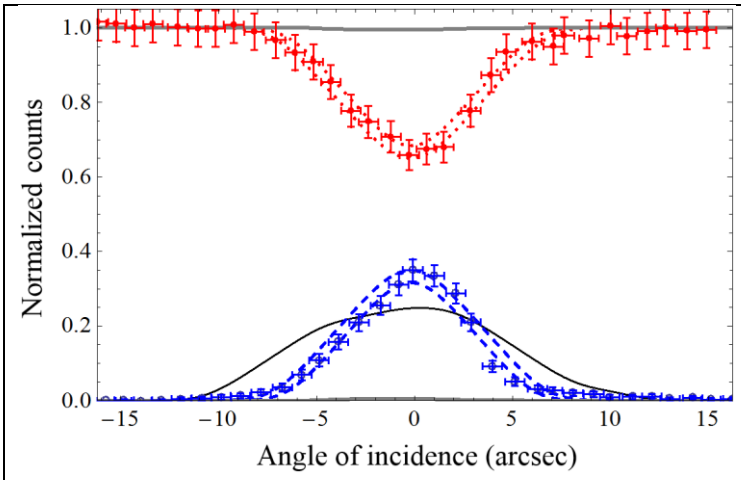

Figure 3-53

RCs of the $(\bar{4}22)$ *diffracting planes of the crystal bent by QM. Filled red circles plot the intensity of the transmitted beam, whereas the empty blue circles plot the intensity of the diffracted beam. Dotted red bands and blue dashed bands represent the fitted result for the transmitted and diffracted beam. Black continuous functions represent the expected intensity of the diffracted beam. The asymmetry in this curve is caused by the grooves, which removed part of the crystalline material. Grey continuous functions represent the expected results for flat diffracting planes. This latter function is almost invisible for the diffracted beam.*

A 5 mm thick pure Si wafer was diced to form a plate using a high-precision dicing saw (DISCO™ DAD3220). The plate dimension was 20 × 10 × 5 mm^3, the main face is oriented as $(\bar{4}22)$, while the 10 × 5 mm^3 face is oriented as (111). The largest surface of the crystal was grooved along one direction, parallel to the dimension 10 mm. The grooves were 4.5 mm deep, and then the material left under the grooves was 0.5 mm. The distance between the grooves was 1 mm, while the width of the grooves was 0.25 mm. Thus, the crystal appeared as an array of lamellae with dimension 0.75 × 10 × 4.5 mm^3 over a base 0.5 thick. The curvature was measured using an optical profilometer (VEECO™ NT1100), resulting in a cylindrical curvature. The primary radius of curvature was R = (23.2 ± 1.2) m over the longest dimension. Then, $(\bar{4}22)$ planes are expected to be bent by QM to a radius of curvature R_{QM} = (81.7 ± 4.1) m, as seen in (4 Innovative crystals for hard X-ray lenses).

The sample was tested through γ -ray diffraction at ILL (Grenoble, France) at DIGRA facility, under a γ-ray beam of energy 181.931 keV and monochromaticity $\Delta E/E \approx 10^{-6}$. Beam divergence after the Si (220) monochromator was 1 arcsec, as measured by recording a rocking curve (RC) of the monochromator itself. Collimated-beam size dimension was 1 mm on the diffraction plane (yz) and 5 mm on the plane (xz), z being the direction of the beam. Characterization of the sample was carried

out by performing RCs. The measured angular distribution consisted of the convolution between the portion of primary curvature, as seen by the beam, and the secondary curvature. The primary curvature seen by the beam was calculated from the width of the collimated beam (1 mm) and the primary radius of curvature. The divergence of the beam was also included, by convolving the obtained distribution with a Gaussian of $\sigma = 1$ arcsec. Finally, a morphological factor was included to consider the part of the sample that cannot diffract, i.e., the portion of material removed during the grooving process.

The RC profile of the $(\bar{4}22)$ planes had a passband width smaller than expected (Figure 3-53). However, the diffraction efficiency and the curvature radius of $(\bar{4}22)$ planes were fitted from the experimental data (Table 3-2). The QM radius of curvature resulted smaller than expected. A possible explanation is the difficulty of the curvature to propagate through so thick lamellae, which are nearly divided from each other. However, the RC profile was smooth and symmetric, and it was far different from the profile for flat planes. Indeed, the fitted QM curvature was still 45 % of the expected curvature. This sample proves that the grooving method can induce a QM curvature in thick crystals, even if this curvature partially relaxes.

Lattice plane	R_{QM} (m)	Aperture (arcsec)	Diffraction Efficiency
$(\bar{4}22)$ Expected	81.7 ± 4.1	13.2 ± 0.7	0.31 ± 0.05
$(\bar{4}22)$ Fitted	170.8 ± 8.5	6.0 ± 0.3	0.55 ± 0.05

Table 3-2

Expected and fitted parameters for the $(\bar{4}22)$ planes bent by QM. The aperture angle and the diffraction efficiency were left as free parameters in the fitting. Both resulted compatible with a radius of curvature of 170.8 m over a thickness of 5 mm.

The primary curvature of the sample was tested by taking a RC profile of the (111) planes. The beam passed through the 20 mm dimension and through the grooves. A primary radius of curvature of 23.2 m over a thickness of 20 mm results in an expected aperture angle of 178 arcsec. A uniform and broad box-shape RC with diffraction efficiency peaking at 0.23 is expected for the sample. Conversely, the measured RC has the shape visible in Figure 3-54. Multiple peaks appear, even if they are not well distinguishable one from the other. Diffraction efficiency is far lower than expected, with the highest peak approaching 0.1. The passband width is smaller than expected. This RC reveals a strong degradation in the crystalline

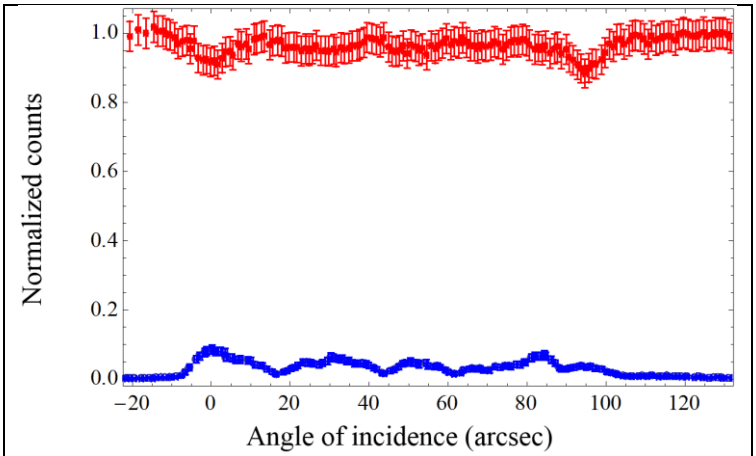

Figure 3-54

RCs of the primary bent (111) diffracting planes of the crystal. Filled red circles plot the intensity of the transmitted beam, whereas the empty blue circles plot the intensity of the diffracted beam. Different peaks are visible, probably due to the different diffraction properties of the lamellae due to the degradation of the lattice quality.

material. Indeed, previous experiments revealed degradation of the lattice quality of the material between the grooves for diffraction by primary CDPs (3.3.2 Early experimentation with primary CDPs crystals). This process is taken to the extreme consequences in the sample analyzed in this section. Indeed, diffraction efficiency is so degraded that some lamellae produce a very small diffraction response, thus creating depths in the RC profile.

The (111) planes were also tested in the direction were no curvature is present. A RC profile was recorded while the beam passed through the 10 mm dimension (Figure 3-55). The resolution of the experimental setup is larger than the Darwin width of (111) planes at the energy of the experiment δ_W = 0.29. Thus, a RC of Gaussian shape is expected. The peak reflectivity of the measured RC is compatible with the expectation. However, the profile is far larger than expected. The experimental points were fitted with the expected RC profile for a mosaic crystal with unknown mosaic spread. The diffraction profile of a mosaic crystal with mosaicity 7 arcsec turned out to fit well the experimental points. The RC in Figure 3-54 highlighted degradation in the crystalline material, but this degradation was not quantitatively measurable. In fact, diffraction planes were expected to be uniformly bent, and it is not easy to predict how CDPs degrade because of crystalline imperfections. Instead, the lattice planes for the RC in Figure 3-55 were expected to be flat, and it is relatively easy to quantify how perfect flat planes degrade. Thus, the RC in Figure 3-55 allows to quantitatively estimating the lattice degradation as a mosaicity of 7 arcsec. Figure 3-55 allows to quantitatively estimating the lattice degradation as a mosaicity of 7 arcsec. A question rising from the analysis in this section is why $(\bar{4}22)$ planes seem less touched by the degradation of the lattice perfection due to the severe grooving. In fact, it appears there is a directionality in the dislocations. This result may be explained by the type of damaged dealt by the grooving process. In fact, the directionality of the dislocations seem to follow the rotation of the diamond blade used for grooving. If this holds true, dislocations should cause a misalignment as a rotation over the $(\bar{4}22)$) planes. Then, the $(\bar{4}22)$ planes are unaffected, while the orthogonal planes as (111) are affected.

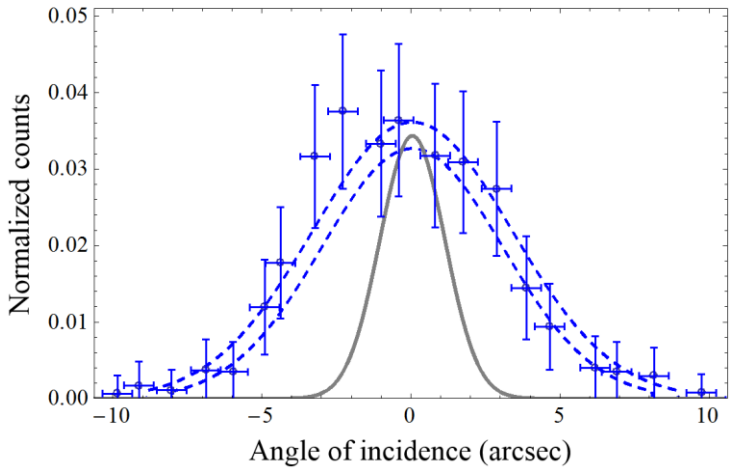

Figure 3-55

RC of the (111) diffracting planes of the crystal through the direction where no curvature is present. Empty blue circles plot the intensity of the diffracted beam. Grey continuous functions represent the expected results for flat perfect diffracting planes. Blue dashed bands represent the fitted result for the diffracted beam considering a mosaicity of 7 arcsec.

Another question rising from the analysis is why the $(\bar{4}22)$ planes maintain a large portion of the impressed curvature, while the grooved (111) planes do not the same. The explanation may be two-fold. First, we know that the un-grooved part of the sample (i.e. base) is cylindrically bent because it was measured by profilometry. The $(\bar{4}22)$ planes are connected to the base, therefore the primary curvature induces QM curvature in the $(\bar{4}22)$ planes. Contrary, the (111) planes between the grooves are not connected to the base, therefore they are less and less affected by the primary curvature moving far from the base. Moreover, cylindrically bent (111) planes induce a QM cylindrical curvature in $(\bar{4}22)$ planes, but the opposite is not true. Indeed, the main face of lamellae

is $(\bar{4}22)$ and lamellae are cylindrically bent, but a curvature is not induced in the orthogonal (111) planes

A Si slab 5 mm thick was bent by the grooving process and it was tested in this section. The primary curvature resulted uniform by profilometric analysis. The principal diffraction planes of the sample were tested by performing RCs. Lattice planes bent by QM showed a high diffraction efficiency and they resulted uniformly curved, even if this curvature was smaller than expected. Conversely, the diffraction properties of the primary bent planes were strongly deteriorated. This sample may be used as a focusing QM CDPs crystal, but not as a primary CDPs crystal. Moreover, even if the curvature of QM bent planes was uniform, its magnitude was hardly controllable by the manufacturing process. Then, it may be preferable to develop alternative methods to induce a self-standing curvature in crystals with thickness above 2 mm.

4 Innovative crystals for hard X-ray lenses

This section of the thesis focuses on technological development and production of innovative crystals for the construction of hard X-ray lenses. The construction of Laue lenses has been simplified with the introduction of focusing crystals within the LAUE Project (3 The Laue Project). However, the work on crystal for Laue lenses did not end with the LAUE Project, but it continued with a series of technological innovations with the aim to increase the maximum resolution and sensitivity achievable by Laue lenses. These innovations include the introduction of crystals with multiple curvatures and new focusing crystals, the study of novel methods with which to produce crystals with CDPs, the construction of stacks of multi-crystals, the use of curved asymmetric diffraction planes. The experimental tests were performed at the facilities of ESRF (European Synchrotron Radiation Facility, Grenoble, France), ILL (Institut Laue-Langevin, Grenoble, France).

4.1 Crystals with non-standard quasi-mosaic reflections – (422) and (311)

Current applications about QM crystals take advantage of interaction with (111) planes because such planes have the highest electronic density, which brings to high diffraction efficiency. Indeed, the (111) planes are not the only ones undergoing the QM effect. As an example, in (Guidi V. M. A., 2009) it was proposed that bending of (211) planes results in high-efficiency steering of negatively charged particle via axial channeling. Diffraction by (211) planes is forbidden, so (422) planes are commonly used. The quasi-mosaic effect can also affect the (311) lying of planes, which are among the most efficient planes for diffracting X-rays. If such crystals were applied to build up a Laue lens in combination with already existing (111) QM crystals, an extension of the lens area may be achieved. Indeed, planes (111), (311) and (422) can diffract photons of the same energy at very different Bragg's angles. This means that (111), (311) and (422) QM crystals placed in different positions could be arranged to build up a Laue lens, featuring significant enhancement of the area undergoing diffraction.

Type of curvature	Spherical	Cylindrical	Cylindrical
Primary surface	(211)	(111)	(211)
QM diffraction planes	(111)	(422)	(311)
R_P/R_{QM} (Si)	- 0.38	0.28	0.29
R_P/R_{QM} (Ge)	- 0.42	0.31	0.32

Table 4-1

Quasi-mosaicity occurs in different conditions for different lying of planes. (111) are bent by QM when a crystal with (211) primary surface undergoes a spherical curvature. (422) and (311) are bent by QM when a cylindrical curvature affects a crystal with primary surface (111) and (211) respectively. The ratio between the primary and QM radii of curvature change for each case.

In Figure 4-1 is shown the theoretical diffraction efficiency of Si and Ge crystals, by taking into account a QM angular spread of 5 arcsec, that is the average value for QM crystals 2 mm thick. Diffraction efficiency of planes with high crystallographic indices is lower with respect to that for low indices. However, (422) and (311) crystals can be arranged in the outermost part of a lens because of the larger Bragg angle. Indeed, the distance r from the axis of the lens at which a crystal can diffract the radiation onto the detector is proportional to the Bragg angle, i.e. r depends on the crystallographic planes used for diffraction. Using the approximation for small angle, it is $r = f\ tan(2\theta_B) \propto \sqrt{h^2 + k^2 + l^2}$ where (h, k, l) are the Miller indices of the planes used for diffraction. Even if the diffraction efficiency for such planes is lower than for (111) ones, the external position guarantees a large geometric area, resulting in a large effective area.

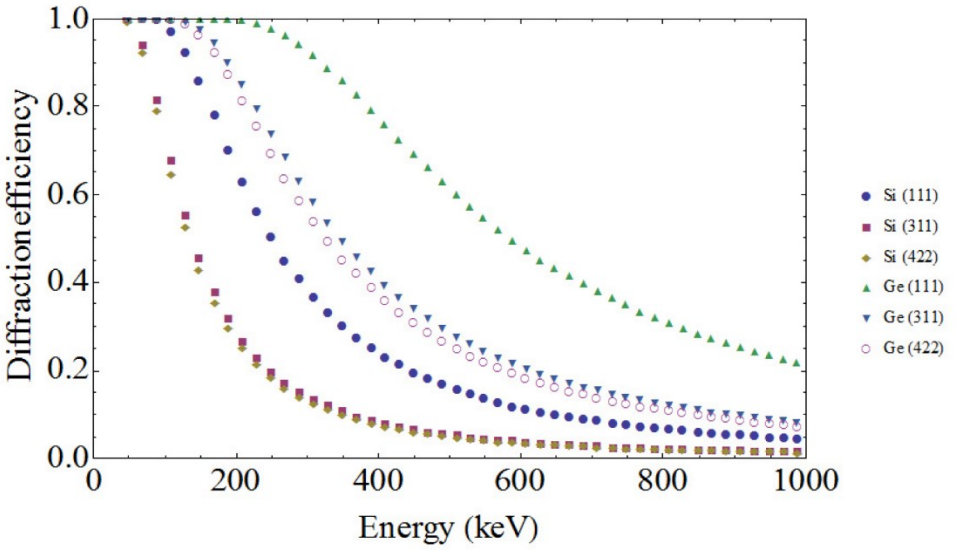

Figure 4-1

Theoretical diffraction efficiency for CDPs with different lying of planes. The thickness traversed by the beam was set to be 2 mm, the angular spread 5 arcsec, then the curvature radius was 82.5 m.

A QM crystal implementing (422) diffraction was tested by X-ray diffraction in transmission geometry at the Institut Laue-Langevin (ILL, Grenoble, France) at DIGRA facility. A permanent cylindrical curvature was induced to the sample by the method in (Bellucci V. C., 2011b). Tile size was 100 mm × 20 mm × 3 mm, primary radius of curvature was (21.2 ± 1.1) m as measured by an interferometric profilometer, the QM radius of curvature was (74.6 ± 3.7) m leading to an angular aperture of 8.3 arcsec. X-ray beam energy was E = 181.931 keV with monochromaticity $\Delta E/E \approx 10^{-6}$, the beam divergence was 1 arcsec. Collimated-beam size was 0.4 mm on the diffraction plane and 3 mm on the perpendicular plane. Characterization of the samples was carried out by performing RCs. Thus, the photon beam hit the $(\bar{1}11)$ surface of the sample and underwent diffraction

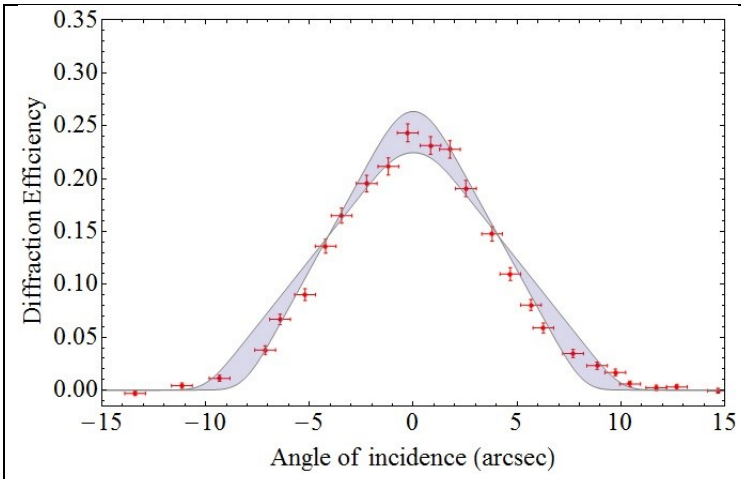

Figure 4-2

Experimental and theoretical RCs of (422) Si CDPs bent by QM. Red crosses plot the intensity of measured diffracted beam with their uncertainty bar. The gray area represents the expected result as calculated by taking into account the experimental uncertainties.

by bent (422) planes. Diffraction efficiency was measured on the center of the sample and its RC is reported in Figure 4-2. In the theoretical expectation (gray area) both primary and secondary curvatures were accounted for. From the theory of elasticity, the ratio of QM curvature, R_{QM}, to the primary one, R_P, is fixed at $R_{QM}/R_P = 3.518$ for Si (422). The angular distribution after diffraction consists in the convolution between the distribution due to the portion of primary curvature seen by the beam, the distribution due to secondary curvature, and the divergence of the beam represented by a Gaussian distribution of σ = 1 arcsec. Figure 4-2 highlights very good agreement between theoretical expectation relying on quasi mosaicity and experimental results.

Then, a QM crystal implementing (311) diffraction was produced at SSL by the grooving method and analyzed at the ILL-DIGRA facility. Tile size was 15 mm × 15 mm × 2 mm, primary radius of curvature is (25.0 ± 1.2) m as measured by an interferometric profilometer, the QM radius of curvature was (86.4 ± 4.3) m leading to an angular aperture of 4.8 arcsec. The grooves were manufactured in such a way to obtain a cylindrical curvature of the sample, i.e., only along the x axis. In this case, the collimated beam size was 1×1 mm^2. Characterization of the sample was carried out by performing RCs. The diffraction efficiency was measured at the center of the samples and the pertaining RC are reported in Figure 4-3. Also in this case the RC is the result of the convolution of three effects: the QM curvature, the primary curvature, and the divergence of the X-ray beam. Experimental results agree with expectations also in this case.

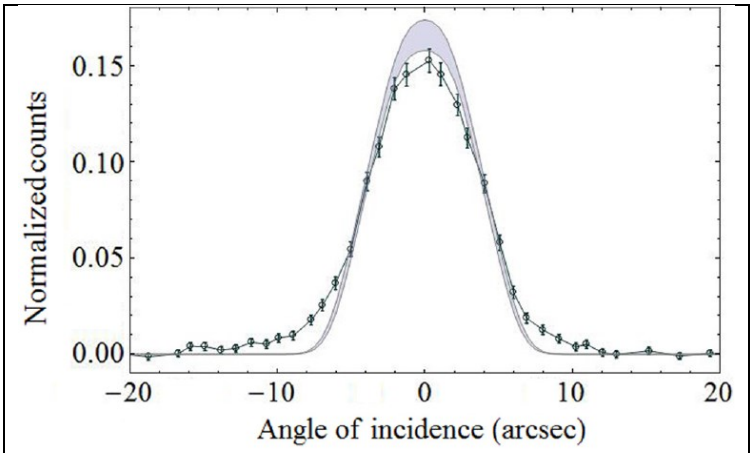

Figure 4-3

Experimental and theoretical RCs of the (311) QM CDPs. a) The blue empty circles plot the intensity of measured diffracted beam with their uncertainty bar, whereas the gray area represents the expected result as calculated by taking into account the experimental uncertainties.

First, a possible scheme for a Laue lens composed by Si and Ge QM tiles implementing (111) and (422) diffraction planes was designed through Monte Carlo simulation and analytical modeling. An incoming photon beam with uniform energy distribution in the range 100–300 keV (the energy of the Laue project) has been considered. The lens was chosen to have a focal distance of f = 20 m, thus the primary radius of curvature of the tiles must be R_P = 40 m. In this simulation, the crystals were chosen to have all the same tile size $L_P \times L_{QM} \times T_0$ with L_{QM} = 1 cm, L_P = 2 cm, T_0 = 5 mm. This tile size reduces the blank space between tiles, while T_0 is chosen in order to guarantee high reflectivity. Large values of T_0 lead to higher reflectivity and lower spatial resolution on the focal plane, while smaller values of T_0 decrease the reflectivity but increase the focusing capability. We considered the crystal tiles to be disposed as concentric rings onto the spherical calotte of a Laue lens with a focal distance f. The lens is composed of 100 rings, the inner radius of the lens resulted 0.25 m, while the outer radius was 2.25 m. In the small-angle approximation, the energy passband of a crystal in a ring is given by $\Delta E \simeq 2\Omega_P E f/r$ where r is the radius of the ring, Ω_P is the bending angle induced in the tile by primary curvature and E the mean energy diffracted by the ring. This latter depends on the crystal reflection planes as $E = \frac{hc}{2d_{hkl}\sin\left[\frac{1}{2}\tan^{-1}(r/f)\right]} \simeq 12.4\frac{f}{d_{hkl}r}$

The effective area of an instrument is an important parameter to quantify the number of photons the lens can focus under exposure to a certain photon flux. As for any tile in the lens, the effective area at a given energy is defined as the geometric area exposed to the photon flux, by the reflectivity of the tile at the energy of interest. Because of the finite angle Ω_{QM} exposed to photon flux, just a part of the tile is capable of diffracting a certain photon energy. The effective area of the whole lens is the sum of the effective areas of the tiles composing the lens. The effective area for each tile is:

$$A_{eff}^{tile}(E) = r_{QM}(E) \cdot A_{geometric}^{tile} = r_{QM}(E) \cdot L_{QM} R_P \Omega_{QM}$$

Another quantifier of the focusing capability of an instrument is the focusing factor G, defined as

$$G = f_{ph} \frac{A_{eff}}{A_d}$$

where A_{eff} is the effective area of the lens and A_d is the area of the focal spot which contains a fraction f_{ph} of photons reflected by the lens. Physically, it represents the number of photons enclosed in a focal spot of radius R_{spot}, divided by the area of the focal spot, and normalized with respect to the photon flux impinging on the lens. The radius of the focal spot R_{spot} was fixed at 4.64 mm in order to enclose f_{ph} = 90% of the diffracted photons, cutting the tails of the distribution (Figure 4-4). The lens was designed to have an effective area as smooth as possible with respect to an energy variation (Figure 4-5). Focusing factor was also simultaneously maximized, in order to enhance resolution and sensitivity of the lens (Figure 4-6).

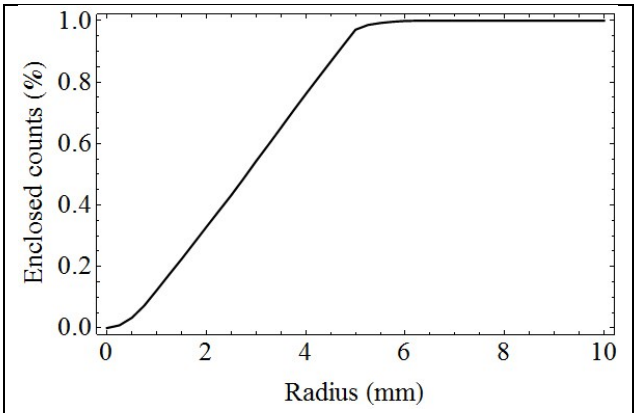

Figure 4-4

Fraction of enclosed photons vs. radius of the focal spot enclosing the photons on the focal plane. The radius corresponding to 90 % of the enclosed photons was chosen for the simulation in order to cut the tails of the focal distribution R_{spot} = 4.64mm.

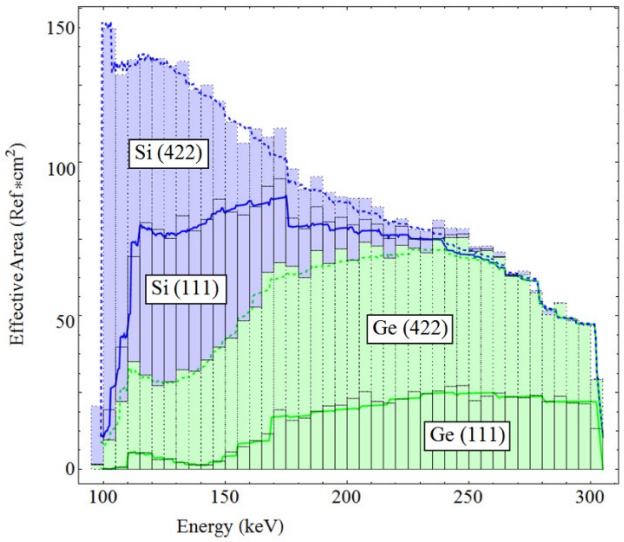

Figure 4-5

Effective area per unit energy of the lens composed of (111) and (422) QM crystals. The contributions of the tiles of different species is visible. Tiles were positioned in the lens in order to maximize effective area in the energy range 100–300 keV and made the profile as smooth as possible with respect to the energy variation.

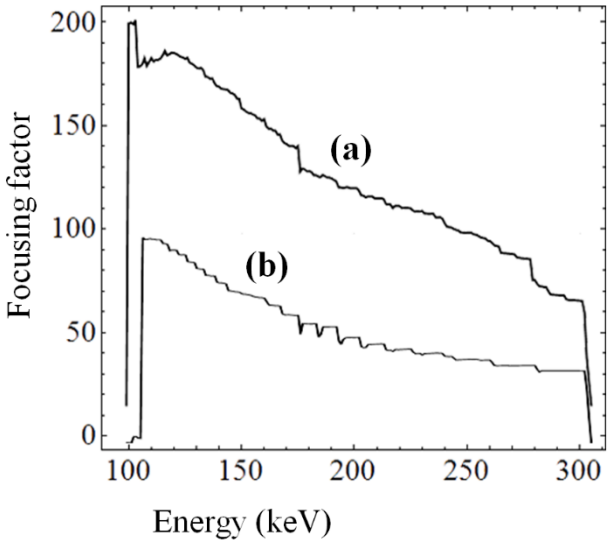

Figure 4-6

(a) Focusing factor of a lens compose by QM (422) and (111) crystalline tiles, or (b) composed by QM (111) tiles only, in the energy range of the lens 100–300 keV.

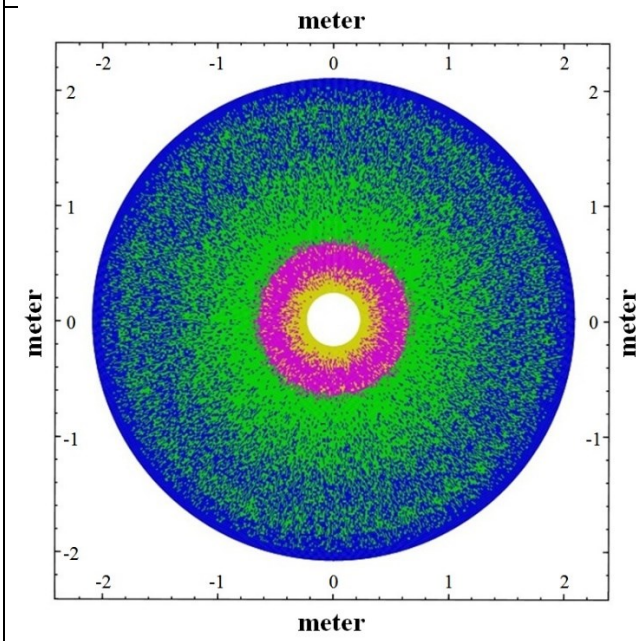

Figure 4-7

Arrangement of crystalline tiles over the calotte of the simulated Laue lens composed of (111) and (422) QM crystals. Yellow rectangles in the inner part of the lens represent Ge tiles implementing (111) diffraction, while fuchsia rectangles of the second corona from the center stand for Si tiles implementing (111) diffraction. Green and blue rectangles in the third and fourth corona from the center respectively represent Ge and Si tiles having (422) diffraction planes.

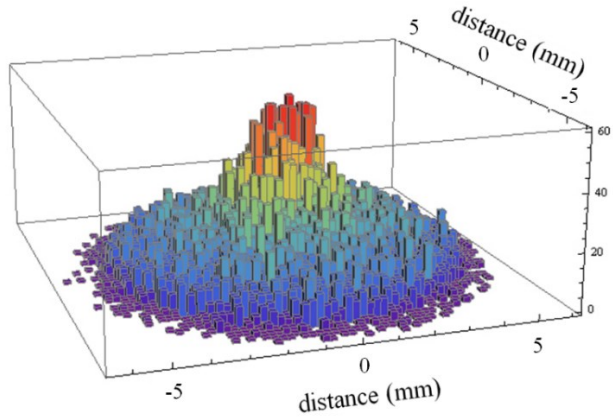

Figure 4-8

Photon distribution onto the focal plane of the lens composed of (111) and (422) QM crystals in arbitrary units. Concentration of photons is high in the focal point and rapidly decreases far from the center.

Figure 4-7 shows a possible arrangement of QM tiles in the designed Laue lens. Diffraction from (422) planes occurs at a Bragg angle much larger than in the case of (111) planes at the same energy. Thus, tiles implementing (111) diffraction planes occupy the innermost part of the lens, while (422) tiles occupy the outermost region. The reflectivity for (422) planes is lower than for (111) planes, but the external position guarantees a larger geometric area, resulting in a larger effective area. Thus, we demonstrated that exist new locations where to place the tiles in a Laue lens, allowing a wider selection of crystals to focus photons with the same energy. Moreover, this configuration works with Ge and Si crystals distinctively owing to their different Bragg angle, allowing still more locations for crystalline tiles. For each orientation Ge and Si tiles are used with Ge at lower radius. The major contribution to the effective area is provided by the tiles using (422) diffraction (Figure 4-5). Si provides the largest part of effective area at low energies as expected by a light material. Ge tiles, being composed of a material with higher atomic number, maximize their reflectivity for high energies, providing the largest part of effective area in this zone. For the sake of comparison, we simulated the performance of a Laue lens built up by solely Si and Ge QM (111) tiles and optimized for the purpose. Dimension of QM tiles is the same as well as curvature radius and energy passband of the lens. A lens made of (111) QM crystals results in a smaller effective area and a smaller focusing factor, as visible in Fig.6. The focusing factor of a lens implementing both species of QM crystals is about the double of a lens implementing only (111) QM crystals. In summary, building up a lens with improved performance by the use of QM (422) diffraction planes can be envisaged.

Then, a Laue lens featuring all the three QM orientations (111), (311) and (422) was simulated. The building parameters of the crystalline tiles and of the lens are the same, but the QM (311) crystals are also included. As expected, the effective area results higher than in the previous scenario (Figure 4-9). Indeed, exploiting (111), (422) and (311) diffracting planes would permit the fabrication of a Laue lens with the geometric area one order of magnitude larger than for a lens solely composed of (111) QM crystals. Finally, the performance of the lens has been expressed in terms of the most often acknowledged quantifier recognized by the community of astrophysicists, namely the sensitivity, that is, the lowest flux detectable with n_σ = 3 sigma significance, for the cases of continuum-line emissions, i.e. $\Delta E/E$ = 1/2. As before, R_{spot} was fixed at 4.64 mm in order to enclose f_{ph} = 90% of the diffracted photons (Figure 4-4). The background B was 1.5×10^{-4} $ph/(cm^2 s\ keV)$ constant over the considered energy range. The sensitivity $S(E)$ was calculated as follows:

$$S(E) = \frac{n_\sigma}{G(E)} \sqrt{\frac{B}{\pi R_{spot}^2 \Delta T E/2}}$$

where ΔT is the exposure time. The result is shown in Figure 4-13, which is in line with the sensitivity of the proposed Laue lens for other Laue lens proposals, such as the Gamma Ray Imager (GRI) (Knodlseder, 2009). Indeed, the strong focusing exerted by the QM effect abundantly compensates for the smaller effective area of the QM-based Laue lens. In fact, the property of QM crystals to focus on a spot smaller than the size of the diffracting crystals raises the sensitivity of the lens. Another advantage of the proposed lens is the short focal length that allows the lens to be accommodated in one spacecraft only despite its relatively large diameter. Moreover, the light materials composing the crystals result in a modest weight (284 kg) for the lens.

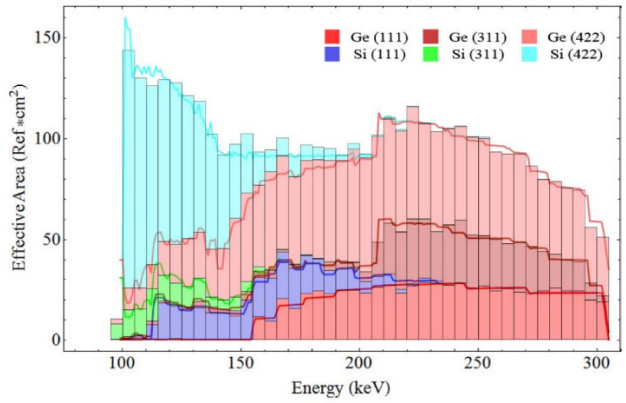

Figure 4-9

Effective area per unit energy of the lens composed of the three species of QM crystals. The contributions of the tiles of different species are visible. Tiles were positioned in the lens to maximize effective area in the energy range 100-300 keV and made the profile as smooth as possible with respect to energy variation. The histogram is calculated analytically, while the continuous lines are calculated with a Monte Carlo simulation.

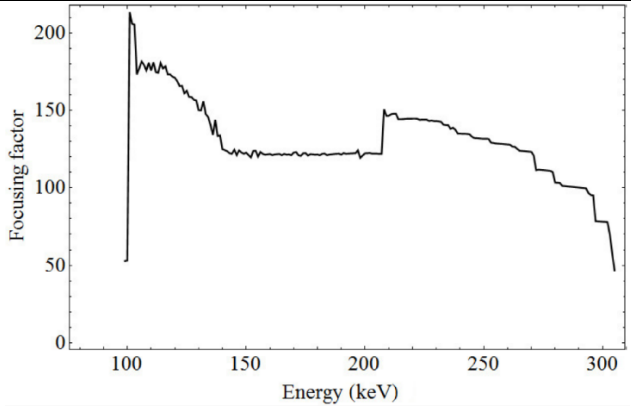

Figure 4-10

Focusing factor of the simulated lens composed of the three species of QM crystals in the energy range of 100-300 keV.

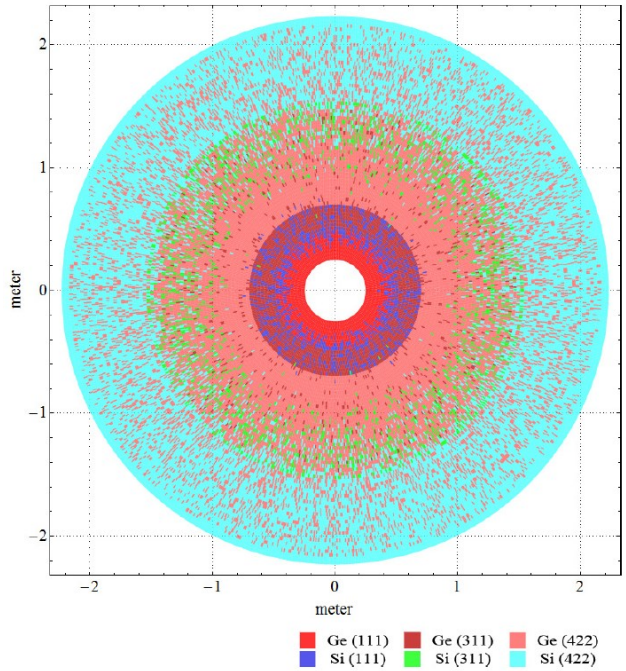

Figure 4-11

Arrangement of crystalline tiles over the calotte of the simulated Laue lens composed of the three species of QM crystals. The legend describes the diffracting plane employed.

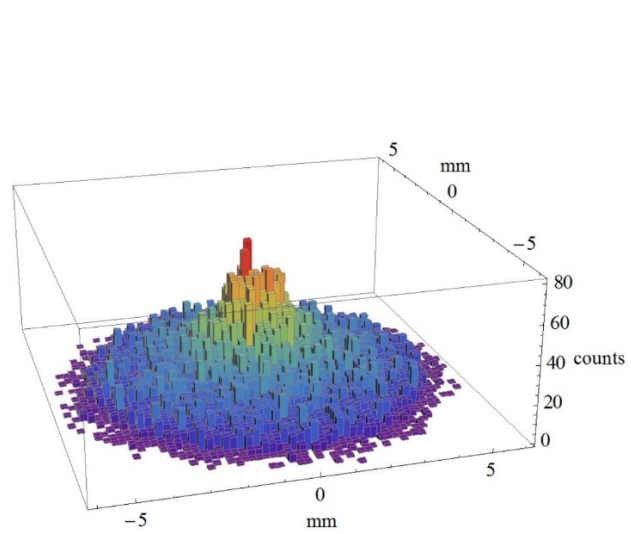

Figure 4-12

Photon distribution onto the focal plane of the lens composed of the three species of QM crystals in arbitrary units. Concentration of photons is high in the focal point and rapidly decreases far from the center.

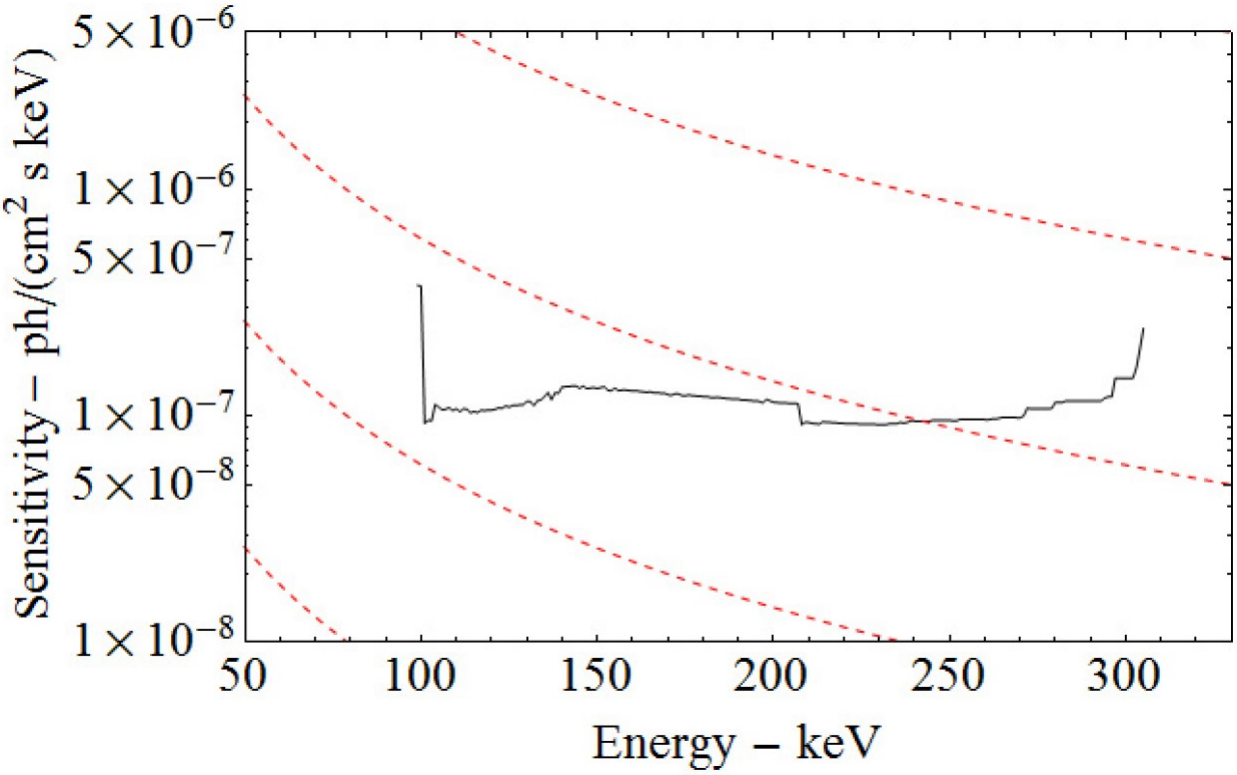

Figure 4-13

Predicted 3σ detection sensitivities for continuum emission, assuming an exposure time of 100 ks and ΔE/E = 1/2. The background was set at 1.5 × 10^{-4} ph/(cm^2 s keV).

4.2 Tensile films for producing CDPs crystals

Crystals with a self-standing curvature are a requirement for building a Laue lens, since the use of holders to induce a curvature is not possible. In fact, Laue lenses for astronomical observation need to be light-weighted, as the observation of celestial X-ray sources is possible only out of the atmosphere, i.e. on satellite-borne experiments. Laue lenses for medical imaging need to be small because of their short focal lengths, so that the diffracting elements need to be very close-packed. Crystals with self-standing curvature do not need any holding device for bending, so they simplify the implementation of the two main applications of a Laue lens. Although for applications of X-ray concentration self-standing bent crystals are mandatory, so far the manufacture of self-standing bent crystalline plates is a technological problem yet to solve. Indeed, no manufacturing process has been able to bend a macroscopic crystalline plate with an important and uniform curvature without side problems. Mechanical holders are generally used for bending macroscopic objects, but they cannot be used when the weight or the space occupied by the holder is an issue. Thermal gradients have been applied to perfect single crystals to obtain a bending (Smither et al., 2005), but this method is energy consuming and not suitable to a space-borne observatory. A crystal having curved diffracting planes can also be obtained by concentration-gradient techniques, i.e., by growing a two-component crystal with graded composition along the growth axis (Keitel et al., 1999; Abrosimov, 2005; Erko et al., 1996), but the crystalline quality is usually poor. A self-standing curved crystal can also be obtained by a controlled surface damage through a mechanical lapping or grooving process performed on one side of a crystal (Ferrari et al., 2013, Bellucci et al., 2011a; Camattari et al., 2013b), as we saw in (3.3.1 The indentation method). However, these techniques it is difficult to obtain bent samples thicker than 1 - 2 millimeters, and the process causes several crystal damages within the sample. As the last two methods, temperature molding has been used for inducing a permanent bending in crystals, but it degrades the crystalline quality of the object. In this part of the thesis, we develop innovative techniques to produce self-standing bent crystals. They consists in the deposition of tensile films on the surface of the crystal plates, or in the growing of tensile films in the crystal itself.

4.2.1 Thin films

The deposition of thin films may be a viable technique to obtain self-standing bent crystals with a controlled and uniform curvature. The curvature induced by film deposition is already well-known in the electronics sector as a drawback of device manufacturing. The stress due to deposition of the most common materials has been measure, and it is usually minimized during device manufacturing. This stress can be maximized with a different application of the knowledge of the processes.

	Nitride	Si amorphous	SiO2 deposition	Metal (Al)	C	CSi	Ge	SiO2 growth
Thickness range (μm)	0.01 – 0.45	0.1 – 10	0.05 – 15	0.05 – 15	0.05 – 15	0.01 – 2	0.05 – 15	0.05 – 15
Film stress (MPa)	+800	-1200 - +500	+250	+10 – +50	-1000	-1000	-300	-320
Radius of curvature (m)	+43	-30/+70	+138	+3450 – +690	-34.5	-34.5	-115	-108

Table 4-2

Properties of the most common materials used for deposition. The first line shows the typical deposited thicknesses. The second line shows the stress of the deposited film. The third line shows the radius of curvature of a Si slab deposited with a film 1 μm thick. The Si slab has thickness 1 mm, the main face is oriented as (111)*, while the radius of curvature is calculated along the direction* $(\bar{1}10)$.

Silicon micromachining techniques provides a wide range of processes to deposit thin films on silicon substrates. Deposition techniques are divided in two large areas: chemical and physical depositions. Chemical depositions involves a fluid or gas precursor which undergoes a chemical change at a solid surface, leaving a solid layer. Chemical deposition of crystalline layers is particularly effective in producing stress because of the large stiffness of the deposited crystalline structures. A crystalline structure can be grown on a mono-crystalline slab only if the reticular structures of the two species are not too different. For this reason, the materials usually deposited on mono-crystalline Si by chemical means are C, CSi, or Ge. Physical deposition uses thermodynamic, mechanical, or electromechanical means to produce a thin film of solid. Examples of materials usually deposited on mono-crystalline Si by physical means are nitride, amorphous Si, SiO_2, metals. In the case of metal deposition, aluminum should be used for reaching large curvatures. Indeed, aluminum is a common metal, easy to deposit, and with a large coefficient of thermal expansion. A third way to produce a thin film on a Si slab is to convert part of the surface Si in another material, as in the case of thermal SiO_2 growth. In this case, a Si slab is exposed to a reactive environment at high temperature, so a certain thickness of the Si slab is turned in SiO_2. The SiO_2 layer has a different volume than the precursor mono-crystalline Si layer, thus a uniform strain field is generated.

The largest part of thin film manufacturing techniques are carried out at elevated temperatures. For example, dissociation of the precursors used in chemical depositions are typically reached placing the sample in a heated reaction chamber. In physical deposition, instead, the material to be deposited is placed in an energetic, entropic environment, so that particles of material escape from its surface. Facing this source is a cooler surface which draws energy from these particles as they arrive, allowing them to form a solid layer. In order to allow the particles to travel as freely as possible, the whole

system is kept within a vacuum deposition chamber. As a consequence of cooling of the sample from the deposition temperature to room temperature, thermal stress generates in the film and in the substrate, causing a permanent deformation of the sample. Moreover, stress is generated in the film during the film growth. The origin of this stress is very peculiar for every material and for every growth process. The stress due to the film growth sums up with the thermal stress, producing a curvature that can be calculated from the Stoney's equation:

$$R = \frac{E}{6(1-\nu)} \frac{h_s^2}{h_f} \frac{1}{S}$$

where h_s is the substrate thickness, h_f is the film thickness, E is Young's modulus, ν is Poisson's ratio, R is the radius of curvature, S the stress. Because Si is an anisotropic material, this formula is an approximation valid along a certain direction over a crystalline slab. For a detailed calculation of the expected curvature, the formulae (7 Appendix I - Theory of elasticity at the first order) have to be applied.

Deposition of thin films allows achievement of a self-standing bent structure, removing the need of a mechanical bender, thus providing space-saving samples of reduced weight. Anyway, deposition of thin films have drawbacks. First, deposited thin films present important delamination problems. Indeed, the stress between the substrate and the deposited film has not to be too high, otherwise delamination of the film from the substrate occurs, or even cracks in the film or in the substrate. Just the thermal SiO_2 growth do not produce delamination problems between the analyzed techniques for producing a tensile thin film. Indeed, in this last case, the tensile layer is embedded in the bulk crystalline slab and it cannot delaminate. Second problem, even if the stress induced by thin films is important, the integrated stress is not enough to bend thick crystalline slabs, i.e. thickness above 2 mm. Indeed, the typical thickness of thin films is below 1 μm. Long curing cycles can produce thicker films, but they usually put the manufacturing machines under stress. For these reasons, after some tests the focus of this thesis work moved on the production of thick tensile films to bend thick crystalline slabs (thickness > 2 mm) (4.2.2 Thick films - CFRP), and to ion implantation as a reliable method to bend thin slabs (thickness < 1 mm) (4.2.3 Ion implantation).

4.2.2 Thick films - CFRP

In this part, we develop an innovative technique to produce thick self-standing bent crystals consisting in the deposition of a thick film of carbon fiber reinforced polymer (CFRP). The stiffness of carbon fiber is one of the highest known, so it is ideal for bending a high-stiffness material as mono-crystalline Si. Moreover, CFRP can be growth on the surface of a Si slab. This method allows bending of crystals as thick as 5 mm with an important curvature. As an example of the method, two self-standing bent silicon samples were produced and tested. The first sample is a $20\times20\times5$ mm^3 crystal spherically bent by CFRP deposition only, and it was produced to be used as a primary CDPs crystal (3.2.1 Primary CDP). The second sample is a cylindrically bent $20\times100\times5$ mm^3 crystal. It was first bent by an holder, CFRP was deposited on the surface of the crystal, then the sample was removed from the holder. The second sample was produced to be used as a focusing crystal with (422) QM CDPs.

The two samples were shaped at SSL (Ferrara, Italy), through a high precision dicing saw (DISCO^{TM} DAD3220). Then, the curvature of the samples was obtained by the deposition of a thick film of CFRP at RIBA (Faenza, Italy). The surface profile of the samples was measured at SLL by an interferometric profilometer before and after the deposition process. The first sample resulted spherically bent with a radius of curvature of 95 m, while the second sample was cylindrically bent with a radius of 30 m. For the first sample, the bending of the laminate was entirely due to the CFRP curing cycle. Indeed, two materials compose CFRPs: layers of carbon fibers tissue and epoxy resin. The epoxy resin acts as a matrix that keeps the carbon fiber layers together. When the resin is cured, it shrinks down reducing the volume of the composite, so turning the CFRP layer in a tensile layer. Moreover, the curing cycle occurs at high temperature, so the different thermal expansion of CFRP and Si has to be considered. The coefficient of thermal expansion of CFRP and Si mono-crystal respectively are -0.1×10^{-6} K^{-1} and 2.4×10^{-6} K^{-1}. The different thermal expansion of the deposited film and of the substrate produce a stress which contributes to the curvature. The stress is difficult to be predicted a priory, but it can be estimated from the sample curvature. For the first Si sample the integrated stress is 10.0 kPa m. A mechanical holder cylindrically bent the second sample to the curvature radius of 20 m. Then, CFRP was deposited on its surface as in the case of the first sample. When the CFRP was cured, the sample was removed from the holder. In this case, the stress on the main surface is even more difficult to predict. However, also in this case the integrated stress can be estimated by the curvature of the sample as 28.7 kPa m.

The two samples were tested through X-ray diffraction at beamline ID15A of ESRF, by a highly monochromatic and collimated beam tuned at the energy E = 150 keV, monochromaticity was $\Delta E/E = 2\times10^{-3}$. The characterization of the samples was carried out by performing rocking curves (RCs). The radius of curvature R of the diffracting planes depends on the measured angular spread Ω, and on the sample thickness traversed by the beam. For sample 1, the radius of curvature results $R = T_0/\Omega = 94$ m. For sample 2, it turns out $R = T_0/\Omega = 103$ m. Owing to the theory of elasticity in an anisotropic medium, the primary curvature radius can be derived as $R_P = R/3.542 = 30$ m. This is the radius of curvature imprinted thanks to the carbon fiber deposition. The recorded diffraction efficiencies are very high, though for both crystals there is a difference between experimental and theoretical efficiency of about 15%. This discrepancy could be attributed to the method used to bind the carbon fiber to the samples, which may have degraded the crystalline structure.

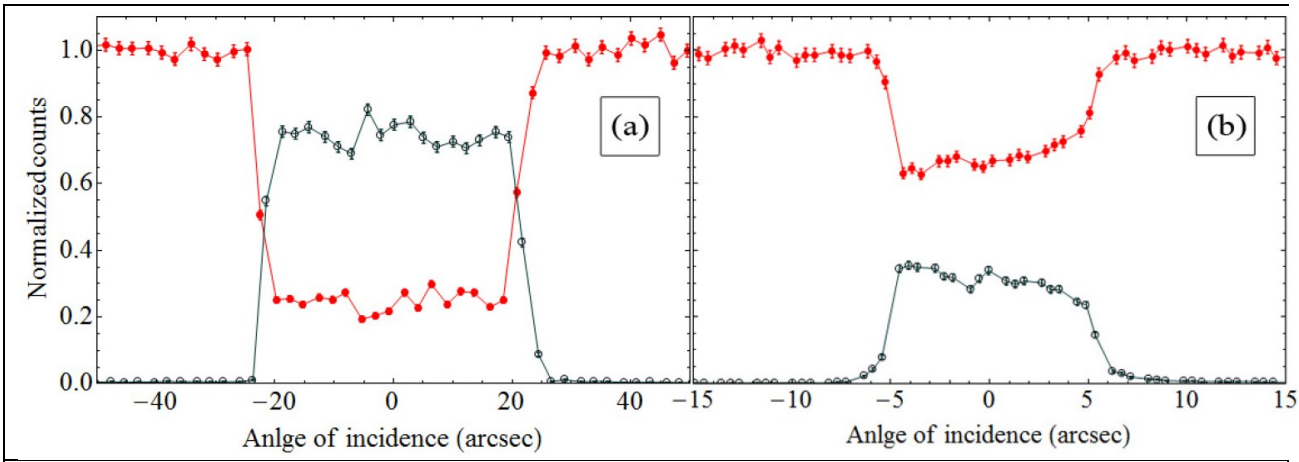

Figure 4-14

Experimental RCs. Filled red circles plot the intensity of the transmitted beam, whereas empty blue circles plot the intensity of the diffracted beam. a) Sample 1, (111) primary bent CDPs, the beam goes through 20 mm of crystal thickness. b) Sample 2, (422) QM CDPs, the beam goes through 5 mm of crystal thickness.

The first sample (size 20×20×5 mm^3) was tested by X-ray diffraction tomography at beamline BM05 of ESRF. The beam was polychromatic with energy range 6 – 200 keV, and the beam had size 16 × 7 mm^2. The beam entered the sample from the concave face, i.e. the face without CFRP. The characterization of the sample was carried out by recording the diffraction images on photographic films (Figure 4-15. The curvature of the sample causes defocusing of the beam, that the diffraction spots on the photographic film are further apart from each other, thus better separable. Tomographic images are uniform for perfect crystals, while non-uniformities in the images highlight dislocations or distortions in the lattice. The tomographic images of the sample highlight strong distortions (Figure 4-15 a – b). The distortions in the sample can be divided in two types. The first type of distortion is the uniform curvature of the sample, which causes the diffraction spots to be deformed as a spherical calotte as the result of the beam defocusing. The second contribution is the local deformations caused by the concentrations of stress due to the non-homogeneity of CFRP at small scale (< 1mm). Indeed, the CFRP is composed of a tissue of carbon fiber with fabric size 0.5 mm in a matrix of epoxy resin. The stiffness of the carbon fibers is far larger than the stiffness of the resin, so the stress produced by the CFRP on the crystal is modulated by the geometry of the fabric. Indeed, Figure 4-15 a – b highlight deformations with step 0.5 mm, compatible with the structure of the fabric. Tomographic images allows to distinguish the deformations due to the vertical threads of the fabric (Figure 4-15 a) and to the horizontal threads (Figure 4-15 b).

An improvement in the deposition technique of CFRP may reduce the concentrations of stress thus leading to better diffraction performance of crystals bent by this method. Anyway, deposition of a thick film of carbon fiber proved to be an effective method to bend thick crystals. The study on CFRP deposition may allow a fine modulation of the final curvature by simply adjusting the deposition parameters. The method is expected to work also with different kind of crystals, such as germanium, gallium arsenide, copper, etc.

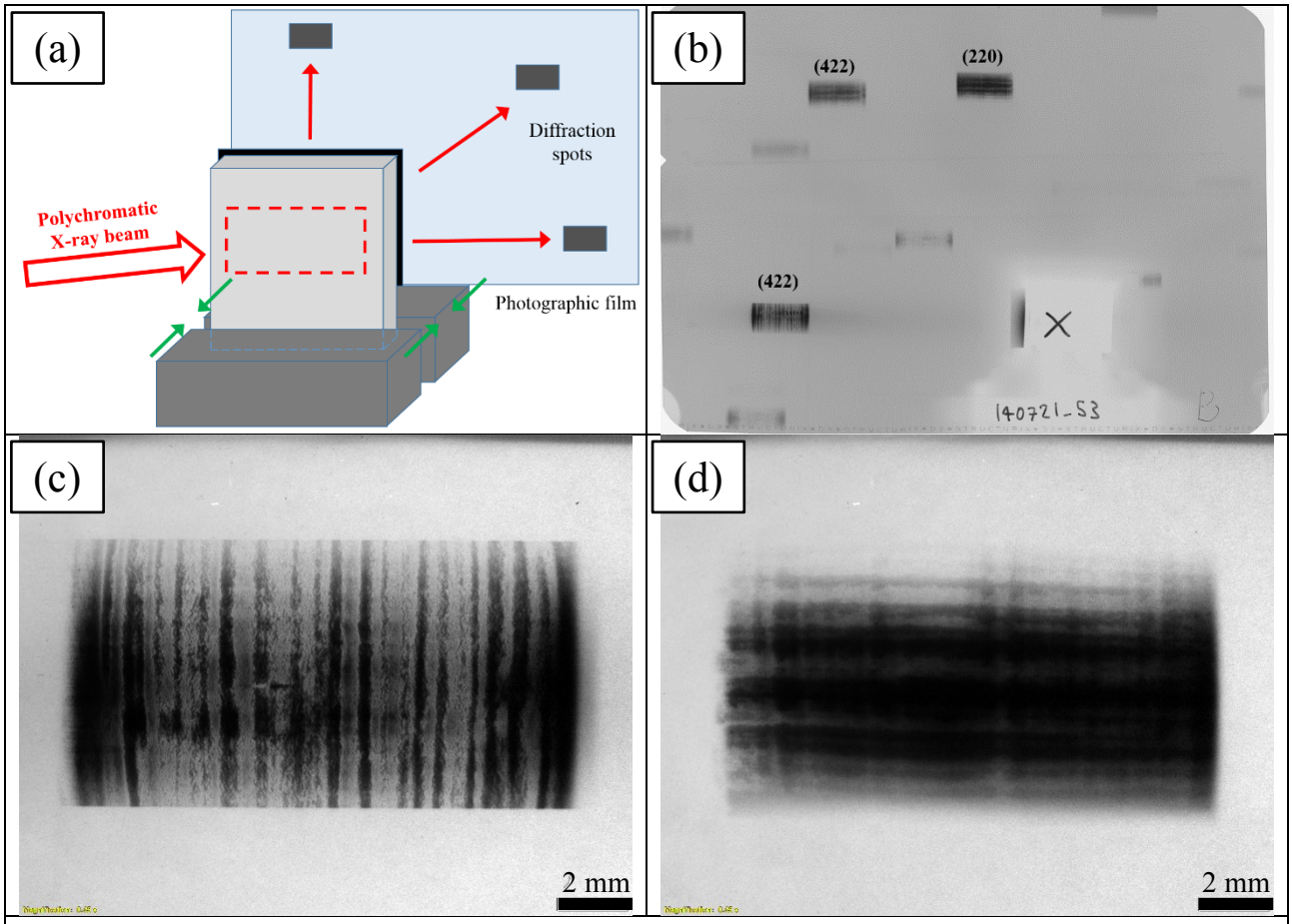

Figure 4-15

(a) Scheme of the experimental setup for the tomographic analysis of the sample first sample (size 20×20×5 mm^3). The sample is hold in position by a clamp, while a polychromatic X-ray beam with size 16 × 7 mm^2 enters through the concave face of the sample. Different lattice planes diffract the X-ray beam, resulting in multiple spots on a photographic film. (b) Photographic film with multiple diffraction spots from the sample. The principal lattice orientations are named by their Miller indices. (c) Detail of the (422) diffraction spot on the bottom-left of the photographic film. Diffraction by vertical lattice planes produced this spot, so the spot highlights deformations on the horizontal direction. A uniform spherical deformation is evident. Deformations with step about 0.5 mm are also evident. These deformations are uniform along the vertical direction. (d) Detail of the (220) diffraction spot on the top of the photographic film. Diffraction by horizontal lattice planes produced this spot, so the spot highlights deformations on the vertical direction. A uniform spherical deformation is evident, as smaller deformations having a repetitive scheme. These deformations are uniform along the horizontal direction.

4.2.3 Ion implantation

Ion implantation has been used in the semiconductor industry for several decades. A drawback of this process for semiconductor manufacturing was the production of stress in the implanted material (Burnett, 1985), (Wanga, 2004). This early disadvantage was turned into a technology for the correction of stresses in thin films and substrates. Implanting high-energy ions into a substrate imparts large compressive stresses, causing repeatable and controllable deformation of the substrate. Ion implantation was used for the correction of shape errors in x-ray stepper masks (Itoh. M., 1991), x-ray mirrors (Chalifoux B., 2013), and MEMS deformable mirrors (Bifano T, 2002).

Dose $10^{16}cm^{-2}$	**Energy of the ions (keV)**		
Ion species	50	100	150
He^+	✓	✓	✓
Ar^+	✓	✓	✓
Kr^+	✓	✓	✓

Table 4-3

Grid of the tests performed by varying type of ion and implantation energy.

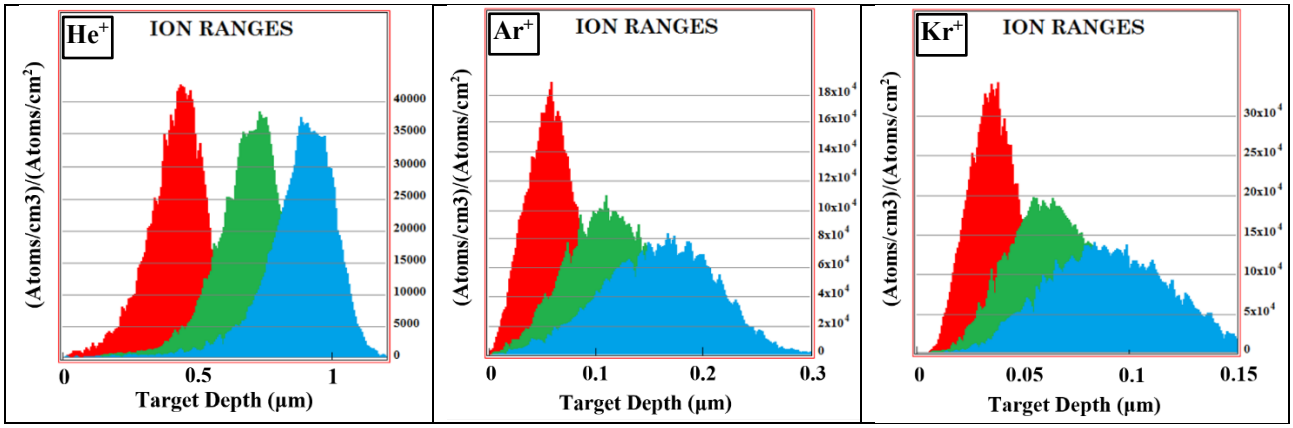

Figure 4-16

Depth distribution of implanted ions in a monocrystalline Si substrate for He^+, Ar^+, Kr^+ ions at 50 KeV (red distribution), 100 keV (green distribution), 150 keV (blue distribution). The units in ordinate are arbitrary. The ion range for He^+ ions is 416 nm (50 keV), 671 nm (100 keV), 874 nm (150 keV). The ion range for Ar^+ ions is 58 nm (50 keV), 109 nm (100 keV), 158 nm (150 keV). The ion range for Kr+ ions is 37 nm (50 keV), 65 nm (100 keV), 89 nm (150 keV). Most of the defects induced in the Si structure are concentrated around the stopping point of the ions. Defects are the source of the stress in the substrate. The ion implantation process produced a tensile layer buried into the substrate. This layer is part of the structure of the substrate, thus it is not affected by delamination. The depth reached by the implanted ions is very small compared to the crystal thickness, usually hundreds of µm. Then, dislocations do not affect the crystalline structure of the bulk.

Ion implantation has never been used as the only process for the manufacture of a bent object. Indeed, the stress achieved by ion implantation has been too low for this purpose. The objects presented in this section are macroscopic Si monocrystalline plate uniformly bent by ion implantation only. Commercially available pure Si monocrystalline wafer was diced to form plates of 10×10 mm^2 using a high-precision dicing saw (DISCO™ DAD3220). The use of square samples eliminates the possibility of producing the anisotropies in the deformation due to the geometric shape of the samples. Monocrystalline silicon is an anisotropic material, thus its elastic constants are direction dependent. One of the purpose of this work is to determine if the curvature induced by ion implantation is uniform. Direction-dependent elastic constants may interfere with the stress induced by ion

implantation. The result may be a non–uniform curvature even if under a uniform stress field. Nevertheless, the (111) Si lattice plane presents isotropic elastic constants. Thus, the samples were produced with the largest face oriented as (111). Then, the deformation obtained after ion implantation is entirely due to the implantation process. The morphological profile of the samples was measured by using an optical profilometer (VEECO^{TM} NT1100). These processes were done at Sensor and Semiconductor Laboratory (Ferrara, Italy).

The silicon samples were implanted with He+, Ar+ and Kr+ at the INFN Laboratories of Legnaro (Padova, Italy). The ion implantation system used in this work consists of a commercial broad beam ion source mounted in a vacuum chamber. Chemically neutral helium gas entered the source while electrons emitted by a tungsten filament cathode ionized the gas, and the ions were accelerated at the energy of 50 keV, 100 keV or 150 keV. The beam's current flux density was found to be temporally and spatially uniform to within 5% over the area of the 150 mm diameter sample holder. The dose implanted into the sample was $1*10^{16}$ A/cm^2. The morphological profile of the sample was measured again after the ion implantation process.

The implantation process accelerates the ions towards the sample surface. The cross section of the ions is sufficiently small that they pass through the surface. Then, electronic and nuclear forces within the substrate slow them off. The penetration depth strongly depends upon the ion species and the implantation energy (Wolf, 1986). Implanted ions stop in a narrow range of depths, forming a concentration profile similar to a Bragg curve. As the ions pass through the sample, they lose their kinetic energy colliding with the material, and breaking covalent atomic bonds. A thin layer of the sample is amorphized under the impact of the ion beam. When stopped, the ions take up space in the substrate too. Previous studies of deformation due to implantation indicate that this damage causes expansion of silicon (Vook, 1962), (Meek, 1971), (EerNisse, 1971),. The implantation process imparts a repeatable sub-surface stress, creating a tensile layer buried in the substrate structure (Itoh. M.,

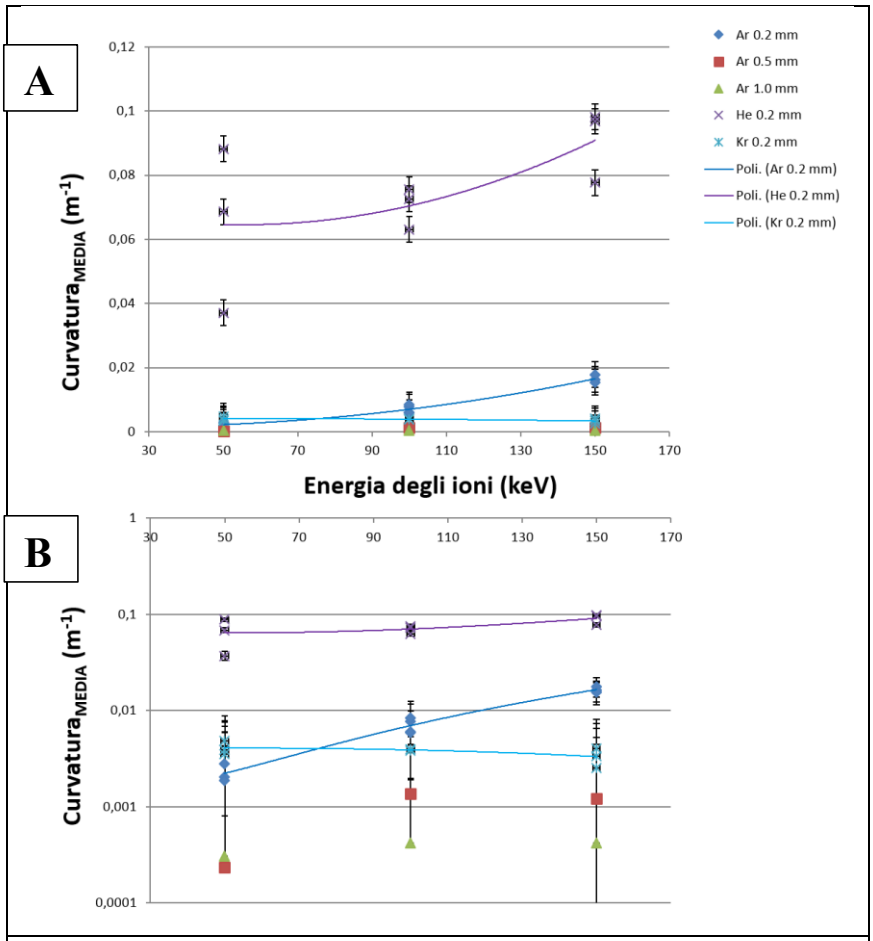

Figure 4-17

(A)Implantation energy vs curvature of the samples, and (B) in logarithmic scale. Different colors are used for samples with different thickness and energy of the implanted ions. The curvature of each sample is calculated as the average of the curvatures along the x and y directions on the sample surface.

1991), (Misra, 1999), (Burnett, 1985). Theoretical model of production of stress in ion-implanted silicon have been proposed. They are based on the assumptions that the point defects are the source of mechanical stress (Tamulevicius, 1998). If the ion implantation process is uniform over the surface, the tensile stress is uniform too, thus inducing the sample to bend as a spherical calotte (Stoney, 1909).

Subtraction of the morphological profiles before and after the ion implantation process was done for every sample. A vertical precision of the profilometer is 1 nm, which corresponds to a radius of curvature of the order of one kilometer. This is the limit of analysis of the instrument. As first analysis, samples of thicknesses 0.2 mm, 0.5 mm, 1 mm were produced and they were implanted with a dose of 10^{16}cm^{-2} of Ar + ions. The implantation energies were 50 keV, 100 keV, 150 keV. At least three samples were produced for every combination of implantation energy and thickness. Samples of thickness 0.5 mm and 1 mm showed a negligible curvature after implantation. In contrast, the samples of thickness 0.2 mm had a considerable curvature, which increased with the implantation energy of the ions. The larger radius of curvature was 50 m, attained with an implantation energy of 150 keV. In fact, according to the theory of elasticity, for the same surface stress the curvature imprinted to a square plate is approximately proportional to the reciprocal of the cube of the thickness ($C \propto 1/spessore^3$). So, for samples of thickness 0.5 mm a curvature 15.6 times lower is expected, with radii of curvature of the order of 800 m. Thus, for thickness of 1 mm a curvature 125 times lower is expected, with radii of curvature larger than 6000 m. These radii of curvature are greater than the maximum radius the profilometer can measure, so the sample appears flat.

The type of ion implanted strongly influence the type and the amount of damage to the substrate, and hence the curvature induced. Argon is an element with intermediate mass between those implantable. Then, the implantation process was repeated using helium (light ion) and krypton (heavy ion). In order to maximize the induced deformation only samples of thickness 0.2 mm were used. This choice made easier to analyze the deformation effect. The data of the analysis of all samples are shown in Figure 4-17. The larger curvature is obtained in the samples implanted with helium, which achieve a radius of curvature of the order of 10 m when the energy of implantation is 50 keV. In contrast, radii of curvature in the order of 300 m were obtained using krypton, i.e. lower than in the case of use of argon. Figure 4-18 compares the curvature along the two axes for the samples produced, showing a fairly uniform curvature.

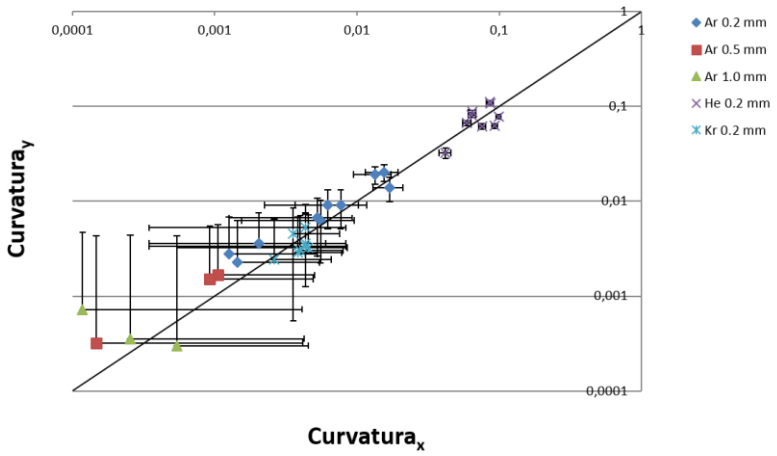

Figure 4-18

Curvature along the x axis vs curvature along the y axis, both in logarithmic scale, for the samples analyzed. The oblique line across the graph is to the bisector of the quadrant for which $C_x = C_y$.

It is a uniform spherical curvature, with radius of curvature of (10.5 +- 1) m over the entire surface. Ion implantation induced an integrated stress *S* of 140 Pa*m on this sample, as calculated from the Stoney's equation:

$$S = \frac{E}{6(1-\nu)}\frac{h_s^2}{R}$$

where h_s is the substrate thickness, E is Young's modulus, ν is Poisson's ratio, R is the radius of curvature. The integrated stress is used here because, unlike with a deposited film, there is no well-defined film thickness. The curvature is the largest jet achieved in literature for a macroscopic Si sample implanted with ions under the MeV energy. Nevertheless, the use of ion implantation for bending macroscopic crystals has two drawbacks. First, it was possible to achieve a large bending for a thin wafer, 0.2 mm thick. The stress achieved is large for an ion implantation process, but it is small when compared with the stress induced by the standard methods for bending macroscopic crystals. Extensive studies of He+ ion implantation at higher energy may be necessary to maximize the stress, thus making this process useful for bending thicker substrates. Otherwise, if an application needs very thick bent crystals, thin bent crystals may be stacked as in (Bellucci V. C., 2014). The second drawback is purely technological, since commercial implanters are only capable to apply a uniform dose distribution. Therefore, the stress field created is uniform, and the substrate can only be bent as a calotte. Nevertheless, complex curvatures can be achieved by modulating the implant dose over the surface with a photoresist mask (Chalifoux B., 2013).

The sample was tested through X-ray diffraction at beamline ID15A of ESRF. A highly monochromatic and collimated beam was tuned to 150 keV, the monochromaticity was $\Delta E/E = 2x10^{-3}$, the beam size was 50x50 um^2. The sample was analyzed in transmission geometry, with the diffracted and transmitted beams passing through the entire crystal thickness, to test the bulk crystalline quality. The characterization was carried out by performing rocking curves (RCs). The best way for testing a bulk crystalline structure by X-ray diffraction is to diffract photons by curved lattice planes. Indeed, the RC profile of a curved diffraction plane without dislocations is far different from the RC profile of a mosaicized plane. However, all the lattice planes orthogonal to the (111) main surface are flat. In this case, the curved lattice planes with the highest reflectivity are the (311) asymmetric planes, holding an asymmetry angle of φ = 58.52° from the (111) surface. The diffraction analysis was performed by these planes.

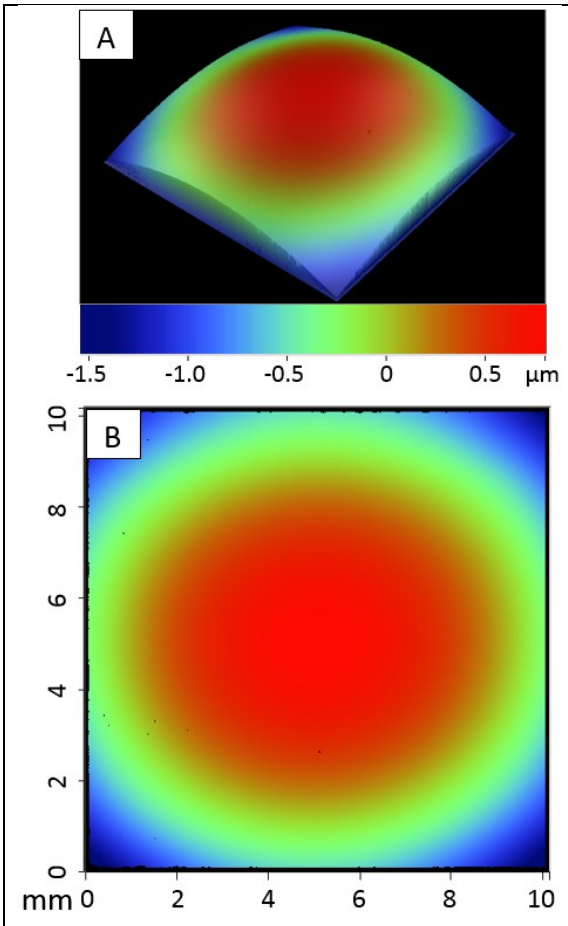

Figure 4-19

(A) 3D profile and (B) 2D profile of the deformation of the sample due to the implantation process. The images were obtained by subtraction between the profile of the sample before and after the ion implantation. A (111) oriented Si plate was choose because this orientation lacks crystalline anisotropy. Ion implantation produced a uniform strain field, so the result is a spherical calotte with curvature radius (10.5 ± 1) m all over the sample.

Diffraction analysis of the internal lattice planes of the sample are shown in Figure 4-20.The recorded RCs are the result of three physical contributions. The first contribution is due to the diffraction performance of CDPs, which depends from the curvature radius. Owing to the theory of elasticity in an anisotropic medium, in this case the curvature radius of diffracting planes is R_D = R/0.45 = 22 m. On the strength of morphological characterization of the major surfaces of the plate, it is reasonable to assume a uniform curvature for the diffracting planes. Then, a uniform curvature contributes as a uniform function. The second contribution to RCs is due to the primary curvature. The third contribution is the angular resolution reached by the experimental setup. The finite divergence of the beam and the resolution of the rotational stage can be modelled by Gaussian distributions with standard deviation of 0.15 arcsec and 0.2 arcsec respectively. Then, the resolution of the experimental setup is a Gaussian distribution with standard deviation σ = 0.25 arcsec. Experimental results are in line with the expectations, showing that the implantation process did not damage the bulk. The lattice planes resulted free from dislocations and perfectly bent. Crystalline quality is maintained, indeed, dislocations induced by ion implantation affect only a very superficial layer of the material.

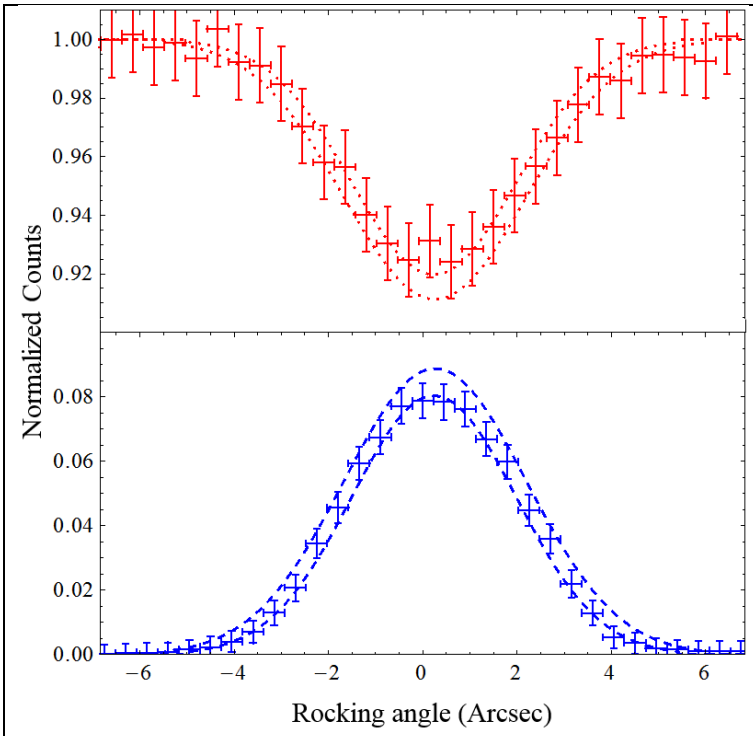

Figure 4-20

Rocking curves for X-ray diffraction through the bulk of the sample. Photon energy is 150 keV, the diffraction planes are the (311) asymmetric planes tilted by φ = 58.52° from the main (111) surface. The diffracted and transmitted beams pass through the entire crystal thickness. Crosses plot the experimental intensity for the diffracted (blue) and the transmitted (red) beam. Uniformly bent lattice planes without dislocations are expected from the implantation process. Dashed lines plot the expected profile for the diffracted (blue) and transmitted (red) beam. The simulation accounts for the uncertainties of experimental parameters.

Ion implantation was used for inducing a self-standing curvature in a Si monocrystalline plate. The curvature was uniform over the surface, and larger than any curvature achieved in literature for a macroscopic Si sample implanted with ions under the MeV energy. The process of ion implantation induces stress in a thin layer over the surface of the plate. Then, it allows to manufacture crystals with a self standing curvature without delamination problems, and without adding material. Indeed, the stressed layer is buried into the crystal. The crystalline structure of the bulk material is maintained intact. The thickness and curvature of the self-standing bent crystal are enough for its application as a concentrator of hard X-rays. Moreover, the bent crystal described in this section demonstrates that the possibilities of ion implantation as a process for the controlled deformation of thin films and substrates have been underestimated. Because of the important curvature achievable, ion implantation may become a procedure largely implement for the correction of shape errors. Ion implantation based on He+ may become a standard for the correction of shape errors in x-ray stepper masks, x-ray mirrors and MEMS mirrors.

The process of ion implantation may be also useful in the field of charged particles optics. CDPs crystals are used for manipulating high energy charged particles by channeling phenomena. Charged particles are confined within lattice planes or rows of atoms, thus particles are forced to follow the curvature of CDPs. Particles trapped inside CDPs can undergo a deviation equivalent to the deviation produced by a magnetic field of 1000 Tesla. This phenomenon is useful in accelerator technology for the manipulation of charged particles. This technology is under development for the extraction of particles beams without the need for bending magnets. CDPs may be also used for removing the halo of secondary particles around a particle beam trapped in an accelerator. Crystal used for these application need to be rather thin, with thickness below 1 mm. Indeed, an ideal crystal thickness is in the order of 10 μm. Crystals with this thickness are being developed at SSL in the form of mono-crystalline Si membranes supported by a thick frame Figure (4-21 a) . Flat membranes already shown good channeling performances (Scandale W. A., 2014). Nevertheless, the production of crystals so thin with a uniform curvature is a technological challenge yet to achieve.

Ion implantation showed to be an effective method for bending crystals to a desired curvature. During this thesis work, a membrane useful for particles channeling was implanted by He^+ ions at 150 keV, following the procedure described in the previous sections. The frame of the membrane has size $(10 \pm 0.025) \times (10 \pm 0.025) \times (1 \pm 0.025)$ mm^3, while the membrane has size $(5 \pm 0.025) \times (5 \pm 0.025) \times (0.011 \pm 0.001)$ mm^3. The main surface of the membrane is oriented as (001), while the long sides have direction (110) and $(\bar{1}10)$ respectively. The (111) lying of planes have the highest electronic density, so they are ideal for channeling. Therefore, it would be ideal to have (111) planes orthogonal to the main face of the membrane. Nevertheless, this is impossible because of the manufacturing process of the membrane, which involves direction-selective etching (Scandale W. A., 2014). However, it is possible to choose an asymmetric lying of planes with orientation (111), as explained in (4.4 Tilted CDPs crystals). Indeed, there are two lying of planes with orientation (111) and $(11\bar{1})$, asymmetry + 35.26° and - 35.26° relative to the (110) direction. These planes are the useful ones for channeling. The membrane was analyzed by an optical profilometer after the implantation process. The center of the membrane resulted uniformly bent as a spherical calotte (Figure 4-21), with curvature radius of about 90 mm. The rate between the primary curvature and the curvature induced in the (111) asymmetric planes is 0.279. Then, the (111) asymmetric planes are bent to a curvature radius of 320 mm. The magnitude of the curvature radius is useful for application of this membrane for steering high energy charged particles via channeling. Mono-crystalline membranes bent by ion implantation will be the subject of channeling experiments at the accelerator MAMI (Mainz, Germany) on the next year (2015).

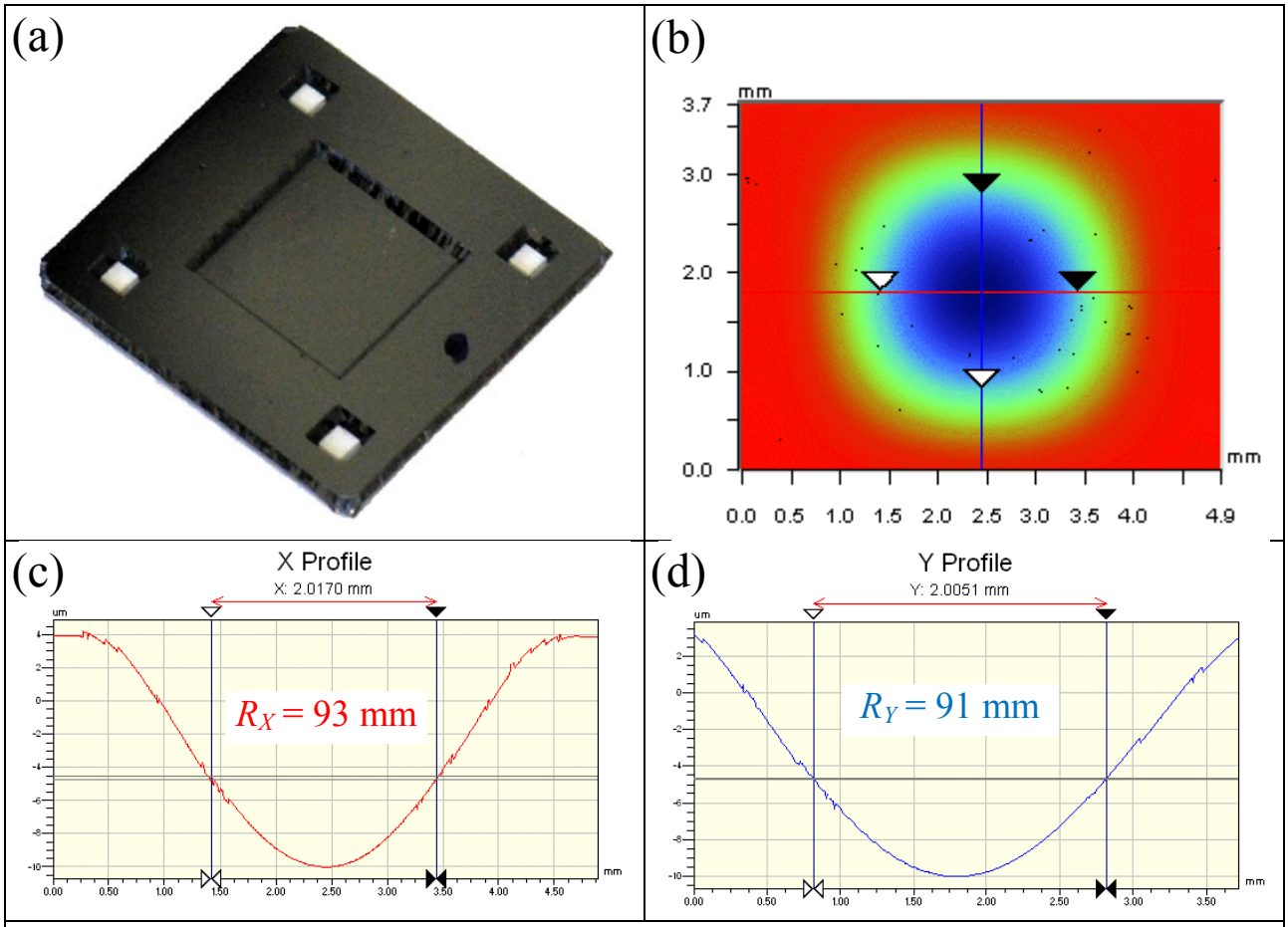

Figure 4-21

(a) Picture of a mono-crystalline Si membrane for channeling experiments. This membrane underwent ion implantation by He^+ ions at 150 keV. (b) Profilometric 2D image of the center of the implanted membrane. The center resulted bent as a spherical calotte. The last two figures show a section along the horizontal direction (c) and along the vertical direction (d) of the center of the membrane. The curvature radius is about 90 mm.

The membrane was implanted in the same implantation process of the $10 \times 10 \times 0.2 \pm 0.025$ mm^3 sample describe in the previous paragraphs. This sample had a curvature radius of (10.5 ± 1) m. Then, following the Stoney's formula, the membrane should have radius of curvature in the range 19 – 54 mm considering the experimental errors. However, the measured radius of curvature of the membrane was about 90 mm. This discrepancy is probably due to the thick frame that sustains the membrane. Indeed, the frame prevents the membrane to fully bend. To validate this hypothesis, the membrane was taken out of the frame and then it was analyzed through the profilometer. The fragments of the membrane resulted bent with a curvature radius of 40 mm, compatible with the hypothesis.

Figure 4-22

(a) Profilometric 2D image of the center of a fragment of the implanted membrane after it was taken out of the supporting frame. The fragment of the membrane is bent as a spherical calotte. The last two figures show a section along the horizontal direction (b) and along the vertical direction (c) of the center of the membrane fragment. The radius of curvature is 40 mm.

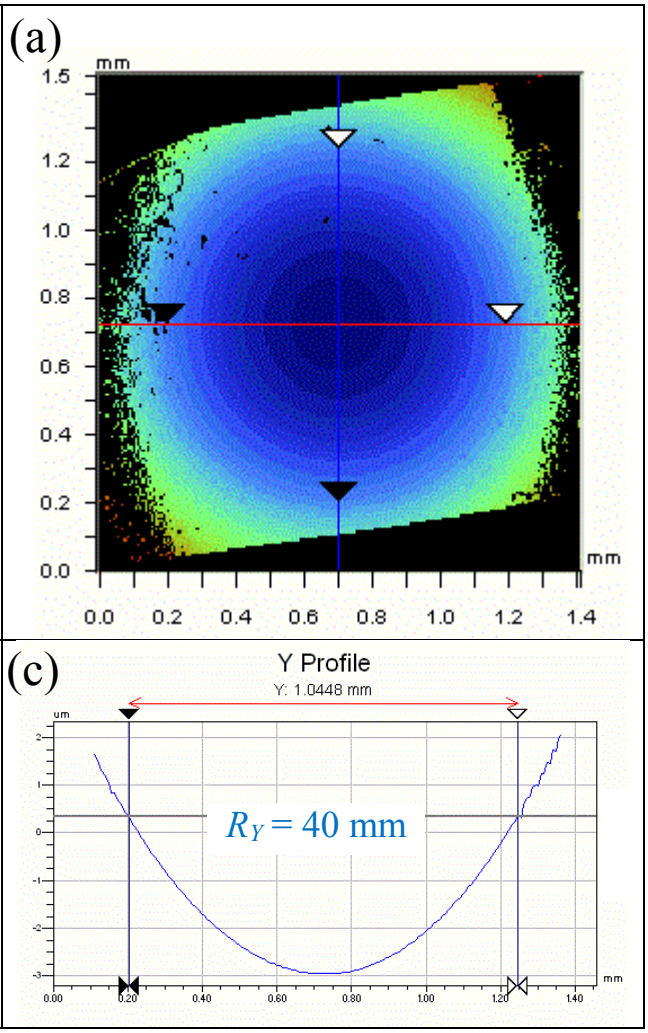

4.3 Multi-crystals

Most of the hard X-ray optics applications of curved crystals require self-standing crystal plates thicker than some millimeters (Malgrange, 2002) (Barriére N. R., 2009) order to maximize diffraction efficiency. Some applications even require thicknesses in the order of the centimeter. As seen in the previous chapters, realization of CDP crystals with thickness of several millimeters is technologically demanding. Just recently, it was possible to manufacture self-standing CDPs crystals with thickness up to 5 mm by CFRP deposition (4.2.2 Thick films - CFRP). Anyway, it is impossible to bend Si crystals of thickness 5 mm to a curvature radius larger than 20 m because this condition is the limit for the material to break. Crystals thicker than 5 mm cannot be bent to a curvature radius of 20 m or lower without breaking. To solve this problem, ingots were growth via concentration-gradient technique (Abrosimov, 2005). The bulk lattice planes of such crystals present a curvature, which does not depend from the crystal thickness. However, CDPs crystals are not easy to manufacture by such a method, and the crystalline quality is usually low. Moreover, this technique is difficult to apply and it cannot meet the need for reproducible fabrication of large numbers of crystals for Laue lenses.

A possible solution may be the construction of a multi-crystal, i.e., a stacking of equally curved crystal plates, aligned with each other with high accuracy. Thanks to the stacking, it would be possible to realize optical elements with arbitrarily large size. A multi-crystal stack can be designed as a primary CDPs crystal or a focusing QM CDPs crystal. Stacking of curved crystalline plates has already been used in neutron diffraction either in Bragg or in Laue geometry. However, for neutron diffraction the tolerances on the angles are much looser than for X-ray diffraction. Then, for neutron diffraction, the alignment between the crystals composing the multi-crystals is not so critical. On the contrary, the crystals composing a multi-crystals stack for X-ray diffraction need to be very well aligned. In this section, we have demonstrated the advantages of multi-crystals for X-ray optics. Then, multi-crystals have been built by different methods and they have been tested.

4.3.1 Design of multi-crystals

Multi-crystals can be built by stacking primary CDPs or quasi-mosaic CDPs. These two types of multi-crystal function differently under X-ray diffraction.

4.3.1.1 Primary CDPs multi-crystals

A pile of ideally identical primary CDPs crystals composes a primary bent multi-crystal (Figure 4-25). The X-ray beam enters the multi-crystal from the side showing the smallest surface of the crystals. The beam flux is equally distributed over the crystals composing the multi-crystal, that each crystal intercepts just a fraction of the beam. For the typical energies of operation (E > 100 keV) we can consider the Bragg angle small. Then, we can consider that every photon enters and exit the multi-crystal through the same crystal. This approximation holds true for crystals with realistic thickness (1-2 mm). Indeed, the fraction of photons going through more than one crystal is very small. If we consider the curvature uniform, the passband for photon diffraction of each crystal exhibits a typical rectangular distribution.

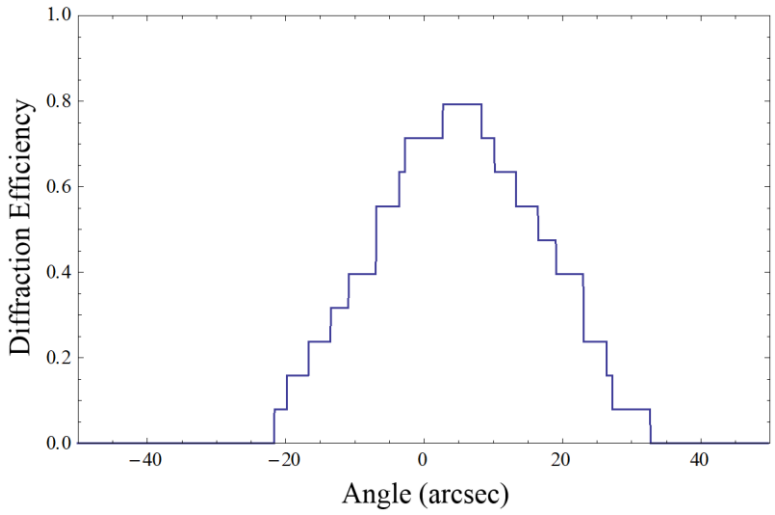

Figure 4-23

Example of the expected response for a stack of primary CDPs crystals. The stack is made of 10 crystals with thickness 10 mm, the primary Si (111) *diffraction planes are bent at a radius of 70 m, yielding a photon passband of 30 arcsec for each crystal. The energy of impinging photons is 150 keV, a typical energy of operation. The primary passbands are randomly misaligned with respect to each other, with a mean misalignment of 10 arcsec. Diffraction efficiency of each crystal is 79.3 % under this working condition. Since each crystal intercepts just a fraction of the beam, the diffraction efficiency of the crystal passbands sum up where they superpose. The response function of the multi-crystal results in a Gaussian-like shape.*

Then, the passband of the stack is the union of the passbands of all the crystal lamellae. If the lamellae were perfectly aligned, their passbands would superpose, and the total passband of the multi-crystal would be equal to the passband of an individual primary CDPs crystal. Nevertheless, the area exposed to the beam would increase. The increase in the exposed area is very important for the use of primary CDPs crystals as optical elements. However, the process of crystals stacking one on top of the other naturally induces random misalignments in their reciprocal orientation (Neri, 2013). These random misalignments are very difficult to prevent. However, it is possible to minimize the misalignments to less than the angle of curvature of the primary CDPs crystals. Thus, the passbands of the crystals superpose with a small random misalignment. Since each crystal intercepts just a fraction of the beam, the diffraction efficiency of the crystal passbands sum up where they superpose. The total passband of the multi-crystal results in a Gaussian-like shape (Figure 4-23). The shape of this passband is similar to the Gaussian-shape passband of mosaic crystals (1.2.3 Mosaic crystals). Indeed, the passband of mosaic crystals is the results of the random misalignment between crystallites. However, the diffraction efficiency of mosaic crystals is limited to 0.5, while the diffraction efficiency of a multi-crystal can approach 1. Moreover, the FWHM of the passband of mosaic crystals is not well controllable because it depends on the nature of the material and on small

variations in the manufacture process. Conversely, the FWHM of the passband of primary CDPs multi-crystals mainly depend on the curvature of the bent crystals.

4.3.1.2 Quasi-mosaic CDPs multi-crystals

The QM effect produces a uniform curvature. Thus, for a single crystal, the passband for photon diffraction in a single point exhibits a typical rectangular distribution (Bellucci V. C., 2011b) (Camattari R. G., 2013). For a beam with macroscopic dimension, the superficial curvature has to be taken into account, so that the passband is the convolution of two rectangular functions, one for the primary curvature and another for the secondary one. The convolution is a trapezoidal function. Then, the passband of the stack is the union of the passbands of all the crystal lamellae. If the lamellae were perfectly aligned, their passbands would superpose, i.e. the total passband of a stack would be equal to the passband of an individual lamella. This circumstance is not favorable to build up a Laue lens because it does not widen the passband and, if the efficiency of each individual crystal is very high, the rise of the total reflectivity of the stack would be low. The process of crystals stacking one on top of the other naturally induces random misalignments in their reciprocal orientation (Neri, 2013), which would circumvent the problem.

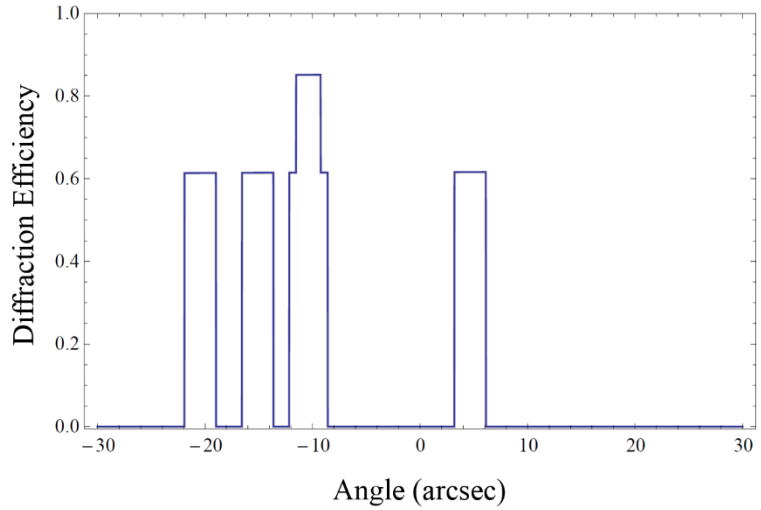

Figure 4-24

Example of the expected response for a stack of QM CDPs crystals, considering only the contribution due to the QM curvature. Neglecting the smoothing effect of primary curvature allows to highlight the QM passband for each crystal composing the stack. In the example the stack is made of 5 crystals with thickness 2 mm, the QM Si $(4\bar{2}\bar{2})$ *diffraction plane is bent at a radius of 140 m, yielding a photon passband of 3 arcsec for each crystal. The energy of impinging photons is 150 keV, a typical energy of operation. The QM passbands are randomly misaligned with respect to each other, with a mean misalignment of 10 arcsec. Three of the QM passbands are well separated, while two QM passbands superpose one another. Since diffraction efficiency of each crystal is 61.6 % under this working condition, superposition of the QM passbands can only increase diffraction efficiency up to 85.2 % in the area of superposition.*

Figure 4-24 shows an example of the expected passband due to QM curvature only, in the case of a stack of five randomly misaligned QM crystals. In this case, the contribution of the primary curvature has not been included in order to highlight the contribution of QM passbands. Here, Si $(4\bar{2}\bar{2})$ QM diffraction planes are bent to a curvature radius of 140 m, crystal thickness is 2 mm, and the energy of impinging photons is 150 keV. In the case shown in the figure, the QM passband of two crystals superpose, generating only a small increase in reflectivity, and nearly no increase in the total passband of the stack. The passbands of the other crystals are positioned one near each other, thereby increasing the total passband width. The passband due to primary curvature is typically one order of magnitude larger than that for QM curvature, wide enough to smoothen the final passband without leaving gaps. In summary, a balanced tradeoff between diffraction efficiency and passband width is the condition for which the responses of all the secondary curvatures are not overlapped to each other

and they lie within one individual primary passband. In this case, the arrangement of the secondary responses is not so crucial and that helps a lot in the preparation of a stack with these characteristics.

4.3.2 Experimental & Methods

4.3.2.1 Stack of grooved crystals

The first method for producing a multi-crystal was to stack together equally bent crystals obtained by the grooving method, thus producing primary CDPs multi-crystals or focusing QM CDPs multi-crystals. In this section, we built primary CDPs multi-crystals by stacking Si crystals bent by the grooving method (Figure 4-25). The surface of each crystal highlights the grooves on the convex side while the opposite surface is concave. Commercially available pure Si wafer was diced to form three plates using a high precision dicing saw (DISCO^{TM} DAD3220). The plates were 1 mm thick and their orientation was (111), because such planes are normally selected for X/γ-ray focusing owing to their high reflectivity. The plates were cut from the same wafer to minimize the misalignment due to the wafer misscut. Indeed, commercial wafers usually have a misscut tolerance between different wafers of 0.5° = 1800 arcsec, while the crystals composing the stack should be aligned within 60 arcsec. Grooves were manufactured on the surface of the plates along one direction. Preliminary characterization of every plate through optical profilometry (VEECO^{TM} NT1100) guaranteed that they were morphologically equivalent (Figure 4-26). Base wafers are normally not planar, so that they exhibit an initial shape that depends on the manufacturing processes for producing the wafer. Typically, this shape is purely "morphological", i.e., the crystalline planes are flat. The morphological shape of the surfaces of crystals is responsible for most of the misalignment between the crystals composing the stack. we used double polished (DP) wafers in order to minimize the morphological contribute. Even if polished, the surface of wafers usually have a TTV of few μm. As an example, a thickness variation of 1 μm over a surface of length 1 cm produces a misalignment between the stacked crystals of 20 arcsec. In order to reduce this misalignment, we diced the crystals from near locations in the original wafer, and we made the crystals as long as possible. The grooves induce additional curvature, which is accompanied by bending of the crystalline planes. According to (Barriére N. G.-X., 2010) (Bellucci V. C., 2011b), the curvature of lattice planes is the difference between measured curvatures after and before grooving. Hence, subtraction of the profiles before and after the grooving process was done for every plate. Profilometric characterization was carried out on the back face of each plate. A s a result of grooving, an ellipsoidal surface appeared, with the smallest curvature radius perpendicular to the grooves. The crystals were finally mounted on a hot plate and

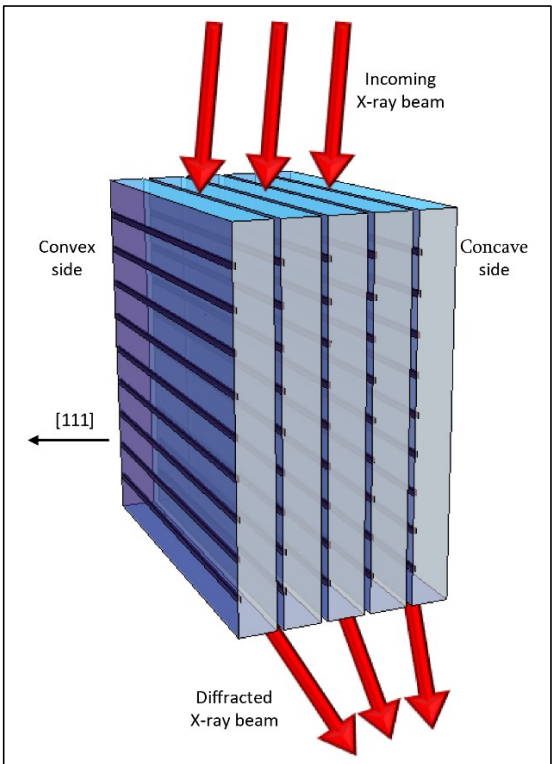

Figure 4-25

A stack of primary bent curved crystals is proposed as an optical component for focusing of X- and γ-rays. Crystal curvature owes to grooving a surface of each plate, which takes a concave geometry. In Laue lens scheme, high-energy photons enter nearly parallel to the CDP, suffer diffraction and undergo focusing onto the detector. For neutron diffraction, it can be used either in Bragg or Laue geometry.

bonded one over the other to form a stack (Figure 4-26 g) by using a commercially available zero-stress thermal paste, resulting in no curvature change after the bonding. At nominal temperature, the glue melts and solidifies on cooling, yielding a stable stack of plates. To verify that bonding did not alter the morphology of the crystals, subtraction of the morphological profiles before and after the bonding was done to the crystal on the top of the stack. The three stacked crystals had size 45×10×1 mm^3, so the multi-crystal had size 45×10×3 mm^3.

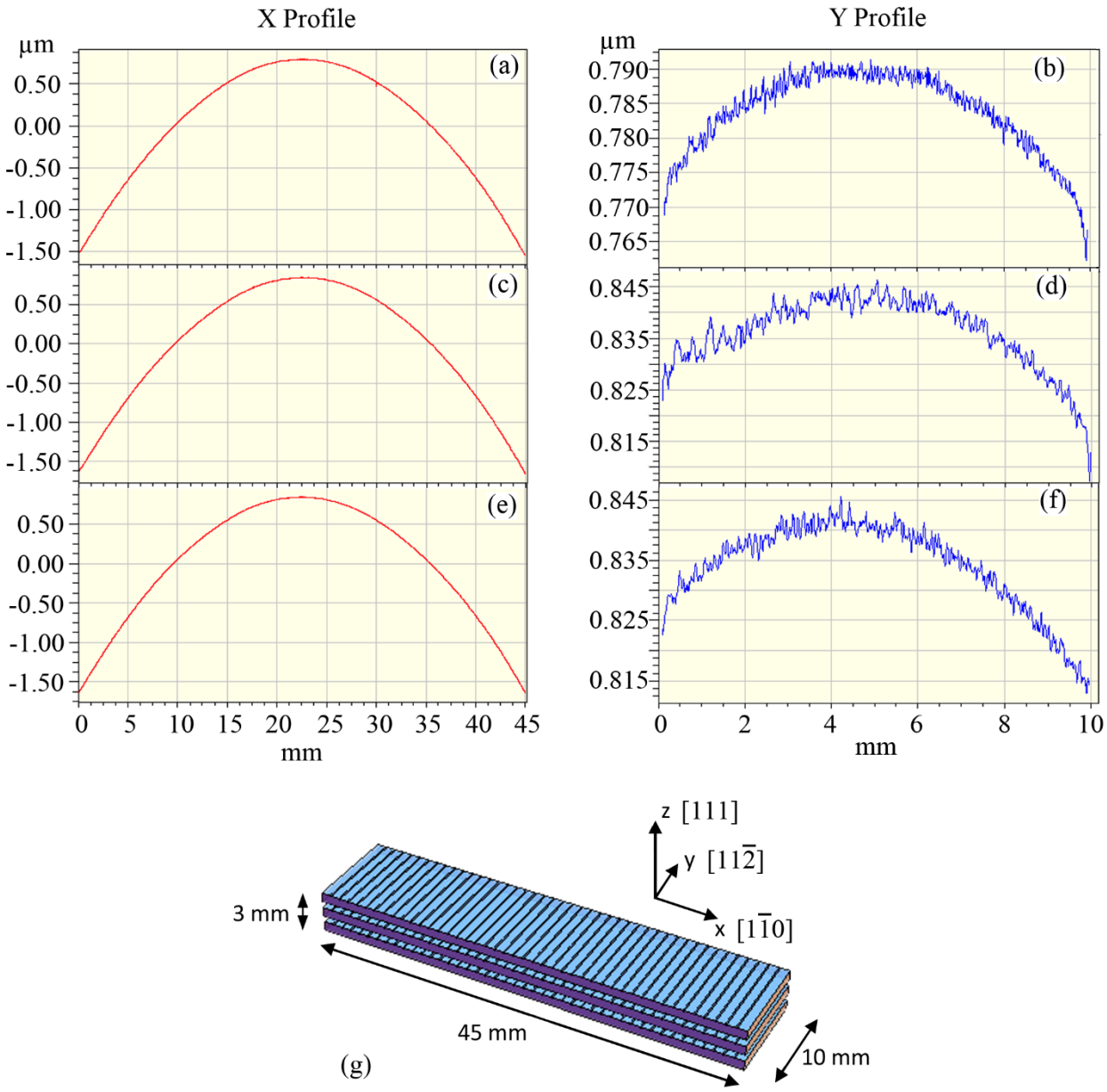

Figure 4-26

Optical profilometric scans of the surface without grooves of all the Si plates. Cross sections of the deformation patterns along x (a, c, e) and y (b, d, f) directions are highlighted, as taken on the center of the samples. The two main curvature radii of the plates are 110 m and 640 m (a, b), 100 m and 600 m (c, d), 100 m and 610 m (e, f) along x and y, respectively. The curvature radius along x corresponds to a bending angle of 84.4 arcsec (a) and 92.8 arcsec (c, e) as given by the ratio between the length of the crystal (along x) over the curvature radius. Stacking of Si crystals was obtained by bonding the plates one over the other thanks by a low-stress thermal paste. As visible, grooves were manufactured on the surface of each plate along y direction (g).

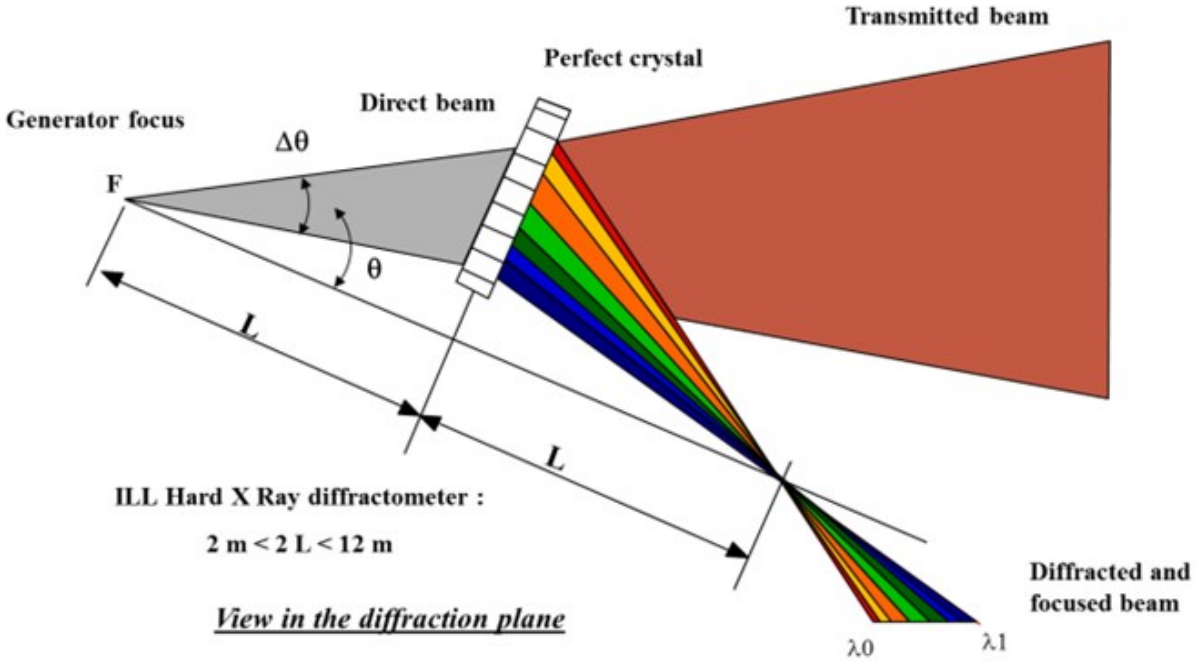

Figure 4-27

Schematic representation of the in-plane focusing of a divergent polychromatic X-ray beam by a crystal in Laue geometry. If the distance from the source to the crystal is equal to the distance from the crystal to the focal point, all diffracted rays converge to a point and a distribution of wavelengths is selected.

The multi-crystal was tested through X-ray diffraction at ILL (Grenoble, France) by using a hard X-ray diffractometer based on the method of X-ray focusing for transmission (Laue) geometry (Guinier, 1949) (Bastie, 1996) (Hamelin B., 1998) (Hamelin B., 2002). A schematic diagram of this technique is shown in Figure 4-27. The diffractometer uses a polychromatic and divergent X-ray beam (energy range between 80 and 450 keV). The size of the X-ray source was 1×1 mm^2. Since Bragg angles were small (0.5 – 1 degree), diffraction peaks were located close to the direct beam, thus allowing the observation of peaks from several crystallographic planes. These latter were observed thanks to a high-resolution and sensitive X-ray image intensifier coupled with a CCD camera, featuring a spatial resolution of about 0.35 mm (pixel size). Analysis times were typically from a few seconds to a few minutes. The distance between sample and generator focus was set to be 4.45 m, thus determining a lattice tilt maximum sensitivity of 8.1 arcsec, as given by the formula $S = (P \times 206.3)/d$ where S is the resolution in arcsec, P is the pixel size in μm, d is the distance between generator focus and detector (mm) and 206.3 the factor that converts radians to arcsec. Finally, a slit with variable size positioned just before the sample delimited the width of the X-ray beam. The multi-crystal was measured in two different configurations as shown in Figure 4-28. In the former case the beam was set quasi-parallel to the z direction, and in the latter quasi-parallel to the x direction. Beam size was 10×1 mm^2 and 10×0.5 mm^2, respectively.

Proper bonding of neighbouring plates in a stack (Figure 4-29 a) is mandatory to ensure a good alignment of the diffracting planes and thus a well-defined focal spot on the detector. In fact, neighbouring plates can be affected by three kinds of misalignment with respect to each other, expressed by misalignment angles φ_b, φ_c, φ_d, as shown in Figure 4-29 b, c, d respectively. Consider

λ and θ_B the wavelength and the Bragg diffraction angle of a photon beam in the case of no misalignment (Figure 4-29 a). The photon beam is quasi-parallel to the x axis and undergoes diffraction by the lattice planes perpendicular to z axis (i.e. (111) planes). The wavelength of a photon undergoing diffraction by a plate misaligned as in Figure 4-29 b is:

$$\lambda'_b = \frac{\lambda \sin(\theta_B - \varphi_b)}{\sin \theta_B} \sim \lambda(1 - \varphi_b \cot \theta_B) \qquad \textit{Equation 11}$$

where φ_b is assumed to be small. In the case of Figure 4-29 c, the photon wavelength under diffraction is:

$$\lambda'_c = \lambda \cos \varphi_c \sim \lambda \left(1 - \frac{\varphi_c^2}{2}\right) \qquad \textit{Equation 12}$$

Finally, for the case of Figure 4-29 d, there is no variation of wavelength:

$$\lambda'_d = \lambda \text{ for any } \varphi_d \qquad \textit{Equation 13}$$

Thus, misalignment φ_b is critical (first order contribution), φ_c is less important (second order contribution), and φ_d is unimportant. The standard configuration for a stack of primary CDPs crystals in a X-ray lens is with the photon beam parallel to the x direction (Figure 4-28 b), to exploit diffraction by curved (111) planes. For fabrication of a stack of plate-like curved crystals, special care must be paid to avoid the first misalignment. However, for complete characterization of the misalignments in the stack, photons diffracted by lattice planes perpendicular to y axis (i.e. $(22\bar{4})$) will also be analyzed, while keeping the photon beam quasi-parallel to the x direction as in Figure 4-28 b. In this case, the rank of misalignments changes, because misalignment φ_d becomes critical, φ_c less important and φ_b unimportant. Thus, the formulas for the wavelengths under Bragg diffraction are expressed by substituting φ_d, φ_c, φ_b in Equation 11Equation 12Equation 13 respectively. Trivially, no diffraction is possible by the planes perpendicular to the x axis. With the aim to achieve still more information about the misalignments, the stack of crystals will be exposed to an X-ray beam quasi-parallel to the z axis, as in Figure 4-28 a. In this case, for diffraction by the planes perpendicular to the x axis (i.e. $(2\bar{2}0)$), misalignment φ_b is critical, φ_d less important and φ_c unimportant. For the same beam configuration and diffraction by planes perpendicular to y axis, misalignment φ_c is critical, φ_d less important and φ_b unimportant. In this configuration, diffraction by the planes perpendicular to z axis is impossible.

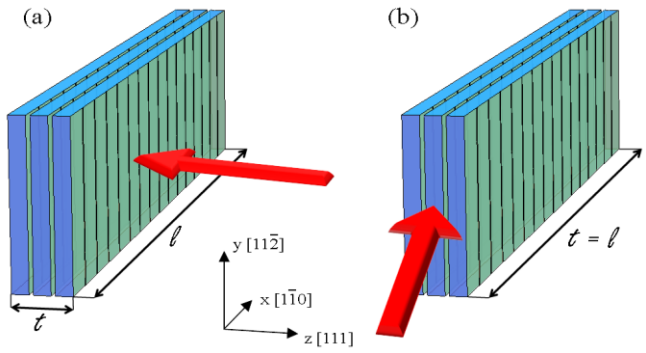

Figure 4-28

Probe X-ray beam (red arrow) enters the stack quasi-parallel to the $(2\bar{2}0)$ (a) or to the (111) crystallographic planes (b). In case (a), beam size along x and y axes was 1 mm and 10 mm, respectively. In case (b), beam size was 0.5 mm along z and 10 mm along y axis.

For a diffractometer as in (Stockmeier, 2008), scattering from a straight crystal will result in a line profile onto a detector located at the focusing position. The FWHM of the intensity profile taken on a cross section perpendicular to the diffraction line is solely determined by the size of the X-ray source and the thickness of the crystal. Conversely, for a curved crystal the width of the

intensity profile is also related to the deformation of diffracting planes, i.e., to the bending angle of the curved crystal. In particular, in contrast to a straight crystal, a curved crystal can concentrate the diffracted X-rays on a smaller focal distance (converging mode) or on a larger distance (diverging mode). For the configuration as in Figure 4-28 a, a crystal is in converging mode if it exposes the grooved side (convex) to the incident beam. It is in diverging mode when it exposes the side without grooves (concave) to the beam. On the contrary, for the configuration as in Figure 4-28 b, a crystal is in converging mode if it exposes the ungrooved side to the incident beam, and it is in diverging mode when it exposes the side with the grooves. The line width δ at the detector was obtained by combining the formulas of the focal spot size in (Rekveldt, 1983) (Stockmeier, 2008) under small-angle approximation.

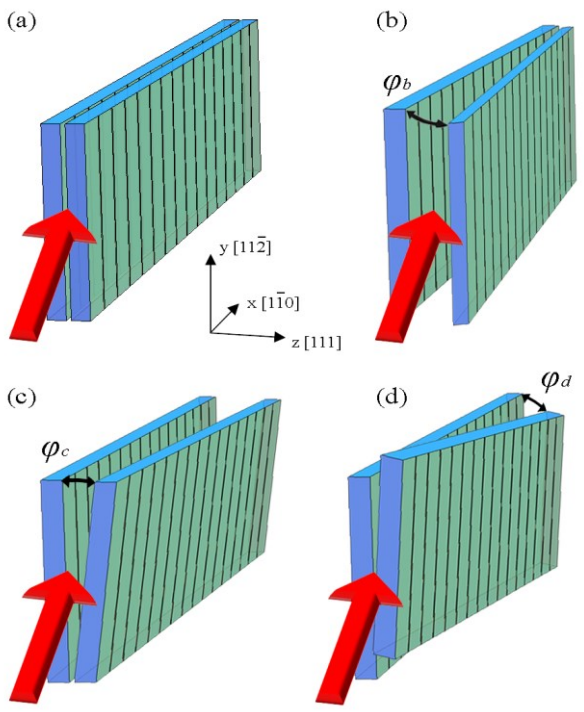

Figure 4-29

Perfect bonding of plates in a stack (a). To achieve a well-defined focal spot on the detector, misaligned by angle φ_b is critical (b), by angle φ_c is less important (c), by angle φ_d is indifferent (d).

$$\delta = \sqrt{a^2 + \left(2t\theta_B \pm 2f\frac{l}{R}\right)^2} \qquad \textbf{Equation 14}$$

The sign (+) holds for the diverging mode, the sign (-) for the converging mode, a is the size of the X-ray source, t is the crystal thickness traversed by radiation, f is the sample-to-detector distance, l is the length of the crystal bent by curvature radius R (see Figure 4-28). The equation holds true for both geometries in Figure 4-28, the term $2t\theta_B$ is the contribution of broadening due to the thickness of the sample, while $2f\,{}^{l}/_{R}$ represents the contribution of bending ($l = t$ for the case sketched in Figure 4-28 b).

The beam was set quasi-parallel to the z axis (see Figure 4-28 a) and in diverging mode. Figure 4-30 a, b, c, d and e show the diffraction patterns as taken at different values of coordinate x while Figure 4-30 f, g, h, i and j highlight the cross-section area of the focal spot due to diffraction by $(2\bar{2}0)$ planes. As can be seen, a single and well-defined spot on the detector is visible up to 10 mm from the other side of the stack, i.e., the critical misalignment φ_b was very low. At each position, the FWHM of the Gaussian intensity profile satisfies the theoretical prediction by Equation 14. At nearly 8 mm far from the other edge of the multi-crystal (x = 37 mm) and throughout its remaining side, the profile of the focal spot was no longer a single Gaussian. Another diffraction peak appeared at an angle shifted apart by 27 arcsec (1.15 mm), meaning that two of the plates were slightly misaligned to each other because of a not perfect bond near the stack edge.

Diffraction spots by other planes are also present, from which some information can be drawn. The diffraction spot of $(22\bar{4})$ planes, 90° tilted respect the $(2\bar{2}0)$ diffraction spot, would provide direct information about misalignment φ_c. Unfortunately, this spot is not visible, because the beam is nearly parallel to the longer side of the stack, making the Bragg angle very low, thus setting the energy of the $(22\bar{4})$ reflection above the instrumental limit of 450 keV. In absence of the $(22\bar{4})$ diffraction spot, reflections by other planes can be used to estimate φ_c. In particular, $(20\bar{2})$ planes are just 30° tilted

with respect to the $(22\bar{4})$ and their diffraction spot is clearly visible in the upper part of Figure 4-30a. A significant misalignment φ_c would split the skew planes $(20\bar{2})$. Such splitting was not observed, an indication that misalignment φ_c is very low.

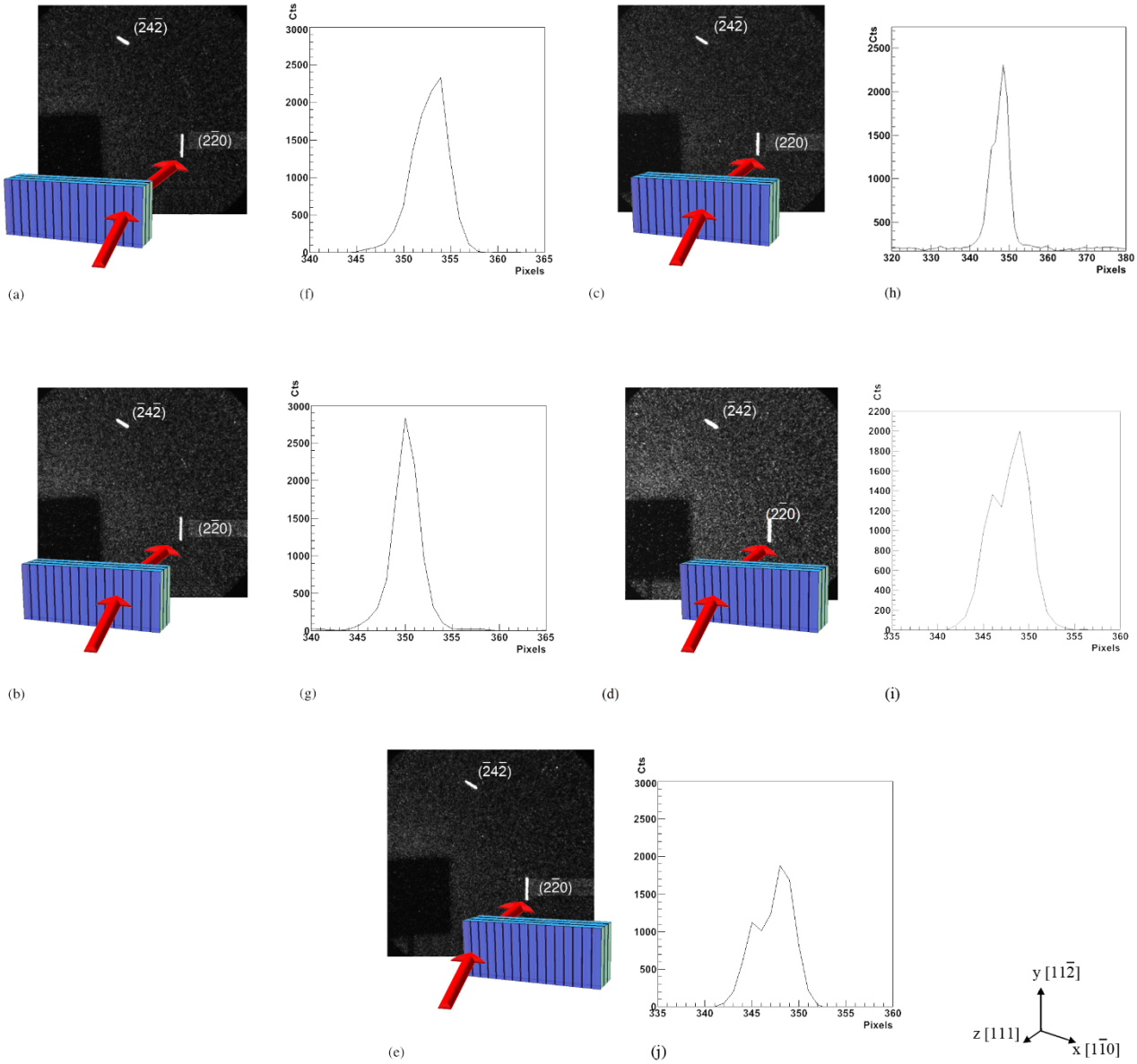

Figure 4-30

Diffraction patterns obtained with the beam (10×1 mm²) quasi-parallel to the z axis at several distances from the edge of the sample, i.e., at (a) x = 1 mm, (b) x = 21 mm, (c) x = 35 mm, (d) x = 39 mm, (e) x = 43 mm, associated with horizontal average cross-sections corresponding to the (2$\bar{2}$0)-diffraction (f, g, h, i and j). A single and well-defined focal spot was recorded up to 35 mm from the edge of the Si stack. Misalignment of (2$\bar{2}$0) planes, as visible by the presence of another diffraction peak, starts at x = 37 mm up to the edge of the multi-crystal and keeps constant throughout its remaining side. The distance between sample and detector was 4.45 m.

The stack was then investigated with the beam quasi-parallel to the *x* axis (as in Figure 4-28 b), the crystal being in converging mode. Indeed, this measurement represents the scheme for functional operation of a multi-crystal as an optical component for a Laue lens through diffraction by (111) planes (see Figure 4-25). Results in Figure 4-31 a – b show the diffraction spots of several crystallographic planes and the cross-section area corresponding to the (111) planes. As can be noticed, diffraction from (111) planes of the three plates results in a single and well-defined focal

spot on the detector, meaning that the critical misalignment φ_b is negligible. The FWHM of the intensity profile due to (111) planes is in agreement with Equation 14, i.e., 1.75 mm (5 pixels). When the beam impinged onto the stack in diverging mode with respect to the (111) planes, X-ray diffraction from CDP resulted in a defined focal spot on the detector (Figure 4-31 c), the width of the intensity profile (Figure 4-31 d) being approximately 4 mm (10.5 pixels). As expected, the focal spot on the detector was smaller in converging mode than for in the diverging case. In summary, the multi-crystal behaves as it were a single crystal from the point of view of diffraction by (111) planes. This observation is important because it proves the functionality of the stack of crystals for the applications which it is designed for.

Diffraction spots by other planes are also present, consisting in three distinct spots in this case. For the same reason discussed in the paragraph above, the diffraction spot of $(22\bar{4})$ planes is not visible, but is possible to obtain information about misalignment φ_d by other planes. In particular, $(11\bar{3})$ planes are tilted by just 10° with respect to $(22\bar{4})$, and their diffraction spots are clearly visible. Thus, although (111) planes are not critically misaligned, diffraction from $(11\bar{3})$ planes resulted in three focal spots, meaning that the plates suffer from a misalignment φ_d. However, this misorientation does not affect the efficiency of the (111) diffraction, showing that a tolerance is allowed in the alignment of the CDP crystals inside the stack while not affecting the total performance. The alignment of the plates in the stack was also investigated in converging mode at several distances from the edge of the sample, by an X-ray beam with smaller size (10×0.5 mm^2). Results in Figure 4-32 confirm that the stack of Si crystals behaves as it were a single crystal and no critical misalignment of the CDP occurs.

The stack of grooved Si crystals has proven to yield a well-defined focal spot under X-ray diffraction, highlighting sufficiently good alignment of the CDP in the stack. In this way the stack behaves as it were a single crystal from the point of view of diffraction by (111) planes. Some misalignment between the plates has been shown to occur at the edges of the stack, thus the homogeneity of the thickness should be controlled in a better manner. The plates in the stack are self-standing CDP crystals, whose curvature can be controlled by simply adjusting experimental parameters of surface grooving. This technology opens up a viable way to build up optical components for X- or γ-ray diffraction of any size.

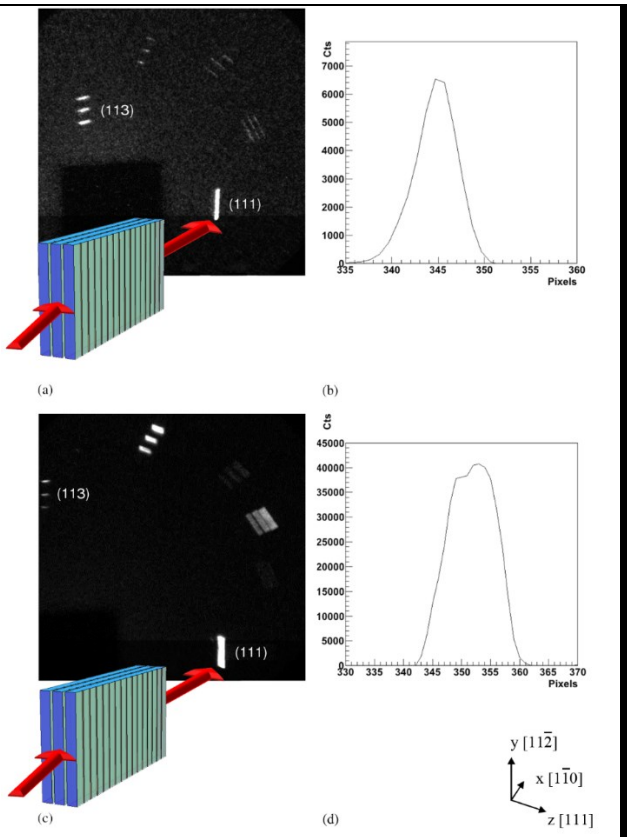

Figure 4-31

Diffraction patterns recorded with the beam 10×1 mm^2, in converging mode (a). Horizontal average cross-section of the focal spot corresponding to (111) diffraction is highlighted (b). Notice that diffraction from (111) planes results in a single and well-defined focal spot (FWHM = 1.75 mm) on the detector. As the beam (10×1 mm^2) is in diverging mode with respect to the CDP (c and d), the focal spot from (111) planes is nearly well defined, its FWHM being approximately 4 mm. Here the diffraction peaks correspond to energies of 247 keV and 169 keV for converging and diverging mode, respectively. The distance between sample and detector was 4.45 m.

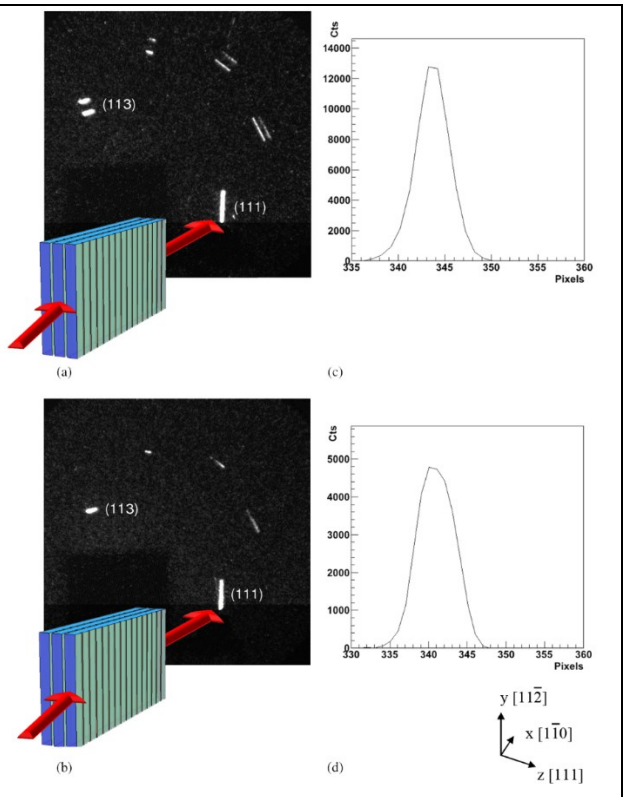

Figure 4-32

Diffraction patterns recorded with the beam 10×0.5 mm^2, in converging mode, at several distances from the edge of the stack, i.e., at (a) z = 1.5 mm, (b) z = 2.5 mm. The horizontal cross-sections (c and d) of the profile due to (111)-diffraction confirm that the stack behaves as it were a single crystal. For both cases, the energy at which diffraction by (111) planes occurs is about 250 keV. The distance between the stack and detector was 4.45 m.

4.3.2.2 Stack of lamellae

The work below provides first results about the feasibility of a self-standing stack composed of QM crystals. Ten thin Si crystalline lamellae were stacked, and then the planes affected by the quasi-mosaic effect were tested by polychromatic X-ray diffraction. The multi-crystal behaved as one diffracting element, yielding a broad and smooth diffraction profile. The self-standing stack analyzed in this section was produced with a curvature far larger than the previous stacks to allow a better analysis of the misalignment between lamellae. In fact, if the curvature radius of the lamellae was the value realistically useful for astrophysical applications (tens of meters), diffraction efficiency of QM planes would be nearly 1, not resulting in a clear distinction of the positions of QM passbands whereas these latter superpose each other. The optimal condition for a better analysis would be that each lamella diffracted a very small part of the beam. A decrease in diffraction efficiency is possible by over-bending the diffraction planes beyond a certain limit called critical curvature radius R_C (Malgrange, 2002) (Bellucci V. G., 2013), so that the diffraction efficiency falls off. For this reason, the QM stack was manufactured with a very large curvature, in order to have diffraction efficiency of each lamellae to be about 1 %. Thus, the beam interacting with each lamellae would have nearly the same intensity. In this case, each crystal would produce a diffraction image of nearly-equal intensity regardless of passband superposition between them. The diffraction image of all the crystals would sum up on the detector, and the superposition of their passbands would be clearly visible in the total diffraction image as an increase in counts. As an example, the reflectivity of one lamella under this condition at 100 keV was 1.2 %, while the superposition of all the photon passband of the lamellae would give a reflectivity of 11 % at the same energy.

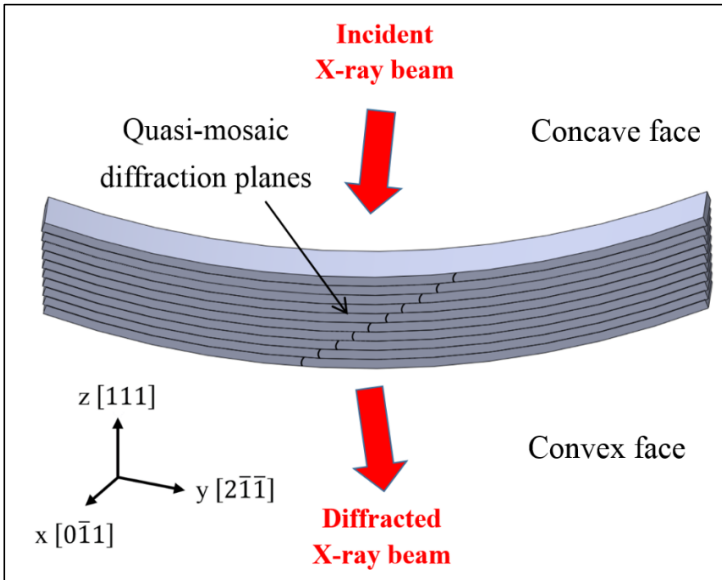

Figure 4-33

Representation of a stack of QM crystals undergoing diffraction as in the experiment. The beam enters the stack from the convex face, undergoes diffraction from $(4\bar{2}\bar{2})$ *QM planes, and exits the stack from the concave face. Realistically, the stacking process induces a small random misalignement between each crystal.*

Commercially available pure Si wafer was diced to form ten plates by using a high precision dicing saw (DISCO^{TM} DAD3220). The plates were 0.2 mm thick, with lateral dimension 5 mm x 45 mm. Lattice orientation of the largest surface was (111), while the surface with dimension 0.2 mm x 5 mm had crystalline orientation $(2\bar{1}\bar{1})$. By using a low-stress thermal resin, the crystals were bonded one over the other to form a stack (Figure 4-33). This latter was then mounted on a specifically designed rigid holder realized at our laboratories. The holder imparted to the stack a controlled primary cylindrical curvature (0.2 m nominally) that resulted in a secondary curvature of the $(2\bar{1}\bar{1})$ planes due to the QM effect. Finally, the holder was positioned on a hot plate where, at nominal temperature, the resin solidified, yielding a self-standing curved stack of plates. The production

method is similar to that in (Smither, 2008). To verify the curvature imparted to the stack, subtraction of the morphological profiles before and after the mechanical process was done through optical profilometry (VEECO^{TM} NT1100). This analysis was executed at the center of the stack for the crystal on the top and on the back faces of the stack (

Figure 4-34). These two faces presented a different curvature radius, probably because of the resin was not able to maintain the crystal plates at the same curvature radii at such high curvature. It was impossible to carry out the same analysis on the edges of the stack, because the large quantity of glue blur at the clamping points caused significant optical errors when interferometric analysis was attempted.

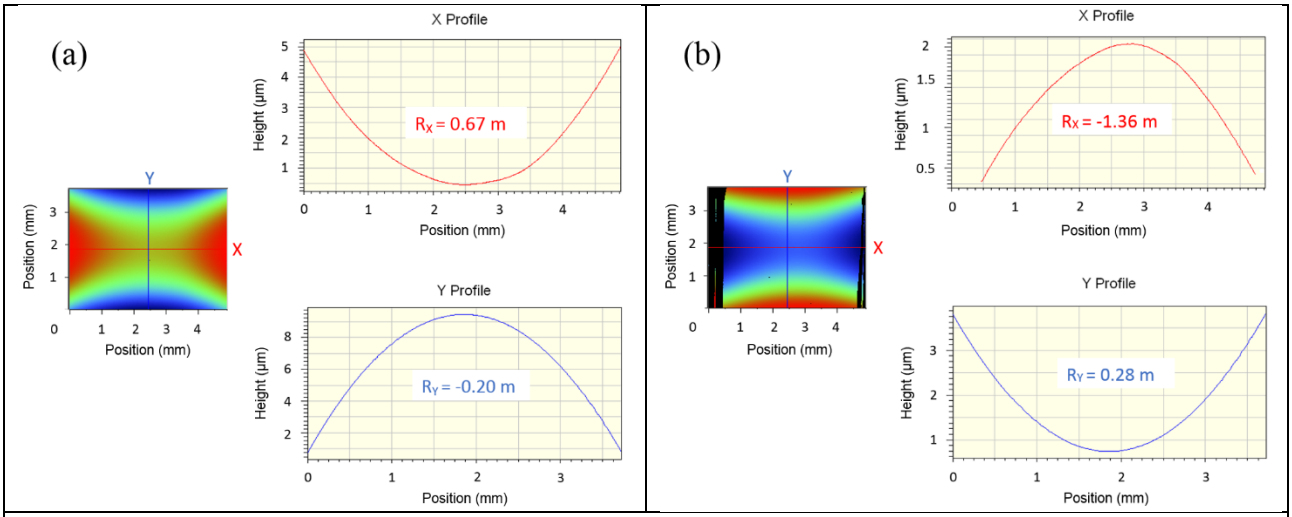

Figure 4-34

Profilometric analysis at the center of the sample as taken on the convex (a) and concave (b) surface. In both cases, it is possible to see a uniform curvature in the Y direction, i.e. the direction of the primary curvature used for focusing. Curvature on the X direction is produced by anticlastic deformation. The curvature radii in cases (a) and (b) are different, probably because of the limited stiffness of the glue used for binding the crystals together in the stack. For the case (b), it is possible to see some optical errors caused by the glue blur at the border of the image.

The stack was tested through X-ray diffraction at ILL (Grenoble, France) by using a hard x-ray diffractometer based on a focusing effect, occurring when a divergent and polychromatic X-ray beam diffracts through a crystal (Stockmeier, 2008). This technique is schematically represented in (4.3.2.1 Stack). The CCD camera featured a spatial resolution of about 0.35 mm (one pixel size). The source has dimension 1×1 mm^2, while the distance between sample and source was set at 4.45 m, thus determining a maximum tilt sensitivity of 8.1 arcsec. A slit with variable size was positioned just before the sample in order to delimit the width of the X-ray beam. The multi-crystal was analyzed with the beam penetrating through its 45×5 mm^2 surface at different distances from the edge of the sample, quasi-parallel to the $(4\bar{2}\bar{2})$ planes. The beam entered the sample through its concave side. We preferred this configuration because it allowed a better resolution than in the case where the beam entered the sample through the convex side. A sketch of the configuration is shown in Figure 4-33. Beam size was chosen to be 0.5 × 5 mm^2. The width of the diffraction lines is directly related to lattice distortion of the crystal under analysis.

Figure 4-35 a shows a diffraction image of the center of the stack, while Figure 4-35 b shows a diffraction image taken near the edge on the stack. The diffraction pattern of the center is broad and

uniform, even if some asymmetries are visible, both in the 2D image and in its cross section. In the 2D image, the asymmetry is probably the result of some torsion in the crystal, which does not appreciably influence the performance of the stack. In the cross section, the asymmetry in the shape of the distribution is probably due to the random misalignment between the crystal plates in the stack. At the opposite, the diffraction pattern taken near the edge of the stack presents different well-defined peaks and valleys. This is a result of the manufacturing process used to obtain the stack. In fact, the holder used for bending the stack induced nearly no curvature at the clamping points of the crystal, thus producing a stack of nearly-flat crystals at the edges. Then, the bending contribution due to both primary and QM curvatures is smaller than the misalignment between the plates, showing the structure of the multi-crystal in the diffraction pattern.

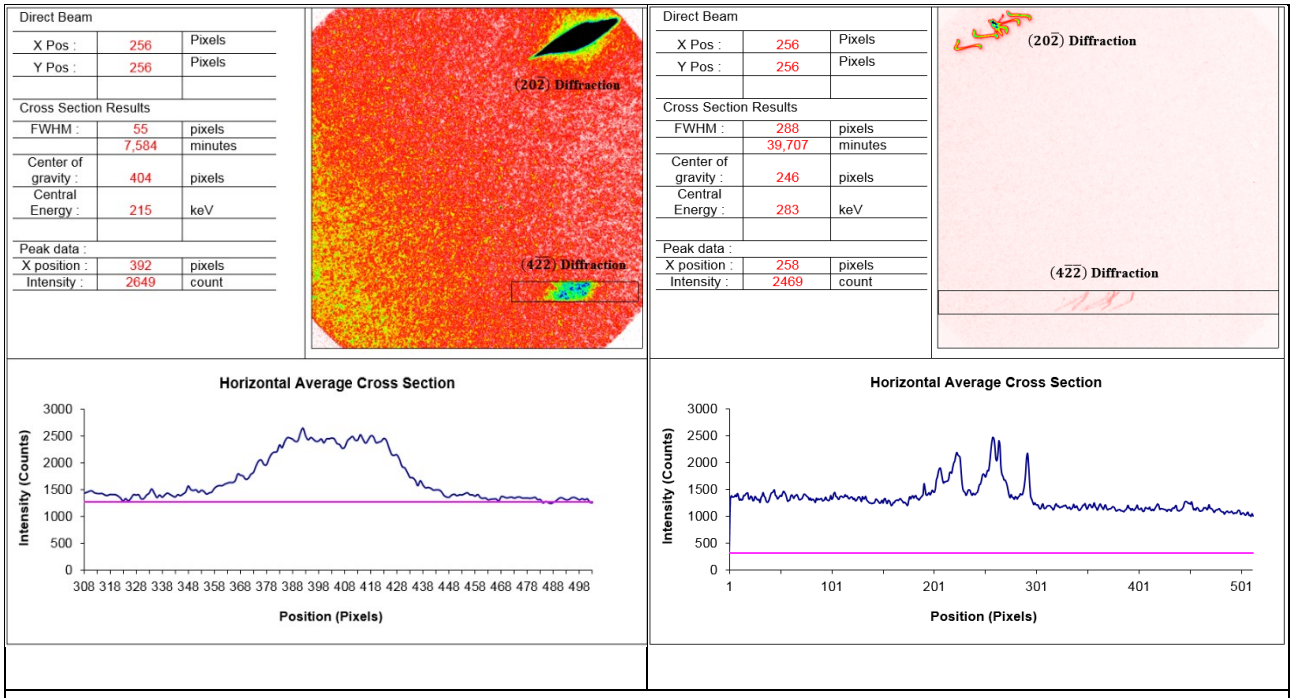

Figure 4-35

Unelaborated experimental diffraction image for the center (a) and for the edge of the QM stack (b). For both cases, multiple information is given. The table on the top-left provides information about the beam position, and first data for the cross-section of QM $(4\bar{2}\bar{2})$ *diffraction distribution. On the top-right a 2D image of the diffraction spots produced on the detector is shown. QM* $(4\bar{2}\bar{2})$ *diffraction distribution is highlighted in the bottom-right of the 2D image, while another diffraction spot corresponding to* $(20\bar{2})$ *reflection is clearly visible.* $(20\bar{2})$ *reflection is always more intense than that for the* $(4\bar{2}\bar{2})$*. (a) Both distributions have an oblique-shape, which highlights some torsion in the stack. The 1D graphic on the bottom is the mean cross section of the QM* $(4\bar{2}\bar{2})$ *diffraction distribution. A smooth shape is evident, which means that the crystals composing the stack are far less misaligned than the contribution of the primary curvature. The slightly asymmetric shape is probably produced by the random misalignment of the passbands composing this cross-section. (b) From the 2D image is evident the misalignment between the crystals composing the stack with some torsion. In fact, both the QM* $(4\bar{2}\bar{2})$ *and the* $(20\bar{2})$ *diffraction distributions are divided into multiple spots, each one with different shape. From the 1D cross section of the QM* $(4\bar{2}\bar{2})$ *diffraction distribution at the bottom, the structure of the stack is evident. Indeed, multiple diffraction peaks are visible corresponding to the crystals composing the stack. Because of the smaller curvature of the crystals, there is no complete overlap. A misalignment between each crystal larger than in case (a) is also evident.*

Figure 4-36 a, b show the elaborated experimental data with their errors. In both cases, the noise baseline was subtracted to the diffraction patterns. Errors are shown as black-, gray-, white-shaded zones up to three times the standard deviation, in units of the latter. The standard deviation was calculated from the counting rate far from the diffraction spot, in order to consider the errors due to electronic noise and diffused photons, which are present in an experimental setup relying on an uncollimated detector.

Figure 4-36 c, d compare experimental data with theoretical expectations. In these cases, the noise baseline was subtracted, too. The red step-like distribution represents the best fit for the superposition of the QM passbands only, without the contribution due to the superficial curvature. The green dotted curve represents the theoretical diffraction profile, without considering the random noise. The QM passbands positions were derived by a computer simulation, by changing the positions of the passbands until the diffraction profile best fits the experimental data. At the center of the stack (Figure 4-36 c), a progressive primary bending was assumed along the stack thickness, from 0.20 m at the top face of the stack, to 0.28 m at the back face, the instrumental uncertainty being 5 %. Then, the primary curvature contributed to the diffraction distribution with a broadening from 368 arcsec to 516 arcsec. The QM passband width of lamellae was know through the theory of elasticity to range from 42 arsec to 59 arcsec. The expected diffraction profile was calculated as the summation of the contribution of each crystal in the stack. The torsion of the stack results in a further broadening of the cross section by (148 ± 16) arcsec. Through best fit of the QM passbands and taking into account the superficial curvature and the torsion, it resulted in a misalignment between the lamellae less than 16 arcsec (2 pixels), consistently with the misalignment already achieved for stacked crystals. A typical lamella built with a curvature radius useful for straight application in astrophysics would have a QM passband width in the order of few arcsecs. In this case, a misalignment between passbands in the order of 16 arcsecs or lower would be ideal. At the opposite, the single contributions of the lamellae are well visible at the edge of the stack (Figure 4-36 d). The maximum misalignments between lamellae is (694 ± 8) arcsec, while the mean misalignment is (172 ± 8) arcsec. In fact, the manufacturing method is likely to induce stronger stress and extra random misalignments at the clamping points with the holder, i.e. at the edges of the stack. In this case, the smaller curvature also lowers the passband due to primary curvature to less than the misalignment between crystals. The curvature radius at the border can be calculated by changing the primary curvature in order to match the width of the peaks in diffraction data. The primary curvature radius results to be (3.94 ± 0.60) m, so that the spread due to the primary curvature is (26 ± 4) arcsec, and the expected QM passband is (3 ± 0.5) arcsec. The uncertainty is mainly due to the resolution of the detector.

The experimental measurements allows one to conclude that a stack of quasi-mosaic crystals can be built up with suitable reciprocal misalignment to achieve a broad and smooth passband. Despite the crystals were far more bent than for the previous stacks, the reciprocal alignment remained good. The relative alignment of the QM crystals allows one to stack a multitude of thin lamellae to obtain thick diffracting elements. Clearly, for the preparation method we used, it is necessary to cut out the parts near the edges at the clamp positions. In spite of this limitation, the method of QM stacking proved to work.

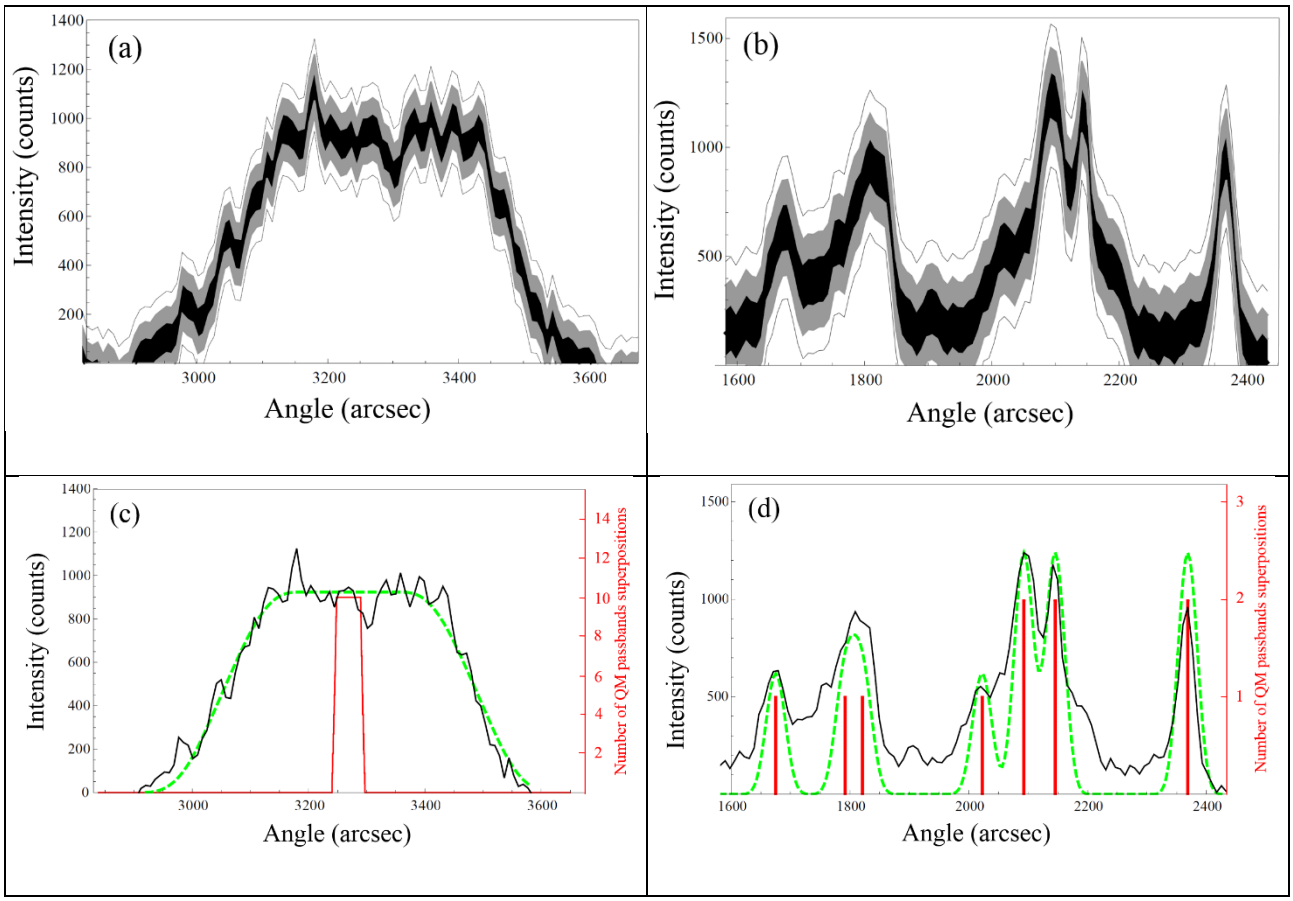

Figure 4-36

(a),(b) experimental data with their uncertainty in units of the standard deviation at the center and at the edge of the QM stack. The black-, gray-, white-shaded areas correspond to an experimental uncertainty of less than one, two, and three standard deviations respectively, (c) and (d) compare the experimental data with the theoretical calculation for the mean distribution of the diffraction cross-section at the center and at the edge of the QM stack. In each case, the noise baseline was subtracted to experimental data. In (c),(d), the continuous black curve represents experimental data. The green dashed curve represents the theoretical expected diffraction distribution, taking into account the position of QM passbands of the crystals composing the stack, the smoothing contribution of primary curvature, the torsion and the finite size of the source. The red continuous step-like image represents the best-fit positions of the QM passbands and their superposition, in units of the number of passbands superposing in each point. At the stack center (c) the misalignment between passbands is lower than 16 arcsec, the stack responds as one diffracting element, resulting in a broad and smooth diffraction profile. At the stack edge (graphics (d)) the passbands shrink down because of the smaller curvature, and the misalignments rise, so that they do not appreciably superpose.

4.4 Tilted CDPs crystals

Crystals inherently feature anisotropy of their physical properties and, in particular, of their mechanical characteristics. As a slab of isotropic material is bent, it exhibits curvatures on the main faces, while the planes orthogonal to the main surfaces keep flat. Skew planes exhibit a curvature equal to the projection of the main curvature on them. Differently, for an anisotropic material such as a crystal, the direction-dependent components of the stiffness tensor induce a more complex curvature field. As X-ray diffraction occurs in lattice planes orthogonal to the main surfaces, the deformations that appear due to anisotropy are conventionally named quasi-mosaic (QM) curvatures. Diffracting planes orthogonal to the main surfaces are called Laue symmetric planes. The secondary QM curvature, affecting the symmetric diffracting planes, is used for rising the flux of diffracted photons. Indeed, in case of no curvature, the flux of diffracted photons would be that for a perfect crystal, i.e. a relatively low figure. Unfortunately, the theory of linear elasticity envisages the impossibility to induce the quasi-mosaic curvature to any family of symmetric lattice planes. Presently, only few crystalline orientations (e.g. (111), (311) and (422)) have been tested to exhibit the QM curvature (4 Innovative crystals for hard X-ray lenses). However, crystals highlighting the QM effect can show a curvature driven by anisotropy along asymmetric planes too, i.e. the planes not orthogonal to the main surfaces, or along skew planes. Indeed, some families of lattice planes, which would be flat in the symmetric configuration, can be bent for planes not-parallel to any surface.

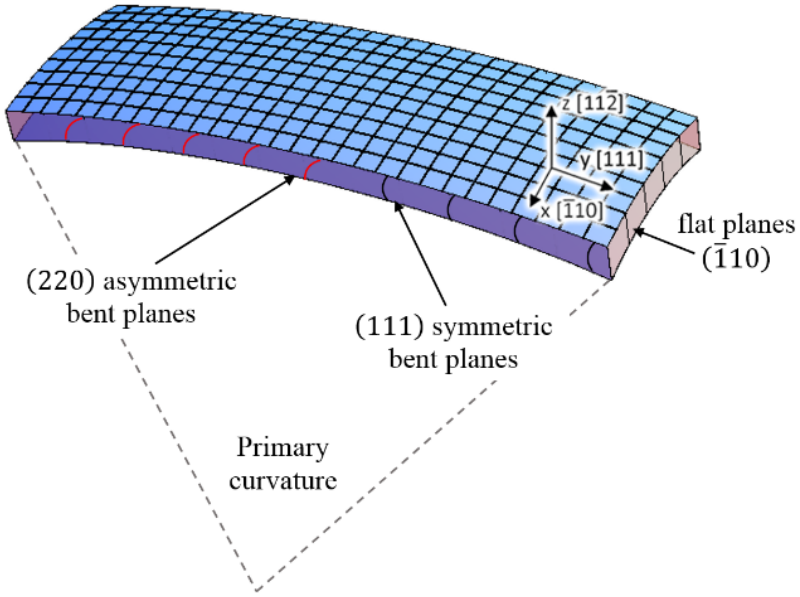

Figure 4-37

Sketch of a Ge grooved sample produced during the LAUE Project. Curved (111) QM symmetric planes and (220) asymmetric lattice planes are highlighted.

The opportunity to implement any kind of lattice diffraction with bent planes, or at least the principal ones, is important for application of crystals with internal curvatures as focusing X-rays optical elements. The possibility to use any lattice reflection is a necessary condition for the employment of focusing crystals in the construction of monochromatic Laue lenses (Roa, 2005) (Adler, 2003). Moreover, we already demonstrated that the possibility to use different lattice reflections in focusing crystals would increase the sensitivity of polychromatic Laue lenses (4 Innovative crystals for hard X-ray lenses). In this section, we show the focusing capability of bent crystals due to diffraction by lattice planes in asymmetric configuration or skew planes, in particular (220) planes. This achievement is important because the (220) planes exhibit a strong diffracting power, but no curvature of such planes can be observed in symmetric mode for focusing crystals. Crystals with (220) CDPs can be arranged in a polychromatic Laue lens without superposition with the crystals relying on standard (111) symmetric bent planes, significantly increasing the geometric

area of the lens. A method for calculating the curvatures induced by crystalline anisotropy in any family of lattice planes is also presented. Finally, the experimental results were compared with the expectations showing good agreement. The availability of focusing crystals implementing any diffracting planes with a significant curvature opens up the possibility for a leap in sensitivity for polychromatic Laue lenses, and envisage the feasibility of monochromatic Laue lenses with focusing elements.

4.4.1 Theoretical

Anisotropy of the elastic constants is a peculiar feature of crystalline materials. Consider a flat crystal with the shape of a plate and its main morphological surfaces as atomic planes. A primary curvature to the plate can induce secondary curvatures to other atomic planes as a consequence of anisotropy. The secondary curvatures are strictly bound to the elastic constants of the material, i.e. to the components of the compliance tensor S_{ij} (7 Theory of elasticity at the first order). Silicon is a brittle material at room temperature, and its stress-strain curve is linear up to the breaking point ((Milman, 2007)). Then, curvatures in silicon are always treated with the theory of linear elasticity. The curvature induced in a symmetric plane can be calculated by derivation of the components of the displacement vector $\boldsymbol{p}$ by the coordinates of the frame x, y, z.

$$\boldsymbol{p}(x,y,z) = \begin{pmatrix} u(x,y,z) \\ v(x,y,z) \\ w(x,y,z) \end{pmatrix}; \quad \boldsymbol{r} = \begin{pmatrix} x \\ y \\ z \end{pmatrix}$$

where $\boldsymbol{r}$ is the position vector. A lattice plane can be located by the unit vector orthogonal to its face. Consider θ the azimuthal angle, and φ the polar angle, so $rot(\theta,\varphi)$ is the rotation matrix. The curvature of an asymmetric plane is better described by a rotated reference system $\boldsymbol{x'}$, $\boldsymbol{y'}$, $\boldsymbol{z'}$, where $\boldsymbol{x'} = rot(\theta,\varphi).\boldsymbol{x}$, $\boldsymbol{y'} = rot(\theta,\varphi).\boldsymbol{y}$, $\boldsymbol{z'} = rot(\theta,\varphi).\boldsymbol{z}$. For calculating the curvature, it is necessary to derive the deformation vector $\boldsymbol{p}$ by the rotated coordinates x', y', z'. Then, it is necessary to write the deformation vector in the new coordinate system. It follows $\boldsymbol{r'} = (x', y', z') = rot(\theta,\varphi).\boldsymbol{r} \Longrightarrow \boldsymbol{r} = (x,y,z) = rot^{-1}(\theta,\varphi).\boldsymbol{r'}$ Then we can write x, y, z, as a function of x', y', z', θ, φ, and writing the deformation vector as a function of the same variables:

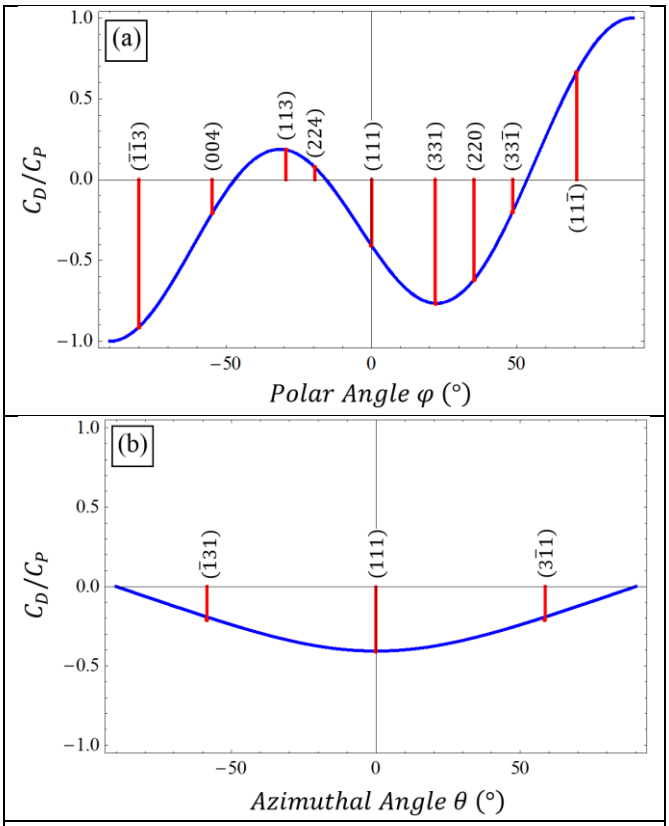

Figure 4-38

Dependence of the curvature ratio C_D/C_P vs. the polar angle φ (a) and the azimuthal angle θ (b) for a Ge sample spherically bent, with main face oriented as (211), and QM curvature of (111) planes. The variation of the curvature ratio is a continuous function as represented by the blue curve. The angle of lattice planes with small Miller indices are shown together with their curvature ratio as red bars.

$$\boldsymbol{p} = \begin{pmatrix} u(x', y', z', \theta, \varphi) \\ v(x', y', z', \theta, \varphi) \\ w(x', y', z', \theta, \varphi) \end{pmatrix}$$

Where for rectangular plate crystals (7.4 Displacement field of a rectangular flexed plate), the components of the displacement field are

$$u = \frac{1}{2}\left[\frac{M_x}{I_x}(S_{51}z^2 + S_{61}yz + 2S_{11}xz) + \frac{M_y}{I_y}(S_{52}z^2 + S_{62}yz + 2S_{12}xz)\right]$$

$$v = \frac{1}{2}\left[\frac{M_x}{I_x}(S_{41}z^2 + 2S_{21}yz + S_{61}xz) + \frac{M_y}{I_y}(S_{42}z^2 + 2S_{22}yz + S_{62}xz)\right]$$

$$w = \frac{1}{2}\left[\frac{M_x}{I_x}(S_{31}z^2 - S_{11}x^2 - S_{12}y^2 - S_{16}xy) + \frac{M_y}{I_y}(S_{32}z^2 - S_{12}x^2 - S_{22}y^2 - S_{26}xy)\right]$$

Then the curvature of the primary surface along the *x* direction is

$$C_P = \frac{\partial^2 w}{\partial y^2} = -\left[\frac{M_x}{I_x}S_{12} + \frac{M_y}{I_y}S_{22}\right]$$

The formula for the curvature is an approximation valid for small deformation. The curvature calculated with the exact formula (e.g. $C_P = \frac{\partial^2 w}{\partial y^2} / \left(1 + \left(\frac{\partial w}{\partial y}\right)^2\right)^{3/2}$) differs of about 10^{-5} % from the curvature calculated with the approximated formula for the samples of this thesis and for the deformation we consider experimentally. The deformation vector relative to the new axes can be calculated by projecting the vector $\boldsymbol{p}$ onto these latters:

$$\boldsymbol{p}' = \begin{pmatrix} \boldsymbol{p}.\boldsymbol{x}' \\ \boldsymbol{p}.\boldsymbol{y}' \\ \boldsymbol{p}.\boldsymbol{z}' \end{pmatrix} = \begin{pmatrix} u'(x', y', z', \theta, \varphi) \\ v'(x', y', z', \theta, \varphi) \\ w'(x', y', z', \theta, \varphi) \end{pmatrix}$$

The curvature along a certain axial direction is the second derivative of one component of the vector $\boldsymbol{p}'$ with respect *x'*, *y'*, or *z'*. For the case of interest, the curvature of the diffraction planes in the *x'z'* plane is

$$C_D = \frac{\partial^2 v'}{\partial z'^2}$$

From this expression, the explicit formula for the curvature of an asymmetric plane rotated by *θ, φ* can be calculated as

$$C_D = \frac{\partial^2 v'}{\partial z'^2} = -\{$$

$$\frac{M_x}{I_x}[$$

$$(S_{51}\cos^2\varphi + S_{61}\sin\varphi(\sin^2\theta - \cos^2\theta)\cos\varphi + 4S_{11}\sin\theta\cos\theta\sin\varphi\cos\varphi)\sin\theta\cos\varphi$$

$$-(S_{41}\cos^2\varphi + 2S_{21}\sin\varphi(\sin^2\theta - \cos^2\theta)\cos\varphi + 2S_{61}\sin\theta\cos\theta\sin\varphi\cos\varphi)\cos\theta\cos\varphi$$

$$-(S_{31}\cos^2\varphi - 4S_{11}(\sin\theta\cos\theta\sin\varphi)^2 - S_{12}\sin^2\varphi(\sin^2\theta - \cos^2\theta)^2 - 2S_{16}\sin\theta\cos\theta\sin^2\varphi(\sin^2\theta - \cos^2\theta))\sin\varphi$$

]

$$+\frac{M_y}{I_y}[$$

$$(S_{52}\cos^2\varphi + S_{62}\sin\varphi(\sin^2\theta - \cos^2\theta)\cos\varphi + 4S_{12}\sin\theta\cos\theta\sin\varphi\cos\varphi)\sin\theta\cos\varphi$$

$$+(S_{42}\cos^2\varphi + 2S_{22}\sin\varphi(\sin^2\theta - \cos^2\theta)\cos\varphi + 2S_{62}\sin\theta\cos\theta\sin\varphi\cos\varphi)\cos\theta\cos\varphi$$

$$-(S_{32}\cos^2\varphi - 4S_{12}(\sin\theta\cos\theta\sin\varphi)^2 - S_{22}\sin^2\varphi(\sin^2\theta - \cos^2\theta)^2 - 2S_{26}\sin\theta\cos\theta\sin^2\varphi(\sin^2\theta - \cos^2\theta))\sin\varphi$$

]

}

The ratio between the curvature of the diffraction planes and the imparted primary curvature, namely the curvature ratio, is a key parameter for planes bent by a secondary effect

$$C_D/C_P = \frac{\partial^2 v'}{\partial z'^2}\Big/\frac{\partial^2 w}{\partial y^2}$$

As an example, for a Ge plate with (11-2) main planes spherically curved by external momenta, quasi-mosaicity occurs for the symmetric (111) planes (7 Appendix). The asymmetry angle of a diffracting plane corresponds to its polar angle φ. Keeping the azimuthal angle θ fixed at position zero and changing φ, the curvature ratio changes as in Figure 4-38 a. As one can see, a certain curvature is present for any lattice plane orientation. Because of anisotropy, the variation of the curvature ratio is not a symmetrical function of φ. Then, keeping φ fixed at position zero and changing θ, the curvature ratio varies as in Figure 4-38 b. In this case, the function is symmetric, because the elastic constants on this plane are symmetric too.

4.4.2 Use of asymmetric CDPs

The first sample tested for highlighting curved asymmetric planes was a self-standing curved Ge monocrystalline sample fabricated within the LAUE Project (3.4 Crystals for the Laue project). The sample had a uniform curvature radius of (38.9 ± 2.0) m along the longest direction. The analysis was done for asymmetric (220) lattice planes, because this is the most intense reflection forbidden for the quasi-mosaic symmetric configuration. Two different instruments were used for testing the sample by diffraction, both instruments are located at the Institut Laue-Langevin (ILL, Grenoble, France).

Lattice plane	Asymmetry φ (°)	C_D / C_P	R_D (m)	Aperture (arcsec)	Diffraction Efficiency
(111)	0	0.406	95.7 ± 5	4.3 ± 0.2	0.55 ± 0.05
(220)	35.26	0.626	62.1 ± 3	8.0 ± 0.4	0.55 ± 0.05
$(11\bar{2})$	90	1	38.9 ± 2	-	-

Table 4-4

Parameters of the main lattice planes.

The facility utilized for the punctual characterization of the sample is named DIGRA, which was specifically built for characterizing instrumentation for astrophysics. The γ–ray beam energy was 181.931 keV and its monochromaticity was $\Delta E/E \approx 10^{-6}$. The beam divergence can be modelled with a Gaussian function with a standard deviation of 1 arcsec. The collimated beam size was 5×1 mm^2. The sample rotary stage had a resolution of 1 arcsec. Characterization was carried out by performing RCs at the center of the sample. Data for the tested diffraction planes are reported in Table 4-4. The recorded RCs in Figure 4-39 are the result of four physical contributions. The first contribution is due to the curvature of the diffracting planes. On the strength of morphological characterization of the major surfaces of the plate, it is reasonable to assume a uniform curvature for all (symmetric and asymmetric) diffracting planes. Then, a uniform curvature contributes as a uniform function. The second contribution to RCs is due to the primary curvature. The beam width was finite (1 mm in this case) and hit the diffracting planes slightly rotated to each other as a consequence of the primary curvature. Moreover, the diffracting planes rotated deep into the crystal, because the beam did not enter the crystal perpendicular to the main face. These phenomena produce a trapezoidal response function, i.e. the convolution of two independent uniform distributions. Then, the voids generated by the grooving process have to be taken into account. The response function is decreased in the zones where the material lacks. Thus, the response function due to the primary curvature results in a trapezoidal-like shape with depths where the grooving process created voids. The third contribution to be considered is a slight degradation of the monocrystalline structure induced by the manufacture process. The scarce knowledge on the distribution of dislocations, defects and cracks in the crystal makes it unfeasible to predict quantitatively this contribution a priori. Such an effect is modelled by a decrease in diffraction efficiency by an unknown value to be estimated through a fit (3.4 Crystals for the Laue project). The fourth contribution is the angular resolution reached by the experimental setup. The finite divergence of the beam and the resolution of the rotational stage can be modelled by Gaussian distributions with standard deviation of 1 arcsec and 0.4 arcsec respectively. Then, the resolution of the experimental setup is a Gaussian distribution with standard deviation σ = 1.18 arcsec.

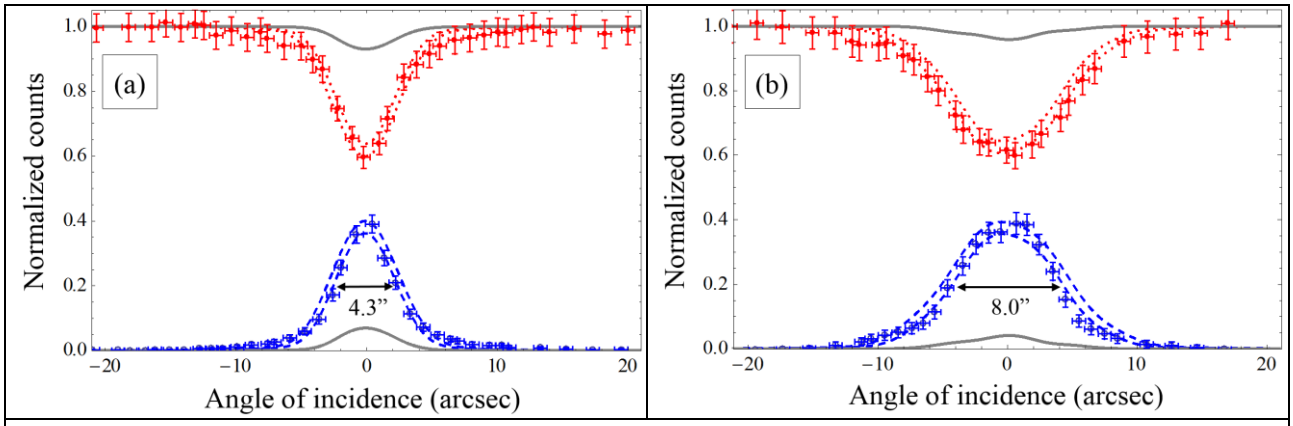

Figure 4-39

RCs of the (111) symmetric (a) and (220) asymmetric (b) diffracting planes of the crystal. Filled red circles plot the intensity of the transmitted beam, whereas the empty blue circles plot the intensity of the diffracted beam. Dotted red bands and blue dashed bands represent the expected result for the transmitted and diffracted beam. Grey continuous functions represent the expected results for flat diffracting planes.

Figure 4-39 a shows the experimental data for (111) symmetric reflection, compared with the expectation. Figure 4-39 b shows the same data for (220) asymmetric reflection. Calculation of the RCs were carried out by convolving the four contributions. The figures highlight good agreement between the theoretical expectation and the experimental results. Diffraction efficiency was an output of the fit, resulting in (55 ± 5) % for either the symmetric or asymmetric mode. The peaks of the experimental RCs are lower than 55 % as a consequence of the convolution. Efficiency was a good figure of merit inasmuch as it is higher than for any other performance achievable by mosaic crystals. Such evidence also indicates that the structure degradation due to the grooving (the third contribution) was not severe. The width of the diffraction profile is an important parameter of merit, because it is proportional to the fraction of incident photons diffracted by the crystal. As expected, the diffraction profile for (220) asymmetric reflection is wider than for (111) symmetric reflection. Moreover, among symmetric planes, the (111) planes exhibit the largest curvature (4 Innovative crystals for hard X-ray lenses), i.e. the larger diffraction profile. That makes the photon passband of (220) asymmetric planes larger than for any symmetric reflection. This observation may have an important impact on future developments of bent focusing crystals. Indeed, it proves that the asymmetric reflections can be also employed to rise the fraction of incident photons diffracted by the crystal.

In order to highlight the focusing effect driven by the sample primary curvature, the crystal was then analyzed through a diverging and polychromatic X-ray source (3.4.2.2 White-light diffractometer). The experiments was performed with X-rays emitted in the energy range 80 - 420 keV, with a continuous spectrum without characteristic lines. A sketch of the experimental configuration is shown in Figure 4-40. X-rays with different energies were diffracted towards a common focal point. The beam divergence ε was delimited to 0.1° by a squared collimator with aperture s = 9.5 mm positioned at 3.03 m far from the source. The size of the beam at the sample position resulted to be 14.5×14.5 mm^2. The extension of the crystal surface irradiated by the beam depended upon the asymmetry angle. The irradiated zone in symmetrical configuration was 10×14.5 mm^2, while for (220) asymmetric planes this latter resulted 10×17.7 mm^2. The crystal behaved as a cylindrical lens because the focusing effect only occurred in the scattering plane. Thus, diffraction of a polychromatic and divergent beam produced a line onto the detector (3.4.2.2 White-light diffractometer). Consider the case of a perfect

crystal and the sample-to-detector distance L_D equal to source-to-sample distance L_S. The width of the diffraction spot depends only on the X-ray source size and on the crystal thickness traversed by the beam. Conversely, a curved crystal can concentrate the diffracted X-rays at either smaller or larger distance. Indeed, it is possible to calculate the position of the image

$$\frac{1}{L_i} = \frac{1 - \theta_B \tan\varphi}{L_S} + \frac{2}{R_P \cos\varphi}$$

where L_i is the image distance for a crystal bent with primary radius of curvature R_P, diffracting photons at the Bragg angle θ_B, by lattice planes with asymmetry angle φ. We set the convention $R_P < 0$ when the incoming beam enters the crystal through the concave surface (

Figure 4-40 a), and $R_P > 0$ in the opposite case (

Figure 4-40 b). The presence of asymmetry changes the focusing distance of the experimental apparatus in $(L_S/1 - \theta_B \tan\varphi)$. Asymmetry also changes the focusing distance of the curved crystal that results $f' = R_P cos\varphi/2$. The FWHM of the diffraction spot on the detector is expected to be

$$\delta = \sqrt{a^2 + \left(\frac{2t}{\cos\varphi}\left|\theta_B + \frac{L_D}{R_D}\right| + l\left|(1 + \theta_B \tan\varphi) - \frac{L_D}{L_i}\right|\right)^2}$$

where a is the source diameter, t the sample thickness, l the size of the beam on the crystal surface. R_D is the curvature radius of the diffracting planes, the signs convention for R_P holds for R_D too. The term $2t\theta_B/\cos\varphi$ represents the contribution of the sample thickness. The curvature of diffracting planes changes the FWHM of the spot but not the image distance L_i, such curvature produces the term $2L_D\, t/R_D \cos\varphi$. The term $l(1 + \theta_B \tan\varphi)$ is for the effective size of the crystal as seen by the beam. When $L_D = L_S$ and the diffraction planes are symmetric, the formula described in (4.3.2.2 Stack) is obtained.

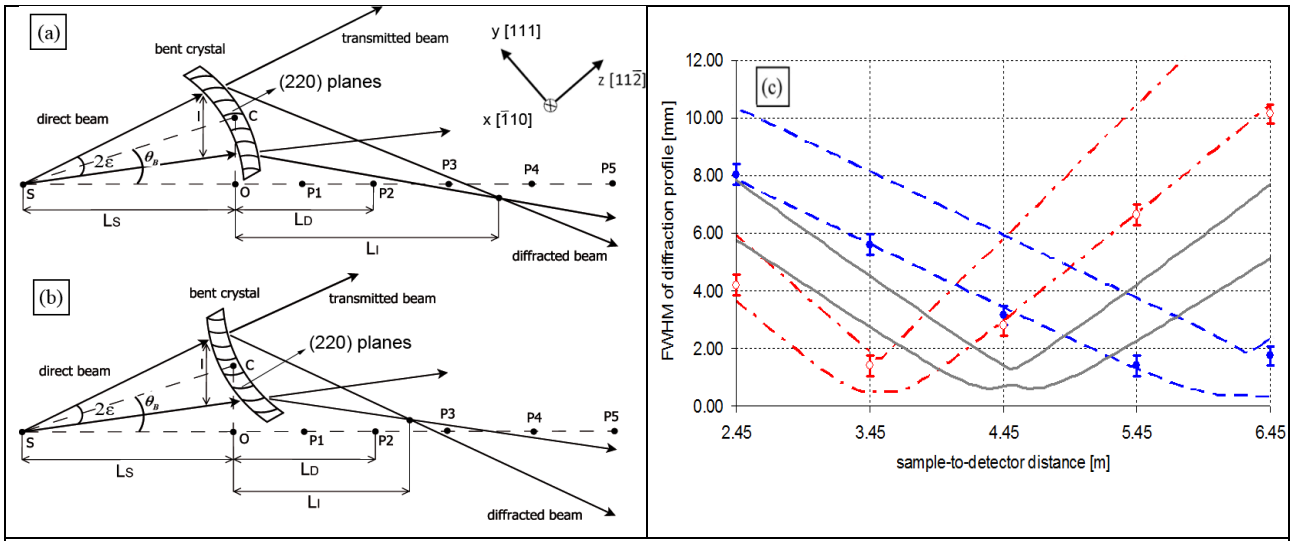

Figure 4-40

Schematic representation of the experiment. A divergent polychromatic X-ray beam passes through a bent crystal and is diffracted through curved (220) planes with asymmetry φ = 35.26°. Depending on the sign of R_P, the image distance increases (a) or decreases (b). (c) FWHM of the diffraction spot plotted as a function of sample-to-detector distance L_D. Blue filled circles plot the measured width for the case (a) and red empty circles are for the case (b). Dashed lines enclose the range of the expected width considering the uncertainty over parameters.

The focusing capability of the sample was proved by recording the width of the diffraction spot onto the detector for different sample-to-detector distance L_D. The analysis was firstly carried out with the beam impinging onto the crystal surface from its concave side (see Figure 4-40 a). The sample-to-detector distance L_D was changed by steps of 1.00 m, starting from 2.45 m for P_1 to 6.45 m for P_5. Then, the crystal was rotated of 180° around the x-axis (see Figure 4-40 b), and the analysis was repeated. The results for diffraction by (220) asymmetric planes are displayed in Figure 4-40 c, the experimental results well fit the expectations. The same analysis for symmetric (111) planes can be found in (3.4.2.2 White-light diffractometer). The data points produced in the two cases are nearly identical because the range of expected values strongly superpose considering the experimental uncertainties. The figure below plots the ranges of expected values for the (111) symmetric diffraction (brown bands) and for the (220) asymmetric diffraction (blue bands). Then, experimental points for diffractions (111) and (220) are expected to be rather close.

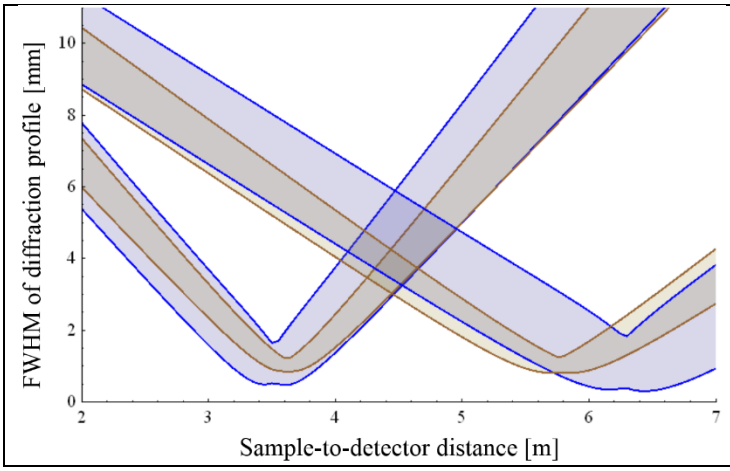

Figure 4-41

Range of expected FWHM of the diffraction spot for (111) symmetric (brown bands) and (220) asymmetric (blue bands) CDPs of the tested crystal plotted as a function of the sample-to-detector distance L_D. Bands have been calculated considering the uncertainty over parameters.

This section demonstrated that asymmetric planes in a self-standing bent crystal, fabricated by the grooving method, showed good diffraction performance, better than any mosaic crystal under peer conditions. Then, it was showed that the crystal focused hard X-rays by diffraction through asymmetric (220) planes.

4.4.3 Use of skew CDPs

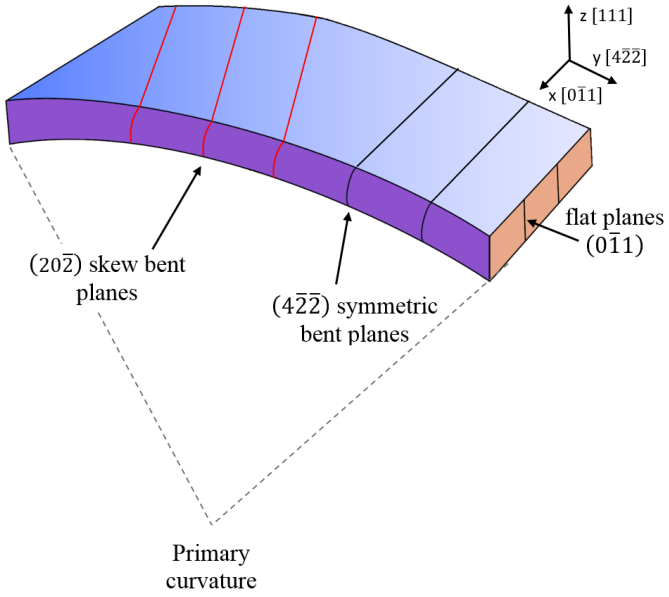

Figure 4-42

Sketch of a crystalline slab cylindrically bent. Curved (4$\bar{2}\bar{2}$) *QM symmetric planes and* (20$\bar{2}$) *skew lattice planes are highlighted.*

Figure 4-42). Crystals highlighting the QM effect can show a curvature driven by anisotropy along skew planes too. Actually, the curvature of skew planes is a projection of the curvature of the standard QM bent planes. However, families of lattice planes, which would be flat in the standard configuration, can be bent over skew planes. Furthermore, these families of lattice planes can have a curvature even if the skew planes are orthogonal to the main surfaces, i.e with asymmetry angle equal to zero. Therefore, the proper use of skew plane allows to produce focusing crystals with any CDPs orientation without the use of asymmetry.

In the previous section, we saw the great potentiality of asymmetric CDPs in focusing crystals for X-ray optics. However, asymmetry in focusing crystals may be a problem for two reasons. The first reason is the change in the focal distance of the crystal. This problem can be mitigated by changing the radius of curvature of the crystal and hence its focal distance to retrieve the change due to the asymmetry. However, this procedure also changes the curvature of the CDPs, and then the fraction of photons diffracted. The second problem is the handling of asymmetric crystals. This problem is purely technological, yet it is essential for the building of Laue lenses. Indeed, a crystal with asymmetry must be mounted inclined on the calotte of the lens. This poses major technological issues about the method for fixing the crystal to the calotte, and about the stability of the same.

Skew planes are lattice planes with azimuthal angle different from zero (

In this section, we will analyze the properties of focusing crystals with skew CDPs and zero asymmetry. In particular, we tested a focusing crystals by diffraction from (220) skew CDPs with zero asymmetry. The (220) family of planes were chosen because the (220) planes exhibit a strong diffracting power, but no curvature of such planes can be observed in the standard QM bent planes. The possibility to implement any kind of lattice diffraction with bent planes and zero asymmetry, or at least the principal ones, greatly simplifies the application of crystals with internal curvatures as focusing X-rays optical elements. Focusing crystals with skew CDPs may be disposed on a Laue lens following the curvature of the calotte, thus eliminating the main technological problem for the implementation of focusing crystals with any kind of CDPs.

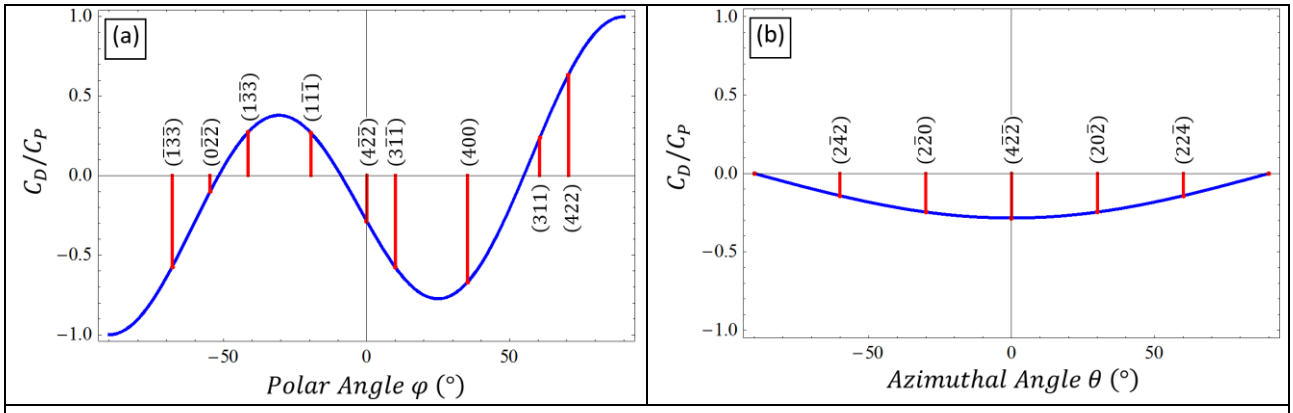

Figure 4-43

Dependence of the curvature ratio C_D/C_P vs. the polar angle φ (a) and the azimuthal angle θ (b) for a sample cylindrically bent, with main face oriented as (111), and QM curvature of (422) planes. The variation of the curvature ratio is a continuous function as represented by the blue curve. The angle of lattice planes with small Miller indices are shown together with their curvature ratio as red bars.

The crystal tested in this section was built in collaboration between SSL (Ferrara, Italy), and RIBA (Faenza, Italy). A Si wafer was shaped in a 20×100×5 mm^3 slab at SSL, through a high precision dicing saw (DISCO™ DAD3220). Then, the sample was cylindrically bent by the deposition of a thick film of CFRP at RIBA. The main face of the sample was oriented as (111), while the (422) planes were bent by QM (Figure 4-42). This crystal was already tested in (4.2.2 Thick films - CFRP) to prove that the deposition of CFRP is a method to induce curvature in thick crystals. The surface profile of the samples was measured at SLL by an interferometric profilometer before and after the deposition process. The sample resulted cylindrically bent with a radius of 20 m.

Lattice plane	Azimuthal angle θ (°)	C_D / C_P	R_D (m)	Aperture (arcsec)	Diffraction Efficiency
$(4\bar{2}\bar{2})$	0	0.284	70.4 ± 3.5	14.7 ± 0.7	0.38 ± 0.05
$(20\bar{2})$	30	0.246	81.3 ± 4.1	12.7 ± 0.6	0.80 ± 0.05
$(0\bar{1}1)$	90	0	0	-	-
(111)	-	1	20.0 ± 1.0	-	-

Table 4-5

Parameters of the main lattice planes.

The sample was tested through X-ray diffraction at beamline ID15A of ESRF, by a highly monochromatic and collimated beam tuned at the energy E = 150 keV, monochromaticity was ΔE/E = 2×10^{-3}. The characterization of the samples was carried out by performing rocking curves (RCs). Figure 4-44 shows the RC of skew $(20\bar{2})$ bent planes. As expected, diffraction efficiency is very high, since the (220) family of planes has a very high diffraction efficiency. Experimental results well fit the expectation. The focusing capability of the sample was not tested by the polychromatic

diffractometer (4.4.2 Use of asymmetric CDPs), as for the focusing crystal with asymmetric CDPs. Indeed, it was not possible to reserve more beam-time at this instrument.

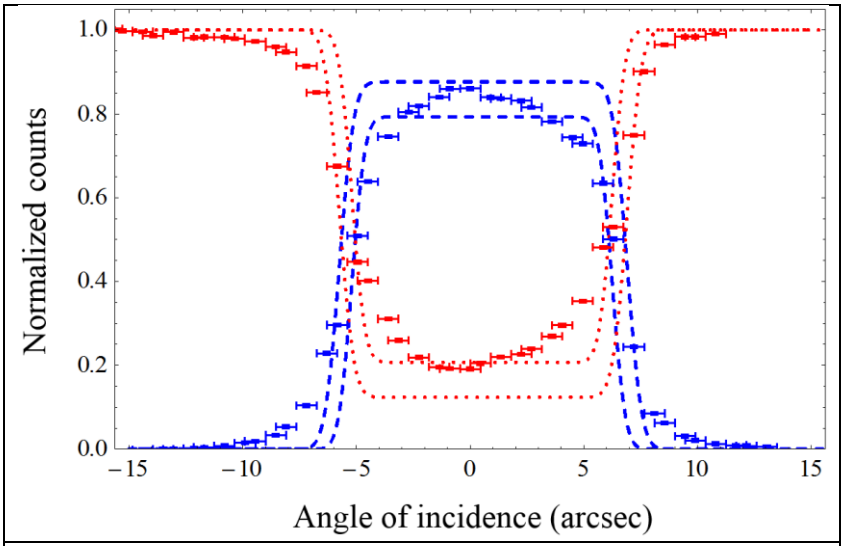

Figure 4-44

RC of the $(20\bar{2})$ *skew diffracting planes of the crystal. Filled red circles plot the intensity of the transmitted beam, whereas the empty blue circles plot the intensity of the diffracted beam. Dotted red bands and blue dashed bands represent the expected result for the transmitted and diffracted beam.*

The use of skew CDPs completely solve the main technological problems for the use of focusing crystals with any kind of CDPs in Laue lenses. Then, an effective use of the technology of focusing crystals in Laue lenses become possible. The use of these crystals in Laue lenses would increase the sensitivity and resolution of the same, thus increasing the TRL of Laue lenses.

5 Parametric X-ray Radiation (PXR) in Laue lenses

A Laue lens may be applied in astrophysics for high-sensitivity observations of cosmic phenomena on satellite-borne focusing telescope, attaining unprecedented sensitivity in the observation of hard X-rays celestial sources. For this application, a Laue lens would be placed in space, where an environment populated of high energy charged particles is present. Charged particles moving through a medium of periodically varying permittivity (e.g. crystals) generates optical radiation, as was first predicted by (Fainberg Y. B., 1957), titled ‘‘parametric Cherenkov radiation’’. The X-ray radiation of relativistic charged particles moving through a crystal was theoretically considered by (Ter-Mikaelian, 1969) and was given the name ‘‘resonant radiation’’. This radiation of relativistic electrons in a crystal was first observed experimentally in the Bragg direction in 1985 in Tomsk (Soviet Union) by (Vorobiev, 1985) and (Didenko, 1985). Since the 1980s, the term ‘‘parametric X-ray radiation’’ (PXR) has been used in most papers dedicated to investigations of this phenomenon. PXR occurs to be a quasi-monochromatic linearly polarized X-ray radiation, which angular distribution shows sharp maxima (so-called PXR reflections) in the vicinity of the Bragg direction. Indeed, PXR can be described as the diffraction of virtual photons.

The signal produced by PXR of charged particles may constitute a noise that interferes with the photons focused by a Laue lens. In a Laue lens, single crystal tiles occupy positions that X-rays impinging parallel to the lens axis are diffracted to the lens focus, i.e. where diffraction emission maxima, occurring at the Bragg angle, are concentrated. Because of the geometry of the lens, PXR emission maxima are concentrated in the lens focus as well. Distribution of high energy charged particles is mostly isotropic in space, as well would be the PXR signal produced in a Laue lens. Moreover, PXR signal would increase with the increase of the focusing area of the lens, at the opposite of the other noises. The purpose of this section is to estimate the PXR signal produced by a Laue lens and its spatial distribution on the detector, and to compare this signal with the lens expected sensitivity.

5.1 Theory of PXR

From a physical point of view PXR can be considered as a Cherenkov radiation arising at a particle velocity lower than the phase velocity of the electromagnetic wave in the medium, provided that, the medium has a periodical structure of dielectric susceptibility (Fainberg Y. K., 1957). Here, we will describe the understanding of the nature of PXR as the diffraction of virtual photons (Ter-Mikaelian, 1969). This approach readily explains the origination of strong maxima in the PXR angular distribution (PXR reflections) in the vicinity of Bragg directions. The formula for the PXR frequency ω (or energy $\hbar\omega$) at any direction of observation $\vec{\Omega}$ is:

$$E_{PXR} = \hbar\omega_{PXR} = \frac{c\hbar|\vec{g}\cdot\vec{V}|}{c - \sqrt{\varepsilon_0}\vec{V}\cdot\vec{\Omega}}$$

where $\hbar$ is the Planck constant divided by 2π, ε_0 is the constant part of the medium permittivity (average permittivity), $\vec{g}$ is the reciprocal lattice vector of the diffraction plane, $\vec{\Omega}$ is the unit vector in the direction of the detector, c is the velocity of light, $\vec{V}$ the velocity of the incident particle. For comparison, the calculated energy determined by the Bragg law in a crystal for the detector direction is

$$E_B = \hbar\omega_B = \frac{\hbar c|\vec{g}|^2}{2\sqrt{\varepsilon_0}|\vec{\Omega}\cdot\vec{g}|}$$

The angular distribution of virtual photons has a conical shape around the particle trajectory. Maxima in the distribution are observed at an angle

$$\theta_{max} = \gamma_{eff}^{-1} = \sqrt{\gamma^{-2} + |\chi_0|}$$

where χ_0 is the dielectric susceptibility, $\chi_0 = 1 - \varepsilon_0$ and γ is the relativistic factor of incident particle, γ_{eff} is the effective relativistic factor for frequency ω_{PXR} as $\varepsilon_0 = \varepsilon_0(\omega)$. In vacuum $\gamma_{eff}^{-1} = \gamma^{-1}$, but in a medium we always have $\gamma_{eff}^{-1} > \gamma^{-1}$. When the PXR energy $\hbar\omega_{PXR}$ exceeds the atomic energies in the medium, the effective relativistic factor can be written as

$$\gamma_{eff}^{-1} = \sqrt{\gamma^{-2} + \left(\frac{\omega_p}{\omega_{PXR}}\right)^2}$$

where ω_p is the plasma frequency. The production of PXR is shown in Figure 5-1. The angular distribution of real photons in PXR reflection is shown below the particle trajectory. It is in the vicinity of the Bragg direction shown by a dashed line.

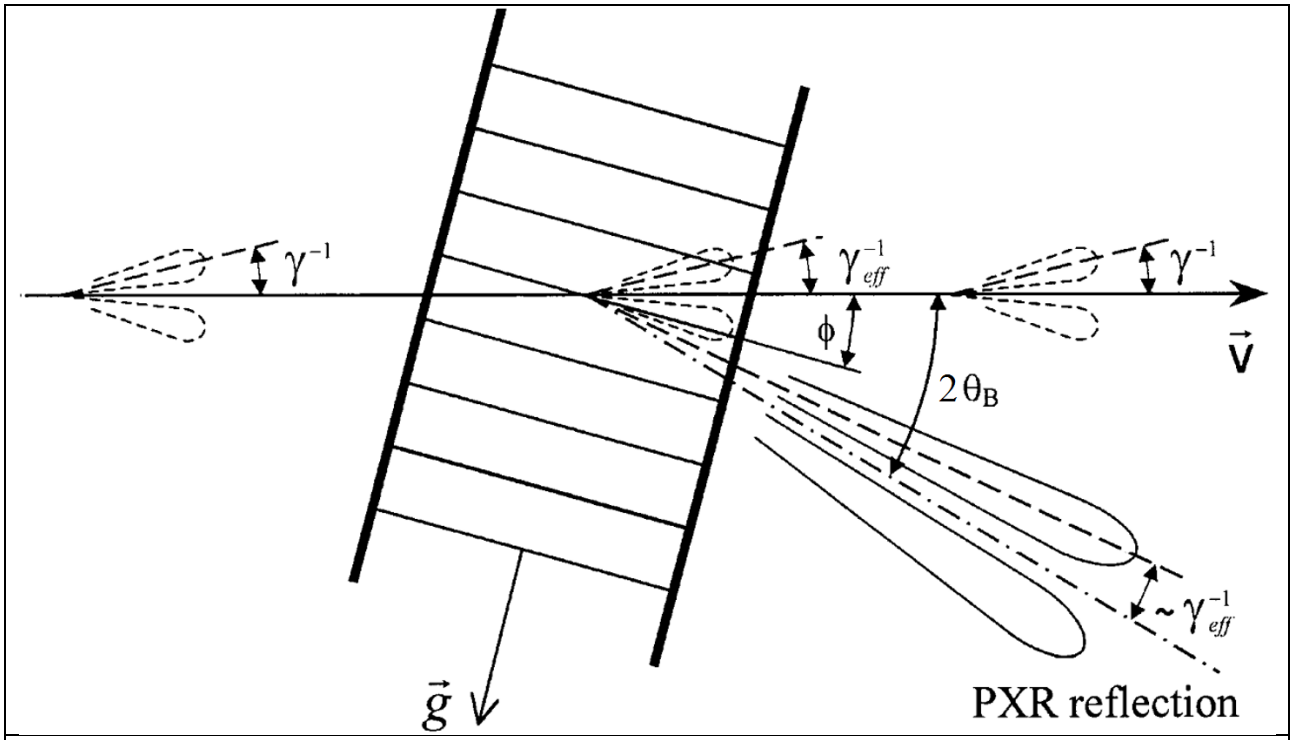

Figure 5-1

The straight line shows the trajectory of a relativistic charged particle traversing a crystalline target. The dashes show crystallographic planes described by the reciprocal lattice vector $\vec{g}$. The angular distributions of virtual photons are shown as dashed curves. The angular distribution of real photons in PXR reflection is shown as continuous curves. The Bragg direction is shown as a dot-dashed line. PXR photons are emitted in a conical shape around the Bragg direction. The angle $2\theta_B$ between the Bragg direction and the vector $\vec{V}$ is equal to twice the angle ϕ between crystallographic planes and the vector $\vec{V}$.

The absolute differential yield of the coherent radiation, from (Shchagin A. P., 1990), is

Equation 15

$$Y_{\vec{g}} = \frac{dN}{ndΩ} = \frac{e^2 \omega L \left|\chi_{\vec{g}}(\omega)\right|^2}{2\pi\hbar\varepsilon_0^3 V\left(\frac{c}{\sqrt{\varepsilon_0}} - \vec{V}\cdot\vec{\Omega}\right)} \cdot \left| \frac{\left(\omega\frac{\sqrt{\varepsilon_0}}{c}\right)\vec{\Omega}\times\left[\left(\omega\frac{\varepsilon_0}{c^2}\right)\vec{V}+\vec{g}\right]}{\left[\left(\omega\frac{\sqrt{\varepsilon_0}}{c}\right)\Omega_\perp - g_\perp\right]^2 + \left(\frac{\omega}{V}\right)^2\left[\left(\frac{1}{\gamma^2}\right)^2 + \left(\frac{V}{c}\right)^2(1-\varepsilon_0)\right]} \right|^2$$

where dN is the number of quanta with frequency $\omega = \omega_{PXR}$ emitted in the solid angle $d\Omega$ as n particles with the charge e pass through a crystal of thickness T; $\chi_{\vec{g}}(w)$ is the Fourier component of the variable part of permittivity; $\Omega_\perp$, $g_\perp$, are the components of $\vec{\Omega}$, $\vec{g}$, perpendicular to $\vec{V}$. Taking into account the attenuation of emitted X-rays traversing the crystal, we have used the factor L as the effective thickness traversed by the particles

$$L = T_e \left|\frac{\vec{t}\cdot\vec{\Omega}}{\vec{t}\cdot\vec{v}}\right| \left[1 - exp\left(-\frac{T}{T_e\left|\vec{t}\cdot\vec{\Omega}\right|}\right)\right]$$

where $T_e = T_e(w)$ is the e-fold attenuation length of radiation with frequency ω; $\vec{t}$ is the unit vector perpendicular to the target plane; and $\vec{v} = \vec{V}/V$. Equation 15 can be applied to an arbitrary target and for arbitrary direction of observation. PXR emission can occur for both Bragg (reflection) and Laue (transmission) geometries, Equation 15 holds for both (Caticha, 1992). PXR reflection has a conical shape around the Bragg direction and has an angular size l/γ. Note that the PXR distribution has its minimum at the cone axis near the exact Bragg direction. The angular size of PXR reflection decreases with incident electron energy increasing, up to the critical energy $E_{crit} = mc^2\omega_{PXR}/\omega_p$. With incident electron energy increasing up to the critical energy E_{crit}, the PXR differential yield at the maxima increases nearly as a square of the electron energy. At $E_{particle} >> E_{crit}$, the PXR differential yield does not depend on $E_{particle}$. The square-law growth of PXR differential yield as a function of incident electron energy was first predicted theoretically in (Dialetis, 1978). In (Shchagin A. V., 1993) the approximately square growth was demonstrated for the first time by an electron beam with energy $E_{particle}$ = 15.7 - 25.7 MeV.

5.2 Flux of cosmic rays on a Laue lens

Cosmic rays (CR) are particles that bombard the Earth's atmosphere from outer space. The largest part of cosmic rays is composed of light particles as electrons, with a small part of positrons. A relevant fraction of cosmic rays is also represented by charged nuclei (Blanco, 2008). The mass composition of such particles reflects, with some differences, the nuclear abundances found in nature (Ave, 2008). Indeed, H nuclei (protons) dominate, and some excess of light nuclei (Li, Be, B) is present. Heavier nuclei, up to Fe, are also part of the cosmic rain. The energies of cosmic rays observed near the Earth extend over a very wide range, from below 10^8 eV to more than 10^{20} eV per particle. The intensity of Galactic cosmic rays is nearly isotropic due to the influence of magnetic fields in the Milky Way (Amenomori, 2006) and because most cosmic rays consist in particles with relatively low energy (Figure 5-2), which

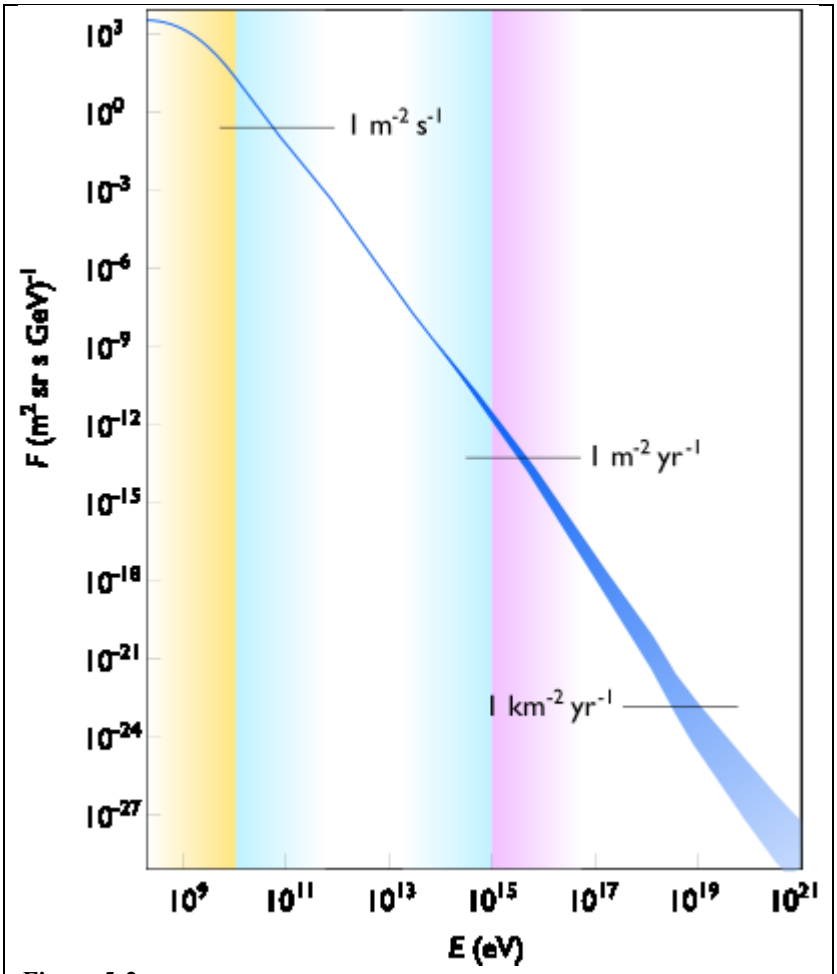

Figure 5-2

Cosmic rays spectrum. The yellow zone is populated by cosmic rays emitted by solar flares. Cosmic rays in the blue zone and in the violet zone are respectively of galactic and extra-galactic origin.

are more subjected to galactic magnetic fields. Most cosmic rays come from within our galaxy, with a low fraction of them (below a few GeV for protons) originating from the Sun atmosphere (flares). Galactic cosmic rays and low energy cosmic rays lose their original directional information; their orbits are deflected by the Galactic magnetic field (GMF) and are randomized by irregular GMF components. Indeed, cosmic rays have traveled on average for many millions of years, some also having interacted with interstellar gas atoms and dusts. Because of this, the PXR signal produced by interaction of cosmic rays with crystals of a Laue lens would be almost isotropic, thus constituting a flat background noise.

5.3 PXR emission by a thin flat crystal

There are several parameters to consider when estimating PXR emission from a flat and thin crystal in traversing geometry. Particles of different species p produce emission of different entity. They interact differently with the electrons of the material because they have different electric charge. Their mass m is even more different, especially between light particles and heavy particles composing CR, i.e. electrons and positrons vs nuclei. Because of that, particles of equal energy but different weight have different velocity. Then, the γ factor is different, thus producing emission of PXR photons of different energy $\hbar\omega_{PXR}$. The energy distribution of CR is also very wide, spanning from 10^7 eV to 10^{15} eV for the most intense part of the CR flux, but reaching even energies of 10^{20} eV. Naturally, PXR emission depends also on the lattice plane $\vec{g}$ considered. Then, it critically depends on the angle between the particle velocity and the lattice planes, i.e. angle between $\vec{g}$ and $\vec{v}$. PXR emission falls off when this angle differs from the Bragg condition more than γ_{eff}^{-1} . Finally, PXR emission is distributed over the observation angle of the detector $\vec{\Omega}$. The PXR yield of a flat and thin crystal with thickness t hit by CR is:

$$Y_{CR}(\vec{g}, E, \vec{v}, \vec{\Omega}, \omega_{PXR}) = \sum_{p} Flux(p, E) \cdot Y(p, \vec{g}, E, \vec{v}, \vec{\Omega}, \omega_{PXR}) \qquad \textbf{Equation 16}$$

Considering the CR flux nearly isotropic, this expression has to be integrated as a variable of $\vec{v}$ over an emisphere, and then as a variable of the energy E of CR. Afterwards, PXR emission of different crystallographic planes $\vec{g}$ can be summed up, thus obtaining the distribution of PXR photons on the detector.

$$Y_{DETECTOR}(\vec{\Omega}, \omega_{PXR}) = \sum_{\vec{g}} \iint Y_{CR}(\vec{g}, E, \vec{v}, \vec{\Omega}, \omega_{PXR})\, dE\, d\vec{v} \qquad \textbf{Equation 17}$$

5.4 PXR emission by a thick CDPs crystal

As said, the PXR emission strongly depends to the angle between particle velocity and lattice planes. When a particle traverses a thick target, its velocity varies because of the interaction with the atoms of the target and the consequent energy loss. Variation of velocity perpendicular to the initial velocity has in particular to be taken in account for PXR phenomena, because for this reason a large fraction of the particles can go out of the PXR condition while traversing the crystal. Because of the small angle tolerance for PXR phenomena, most of the particles go out of the PXR angular tolerance before

undergoing an important energy loss. Therefore, the total energy of the particles can be considered constant traversing the crystal. Energy loss and deflection of particle from the initial direction is primarily due to two processes: inelastic collision with the atomic electrons of the material, and elastic scattering from nuclei. Other phenomena occur when a particle traverse a material, as emission of Cherenkov radiation, nuclear reactions, and Bremsstrahlung. For heavy particles the atomic collision processes dominates, that other processes are extremely rare and give a negligible contribution. For light particles, Bremsstrahlung has also to be taken in account. All these processes are considered during calculations. The average energy loss per unit path length is called the stopping power *dE/dx*. It can be simply calculated by the Bethe-Block formula for heavy particles, that $(dE/dx)_{tot} = (dE/dx)_{collision}$. For light particles, the Bremsstrahlung process has to be considered, that the total stopping power is the sum of the two contributions $(dE/dx)_{tot} = (dE/dx)_{collision} + (dE/dx)_{radiation}$.

What we need to obtain is the distribution of misalignments from the original direction of a particle, with a certain initial energy *E*, and at a certain depth *t* in the material. The condition for PXR emission is very sensitive to the angle between particle velocity and lattice planes. The probability of a head-on collision between CR particles and the atoms composing the medium is very low, that it is possible to consider the transfer of momentum entirely perpendicular to the initial momentum p_i. Consider a layer of material thin enough that probabilistically a single interaction occurs between a CR particle and the atoms composing the medium. Consider particles with initial velocity parallel to *z,* the total momentum transfer $dp_\perp$ per unit of path length is

$$E\{dp_\perp\} = dz \cdot N \sum_n \int_{p_{min}}^{p_{max}} \boldsymbol{p}_n \nabla\sigma|_n \, dp$$

Where N is the number of targets (atoms) for unit volume, *n* is the phenomena that produces a momentum transfer, $\nabla\sigma|_n$ is the differential cross section for the phenomena *n*, $\boldsymbol{p}_n$ is the momentum transferred by it, p_{max} and p_{min} are the maximum and minimum possible momentum transferred by the phenomena *n*. The cross section of the phenomena has cylindrical symmetry around the *z* axis, that the total momentum transferred perpendicular to the *z* axis per unit length is zero $E\{dp_\perp\} = 0$. Moreover, the vector expression can be re-written as a scalar expression:

$$E\{dp_\perp\} = dz \cdot N \sum_n \int_{p_{min}}^{p_{max}} p_n \left.\frac{d\sigma}{dp}\right|_n dp = 0$$

The sum of the component of the velocities perpendicular to the *z* axis does not varies, i.e. it is equal to zero. However, the direction of the component of the velocities perpendicular to the *z* axis spread out. Then, the variance of the distribution that describes these velocities becomes different from zero. We can see this from the variance of the momentum transfer during the scattering phenomena. Therefore, we can calculate the variance of the momentum transfer per unit length as:

$$Var\{dp_\perp\} = E\{dp_\perp^2\} - (E\{dp_\perp\})^2 = E\{dp_\perp^2\} = dz \cdot N \sum_n \int_{p_{min}}^{p_{max}} p_n^2 \left.\frac{d\sigma}{dp}\right|_n dp$$

Now we can consider that the energy transferred in a single process is $\Delta E_n = \frac{p_n^2}{2m}$, and the energy transferred in general is $E = \frac{p^2}{2m}$, so the expression above can be rewritten as:

$$Var\{dp_\perp\} = 2m \cdot dE = dz \cdot 2mN \sum_n \int_{p_{min}}^{p_{max}} \Delta E_n \left.\frac{d\sigma}{dp}\right|_n dp$$

Here we find an expression of the stopping power along the *z* axis

$$\frac{dE}{dz} = N \sum_n \int_{p_{min}}^{p_{max}} \Delta E_n \frac{d\sigma}{dp}\Big|_n \, dp$$

The stopping power along the *z* axis can be calculated by (Leo, 1994). Thus, the variance of momentum perpendicular to *z* at a certain depth *t* in the material can be found integrating the variance of momentum transfer per unit length over the thickness:

$$Var\{p_\perp(t)\} = 2m \int_0^t \frac{dE}{dz} dz$$

The momentum $p_\perp$ can be divided in the two components p_x and p_y as $p_\perp = \sqrt{p_x^2 + p_y^2}$. These two moments can be considered independent and Gaussian distributed, with variance $Var\{p_x\} = Var\{p_y\} = \sigma^2$. Then, distribution of momentum $p_\perp$ can be written as a Rayleigh distribution

$$f(p_\perp) = \frac{p_\perp}{\sigma^2} Exp\left(-\frac{p_\perp^2}{2\sigma^2}\right)$$

With $Var\{p_\perp(t)\} = (2 - \pi/2)\sigma^2$ by definition. Then, it is possible to calculate the σ of the Gaussian distribution of p_x, p_y as $\sigma = \sqrt{Var\{p_\perp(t)\}/(2 - \pi/2)} = \sqrt{\frac{m}{(1-\pi/4)} \int_0^t \frac{dE}{dz} dz}$. The standard deviation of the angle between the velocity of the particles and the *z* axis is

$$Var\{\theta(t)\} = Arctan\left(\frac{Var\{p_\perp\}}{p_i - E\{|p_\perp|\}}\right)$$

$$Var\{\theta_x(t)\} = Var\{\theta_y(t)\} = Arctan\left(\frac{\sigma^2}{p_i - E\{|p_\perp|\}}\right)$$

Where $E\{|p_\perp|\}$ is the mean of the modulus of the $p_\perp$ of the CR particles. The distributions of the particles at a certain depth in the crystal can be written as a function of the angle as:

$$particles_{\theta_x}(t, \theta_x) = \frac{1}{\sqrt{2\pi}\sigma_{\theta_x}} exp\left[-\frac{\theta_x^2}{2\sigma_{\theta_x}^2}\right]$$

$$particles_{\theta_y}(t, \theta_y) = \frac{1}{\sqrt{2\pi}\sigma_{\theta_y}} exp\left[-\frac{\theta_y^2}{2\sigma_{\theta_y}^2}\right]$$

$$particles_\theta(t, \theta_x, \theta_y) = particles_{\theta_x}(t, \theta_x) \cdot particles_{\theta_y}(t, \theta_y)$$

Then, it is necessary to integrate the PXR yield over t, θ_x, θ_y, and the above expression Y_{CR} (Equation 16) becomes

$$Y_{CR}(\vec{g}, E, \vec{v}, \vec{\Omega}, \omega_{PXR}) =$$

$$= \sum_p \int_0^T \int_{-\pi/2}^{+\pi/2} \int_{-\pi/2}^{+\pi/2} Flux(p, E) \cdot particles_\theta(t, \theta_x, \theta_y) \cdot Y(p, \vec{g}, E, \vec{v}(\theta_x, \theta_y), \vec{\Omega}, \omega_{PXR}) \, dt \, d\theta_x \, d\theta_y$$

Where *T* is the total thickness of the crystal.

In the case of a curved crystal in transmission geometry, the vector $\vec{g}$ slightly changes respect to the depth t in the crystal. This variation follows the curvature, which has to be considered as function of depth $\vec{g}(t)$. For a uniform curvature, the angle of variation of orientation of lattice planes can be written as $\delta(t) = \frac{\alpha}{T}\left(t - \frac{T}{2}\right)$ where α is the total curvature angle of the crystal.

5.5 Results

A Laue lens is composed of an array of concentric rings, with crystals in each ring at the right angle for photons parallel to the z axis to meet the Bragg angle. The PXR emission of the lens is the sum of the emission of every crystal composing it. In order to compare the PXR emission to the sensitivity of a Laue lens, the distribution in Equation 17 has to be integrated over the size of the crystals, over the dimension of the spot on the detector, and multiplied for the exposition time. Then, the contributions of all the crystals in the lens have to be summed up. As an example, consider a Laue lens with a focal length of 20 m diffracting photons in the energy range 100 – 300 keV. The lens is composed of Si (111) CDPs crystals with aperture angle of 30 arcsec. The photons produced by PXR by CR are shown in Figure 5-3. These photons are about 1×10^{-16} ph/(cm^2 s keV), while the typical sensitivity of a Laue lens is about 1×10^{-7} ph/(cm^2 s keV). Therefore, the signal produced by PXR by CR do not interferes with the measure of photons focused by the Laue lens. Indeed, the PXR signal is so low that it cannot be detected.

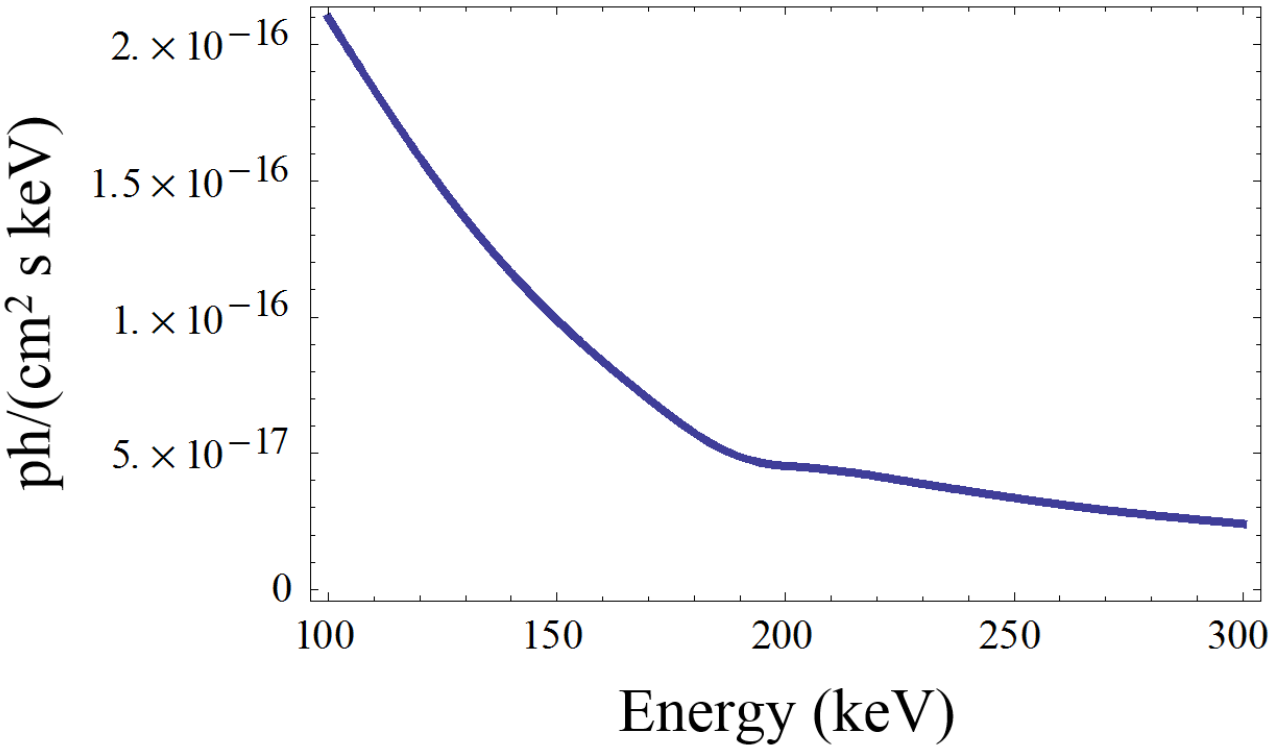

Figure 5-3

Photons produced by PXR on a Laue lens with focal length 20 m, focalizing photons in the energy range 100 – 300 keV, by Si (111) CDPs crystals with aperture angle of 30 arcsec. The exposure time is 100 ks and ΔE/E = 1/2. The photons produced by PXR are less than the typical background photons of 1.5×10^{-4} ph/(cm^2 s keV).

6 Crystalline undulator

The capability of generating powerful monochromatic X- and γ-radiation is a challenging goal of modern research. Indeed, an intense and monochromatic source of X- and γ -rays can be used in fundamental science as well as in technological and medical applications. The state-of-the-art sources allow to produce coherent photons with energy not higher than about 10 keV. Thus, different ways have to be explored to generate photon with higher energies. The usage of a crystalline undulator (CU) has been identified as a promising solution for reaching such a goal. A CU was fabricated through the grooving method (3.3 The indentation method and our crystals), and it was was extensively characterized at SSL (Ferrara, Italy) and ESRF (Grenoble, France) labs.

High-intensity and monochromatic X- and γ-beams are very desirable for a great amount of applications, ranging from fundamental to applied science. Free-electron lasers (FELs) are used to generate intense and monochromatic photons. A FEL can be widely tunable, currently ranging in wavelength from microwaves, through terahertz radiation and infrared, to the visible spectrum, ultraviolet, and X-ray (Wikipedia, 2004). FELs are used in many fields, and some of their elective applications are in medicine as innovative tools for high precise surgery and fat removal and in biology for imagine of fast proteins. However, since the upper limit for superconducting magnets is few tens of Tesla (Schneider-Muntau, 2004), the smallest achievable undulating period λ_u is a few centimeters. Thereby, the energy of emitted coherent photons, $\omega \backsim 2\gamma^2/\omega_u$, turns out to be limited to some tens of keV, with γ being the Lorentz factor and $\omega_u = 2\pi/\lambda_u$. At the state of the art, it would be very difficult or even impossible to generate photon with higher energies with such technique.

To date two approaches have been identified as promising solutions to overcome the current limitations of a FEL. One consists in a magnetic micro-undulator based on MEMS technology, with the undulating period being in the range of 10 μm to 1 mm (Harrison J. J., 2012). Another technique relies on the usage of a crystalline undulator (CU). The main idea of the CU is to impress an oscillatory motion to a bunch of particles exploiting the strong electrostatic field generated by ordered atoms within an oriented crystal (Lindhard, 1965). Indeed, when a particle enters a crystal with a small angle with respect to the major crystallographic planes or axes, the particle trajectory can be confined due to the channeling phenomenon. Since a crystal can tolerate stress and torsion remaining into elastic regime until the breaking point, complex geometry can be achieved to drive particles inside manipulated channels, such as a periodically bent crystal. With the current available techniques, crystals with a undulating geometry can be fabricated with a period ranging from 1 μm to cm. Thus, it is possible to achieve the frequency range of hard X- and γ-ray through a single crystal of few millimeters.

The realization of a working CU requires a high accuracy in the deformation of the crystallographic planes. Indeed, the efficiency of channeling decreases with the presence of crystalline defects (E. Bagli et al., 2013), and the coherence of the emitted X- and γ-rays depends on the periodicity of the crystalline bulk. Different methods have been proposed for the realization of a periodically bent crystal, such as acoustic wave transmission (Baryshevsky, 1980), periodically graded $Si_{1-x}Ge_x$ structures (Breese, 1997) and periodic surface deformations obtainable via superficial grooves (Afonin, 2005) (Bellucci S. e., 2004), laser ablation (Balling, 2009) or film deposition (Guidi V. A., 2005) (Guidi V. L., 2007). The grooving method can represent an optimal solution to produce a CU. Indeed, with such a method it is possible to bend a crystal in a simple and reproducible way. A CU was realized at SSL by manufacturing a series of grooves on a Si crystal. The crystal has size 0.2 × 45.0 × 5.0 mm^3, the main surface is oriented as (111), the dimension 5.0 mm long is oriented as

[110], while the direction 45.0 mm long is oriented as [211]. In particular, an alternating and periodic pattern of parallel grooves 150 μm wide was performed on the largest surfaces of the strip, with the distance between consecutive grooves being 1 mm. The grooves were manufactured by means of a diamond blade through the usage of a DISCO DAD 3220 dicing machine. The groove depth was (54±2) μm. A schematic representation of the sample is reported in Figure 6-1.

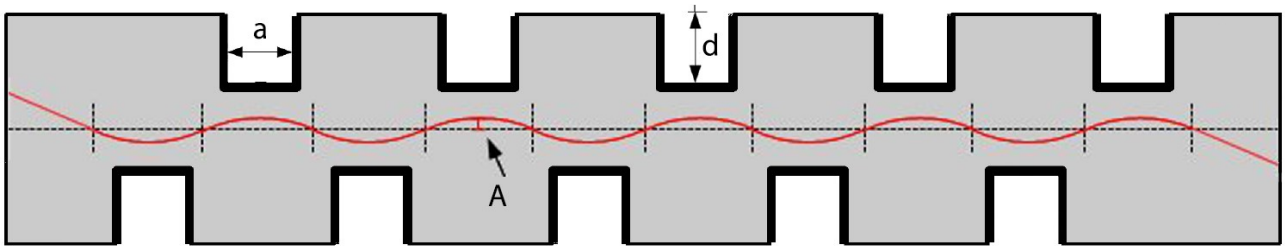

Figure 6-1

Schematic representation of the crystalline undulator obtained through the grooving method. The red line represents the undulated planes on the center of the crystal. A is the amplitude of the undulated planes, a the groove width and d the groove depth.

A morphological analysis of the sample surface was attained by a white-light interferometric profilometer. The profile of the surface before and after the indentation process were subtracted, resulting in an image of the net deformation of the bulk lattice planes. The profilometric pattern of the sample surface is shown in Figure 6-2 a. As a result, it was possible to estimate the amplitude of the crystallographic planes undulation. The averaged value of the undulating amplitude resulted to be (4.5 ± 1.0) nm. The CU was also tested through X-ray diffraction at beamline ID15A of the ESRF (Grenoble, France). A highly monochromatic beam was set at 150 keV, the beam size was 50 × 50 μm^2 wide. The sample was characterized by recording the position of the Bragg peak for the (220) lattice planes, for 50 points in the center along the [110] dimension. A flat reference crystal with identical lattice orientation was set behind the undulator, and its Bragg peak was recorded together with the Bragg peak from the undulator, in order to subtract possible shifting due to instrumental tolerances. The variation of the maximum of the rocking curves as a function of the impact position of the X-ray beam is shown in Figure 6-2 b. The measured average amplitude of undulation was 4.1 ± 0.5 nm with an average period of 0.98 ± 0.03 mm.

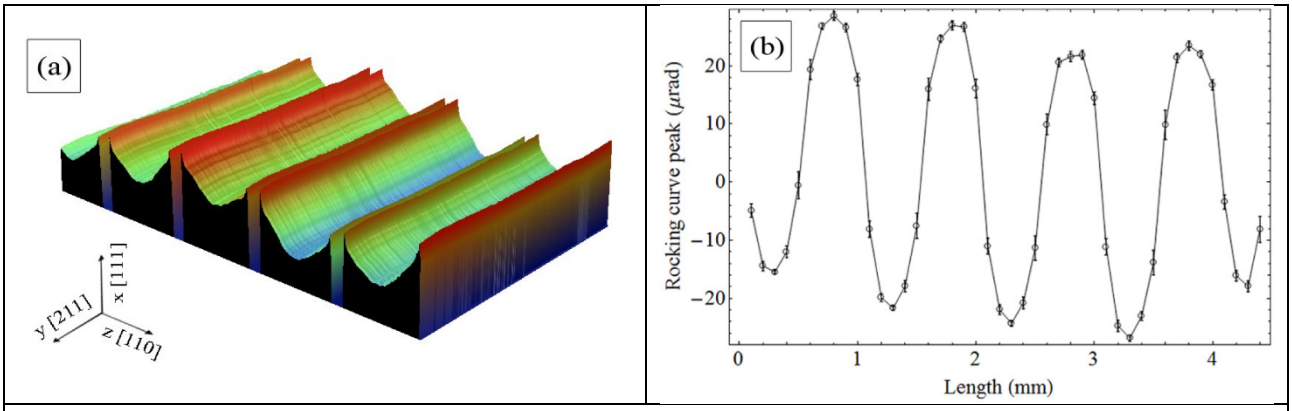

Figure 6-2

Morphological and structural measurement of the sample. (a) 3D view analysis of the sample surface through interferometric profilometry. (b) Angular analysis of (220) planes through X-ray diffraction.

The fabrication of a crystalline undulator via superficial grooves is presented in this section of the thesis. The periodical structure was characterized morphologically via interferometry at SSL (Ferrara, Italy) and structurally with diffraction techniques at ESRF (Grenoble, France) showing good results. The other techniques for inducing a self-standing curvature developed in this thesis work (4.2 Tensile films for producing CDPs crystals) may be also implemented for the realization of crystalline undulators. According to theory (KOROL, 2004), the fabrication parameters of the tested CU are in the optimal range for a 15 GeV positron-based CU, allowing to produce photons with energy in the 0.5-1.0 MeV range. The CU produced in this thesis work will be part of an experiment at the SLAC accelerator (San Francisco, USA) with a 15 GeV positron beam.

Conclusions

This thesis work concentrated on the development of crystals with curve diffraction planes (CDPs) as optical elements for hard X-rays. The doctoral work contributed to the construction of instruments for scientific research.

The theoretical work has touched the development of the dynamic theory of diffraction in order to cover some of its weaknesses in the field of diffraction by curved lattice planes with low curvature. Various applications require CDPs with low curvatures, in particular when crystals with high atomic number are used. In this case, the formalism of dynamical theory is not applicable in a simple way. Thus, it was necessary the development of a treatment dedicated to the purpose. The theoretical previsions were found in line with the experimental results. Therefore, this work led to an extension of the dynamical theory of X-ray diffraction.

The work of technological development and construction of hardware for scientific research focused on the development and production of innovative crystals for the construction of hard X-ray lenses. In particular, the possibilities offered by the curvatures induced by the effect of quasi-mosaicity were investigated. It was shown that by using this phenomenon it is possible to turn a crystal in a small focusing lens with high reflectivity. Therefore, the construction of hard X-ray lenses has been simplified with the introduction of focusing crystals. The thesis work was partially carried out within the LAUE Project, funded by the Italian Space Agency (ASI), whose purpose was the construction of a large-area Laue lenses. The work done during the doctoral thesis has led to a rethinking of the project in order to use focusing crystals and thus to increase the resolution and sensitivity of the lens.

The work on crystal for Laue lenses continued after the LAUE Project with a series of technological innovations with the aim to increase the maximum resolution and sensitivity achievable by Laue lenses. These innovations include the introduction of crystals with multiple curvatures and focusing crystals, the study of novel methods with which to produce crystals with CDPs, the construction of stacks of multi-crystals, the use of curved asymmetric diffraction planes. The new crystals were tests at the facilities of ESRF (European Synchrotron Radiation Facility, Grenoble, France) and ILL (Institut Laue-Langevin, Grenoble, France) showing good results. Therefore, this work led to an increase of the technology readiness level of hard X-ray lenses.

Simulations were also performed to estimate the possible interferences that a Laue lens could suffer in orbit because of the interaction with cosmic rays and the consequent production of parametric X-rays. This source of X-rays may interfere with measurements of celestial X-ray sources. The work has led to the exclusion of this possibility, since the emission of parametric X-rays would be less than the sensitivity of the lens itself.

Finally, the technologies developed to produce CDPs crystals were used for the construction of a crystalline undulator built as a prototype of X-ray source with high-energy and high flux. Lattice planes of a crystals where shaped in an undulated structure. Characterization of these lattice planes showed near-ideal results. High-energy charged particles channeled through these planes would produce coherent X-rays. The prototype will be part of an experiment at the SLAC accelerator (San Francisco, USA).

7 Appendix I - Theory of elasticity at the first order

7.1 Basic concepts

When deformations are small, it is possible to consider the force proportional to the displacement. This approximation is called first order approximation. This is the same condition for validity of Hooke's law. Consider a set of three orthogonal unit vectors fixed to the solid. After the deformation, the unit vectors are distorted in orientation and length. If the deformation is uniform, each fundamental cell of the crystal is deformed in the same way as follows:

$$\begin{aligned}\hat{\boldsymbol{x}} \to \hat{\boldsymbol{x}}' &= (1+\delta_{xx})\hat{\boldsymbol{x}} + \delta_{xy}\hat{\boldsymbol{y}} + \delta_{xz}\hat{\boldsymbol{z}} \\ \hat{\boldsymbol{y}} \to \hat{\boldsymbol{y}}' &= \delta_{yx}\hat{\boldsymbol{x}} + (1+\delta_{yy})\hat{\boldsymbol{y}} + \delta_{yz}\hat{\boldsymbol{z}} \\ \hat{\boldsymbol{z}} \to \hat{\boldsymbol{z}}' &= \delta_{zx}\hat{\boldsymbol{x}} + \delta_{zy}\hat{\boldsymbol{y}} + (1+\delta_{zz})\hat{\boldsymbol{z}}\end{aligned} \tag{A.1}$$

where the parameters $\delta_{\alpha\beta}$ are dimensionless and they define the deformation. $\delta_{\alpha\beta} \ll 1$ is the condition of linearity. The position vector

$$\bar{\boldsymbol{r}} = a\hat{\boldsymbol{x}} + b\hat{\boldsymbol{y}} + c\hat{\boldsymbol{z}} \tag{A.2}$$

after the deformation becomes

$$\bar{\boldsymbol{r}}' = a\hat{\boldsymbol{x}}' + b\hat{\boldsymbol{y}}' + c\hat{\boldsymbol{z}}' \tag{A.3}$$

and the total displacement is given by the vector

$$\bar{\boldsymbol{R}}(\bar{\boldsymbol{r}}) = (\bar{\boldsymbol{r}} - \bar{\boldsymbol{r}}') = a(\hat{\boldsymbol{x}}' - \hat{\boldsymbol{x}}) + b(\hat{\boldsymbol{y}}' - \hat{\boldsymbol{y}}) + c(\hat{\boldsymbol{z}}' - \hat{\boldsymbol{z}}) = \tag{A.4}$$

$$(a\delta_{xx} + b\delta_{yx} + c\delta_{zx})\hat{\boldsymbol{x}} + (a\delta_{xy} + b\delta_{yy} + c\delta_{zy})\hat{\boldsymbol{y}} + (a\delta_{xz} + b\delta_{yz} + c\delta_{zz})\hat{\boldsymbol{z}} \tag{A.5}$$

We can define the three vectors $u(\boldsymbol{r})$, $v(\boldsymbol{r})$ e $w(\boldsymbol{r})$ as the displacement on three axes such that:

$$\bar{\boldsymbol{R}}(\bar{\boldsymbol{r}}) = u(\boldsymbol{r})\hat{\boldsymbol{x}} + v(\boldsymbol{r})\hat{\boldsymbol{y}} + w(\boldsymbol{r})\hat{\boldsymbol{z}} \tag{A.6}$$

If the deformation is not uniform, the local strain have to be specify for u (r), v (r) and w (r). We set the origin of $\bar{\boldsymbol{r}}$ near the region to study and we expand $\bar{\boldsymbol{R}}(\bar{\boldsymbol{r}})$ around $\bar{\boldsymbol{r}} \to 0$, matching (A.5) and (A.6). The expansion at the first order is:

$$\bar{\boldsymbol{R}}(\bar{\boldsymbol{r}}) \cong \bar{\boldsymbol{R}}(\boldsymbol{0}) + \frac{d\bar{\boldsymbol{R}}}{da}a + \frac{d\bar{\boldsymbol{R}}}{db}b + \frac{d\bar{\boldsymbol{R}}}{dc}c \tag{A.7}$$

where $\bar{\boldsymbol{R}}(\boldsymbol{0}) = 0$. It is possible to re-write (A.5) as

$$\bar{\boldsymbol{R}}(\bar{\boldsymbol{r}}) = (\delta_{xx}\hat{\boldsymbol{x}} + \delta_{xy}\hat{\boldsymbol{y}} + \delta_{xz}\hat{\boldsymbol{z}})a + (\delta_{yx}\hat{\boldsymbol{x}} + \delta_{yy}\hat{\boldsymbol{y}} + \delta_{yz}\hat{\boldsymbol{z}})b + (\delta_{zx}\hat{\boldsymbol{x}} + \delta_{zy}\hat{\boldsymbol{y}} + \delta_{zz}\hat{\boldsymbol{z}})c \tag{A.8}$$

And we can re-write (A.6) considering (A.7) as

$$\begin{aligned}\bar{\boldsymbol{R}}(\bar{\boldsymbol{r}}) \cong &\left(\frac{du(\bar{\boldsymbol{r}})}{da}\hat{\boldsymbol{x}} + \frac{dv(\bar{\boldsymbol{r}})}{da}\hat{\boldsymbol{y}} + \frac{dw(\bar{\boldsymbol{r}})}{da}\hat{\boldsymbol{z}}\right)a + \left(\frac{du(\bar{\boldsymbol{r}})}{db}\hat{\boldsymbol{x}} + \frac{dv(\bar{\boldsymbol{r}})}{db}\hat{\boldsymbol{y}} + \frac{dw(\bar{\boldsymbol{r}})}{db}\hat{\boldsymbol{z}}\right)b \\ &+ \left(\frac{du(\bar{\boldsymbol{r}})}{dc}\hat{\boldsymbol{x}} + \frac{dv(\bar{\boldsymbol{r}})}{dc}\hat{\boldsymbol{y}} + \frac{dw(\bar{\boldsymbol{r}})}{dc}\hat{\boldsymbol{z}}\right)c\end{aligned} \tag{A.9}$$

Comparing (A.8) and (A.9) we obtain the following relations

$$\begin{aligned} \delta_{xx} &\cong \frac{du(\bar{\boldsymbol{r}})}{da} & \delta_{yx} &\cong \frac{du(\bar{\boldsymbol{r}})}{db} & \delta_{zx} &\cong \frac{du(\bar{\boldsymbol{r}})}{dc} \\ \delta_{xy} &\cong \frac{dv(\bar{\boldsymbol{r}})}{da} & \delta_{yy} &\cong \frac{dv(\bar{\boldsymbol{r}})}{db} & \delta_{zy} &\cong \frac{dv(\bar{\boldsymbol{r}})}{dc} \\ \delta_{xz} &\cong \frac{dw(\bar{\boldsymbol{r}})}{da} & \delta_{yz} &\cong \frac{dw(\bar{\boldsymbol{r}})}{db} & \delta_{zz} &\cong \frac{dw(\bar{\boldsymbol{r}})}{dc} \end{aligned} \tag{A.10}$$

The parameters $\delta_{\alpha\beta}$ can be redefined through the deformation elements ε_{ij} as

$$\delta_{xx} = \varepsilon_{xx} \qquad \delta_{yy} = \varepsilon_{yy} \qquad \delta_{zz} = \varepsilon_{zz} \tag{A.11}$$

the mixed terms are defined as

$$\varepsilon_{xy} = \hat{\boldsymbol{x}}' \cdot \hat{\boldsymbol{y}}' = \left[(1+\delta_{xx})\hat{\boldsymbol{x}} + \delta_{xy}\hat{\boldsymbol{y}} + \delta_{xz}\hat{\boldsymbol{z}}\right] \cdot \left[\delta_{yx}\hat{\boldsymbol{x}} + \left(1+\delta_{yy}\right)\hat{\boldsymbol{y}} + \delta_{yz}\hat{\boldsymbol{z}}\right] \cong \delta_{xy} + \delta_{yx} \tag{A.12}$$

Then it follows

$$\varepsilon_{xy} = \varepsilon_{yx} \cong \delta_{xy} + \delta_{yx} = \frac{du(\bar{\boldsymbol{r}})}{db} + \frac{dv(\bar{\boldsymbol{r}})}{da} \tag{A.13}$$

$$\varepsilon_{yz} = \varepsilon_{zy} \cong \delta_{yz} + \delta_{zy} = \frac{dv(\bar{\boldsymbol{r}})}{dc} + \frac{dw(\bar{\boldsymbol{r}})}{db} \tag{A.14}$$

$$\varepsilon_{zx} = \varepsilon_{xz} \cong \delta_{zx} + \delta_{xz} = \frac{du(\bar{\boldsymbol{r}})}{dc} + \frac{dw(\bar{\boldsymbol{r}})}{da} \tag{A.15}$$

The terms ε_{ij} are the components of the strain tensor, and they completely define the deformation of the solid. Now consider the stress applied on an infinitesimal cubic volume. There are in general 3 components of the stress normal to the surfaces, and 6 more tangential components, 2 for each surface. The stresses are named σ_{ij}, where the first index represents the direction of the applied force and the second index represents the direction normal to the plane in which the force is applied. We then obtain

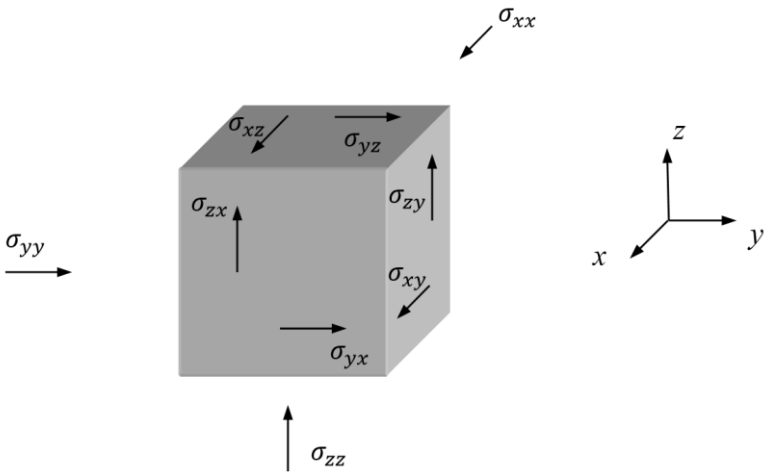

Figure A.1

Imposing the angular acceleration equal to zero, we obtain avrà $\sigma_{xz} = \sigma_{zx}$, $\sigma_{yx} = \sigma_{xy}$ e $\sigma_{zy} = \sigma_{zx}$, thereby the degrees of freedom are reduced from 9 to 6. In conditions of linearity the deformation ε is proportional to the effort σ , then

$$\varepsilon_{ij} = S_{ijkl}\sigma_{kl} \tag{A.16}$$

where the terms *S* compose the tensor of the elastic constants. Similarly

$$\sigma_{ij} = C_{ijkl}\varepsilon_{kl} \tag{A.17}$$

where the terms *C* are the constants of the stiffness tensor. The indices *i, j, k* e *l* have values from 1 to 3, and by convention they are considered:

11 = 1, 32 = 4,
22 = 2, 31 = 5,
33 = 3, 21 = 6.

$$\begin{pmatrix}\varepsilon_1\\ \varepsilon_2\\ \varepsilon_3\\ \varepsilon_4\\ \varepsilon_5\\ \varepsilon_6\end{pmatrix} = \begin{pmatrix}\varepsilon_x\\ \varepsilon_y\\ \varepsilon_z\\ \gamma_{yz}\\ \gamma_{xz}\\ \gamma_{xy}\end{pmatrix} \qquad \begin{pmatrix}\sigma_1\\ \sigma_2\\ \sigma_3\\ \sigma_4\\ \sigma_5\\ \sigma_6\end{pmatrix} = \begin{pmatrix}\sigma_x\\ \sigma_y\\ \sigma_z\\ \tau_{yz}\\ \tau_{xz}\\ \tau_{xy}\end{pmatrix}$$

strain *stress*

ε_x, ε_y and ε_z represent the linear expansion while γ_{yz}, γ_{xz} e γ_{xy} represent the twists. σ_x, σ_y e σ_z represent the normal stresses, or pressures, while τ_{yz}, τ_{xz} e τ_{xy} represent the tangential stresses. The tensors C and S are represented by matrices 6 × 6.

$$C = \begin{pmatrix} C_{11} & C_{12} & C_{13} & C_{14} & C_{15} & C_{16}\\ C_{21} & C_{22} & C_{23} & C_{24} & C_{25} & C_{26}\\ C_{31} & C_{32} & C_{33} & C_{34} & C_{35} & C_{36}\\ C_{41} & C_{42} & C_{43} & C_{44} & C_{45} & C_{46}\\ C_{51} & C_{52} & C_{53} & C_{54} & C_{55} & C_{56}\\ C_{61} & C_{62} & C_{63} & C_{64} & C_{65} & C_{66}\end{pmatrix} \qquad S = \begin{pmatrix} S_{11} & S_{12} & S_{13} & S_{14} & S_{15} & S_{16}\\ S_{21} & S_{22} & S_{23} & S_{24} & S_{25} & S_{26}\\ S_{31} & S_{32} & S_{33} & S_{34} & S_{35} & S_{36}\\ S_{41} & S_{42} & S_{43} & S_{44} & S_{45} & S_{46}\\ S_{51} & S_{52} & S_{53} & S_{54} & S_{55} & S_{56}\\ S_{61} & S_{62} & S_{63} & S_{64} & S_{65} & S_{66}\end{pmatrix}$$

Stiffness constants *Elastic constants*

It can be shown that *S* and *C* are symmetric tensors. If the crystal has a cubic symmetry, the number of independent terms in each tensor drops further. To prove this let us consider a rotation of 120 degrees around the direction [111]: this rotation is a symmetric operation, then the constants of stiffness are conserved. Depending on how the reference system is chosen, after rotation the following permutations are valid:

$x \to y \to z \to x$ $\quad -x \to z \to y \to -x$
$x \to z \to -y \to x$ $\quad -x \to y \to z \to -x$

All the elements on the diagonal have repeated indices, then a change in sign never give problems. In the upper left quadrant, there are elements with an index from 1 to 3, then the type of xx, yy and zz. In this case the change of the sign produced by the rotation is canceled too. All other elements have unpaired indices, and for the rotation of 120 degrees around the [111] they would change the sign, in contradiction with the assumption of symmetry. Therefore, all these elements are zero. For similar reasons of symmetry, the first three terms on the diagonal must be equal, i.e. those with index 11, 22 and 33. Indeed, for the rotations taken into consideration they have to go into one another. Similarly the terms 12, 21, 23, 32, 13 and 31 are equal to each other. Finally, the terms 44, 55 and 66 are equal to each other. Even isotropic materials can be considered systems with cubic symmetry, for which the same deductions made earlier apply. Thus the matrix of the stiffness constants is

$$\begin{pmatrix} C_{11} & C_{12} & C_{12} & 0 & 0 & 0 \\ C_{12} & C_{11} & C_{12} & 0 & 0 & 0 \\ C_{12} & C_{12} & C_{11} & 0 & 0 & 0 \\ 0 & 0 & 0 & C_{44} & 0 & 0 \\ 0 & 0 & 0 & 0 & C_{44} & 0 \\ 0 & 0 & 0 & 0 & 0 & C_{44} \end{pmatrix}$$

and similarly the same for the matrix of the elastic constants. The base in which the matrices [C] and [S] are written is usually chosen taking into account any axes of symmetry of the crystal. Therefore, the matrices must be rewritten with a base useful for the resolution of the problem to treat. Obviously, for the purpose of resolution of the problem, the result is invariant to the chosen basis. Consider for example the case in which the components of the tensor of elastic modules are written in the basis {$\mathbf{e}_1,\mathbf{e}_2,\mathbf{e}_3$}, and you want to rewrite these components in the new base {$\mathbf{m}_1,\mathbf{m}_2,\mathbf{m}_3$. Define now the tensor of rotation Ω through the components of transition $\boldsymbol{m_i \cdot e_j}$

$$\Omega = \begin{pmatrix} \boldsymbol{m_1 \cdot e_1} & \boldsymbol{m_1 \cdot e_2} & \boldsymbol{m_1 \cdot e_3} \\ \boldsymbol{m_2 \cdot e_1} & \boldsymbol{m_2 \cdot e_2} & \boldsymbol{m_2 \cdot e_3} \\ \boldsymbol{m_3 \cdot e_1} & \boldsymbol{m_3 \cdot e_2} & \boldsymbol{m_3 \cdot e_3} \end{pmatrix}$$

This tensor is orthogonal and the following relation holds $\Omega^{\mathrm{T}}\Omega = \Omega\Omega^{\mathrm{T}} = 1$. Then you can calculate the new basis:

$$\sigma_{ij} = \Omega_{\mathrm{jk}}\sigma_{kl}\Omega_{\mathrm{lj}}$$

$$\varepsilon_{ij} = \Omega_{\mathrm{jk}}\varepsilon_{kl}\Omega_{\mathrm{lj}}$$

$$C_{ijkl} = \Omega_{\mathrm{jp}}\Omega_{\mathrm{jq}}C_{pqrs}\Omega_{\mathrm{kr}}\Omega_{\mathrm{ls}}$$

$$S_{ijkl} = \Omega_{\mathrm{jp}}\Omega_{\mathrm{jq}}S_{pqrs}\Omega_{\mathrm{kr}}\Omega_{\mathrm{ls}}$$

The value of the coefficients in the base with greatest symmetry is measured experimentally. The coefficients of silicon and germanium are shown below

	C_{11}	**C_{12}**	**C_{44}**	**S_{11}**	**S_{12}**	**S_{44}**
Dimensione	10^{11} Pa			$(10^{11}$ Pa$)^{-1}$		
Silicio	1,657	0,639	0,796	0,768	-0,214	1,26
Germanio	1,292	0,479	0,670	0,964	-0,260	1,49

With appropriate rotations you can get the tensors [C] and [S] for any crystallographic orientation. Now you can get the Young's modulus and the Poisson's ratio. The Young's modulus is defined as the relationship between pressure and deformation, and it is the measure of the elastic stiffness of a material.

$$E_i = \frac{\sigma_i}{\varepsilon_i} \qquad i = 1,2,3 \tag{A.18}$$

to calculate it, consider a uniaxial deformation $\varepsilon_i = S_{ix}\sigma_x$. Then is results

$$E_i = \frac{1}{S_{ii}} \tag{A.20}$$

If calculated with the components $i = 4,5,6$ it is called the modulus of rigidity

$$G_j = \frac{\tau_j}{\gamma_j} \qquad j = 4,5,6 \tag{A.19}$$

The Poisson ratio is the ratio between the deformation that a solid undergoes in the direction transverse to the applied force and the deformation along the direction of the applied force.

$$\nu = -\frac{\varepsilon_{trasversale}}{\varepsilon_{longitudinale}} \tag{A.21}$$

The purpose of this discussion is to obtain the displacement field for every point in a space define by the analytical form of the vectors $u(r),\ v(r)$. For infinitesimal analysis it results

$$\begin{cases} du = \dfrac{\partial u}{\partial x}dx + \dfrac{\partial u}{\partial y}dy + \dfrac{\partial u}{\partial z}dz \\ dv = \dfrac{\partial v}{\partial x}dx + \dfrac{\partial v}{\partial y}dy + \dfrac{\partial v}{\partial z}dz \\ dw = \dfrac{\partial w}{\partial x}dx + \dfrac{\partial w}{\partial y}dy + \dfrac{\partial w}{\partial z}dz \end{cases} \quad \rightarrow \quad \begin{pmatrix} du \\ dv \\ dw \end{pmatrix} = \nabla u \begin{pmatrix} dx \\ dy \\ dz \end{pmatrix} \tag{A.1}$$

where ∇u is the gradient of displacement. ∇u can be decomposed into a symmetric part and an antisymmetric part $\nabla u = \nabla u_S + \nabla u_A$ where

$$\nabla u_S = \begin{pmatrix} \dfrac{\partial u}{\partial x} & \dfrac{1}{2}\left(\dfrac{\partial u}{\partial y} + \dfrac{\partial v}{\partial x}\right) & \dfrac{1}{2}\left(\dfrac{\partial u}{\partial z} + \dfrac{\partial w}{\partial x}\right) \\ \dfrac{1}{2}\left(\dfrac{\partial u}{\partial y} + \dfrac{\partial v}{\partial x}\right) & \dfrac{\partial v}{\partial y} & \dfrac{1}{2}\left(\dfrac{\partial v}{\partial z} + \dfrac{\partial w}{\partial y}\right) \\ \dfrac{1}{2}\left(\dfrac{\partial u}{\partial z} + \dfrac{\partial w}{\partial x}\right) & \dfrac{1}{2}\left(\dfrac{\partial v}{\partial z} + \dfrac{\partial w}{\partial y}\right) & \dfrac{\partial w}{\partial z} \end{pmatrix} \tag{A.2}$$

$$\nabla u_A = \begin{pmatrix} 0 & \dfrac{1}{2}\left(\dfrac{\partial u}{\partial y} - \dfrac{\partial v}{\partial x}\right) & \dfrac{1}{2}\left(\dfrac{\partial u}{\partial z} - \dfrac{\partial w}{\partial x}\right) \\ -\dfrac{1}{2}\left(\dfrac{\partial u}{\partial y} - \dfrac{\partial v}{\partial x}\right) & 0 & \dfrac{1}{2}\left(\dfrac{\partial v}{\partial z} - \dfrac{\partial w}{\partial y}\right) \\ -\dfrac{1}{2}\left(\dfrac{\partial u}{\partial z} - \dfrac{\partial w}{\partial x}\right) & -\dfrac{1}{2}\left(\dfrac{\partial v}{\partial z} - \dfrac{\partial w}{\partial y}\right) & 0 \end{pmatrix} \tag{A.3}$$

∇u_S describes the deformation of the solid, while ∇u_A describes the rigid rotations of the solid. To analyze the deformation of the solid, the rotations are not useful. Therefore, the displacement gradient can be considered composed only by its symmetric part, neglecting rotations. Then, remembering (A.10), (A.11), (A.13), (A.14) and (A.15), we can write

$$\begin{pmatrix} du \\ dv \\ dw \end{pmatrix} = \begin{pmatrix} \varepsilon_x & {}^1\!/_2\,\gamma_{xy} & {}^1\!/_2\,\gamma_{xz} \\ {}^1\!/_2\,\gamma_{xy} & \varepsilon_y & {}^1\!/_2\,\gamma_{yz} \\ {}^1\!/_2\,\gamma_{xz} & {}^1\!/_2\,\gamma_{yz} & \varepsilon_z \end{pmatrix} \begin{pmatrix} dx \\ dy \\ dz \end{pmatrix} \tag{A.4}$$

7.2 Displacement field of a flexed bar

Consider a flexed bar as in Figure B.1

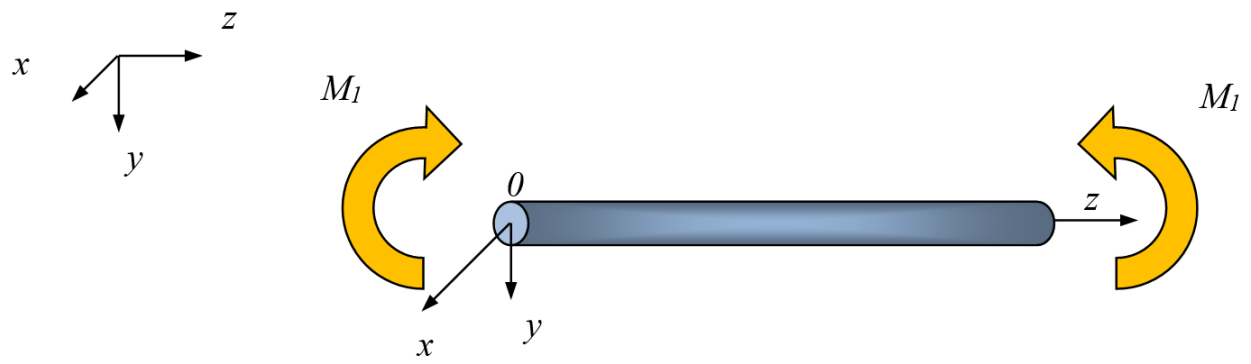

Figure B.1

The problem posed is solved by the semi inverse method of De Saint Venant. In fact, in thin beams, the state of tension and deformation is completely determined as a function of the stress, whatever the external forces from which they derive. In points of the solid at a sufficient distance from the loaded bases, the state of tension not dependent on the particular distribution of external forces, but only by the resultant moment. In this case, the solution for the stress tensor is:

$$\begin{aligned} \sigma_x &= 0 & \tau_{yz} &= 0 \\ \sigma_y &= 0 & \tau_{xz} &= 0 \\ \sigma_z &= \frac{M}{I} y & \tau_{xy} &= 0 \end{aligned} \tag{B.1}$$

where M is the applied moment and I is the moment of inertia. Plus, the following boundary conditions are imposed

$$\begin{aligned} u = v = w = 0 \text{ in the points } &\begin{cases} (x \quad y \quad z) = (0 \quad 0 \quad 0) \\ (x \quad y \quad z) = (0 \quad 0 \quad l) \end{cases} && \text{The ends of the rod are fixed} \\ \frac{dv}{dx} - \frac{du}{dy} &= 0 && \text{The slab is not subjected to rotation} \end{aligned} \tag{B.2}$$

From the theory of elasticity $\varepsilon_{ij} = S_{ijkl}\sigma_{kl}$, then it follows

$$\begin{aligned} \varepsilon_x &= S_{13}\sigma_z \\ \varepsilon_y &= S_{23}\sigma_z \\ \varepsilon_z &= S_{33}\sigma_z \\ \gamma_{yz} &= S_{43}\sigma_z \\ \gamma_{xz} &= S_{53}\sigma_z \\ \gamma_{xy} &= S_{63}\sigma_z \end{aligned} \tag{B.3}$$

Then

$$\frac{du}{dx} = \varepsilon_x = S_{13}\frac{M}{I}y \quad \text{(B.4)} \qquad \frac{du}{dy} + \frac{dv}{dx} = \gamma_{xy} = S_{63}\frac{M}{I}y \quad \text{(B.7)}$$

$$\frac{dv}{dy} = \varepsilon_y = S_{23}\frac{M}{I}y \quad \text{(B.5)} \qquad \frac{du}{dz} + \frac{dw}{dx} = \gamma_{xz} = S_{53}\frac{M}{I}y \quad \text{(B.8)}$$

$$\frac{dw}{dz} = \varepsilon_z = S_{33}\frac{M}{I}y \quad \text{(B.6)} \qquad \frac{dv}{dz} + \frac{dw}{dy} = \gamma_{yz} = S_{43}\frac{M}{I}y \quad \text{(B.9)}$$

and integrating it follows

$$u = S_{13}\frac{M}{I}yx + f(y,z) \quad \text{(B.10)} \qquad S_{13}\frac{M}{I}x + \frac{df(y,z)}{dy} + \frac{dg(x,z)}{dx} = S_{63}\frac{M}{I}y \quad \text{(B.13)}$$

$$v = S_{23}\frac{M}{2I}y^2 + g(x,z) \quad \text{(B.11)} \qquad \frac{df(y,z)}{dz} + \frac{dh(x,y)}{dx} = S_{53}\frac{M}{I}y \quad \text{(B.14)}$$

$$w = S_{33}\frac{M}{I}yz + h(x,y) \quad \text{(B.12)} \qquad \frac{dh(x,y)}{dy} + \frac{dg(x,z)}{dz} + S_{33}\frac{M}{I}z = S_{43}\frac{M}{I}y \quad \text{(B.15)}$$

from (B.14), deriving everything for x it follows

$$\frac{d^2h(x,y)}{dx^2} = 0 \;\rightarrow\; h(x,y) = H_1(y)x + H_2(y) \quad \text{(B.16)}$$

deriving (B.14) by z it follows

$$\frac{d^2f(y,z)}{dz^2} = 0 \;\rightarrow\; f(y,z) = F(y)z + F_2(y) \quad \text{(B.17)}$$

Thus $h(x,y)$ is linear in x while $f(y,z)$ is linear in z. (B.14) becomes

$$F_1(y) + H_1(y) = S_{53}\frac{M}{I}y \quad \text{(B.18)}$$

Therefore $F_1(y)$ and $H_1(y)$ are linear in y. From (B.13), deriving everything by z, it follows

$$\frac{d^2f(y,z)}{dydz} + \frac{d^2g(x,z)}{dxdz} = \frac{dF_1(y)}{dy} + \frac{d^2g(x,z)}{dxdz} = 0 \quad \text{(B.19)}$$

Therefore, since $F_1(y)$ is linear, its derivative with respect to y is a constant. It follows that $g(x,z)$ is linear in x and z. Now derive (B.5) with respect to x.

$$\frac{d^2g(x,z)}{dxdz} + \frac{d^2h(x,y)}{dxdy} = \frac{d^2g(x,z)}{dxdz} + \frac{dH_1(y)}{dy} = 0 \quad \text{(B.20)}$$

from (B.20) and (B.21) it follows

$$\frac{dF_1(y)}{dy} = \frac{dH_1(y)}{dy} \quad \text{(B.21)}$$

then

$$F_1(y) = C_1y + C_{2a} \quad \text{and} \quad H_1(y) = C_1y + C_{2b} \quad \text{(B.22)}$$

Now it is possible to write

$$f(y,z) = C_1yz + C_2z + F_2(y) \quad \text{(B.23)}$$

$$h(x,y) = S_{53}\frac{M}{I}xy - C_1xy - C_2x + H_2(y) \tag{B.24}$$

From (B.13) it follows

$$\frac{dg(x,z)}{dx} + S_{13}\frac{M}{I}x + C_1z = S_{63}\frac{M}{I}y - \frac{dF_2(y)}{dy} = C_3 \tag{B.25}$$

then

$$\frac{dg(x,z)}{dx} = -S_{13}\frac{M}{I}x - C_1z + C_3 \tag{B.26}$$

integrating (B.26) with respect to x it follows

$$g(x,z) = -S_{13}\frac{M}{2I}x^2 - C_1zx + C_3x + G(z) \tag{B.27}$$

Differentiating (B.27) with respect to z it follows

$$\frac{dg(x,z)}{dz} = -C_1x + \frac{dG(z)}{dz} \tag{B.28}$$

From (B.15) it follows

$$\frac{dg(x,z)}{dz} + S_{33}\frac{M}{I}z + S_{53}\frac{M}{I}x - C_1x = S_{43}\frac{M}{I}y - \frac{dH_2(y)}{dy} = C_4 \tag{B.29}$$

Comparing (B.28) and (B.29) and deriving all for x, it follows

$$\frac{d^2g(x,z)}{dxdz} = -C_1 = -S_{53}\frac{M}{I} - C_1 \tag{B.30}$$

The nit is possible to derive C_1

$$C_1 = S_{53}\frac{M}{2I} \tag{B.31}$$

From (B.25) and (B.29) it is possible to derive $F_2(y)$ and $H_2(y)$:

$$\frac{dF_2(y)}{dy} = S_{63}\frac{M}{I} - C_3 \quad \rightarrow \quad F_2(y) = S_{63}\frac{M}{2I}y^2 - C_3y + C_5 \tag{B.32}$$

$$\frac{dH_2(y)}{dy} = S_{43}\frac{M}{I} - C_4 \quad \rightarrow \quad H_2(y) = S_{43}\frac{M}{2I}y^2 - C_4y + C_6 \tag{B.33}$$

Combining (B.28), (B.29) and (B.31) it follows

$$-S_{53}\frac{M}{I}x + \frac{dG(z)}{dz} = C_4 - S_{33}\frac{M}{I}z - S_{53}\frac{M}{I}x \tag{B.34}$$

Therefore, simplifying $-S_{53}\frac{M}{I}x$ and integrating over z it follows

$$G(z) = C_4z - S_{33}\frac{M}{2I}z^2 + C_7 \tag{B.35}$$

Then, combining (B.23), (B.24), (B.27), (B.31), (B.32), (B.33) and (B.35) it follows

$$f(y,z) = S_{53}\frac{M}{2I}yz + C_2 z + S_{63}\frac{M}{2I}y^2 - C_3 y + C_5 \tag{B.36}$$

$$g(x,z) = -S_{13}\frac{M}{2I}x^2 - S_{53}\frac{M}{2I}zx + C_3 x + C_4 z - S_{33}\frac{M}{2I}z^2 + C_7 \tag{B.37}$$

$$h(x,y) = S_{53}\frac{M}{2I}xy - C_2 x + S_{43}\frac{M}{2I}y^2 - C_4 y + C_6 \tag{B.38}$$

Then, it is possible to re-write (B.10), (B.11) and (B.12) with (B.36), (B.37) e (B.38).

$$u = \frac{M}{2I}[2S_{13}xy + S_{53}yz + S_{63}y^2] + C_2 z - C_3 y + C_5 \tag{B.39}$$

$$v = \frac{M}{2I}[S_{23}y^2 - S_{13}x^2 - S_{33}z^2 - S_{53}zx] + C_3 x + C_4 z + C_7 \tag{B.40}$$

$$w = \frac{M}{2I}[2S_{33}yz + S_{53}xy + S_{43}y^2] - C_2 x - C_4 y + C_6 \tag{B.41}$$

We now impose the boundary conditions that the rod is fixed at the top and it does not rotate

$$u = v = w = 0 \begin{cases} (x \quad y \quad z) = (0 \quad 0 \quad 0) \quad \rightarrow \quad C_5 = C_6 = C_7 = 0 \\ (x \quad y \quad z) = (0 \quad 0 \quad l) \quad \rightarrow \quad 0 = C_2 l \quad C_2 = 0 \\ \qquad\qquad\qquad\qquad 0 = -\frac{M}{2I}S_{33}l^2 + C_4 l \quad C_4 = \frac{M}{2I}S_{33}l \end{cases}$$

In the point $(x \quad y \quad z) = (0 \quad 0 \quad 0)$ it results $C_5 = C_6 = C_7 = 0$

In the point $(x \quad y \quad z) = (0 \quad 0 \quad l)$ it results from (B.39), (B.40) e (B.41) respectively the three following equations

$0 = C_2 l \quad \rightarrow \quad C_2 = 0$

$0 = -\frac{M}{2I}S_{33}l^2 + C_4 l \quad \rightarrow \quad C_4 = \frac{M}{2I}S_{33}l$

$0 = 0$

From the condition of non-rotation $\frac{dv}{dx} - \frac{du}{dy} = 0$ it follows

$$\frac{M}{2I}[2S_{13}x + S_{53}z] + C_3 - \frac{M}{2I}[2S_{13}x + S_{33}z] + C_3 = 0 \quad \rightarrow \quad C_3 = 0$$

In conclusion, the following displacement field for the flexed bar applies

$$u = \frac{M}{2I}[2S_{13}xy + S_{53}yz + S_{63}y^2] \tag{B.42}$$

$$v = \frac{M}{2I}[S_{23}y^2 - S_{13}x^2 - S_{33}(z^2 - lz) - S_{53}zx] \tag{B.43}$$

$$w = \frac{M}{2I}[S_{33}y(2z - l) + S_{53}xy + S_{43}y^2] \tag{B.44}$$

Therefore, it is possible to calculate the principal and secondary curvatures and the relationship between the radii of curvature. The principal curvature lies in the yz plane and it is therefore proportional to the second derivative of *v* made with respect to z:

$$\frac{d^2v}{dz^2} = \frac{M}{I} S_{33} \tag{B.45}$$

The anticlastic curvature is in the xy plane and it is proportional to

$$\frac{d^2v}{dx^2} = -\frac{M}{I} S_{13} \tag{B.46}$$

The following ratio between the anticlastic radius of curvature R_a and the principal radius R_p therefore applies

$$\frac{R_a}{R_p} = -\frac{S_{33}}{S_{13}} \tag{B.47}$$

The secondary curvature, called quasi-mosaic curvature, lies in the xy plane and it is proportional to

$$\frac{d^2u}{dy^2} = \frac{M}{I} S_{63} \tag{B.48}$$

The ratio between the quasi-mosaic radius of curvature R_{qm} and the principal radius R_p therefore applies

$$\frac{R_{qm}}{R_p} = \frac{S_{33}}{S_{63}} \tag{B.49}$$

7.3 Displacement field of a square flexed plate

Consider a square plate on which a pair of moments are applied, which for generality can be considered to be different: M1 and M2, respectively along x and y. In terms of the stress tensor, you have

$$\begin{aligned} \sigma_x &= \frac{M_1}{I} z & \tau_{yz} &= 0 \\ \sigma_y &= \frac{M_2}{I} z & \tau_{xz} &= 0 \\ \sigma_z &= 0 & \tau_{xy} &= 0 \end{aligned} \tag{C.1}$$

where *I* is the moment of inertia. Plus, the following boundary conditions are imposed

$$\begin{aligned} \left.\frac{dw}{dx}\right|_0 = \left.\frac{dw}{dy}\right|_0 = 0 & \quad \text{Zero derivative at the center of the plate} \\ \frac{dv}{dx} - \frac{du}{dy} = 0 & \quad \text{The plate is not subjected to rotation} \end{aligned} \tag{C.2}$$

$$u(0) = v(0) = w(0) = 0 \quad \text{The origin does not move}$$

Therefore it follows

$$\begin{aligned}
\varepsilon_x &= S_{11}\sigma_x + S_{12}\sigma_y = \frac{z}{I}(M_1 S_{11} + M_2 S_{12}) = \frac{z}{I}\alpha \\
\varepsilon_y &= S_{21}\sigma_x + S_{22}\sigma_y = \frac{z}{I}(M_1 S_{21} + M_2 S_{22}) = \frac{z}{I}\beta \\
\varepsilon_z &= S_{31}\sigma_x + S_{32}\sigma_y = \frac{z}{I}(M_1 S_{31} + M_2 S_{32}) = \frac{z}{I}\gamma \\
\gamma_{yz} &= S_{41}\sigma_x + S_{42}\sigma_y = \frac{z}{I}(M_1 S_{41} + M_2 S_{42}) = \frac{z}{I}\vartheta \\
\gamma_{xz} &= S_{51}\sigma_x + S_{52}\sigma_y = \frac{z}{I}(M_1 S_{51} + M_2 S_{52}) = \frac{z}{I}\varepsilon \\
\gamma_{xy} &= S_{61}\sigma_x + S_{62}\sigma_y = \frac{z}{I}(M_1 S_{61} + M_2 S_{62}) = \frac{z}{I}\delta
\end{aligned} \tag{C.3}$$

It follows

$$\frac{du}{dx} = \varepsilon_x = \frac{z}{I}\alpha \tag{C.4}$$

$$\frac{dv}{dy} = \varepsilon_y = \frac{z}{I}\beta \tag{C.5}$$

$$\frac{dw}{dz} = \varepsilon_z = \frac{z}{I}\gamma \tag{C.6}$$

$$\frac{du}{dy} + \frac{dv}{dx} = \gamma_{xy} = \frac{z}{I}\delta \tag{C.7}$$

$$\frac{du}{dz} + \frac{dw}{dx} = \gamma_{xz} = \frac{z}{I}\varepsilon \tag{C.8}$$

$$\frac{dv}{dz} + \frac{dw}{dy} = \gamma_{yz} = \frac{z}{I}\vartheta \tag{C.9}$$

Integrating it follows

$$u = \frac{\alpha}{I}zx + f(y,z) \tag{C.10}$$

$$v = \frac{\beta}{I}yz + g(x,z) \tag{C.11}$$

$$w = \frac{\gamma}{2I}z^2 + h(x,y) \tag{C.12}$$

$$\frac{df(y,z)}{dy} + \frac{dg(x,z)}{dx} = \frac{\delta}{I}z \tag{C.13}$$

$$\frac{\alpha}{I}x + \frac{df(y,z)}{dz} + \frac{dh(x,y)}{dx} = \frac{\varepsilon}{I}z \tag{C.14}$$

$$\frac{\beta}{I}y + \frac{dh(x,y)}{dy} + \frac{dg(x,z)}{dz} = \frac{\vartheta}{I}z \tag{C.15}$$

from (C.13) it follows

$$\frac{d^2 f(y,z)}{dy^2} = 0 \;\rightarrow\; f(y,z) = F_1(z)y + F_2(z) \tag{C.16}$$

$$\frac{d^2 g(x,z)}{dx^2} = 0 \;\rightarrow\; g(x,z) = G_1(z)x + G_2(z) \tag{C.17}$$

Therefore $f(y,z)$ is linear in y and $g(x,z)$ is linear in x. (C.13) becomes

$$F_1(z) + G_1(z) = \frac{\delta}{I}z \tag{C.18}$$

Therefore $F_1(z)$ and $G_1(z)$ are linear in z. It follows

$$F_1(z) = C_1 z + C_2 \qquad \text{(C.19)} \qquad G_1(z) = C_3 z + C_4 \qquad \text{(C.20)}$$

$$f(y,z) = C_1 zy + C_2 y + F_2(z) \qquad \text{(C.21)} \qquad g(x,z) = C_3 zx + C_4 x + G_2(z) \qquad \text{(C.22)}$$

Similarly from (C.14) is obtained

$$\frac{d^2 f(y,z)}{dz^2} = \frac{\varepsilon}{I} \;\rightarrow\; \frac{d^2 F_2(z)}{dz^2} = \frac{\varepsilon}{I} \;\rightarrow\; F_2(z) = \frac{\varepsilon}{2I} z^2 + C_5 z + C_6 \qquad \text{(C.23)}$$

Therefore is obtained $f(y,z)$

$$f(y,z) = C_1 zy + C_2 y + \frac{\varepsilon}{2I} z^2 + C_5 z + C_6 \qquad \text{(C.24)}$$

Differentiating (C.14) with respect to x is obtained

$$\frac{d^2 h(x,y)}{dx^2} = -\frac{\alpha}{I} \qquad \text{(C.25)}$$

Differentiating (C.14) with respect to y is obtained

$$\frac{d^2 h(x,y)}{dxdy} + \frac{d^2 f(y,z)}{dzdy} = 0 \qquad \rightarrow \qquad \frac{d^2 h(x,y)}{dxdy} = -C_1 \qquad \text{(C.26)}$$

Differentiating (C.15) with respect to x is obtained

$$\frac{d^2 h(x,y)}{dxdy} + \frac{d^2 g(x,z)}{dxdz} = 0 \qquad \rightarrow \qquad \frac{d^2 h(x,y)}{dxdy} = -C_1 = -\frac{d^2 g(x,z)}{dxdz} \qquad \text{(C.27)}$$

Differentiating (C.15) with respect to y is obtained

$$\frac{d^2 h(x,y)}{dy^2} = -\frac{\beta}{I} \qquad \text{(C.28)}$$

Thus $h(x,y)$ is derived

$$h(x,y) = -\frac{\alpha}{2I} x^2 - C_1 xy - \frac{\beta}{2I} y^2 + C_7 x + C_8 y + C_9 \qquad \text{(C.29)}$$

Differentiating (C.15) with respect to z is obtained

$$\frac{d^2 g(x,z)}{dz^2} = \frac{\vartheta}{I} \;\rightarrow\; \frac{d^2 G_2(z)}{dz^2} = \frac{\vartheta}{I} \;\rightarrow\; G_2(z) = \frac{\vartheta}{2I} z^2 + C_{10} z + C_{11} \qquad \text{(C.30)}$$

Thus $g(x,z)$ is derived

$$g(x,z) = C_3 zx + C_4 x + \frac{\vartheta}{2I} z^2 + C_{10} z + C_{11} \qquad \text{(C.31)}$$

and for comparison of (C.31) and (C.27) is obtained

$$\frac{d^2 g(x,z)}{dxdz} = C_1 = C_3 \qquad \text{(C.32)}$$

Now you can rewrite (C.13) as follows

$$C_1 z + C_2 + C_3 z + C_4 = \frac{\delta}{I} z \tag{C.33}$$

deriving everything by z is obtained

$$C_1 + C_3 = \frac{\delta}{I} \quad \rightarrow \quad C_1 = C_3 = \frac{\delta}{2I} \tag{C.34}$$

So, by combining (C.10), (C.11), (C.12), (C.24), (C.29), (C.32) e (C.34) is obtained

$$u = \frac{\alpha}{I} zx + \frac{\delta}{2I} zy + \frac{\varepsilon}{2I} z^2 + C_2 y + C_5 z + C_6 \tag{C.35}$$

$$v = \frac{\beta}{I} yz + \frac{\delta}{2I} xz + \frac{\vartheta}{2I} z^2 + C_4 x + C_{10} z + C_{11} \tag{C.36}$$

$$w = \frac{\gamma}{2I} z^2 - \frac{\alpha}{2I} x^2 - \frac{\beta}{2I} y^2 - \frac{\delta}{2I} xy + C_7 x + C_8 y + C_9 \tag{C.37}$$

We now impose the boundary conditions.

By $u(0) = v(0) = w(0) = 0$ is obtained $C_6 = C_{11} = C_9 = 0$.

By $\left.\frac{dw}{dx}\right|_0 = 0$ is obtained $C_7 = 0$.

By $\left.\frac{dw}{dy}\right|_0 = 0$ is obtained $C_8 = 0$.

By $\frac{dv}{dx} - \frac{du}{dy} = 0$ is obtained $\frac{\delta}{2I} z + C_4 - \frac{\delta}{2I} z - C_2 = 0 \quad \rightarrow \quad C_4 = C_2$

From (C.13) it is derived

$\frac{df(y,z)}{dy} + \frac{dg(x,z)}{dx} = \frac{\delta}{I} z \quad \rightarrow \quad \frac{\delta}{2I} z + C_2 + \frac{\delta}{2I} z + C_2 = \frac{\delta}{I} z \quad \rightarrow \quad C_4 = C_2 = 0$

From (C.14) it is derived

$\frac{\alpha}{I} x + \frac{df(y,z)}{dz} + \frac{dh(x,y)}{dx} = \frac{\varepsilon}{I} z \quad \rightarrow \quad \frac{\alpha}{I} x + \frac{\delta}{2I} y + \frac{\varepsilon}{I} z + C_5 - \frac{\alpha}{I} x - \frac{\delta}{2I} y = \frac{\varepsilon}{I} z \quad \rightarrow \quad C_5 = 0$

From (C.15) it is derived

$\frac{\beta}{I} y + \frac{dh(x,y)}{dy} + \frac{dg(x,z)}{dz} = \frac{\vartheta}{I} z \quad \rightarrow \quad \frac{\beta}{I} y + \frac{\vartheta}{I} z - \frac{\delta}{2I} x - \frac{\beta}{I} y + \frac{\delta}{2I} x + C_{10} = \frac{\vartheta}{I} z \quad \rightarrow \quad C_{10} = 0$

In conclusion, the displacement field for the square plate applies

$$u = \frac{1}{2I} [M_1 (S_{51} z^2 + S_{61} yz + 2S_{11} xz) + M_2 (S_{52} z^2 + S_{62} yz + 2S_{12} xz)] \tag{C.38}$$

$$v = \frac{1}{2I} [M_1 (S_{41} z^2 + 2S_{21} yz + S_{61} xz) + M_2 (S_{42} z^2 + 2S_{22} yz + S_{62} xz)] \tag{C.39}$$

$$w = \frac{1}{2I} [M_1 (S_{31} z^2 - S_{11} x^2 - S_{12} y^2 - S_{16} xy) + M_2 (S_{32} z^2 - S_{12} x^2 - S_{22} y^2 - S_{26} xy)] \tag{C.40}$$

These three values define completely the three-dimensional displacement field of the plate in the case of a pair of moments applied to the sides of the solid. In this way, one can study the response of the

material for each crystallographic direction. In particular, one can calculate the radius of curvature of the various planes.

The principal curvature along the x axis, in the xz plane, is proportional to the second derivative of the displacement w with respect to x. Then

$$\frac{d^2w}{dx^2} = \frac{1}{I}(-M_1S_{11} - M_2S_{12}) \tag{C.41}$$

Similarly, as regards the principal curvature along the y axis, in the yz plane, we must calculate the second derivative of w with respect to y.

$$\frac{d^2w}{dy^2} = \frac{1}{I}(-M_1S_{12} - M_2S_{22}) \tag{C.42}$$

For any crystallographic direction the terms S_{11}, $S_{12} = S_{21}$ and S_{22} are never zero. The termS_{12} is always smaller and of opposite sign to S_{11}. Similarly S_{21} is always smaller and of opposite sign to S_{22}. You can consider the diagonal terms as those responsible for the principal curvature, while the non-diagonal terms as the anticlasticcontribution to the total curvature.

Following what was done for the principal curvatures, you can calculate the secondary curvatures. For secondary curvatures are those deformations of the solid that are not directly caused by the applied moments, but they follow the main curvature and they depend on the crystallographic direction, so they depend from the anisotropy of the material. In this geometry two secondary curvatures can be calculated, i.e. you can calculate the displacement field for the xz plane or for the yz plane.

First, the deformation on the xz plane is treated. Below you can see a picture of such planes

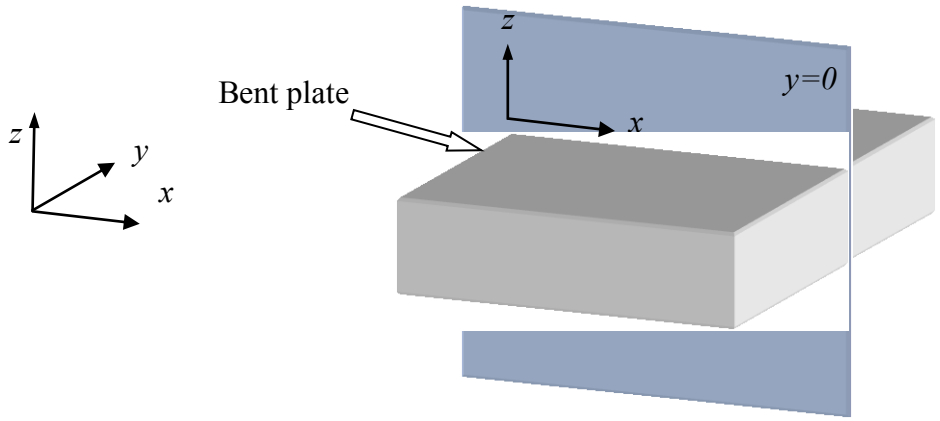

Figure C.1

For these planes the deformation $v(\boldsymbol{x}, \boldsymbol{0}, \boldsymbol{z})$ must consider, that for $M_1 = M_2$ is

$$v = \frac{M}{2I}[(S_{41} + S_{42})z^2 + (S_{61} + S_{62})xz] \tag{C.43}$$

The coefficients S_{ij} in the desired crystallographic direction are obtained from the appropriate rotation matrix of elastic constants. In order to calculate the curvature of the xz planes inside the crystal, it follows

$$\frac{1}{R} \propto \frac{d^2v}{dz^2} = \frac{M}{I}(S_{41} + S_{42}) \tag{C.44}$$

Similarly, you can study the deformation on the plane yz. Below you can see a picture of such planes.

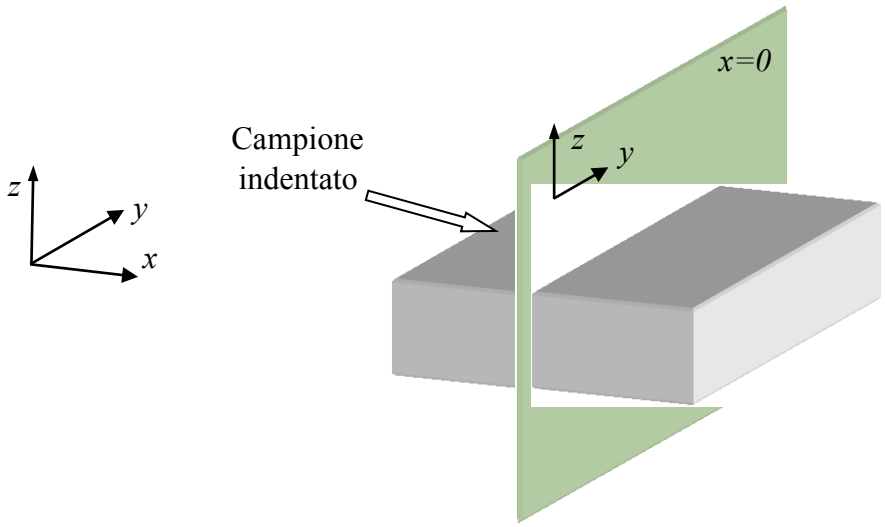

Figure C.2

For these plans the deformation $u(\mathbf{0}, \boldsymbol{y}, \boldsymbol{z})$ must consider, that for $M_1 = M_2$ is

$$u = \frac{M}{2I}[(S_{51} + S_{52})z^2 + (S_{61} + S_{62})yz] \tag{C.45}$$

In order to calculate the curvature of the yz planes inside the crystal, it follows

$$\frac{1}{R} \propto \frac{d^2u}{dz^2} = \frac{M}{I}(S_{51} + S_{52}) \tag{C.46}$$

The secondary curvatures can be analyzed only for certain crystallographic directions. In fact, while the terms of the tensor of elastic constants S_{11}, S_{21}, S_{12} and S_{22} are never zero, the terms S_{41}, S_{42}, S_{52} and S_{52} are not always different from zero. Should they be invalid, there would not be any secondary curvature in the solid. As an example, the matrix of elastic constants for a Si sample with the [110] direction along the z axis is shown in the following

$$S\left[\begin{matrix}1\\1\\-2\end{matrix}, \begin{matrix}1\\1\\1\end{matrix}, \begin{matrix}1\\-1\\0\end{matrix}\right] = \begin{matrix}0.00589997 & -0.000958611 & -0.00155153 & 0 & 0 & -0.00167703\\ -0.000958611 & 0.00530705 & -0.000958611 & 0 & 0 & 0\\ -0.00155153 & -0.000958611 & 0.00589997 & 0 & 0 & 0.00167703\\ 0 & 0 & 0 & 0.0172747 & 0.00335406 & 0\\ 0 & 0 & 0 & 0.00335406 & 0.014903 & 0\\ -0.00167703 & 0 & 0.00167703 & 0 & 0 & 0.0172747\end{matrix}$$

In this matrix the terms $S_{41} = S_{42} = 0$ and $S_{51} = S_{52} = 0$. It may also happen that the two terms, while being non-zero, are one the opposite of the other, as happens for a sample with the main face oriented as (111).

$$S\left[\begin{matrix}1\\0\end{matrix},\begin{matrix}1\\-2\end{matrix},\begin{matrix}1\\1\end{matrix}\right]=\begin{matrix}0.00589997 & -0.00155153 & -0.000958611 & 0.00167703 & 0 & 0\\ -0.00155153 & 0.00589997 & -0.000958611 & -0.00167703 & 0 & 0\\ -0.000958611 & -0.000958611 & 0.00530705 & 0 & 0 & 0\\ 0.00167703 & -0.00167703 & 0 & 0.0172747 & 0 & 0\\ 0 & 0 & 0 & 0 & 0.0172747 & 0.00335406\\ 0 & 0 & 0 & 0 & 0.00335406 & 0.014903\end{matrix}$$

Regarding the samples with the main face (211), we have that $S_{41}+S_{42}$ or $S_{51}+S_{52}$ are not null, and then you can observe secondary curvatures in the xz or yz planes. In fact, for the crystallographic orientation that follows, the tensor of the elastic constants is

$$S\left[\begin{matrix}-1\\1\\0\end{matrix},\begin{matrix}1\\1\\1\end{matrix},\begin{matrix}1\\1\\-2\end{matrix}\right]=\begin{matrix}0.00589997 & -0.000958611 & -0.00155153 & 0.00167703 & 0 & 0\\ -0.000958611 & 0.00530705 & -0.000958611 & 0 & 0 & 0\\ -0.00155153 & -0.000958611 & 0.00589997 & -0.00167703 & 0 & 0\\ 0.00167703 & 0 & -0.00167703 & 0.0172747 & 0 & 0\\ 0 & 0 & 0 & 0 & 0.014903 & 0.00335406\\ 0 & 0 & 0 & 0 & 0.00335406 & 0.0172747\end{matrix}$$

The theoretical shape for the planes xz and yz is shown below:

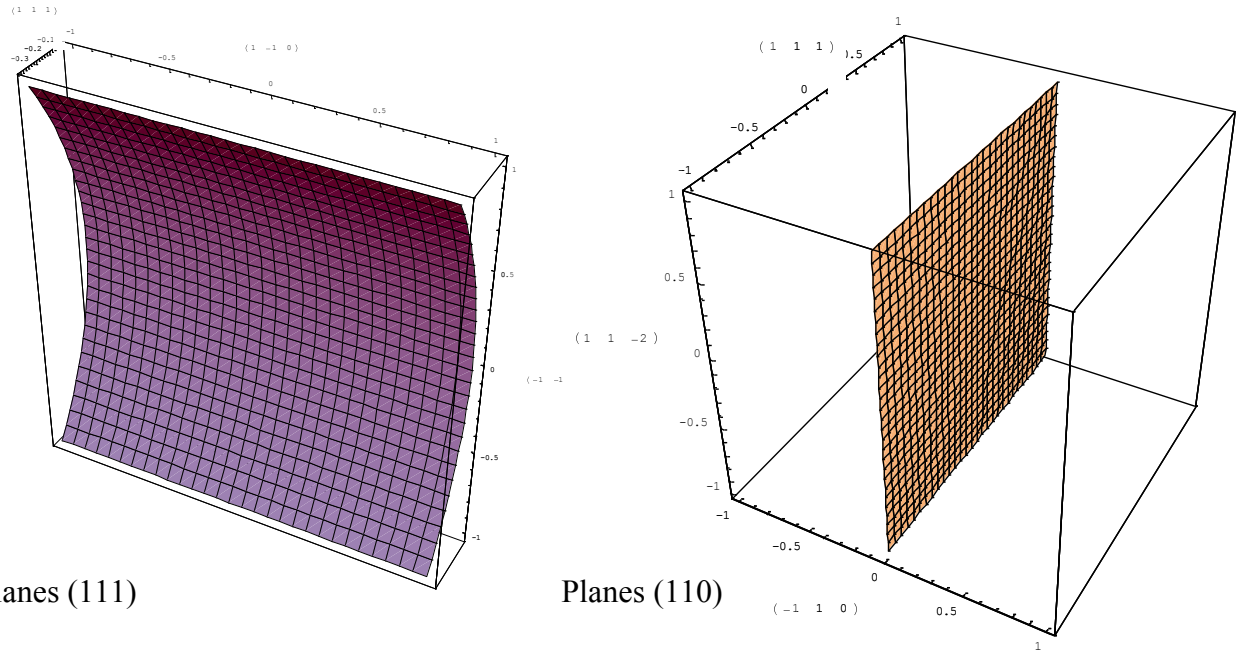

Planes (111) Planes (110)

Figure C.3

In general it is difficult to know analytically M and I, but it can be very helpful to know the relationships that exist between the principal curvatures and the secondary ones. Therefore, even if the moments applied and the moment of inertia of the solid are not known, it is possible to measure the principal curvatures to be able to calculate the secondary curvatures. One can then calculate the ratio between the principal radius of curvature and the secondary radius of curvature on the plane xz

$$\frac{R_s}{R_p} = \frac{S_{12} + S_{22}}{S_{41} + S_{42}} \cong 2{,}6 \tag{C.47}$$

7.4 Displacement field of a rectangular flexed plate

By applying two equal moments to a square crystal plate, it results in a spherical deformation of the larger surface. For a rectangular crystal plate, it can be demonstrated that the ratio between primary and secondary curvatures does not change with respect to the square geometry when the surface stress is constant over the crystal surface. The curvatures of internal planes can be calculated through the displacement field as a function of *u(r)*, *v(r)* and *w(r)*, which are the deformations along the *x*, *y* and *z* axes, respectively. The normal (σ) and tangential (τ) components of the stress tensor are related to the mechanical moments M_x and M_y applied to the crystal as

$$\sigma_x = \frac{M_x}{I_x} z,\ \sigma_y = \frac{M_y}{I_y} z,\ \sigma_z = 0,\ \tau_{yz} = 0,\ \tau_{xz} = 0,\ \tau_{xy} = 0,$$

Where $I_x = \frac{l_x h^3}{12}$, $I_y = \frac{l_y h^3}{12}$ are the moments of inertia of the plate with sides l_x, l_y, thickness *h*, for the stress σ_x, σ_y. By definition, the mechanical moments are:

$$M_x = F_x l_x = \sigma_x A l_x = \sigma_x l_x l_y l_x = \sigma_x l_x^2 l_y$$

$$M_y = F_y l_y = \sigma_y A l_y = \sigma_y l_x l_y l_y = \sigma_y l_x l_y^2$$

Where *A* is the area of the largest face. If the surface stress is uniform $\sigma_x = \sigma_y = \sigma$, and being *u(r)*, *v(r)*, *w(r)* the displacement field along *x*, *y*, *z* direction, the curvature of the largest face along *x*, *y* (principal curvature) is:

$$\frac{1}{R_{Px}} = \frac{d^2 w}{dx^2} = -\left(\frac{M_x}{I_x} S_{11} + \frac{M_y}{I_y} S_{12}\right) = -\sigma \frac{l_x l_y}{\frac{h^3}{12}} (S_{11} + S_{12})$$

$$\frac{1}{R_{Py}} = \frac{d^2 w}{dy^2} = -\left(\frac{M_x}{I_x} S_{12} + \frac{M_y}{I_y} S_{22}\right) = -\sigma \frac{l_x l_y}{\frac{h^3}{12}} (S_{12} + S_{22})$$

S_{ij} being the elastic-tensor coefficients. Choosing y as the direction of the principal curvature, the orthogonal secondary curvature it is:

$$\frac{1}{R_{QM}} = \frac{d^2 v}{dz^2} = \frac{M_x}{I_x} S_{41} + \frac{M_y}{I_y} S_{42} = \sigma \frac{l_x l_y}{\frac{h^3}{12}} (S_{41} + S_{42})$$

The ratio between primary and secondary curvature is

$$\frac{R_{QM}}{R_P} = -\frac{S_{41} + S_{42}}{S_{11} + S_{12}}$$

Thus, as the stress is uniform over the largest surface, the curvatures are independent of the length of the sides of the crystal plate.

7.5 Variation of interplanar spacing

A crystal that is subjected to a curvature along one or more directions change its size also along the directions that are not directly influenced by the curvature. This leads to a change of the interplanar distance in the crystal. Choose a reference system in which the xy plane coincides with the plane of the diffraction lattice that is curved along z, and has the origin of the axes in the center of the crystal. The interplanar distance between the diffraction planes vary continuously along z. In case the crystal has the shape of a curved rod along the longest direction, the deformation along z takes the form (from B.43):

$$w = \frac{M}{2I}\left[S_{23}z^2 - S_{13}x^2 - S_{33}\left(y^2 - \frac{l}{2}|y|\right) - S_{53}yx\right]$$

If the crystal has the form of a square plate to which two moments are applied, the deformation along z takes the form (from C.40):

$$w = \frac{1}{2I}[M_1(S_{31}z^2 - S_{11}x^2 - S_{12}y^2 - S_{16}xy) + M_2(S_{32}z^2 - S_{12}x^2 - S_{22}y^2 - S_{26}xy)]$$

It is possible to hypothesize that the change in the lattice spacing for the diffraction plane considered is uniform along the directions x, y. So it is possible to calculate this variation along a simple direction as x = 0, y = 0, while it is variable along z. Define *d* as the interplanar distance of the lattice when it is not deformed, to the first order the variation of interplanar distance is:

$$\Delta d = d \cdot \left(\frac{\partial}{\partial z} w(x = 0, y = 0, z)\right)$$

at some point z. Define *t* the thickness of the crystal along z, the variation of the interplanar distance along the whole thickness of the crystal is:

$$\Delta d_{tot} = d \cdot \left|\left(\frac{\partial}{\partial z} w(x = 0, y = 0, z)\right)\right|_{z=-t/2}^{z=+t/2}$$

While its variation to the ends of the crystal is:

$$\Delta d_{+} = d \cdot \left(\frac{\partial}{\partial z} w(x = 0, y = 0, z)\right)\Big|_{z=+t/2}$$

$$\Delta d_{-} = d \cdot \left(\frac{\partial}{\partial z} w(x = 0, y = 0, z)\right)\Big|_{z=-t/2}$$

8 Appendix II – List of Publications

- Bellucci, V., Paterno`, G., Camattari, R., Guidi, V., Jentschel, M. & Bastie, P., "High-efficiency diffraction and focusing of X-rays through asymmetric bent crystalline planes" (2015). J. Appl. Cryst., 48
- R Camattari, G Paternò, V Bellucci, V Guidi, "Quasi-mosaicity of (311) planes in silicon and its use in a Laue lens with high-focusing power", Experimental Astronomy (2014), 38, 417-431
- E Bagli, L Bandiera, V Bellucci, A Berra, R Camattari, D De Salvador, G Germogli, V Guidi, L Lanzoni, D Lietti, A Mazzolari, M Prest, VV Tikhomirov, E Vallazza, "Experimental evidence of planar channeling in a periodically bent crystal", The European Physical Journal C (2014) 74 (10), 1-7
- R Camattari, E Dolcini, V Bellucci, A Mazzolari, V Guidi, "High diffraction efficiency with hard X-rays through a thick silicon crystal bent by carbon fiber deposition", Applied Crystallography (2014) 47 (5), 1762-1764
- V Bellucci, R Camattari, V Guidi, P Bastie, "Stack of quasi-mosaic thin lamellae as a diffracting element for Laue lenses", Experimental Astronomy (2014) 38, 25-40
- R Camattari, G Paterno, A Battelli, V Bellucci, P Bastie, V Guidi, "High-efficiency focusing of hard X-rays exploiting the quasi-mosaic effect in a bent germanium crystal", Journal of Applied Crystallography (2014) 47 (2), 799-802
- R Camattari, A Battelli, V Bellucci, V Guidi, "Highly reproducible quasi-mosaic crystals as optical components for a Laue lens", Experimental Astronomy (2014) 37 (1), 1-10
- Vincenzo Liccardo, Enrico Virgilli, Filippo Frontera, Vineeth Valsan, Elisa Buffagni, Claudio Ferrari, Elisa Bonnini, Andrea Zappettini, Vincenzo Guidi, Valerio Bellucci, Riccardo Camattari, "Study and characterization of bent crystals for Laue lenses", Experimental Astronomy (2014) DOI: 10.1007/s10686-014-9425-y
- V Bellucci, R Camattari, V Guidi, "Proposal for a Laue lens relying on hybrid quasi-mosaic curved crystals" (2013) Astronomy and Astrophysics 560, 58
- V Bellucci, R Camattari, V Guidi, "Quasi-mosaicity as a powerful tool to investigate coherent effects" (2013) SPIE Optical Engineering+ Applications, 88610B-88610B-16
- E Virgilli, F Frontera, V Valsan, V Liccardo, V Carassiti, S Squerzanti, M Statera, M Parise, S Chiozzi, F Evangelisti, E Caroli, J Stephen, N Auricchio, S Silvestri, A Basili, F Cassese, L Recanatesi, V Guidi, V Bellucci, R Camattari, C Ferrari, A Zappettini, E Buffagni, E Bonnini, M Pecora, S Mottini, B Negri, "The LAUE project and its main results" (2013) SPIE Optical Engineering+ Applications, 886107-886107-17
- R Camattari, A Battelli, V Bellucci, I Neri, V Guidi, F Frontera "Fabrication of quasi-mosaic Ge crystals for the LAUE project", SPIE Optical Engineering+ Applications (2013) 88610C-88610C-8
- I. Neri, R. Camattari, V. Bellucci, V. Guidi, P. Bastie, "Ordered stacking of crystals with adjustable curvatures for hard X- and γ-ray broadband focusing", Journal of Applied Crystallography (2013) 46 (4), 0-0

- R. Camattari, V. Guidi, V. Bellucci, I. Neri, F. Frontera, M. Jentschel, “Self-standing quasi-mosaic crystals for focusing hard X-rays”, Review of Scientific Instruments (2013) 84, 053110
- V. Guidi, V. Bellucci, R. Camattari, I. Neri, “Curved crystals for high-resolution focusing of X and gamma rays through a Laue lens”, Nuclear Instruments and Methods in Physics Research Section B (2013) 309, 249-253
- V. Bellucci, V. Guidi, R. Camattari, I. Neri, “Calculation of diffraction efficiency for curved crystals with arbitrary curvature radius”, Journal of Applied Crystallography 46 (2), 415-420 2013

Bibliography

Abrosimov, N. V. (2005). Mosaic and gradient SiGe single crystals for gamma ray Laue lenses. *Exp Astron*, 20, 185–194.

Adler, L. W. (2003). Method for combined FDG-PET and radiographic imaging of primary breast cancers. *The Breast Journal* , 9(3), 163 .

Afonin, A. G. (2005). Relativistic Channeling and Related Coherent Phenomena in Strong Fields. *NIMB*, 234, 122.

Amenomori, M. A. (2006). Anisotropy and Corotation of Galactic Cosmic Rays. *Science*, 314:439-443.

Aristov, V. V. (1992). Focusing Properties of a Linear-Phase Bragg-Fresnel Lens. *Jpn. J. Appl. Phys.*, 31, 2616.

Ashcroft, N. W. (1976). *Solid State Physics.* Brooks/Cole, Cengage Learning.

Authier, A. (2001). Dynamical Theory of X-ray Diffraction. *Oxford University Press.*

Authier, A. B. (1970). *Acta Cryst.*, A26, 647.

Ave, M. B.-W. (2008). Composition of Primary Cosmic-Ray Nuclei at High Energies. *The Astrophysical Journal*, 678:262-27.

Baez, A. V. (1952). Resolving power in diffraction microscopy with specialreference to x-rays. *Nature*, 169(4310):963–964.

Balling, P. E. (2009). *NIMB*, 267, 2952.

Ballmoos, P. v. (2005). *Exp. Astron.* , 20, 253–267.

Baricordi, S. B. (2005). *Appl. Phys. Lett.*, 87, 094102.

Barriére, N. G.-X. (2010). *J. of App. Cryst.* , 43, 1519–1521.

Barriére, N. R. (2009). *J. Appl. Cryst.* , 42, 834–845.

Barrière, N. R. (2009). *Journal of Applied Crystallography*, 42, 834 - 845.

Barriére, N. v. (2007). *Proc. SPIE*, 6688, 66880O.

Baryshevsky, v. D. (1980). *Phys. Lett. A*, 77, 61.

Bastie, P. H. (1996). *J. Phys.* , IV. 6.

Bellucci, S. e. (2003). *Phys. Rev. Lett.*, 90, 034801.

Bellucci, S. e. (2004). *Phys. Rev. ST Accel. Beams*, 7, 023501.

Bellucci, V. C. (2011a). *Thin Solid Films*, 520 (3), 1069-1073.

Bellucci, V. C. (2011b). *Exp Astron*, 31, 45–58.

Bellucci, V. C. (2013). Proposal for a Laue lens relying on hybrid quasi-mosaic curved crystals. *Astron. Astrophys.*, 560, 58.

Bellucci, V. C. (2014). Stack of quasi-mosaic thin lamellae as a diffracting element for Laue lenses. *Experimental Astronomy*, 1-16 .

Bellucci, V. G. (2013). Calculation of diffraction efficiency for curved crystals with arbitrary curvature radius. *J. Appl. Cryst.*, 46, 415-420.

Berman, L. S. (2002). Characterization of a Diamond Crystal X-Ray Phase Retarder. *Rev. Sci. Instrum.*, 73, 1502.

Bifano T, J. H. (2002). Elimination of stress-induced curvature in thin film structures. *J. Microelectromechanical Sys.* , 11-5: 592-597.

Blanco, F. L. (2008). Educational Experiments with Cosmic Rays. *Science Education in focus*, pp. 127-172.

Breese, M. (1997). *Nuclear Instruments and Methods in Physics Research Section B: Beam Interactions with Materials and Atoms*, 132, 540.

Burnett, P. a. (1985). An investigation of ion implantation-induced near-surface stresses and their effects in sapphire and glass. *J. Mat. Sci.*, 20, 4624-4646.

Camattari, R. G. (2013). Self-standing quasi-mosaic crystals for focusing hard X-rays. *Rev. Sci. Instrum.* , 84, 053110.

Camattari, R. G. (s.d.). Evidence of high efficiency diffraction of self-standing quasi-mosaic grooved crystals for a high resolution Laue lens. *J. of App. Cryst.*

Caticha, A. (1992). *Phys. Rev. B* , 45 9541.

Chalifoux B., S. E. (2013). High-precision figure correction of x-ray telescope optics using ion implantation. *Proc. SPIE 8861, Optics for EUV, X-Ray, and Gamma-Ray Astronomy VI*, 88610T (September 26, 2013).

Chandrasekaran, K. S. (1959). *Acta Cryst.*, 12, 916-922 .

Della Monica Ferreira, D. e. (2013). Hard x-ray/soft gamma-ray telescope designs for future astrophysics missions. *proc SPIE*, Vol. 8861, 886116.

Dialetis, D. (1978). Generation of coherent X radiation by a relativistic charged particle traveling through a crystal. *Phys. Rev.*, A17, 1113–1122.

Didenko, A. K. (1985). Observation of monochromatic X-ray radiation from 900 MeV electrons transmitting through a diamond crystal. *Phys. Lett. A*, 110, 177–179.

E. Bagli et al. (2013). *Phys. Rev. Lett.* , 110, 175502.

EerNisse, E. P. (1971). *Appl. Phys. Lett.* , 18, 581.

Fainberg, Y. B. (1957). *Soviet Zh. Ehksp. Teor. Fiz.,* , 32, 883 .

Fainberg, Y. K. (1957). Energy losses by a charged particle passing through a laminar dielectric. *Zh. Eksp. Teor. Fiz.*, 32, 883–895.

Frontera, F. &. (2010). *X-Ray Optics and Instrumentation*.

Frontera, F. P. (2006). *Proc. SPIE*, 6266, 626–627.

Frontera, F. V. (2013). *SPIE Conference Series*, Optics for EUV, X-Ray, and Gamma-Ray Astronomy VI, vol. 8861.

Gogotsi, Y. B. (1999). *Semicond. Sci. Technol.* , 14, 936-944.

Guidi V., B. N. (2011a). *Optics for EUV, X-Ray, and Gamma-Ray Astronomy V*, 8147, 81471E–81471E–7.

Guidi V., B. V. (2011b). *J Appl Crys*, 44, 1255–1258.

Guidi V., M. A. (2009). *J. Phys. D: Appl. Phys.*, 42 182005.

Guidi, V. A. (2005). Relativistic Channeling and Related Coherent Phenomena in Strong Fields. *NIMB*, 234, 40.

Guidi, V. B. (2013). *Nucl. Instrum. Methods Phys. Res. Sect. B*, 309, 249–253.

Guidi, V. L. (2007). *Applied Physics Letters* , 90, 114107.

Guinier, A. T. (1949). *Acta Crystallogr.* , 2, 133-138.

Halloin, H. &. (2005). *Exp. Astron.*, 20, 151–170.

Hamelin B., B. P. (1998). *J. Phys.* , IV. 8, 3-8.

Hamelin B., B. P. (2002). *Proceedings of SPIE* , 5168, 471-481.

Hannon, J. P. (1988). *Phys. Rev. Lett.*, 61, 1245.

Harrison, F. A. (2013). The nuclear spectroscopic telescope array (NuSTAR) high-energy x-ray mission. *ApJ*, 770, 103.

Harrison, J. J. (2012). *Phys. Rev. ST Accel. Beams*, 15, 070703.

Huygens, I. M. (2007). Etching of Germanium in Hydrogenperoxide Solutions. *ECS Trans.*, 6, 375.

Itoh. M., H. M. (1991). An ultralow stress tungsten absorber for xray masks. *J. Vac. Sci. Technology B*, 9: 165-168.

IUCr, e. f.-r. (2015, 1 14). *CHAPTER 15 Dynamical X-ray Optics; Electron and Neutron Diffraction*. Tratto da International Union of CRYSTALLOGRAPHY: http://www.iucr.org/publ/50yearsofxraydiffraction/full-text/dynamical-x-ray-optics

Ivanov, Y. P. (2005). *JETP Letters*, 81, 99–101.

Keitel, S. M. (1999). *Acta Cryst.* , A55, 855–863.

Kittel, C. (1986). *Introduction to Solid State Physics.* John Wiley & Sons, Inc.

Knödlseder J., J. P. (2005). The all-sky distribution of 511 keV electron-positron annihilation emission. . *Astronomy & Astrophysics* , 441, 513–532.

Knodlseder, J. v. (2009). *Exp. Astron.*, 23, 121–138.

KOROL, A. V. (2004). *International Journal of Modern Physics E*, 13, 867.

Kuiper, P. e. (1993). *Phys. Rev. Lett.*, 70, 1549.

Kumakhov, M. A. (2000). X ray capillary optics: history of development and present status. *Proceedings of SPIE,*, 4155, 2–12.

L., T.-M. N. (1969). The Influence of the Medium on High Energy Processes at High Energies. *Publishing House of Academy of Science of Armenia, Yerevan*.

Lai, B., Yun, W. B., Legnini, D., Xiao, Y., Crzas, J., Viccaro, P., . . . Grella, L. &. (1992). Hard x-ray phase zone plate fabricated by lithographic techniques. *Applied Physics Letters*, 61, 1877-1879.

Lengeler, B. T. (1998). *Journal of Appl Phys*, 84, 11.

Leo, W. R. (1994). *Techniques for Nuclear and Particle Physics Experiments: A How-to Approach.* Springer-Verlag.

Lindhard, J. D. (1965). *Mat. Fys. Medd.*, 34, 14 .

Lindquist, T. R. (1967). A focusing X-ray telescope for use in the study of extraterrestrial X-ray sources in the energy range 20-140 keV. *Canadian Journal of Physics. Proceedings of the 10th International Conference on Cosmic Rays, Calgary, Alberto, June 19-30, 1967*, vol. 46, p. 1103 46 1103.

Loffredo, G. F. (2005). *Experimental Astronomy*, 20, 413 .

MacDonald, C. A. (2010). Focusing Polycapillary Optics and Their Applications. *X-Ray Optics and Instrumentation*, 867049, 17.

Madsen, K. K. (2009). *Proc. SPIE*, 7437, 743716.

Malgrange, C. (2002). *Cryst. Res. Tech.* , 37, 654–662.

Meek, R. L. (1971). *Radiat. Eff.*, 11, 139.

Milman, Y. V. (2007). *Sci. Sinter.*, 39 67-75.

Misra, A. F. (1999). Residual stresses and ion implantation effects in Cr thin films,. *Nuclear Instruments and Methods in Physics Research B*, 148, 211-215.

Neri, I. C. (2013). Ordered stacking of crystals with adjustable curvatures for hard X- and [gamma]-ray broadband focusing. *J. Appl. Cryst.*, 46, 953-959.

Orlandini, M. (2008/2009). Handouts for the course Astrophysical Measures. p.139-145.

Pellicciotta, D. F. (2006). *IEEE Transactions on Nuclear Science*, 53, 253-258.

Perlmutter, S. A. (1999). Measurements of Omega and Lambda from 42 High-Redshift Supernovae. *ApJ*, 517, 565-586.

Phillips, M. (1993). The absolute magnitudes of Type IA supernovae. *ApJ*, 413, L105-L108.

Pisa, A., Frontera, F., Loffredo, G., Pellicciotta, D. & Auricchio, N. (2005). *Exp. Astron.*, 20, 219–228.

Prins, J. A. (1930). *Z. Phys.*, 63, 477-493.

PSI. (2015, 1 9). *http://www.psi.ch/lmn/diffractive-x-ray-lenses*. Tratto da PSI: http://www.psi.ch/lmn/diffractive-x-ray-lenses

Rekveldt, M. T. (1983). *Nucl. Instrum. Methods.* , 215, 521-527.

Riess, A. G. (1998). Observational Evidence from Supernovae for an Accelerating Universe and a Cosmological Constant. *AJ*, 116, 1009-1038.

Roa, D. S.-G. (2005). *Exp. Astron.* , 20, 229–239.

RXoptics. (2015, 1 9). *REFRACTIVE X-RAY LENSES*. Tratto da RXOPTICS: http://www.rxoptics.de/xrayoptics.html

Sansosti, T. M. (2015, 1 9). *Compound Refractive Lenses for X-Rays*. Tratto da Laser Center: http://laser.physics.sunysb.edu/~tanya/report1/

Sato, S. H. (2000). Polarization-Independent Optical Properties of Liquid Crystal Polarization-Converting Devices. *Jpn. J. Appl. Phys.*, 39, 3442.

Scandale, W. A. (2014). Mirroring of 400 GeV/c protons by an ultra-thin straight crystal. *Physics Letters B*, 734, 1–6.

Scandale, W. C. (2008). *Phys. Rev. ST Accel. Beams*, 11, 063501.

Scandale, W. S. (2007). *Phys. Rev. Lett.* , 98, 154801.

Schmahl, G. R. (1993). X-ray microscopy studies. *Optik*, 93, 95-102.

Schneider-Muntau, H. T. (2004). *Applied Superconductivity*, IEEE Transactions on 14, 1245.

Shchagin, A. P. (1990). *Phys. Lett. A* , 148 485.

Shchagin, A. V. (1993). Absolute differential yield of parametric X-Ray radiation, Preprint KFII 93-32, Kharkov, September 6-10.1993, Tomsk. Russia. *Pmt. Int. Symp. Radiation of Relativistic Electrons in Periodical Structures*, p. 62-75.

Skinner, G. K. (2004). Coded mask imagers when to use them - and when not. *New Astronomy Reviews,*, Volume 48, Issue 1-4, p. 205-208.

Smither, R. (2008). High resolution x-ray and gamma ray imaging using diffraction lenses with mechanically bent crystals. *US 7468516 B2,*.

Staudenmann, J.-L. L. (1985). Determination of beam polarization from integrated Borrmann intensities. *J. Appl. Cryst.*, 18, 519-527.

Stockmeier, M. M. (2008). *J. Appl. Cryst.*, 41, 754-760.

Stöhr, J. (1999). *J. Magn. Magn. Mater.*, 200, 470.

Stoney, G. G. (1909). *Proc. R. Soc. A*, 82, 172.

Sumbaev, O. (1957). *Soviet Phys. JETP*, 5, 1042–1044.

Tamulevicius, S. P. (1998). Integral stress in ion-implanted silicon. *J. Phys. D: Appl. Phys.* , 31 2991–2996.

Ter-Mikaelian, M. (1969). High-Energy Electromagnetic Processes in Condensed Media. *in Russian: Edition of Armenian Academy of Science, Erevan, 1969; in English: Wiley-Interscience, New York, 1972*.

Timoshenko, S. (1970). *Theory of Elasticity.* New-York NY: McGraw-Hill Companies.

Unisantis. (2015, 1 10). *X-ray Polycapillary Optics (X-ray lenses)*. Tratto da Unisantis: http://www.unisantis.com/kumakhov-optics.html

Volkert, C. A. (1990). in Beam-Solid Interactions: Physical Phenomena. *MRS Symposia Proceedings, edited by J. A. Knapp, P. Borgesen, and R. A. Zuhr (Materials Reseach Society, Pittsburgh, PA,* , p. 635.

Vook, F. L. (1962). *Phys. Rev.*, 125, 855.

Vorobiev, S. A. (1985). *JETP Letters* , 41, 1.

Wanga, Q. I. (2004). Curvature-based residual stress measurement for ion-implanted stainless-steel sheet. *Vacuum*, Volume 75, Issue 3, 26 July 2004, Pages 225–229.

White, J. (1950). X-ray diffraction by elastically deformed crystals. *J. Appl. Phys.*, 21 855–859.

Wikipedia. (2004).

Wilkins, S. B. (2003). *Phys. Rev. Lett.*, 90, 187201.

Wolf, S. a. (1986). Silicon Processing for the VLSI Era, Vol. 1: Process Technology]. *Lattice Press*, 283-308.

Zachariasen, W. H. (1945). *Theory of X-rays Diffraction in Crystals.* New York: Wiley.